Technische Universität München
Fakultät für Physik

Max-Planck-Institut für Physik
(Werner-Heisenberg-Institut)

Doctoral Thesis

Surface Characterization of Segmented Germanium Detectors with Alpha, Beta and Gamma Particles

by Lukas Hauertmann

September 1, 2021

Fakultät für Physik der Technischen Universität München

Surface Characterization of Segmented Germanium Detectors with Alpha, Beta and Gamma Particles

Lukas Martin Hauertmann

Vollständiger Abdruck der von der promotionsführenden Einrichtung Fakultät für Physik der Technischen Universität München zur Erlangung des akademischen Grades eines Doktors der Naturwissenschaften (Dr. rer. nat.) genehmigten Dissertation.

Vorsitzender: Prof. Dr. Alejandro Ibarra

Prüfende der Dissertation:

1. Prof. Dr. Allen Caldwell
2. Prof. Dr. Lothar Oberauer

Die Dissertation wurde am 01.09.2021 bei der Technischen Universität München eingereicht und durch die promotionsführende Einrichtung Fakultät für Physik am 13.10.2021 angenommen.

Acknowledgements

There are many people I want to thank for helping me in all different stages of my life and enabling me to achieve everything I have achieved so far.

First of all, I want to thank my whole family. Especially my parents, Sonja and Manfred, who were incredible great parents by enabling me basically everything and supporting me in every decision I made.

I also want to thank all my friends. I cannot list all of them. But here, I want especially to thank Bianca, Fabi, Ferdi and Martin as we endured the study of physics together and had a great time.

And I want to thank Iris, who has been an incredible good supervisor from whom I learned so much. But not only her, I also want to thank Oliver, Xiang, Chris, Anna, Felix H., Felix F., Bela and Allen and all other colleagues. They all made my time at the institute really wonderful.

"The greatest teacher, failure is."
$\sim$ *Yoda*

Abstract

A detailed study of the response of two n-type true-coaxial germanium detectors to alpha, beta and gamma particles is presented. Alpha- and beta-induced events were a substantial part of the background events in $0\nu\beta\beta$ searches performed by the GERDA and MAJORANA collaborations. They are also expected to be important for the follow-up experiment LEGEND. Basically all alpha events induced on passivated surfaces are heavily affected by charge trapping, which can move their observed energy into the signal window. However, their identification is relatively easy, even if only the central contact of a detector is read out, because the trapping leaves a signature on the shape of the pulse of these events. Up to 50 % of beta-induced events on passivated floating surfaces are also affected by charge trapping, albeit a much smaller share of charge carriers are trapped. Thus, there is no signature left on the central pulse. These events can only be identified by analyzing data provided by the multi channel read-out as provided by the experimental detectors investigated for this thesis. The data from a single read-out channel as planned for LEGEND are not sufficient and the continuous spectra of beta sources can lead to unidentified events observed in the signal window. This is important for the selection of detector technologies for LEGEND.

The amount of charge trapping in alpha events on the passivated surfaces was affected by the crystal axes for both detectors. The observed energy of alpha-induced events differs by up to 1 MeV, depending on whether the events are located close to a fast or close to a slow axis. In previous studies, the data were insufficient to detect such an effect.

The effect of the metallization of a segment of a detector underneath a floating surface on the detector response was studied by comparing data taken before and after the segment was fully metallized. Before the metallization, extremely slow segment signals were observed as well as a strong dependence of the signal speed on the distance of the event to the read-out contact. The segment signals were significantly faster after the metallization. However, there was still a small but measurable effect of the distance to the contact.

A new open-source pulse-shape simulation software, *SolidStateDetectors.jl*, for germanium detectors is presented in detail. It features fast 3D field calculations of arbitrary detector geometries including the environment. Its modular structure allows easy implementation of new and improved models describing the physics of a germanium detector. A first model of probabilistic trapping of the charge carriers during the drift through a “surface channel” was developed. The impurity distributions, needed as input to the field calculations, were tuned by fits to capacitance data. The resulting improved pulse shape simulation will improve the evaluation of the experimental backgrounds in experiments like LEGEND, which are based on existing and to be developed germanium detectors.

Abstrakt

Eine Studie über durch Alpha-, Beta- und Gammateilchen ausgelösten Ereignisse in zwei n-type Germaniumdetektoren wurde präsentiert. Alpha- und Betaereignisse bildeten einen Großteil des Untergrundes in den Experimenten GERDA und MAJORANA, mit denen nach $0\nu\beta\beta$ gesucht werden. Auch in dem Folgeexperiment LEGEND wird dies erwartet. In praktisch allen Alphaereignissen auf passivierten Oberflächen bleiben ein substantieller Teil der Ladungsträger im Kristall stecken und werden nicht gesammelt. Das führt dazu, dass die für diese Ereignisse gemessene Energie gegenüber der deponierten Energie stark reduziert ist und sie dadurch in das Signalfenster der Suche nach $0\nu\beta\beta$ fallen können. Allerdings sind Alphaereignisse leicht zu erkennen, da die stark unvollständige Ladungssammlung eine klare Signatur in den gemessenen Pulsen verusacht. Bis zu 50 % der Betaereignisse auf passivierten Oberlächen sind ebenfalls von unvollständiger Ladungssammlung betroffen. Allerdings ist ein weit geringerer Anteil der Ladungsträger betroffen, sodass keine klare Pulssignatur im Zentralkontakt entsteht. Diese Ereignisse können nur durch die Analyse der Pulse der zusätzlichen Kanälen der beiden Testdektoren, die für diese Studie untersucht wurden, identifiziert werden. Das ist wichtig für die Auswahl der Detektortechnologie in LEGEND.

Der Anteil der Ladungsträger in Alphaereignissen, die unter passivierten Oberflächen nicht gesammelt werden können, hängt von der relativen Position der Ereignisse zu den Kristallachsen ab. Je nachdem, ob Alphaereignisse nahe einer schnellen oder langsamen Ache lagen, wurde ein Unterschied von etwa 1 MeV in der rekonstruierten Energie beobachtet. In vorherigen Studien waren die Daten nicht ausreichend um dies zu beobachten.

Der Einfluss der Metallisierung eines Detektorsegments unterhalb einer potentialfreien Oberfläche auf das beobachtete Signal wurde durch den Vergleich von Daten untersucht, die vor und nach der Metallisierung des Segments genommen wurden. Vor der vollen Metallisierung wurden extrem lange Segmentsignale, sowie eine starke Abhängigkeit der Signalgeschwindigkeit vom Abstand des Ereignisses zum Segmentkontakt beobachtet. Nach der vollen Metallisierung waren die Segmentsignale wesentlich schneller. Es bestand jedoch weiterhin eine kleine, aber messbare, Abhängigkeit der Signalgeschwindigkeit vom Abstand des Ereignisses zum Segmentkontakt.

Eine neue Open-Source Simulationssoftware, *SolidStateDetectors.jl*, für Germaniumdetektoren wurde detailiert vorgestellt. Sie ermöglicht schnelle 3D Feldberechnungen beliebiger Detektorgeometrien und Umgebungen. Die modulare Struktur der Softwar erlaubt die einfache Implementierung von neuen und verbesserten Modellen, die die Physik von Germaniumdetektoren beschreiben. Ein erstes Modell für das probabilistische Stoppen von Ladungsträgern in einem sogenannten "Oberlächenkanal" wurde entwickelt. Die Verunreinigungsdichte, die eine Eingabe für die Feldberechnung ist, wurde durch Fitten an Kapazitätsdaten angepasst. Solche verbesserten Signalsimulationen können die Auswertung der experimentellen Untergründe in Experimenten, die wie LEGEND Germaniumdetektoren verwenden, verbessern.

Contents

List of Figures

List of Tables

Introduction and Physics Motivation

As neutrinos have very small interaction cross-sections, their properties are hard to investigate. For a long time, neutrinos were thought to be massless Dirac particles and consequently were included in the standard model (SM) with zero Yukawa couplings to the Higgs field. The observation of neutrino oscillations changed the picture [1]. These oscillations can only be explained if at least two of the neutrinos have non-zero masses.

The oscillation experiments can, however, only provide the mass differences between the neutrinos, they can not provide the absolute mass scale. In addition, they only provide limited information on the ordering of the mass eigenstates, ν_1, ν_2 and ν_3. While solar neutrino oscillation reveal $m_{\nu_1} < m_{\nu_2}$, the sign of $m_{\nu_3} - m_{\nu_1}$ remains undetermined. This problem is known as the mass ordering problem [2]. Upcoming experiments have been designed to provide the data within the next decade to determine which ordering occurs in nature [3, 4].

Another open question concerns the nature of neutrinos, i.e. whether they are, as originally assumed, Dirac or in reality Majorana particles [5]. If they are Majorana particles, they are their own antiparticles. This property would be revealed by detecting neutrinoless double beta decays ($0\nu\beta\beta$) [6]:

$$^{A}_{Z}\mathrm{X} \rightarrow {}^{A}_{Z+2}\mathrm{Y} + 2e^{-} \qquad .$$

As neutrinos are very hard to detect anyhow, this seems at first sight far fetched but the conservation of energy is the key. In this special nuclear decay, two neutrons convert coherently to two protons and only two electrons are emitted. They carry the full energy of the decay, the so-called Q-value. Thus, an exact measurement of the combined energy of the electrons provides the signal. So far, $0\nu\beta\beta$ decay has not been observed. In contrast, neutrino accompanied double beta decay ($2\nu\beta\beta$) has been observed for many isotopes.

The observation of $0\nu\beta\beta$ would, more generally, be the first observation of lepton number violation. This is not part of the SM, but it could be a part of the solution to the matter-antimatter asymmetry problem in the universe [7].

At the time of writing, a number of experimental collaborations had completed searches for $0\nu\beta\beta$. One of them was the GERmanium Detector Array (GERDA) collaboration [8], who searched for $0\nu\beta\beta$ of the isotope ^{76}Ge. Germanium is very suitable for $0\nu\beta\beta$ searches, since, as a semiconductor, it can be used as source and detector at the same time, featuring a very high detection efficiency. GERDA published the best lower limit on the $0\nu\beta\beta$ half-life, $T_{1/2}^{0\nu\beta\beta} > 1.8 \times 10^{26}$ y [9, 10, 11]. Such low half-lifes correspond to very low event rates, e.g., for one kilogram of ^{76}Ge, only ≈ 0.06 $0\nu\beta\beta$ decays per year would be expected for a half-life of $T_{1/2}^{0\nu\beta\beta} = 1.0 \times 10^{26}$ y. Experiments looking for such low event rates, are called low-background experiments because the such low numbers of signal events can only be identified if the backgrounds are extremely low [12].

In 2017, a new collaboration was formed: The Large Enriched Germanium Experiment for Neutrinoless double beta Decay (LEGEND) [13]. This experiment will be realized in two phases. The first phase, LEGEND 200, will be based on ≈ 200 kg of germanium detectors enriched in ^{76}Ge, deployed in the GERDA infrastructure. The final target is a ton-scale experiment, LEGEND 1000, which will probably be similar to GERDA, but improved with respect to background identification. A deep understanding of the germanium detectors is essential to improve background identification beyond what has been achieved for GERDA.

Germanium detectors measure the amount of deposited energy inside very precisely by measuring the created charges [14]. More information about the event, e.g. what kind of particle deposited the energy in the germanium or the position of the interaction, can be obtained through the study of the time evolution of the resulting signal. The time evolution is particularly important for the identification of background events [15]. This is also true for events at the surface of the detector, where the energy reconstruction can fail.

In this thesis, results of studies on specially designed germanium detectors are presented. These studies were performed to provide a better understanding of the fundamental properties of germanium detectors. The focus is on their response to events at or close to their surfaces. A large fraction of the background in GERDA was caused by such events [16, 17].

Chapter 1: An overview of neutrinos, neutrino accompanied and neutrinoless double beta decay is given. Furthermore, the crucial experimental design criteria for experiments searching for $0\nu\beta\beta$ are discussed and an overview of the germanium based experiments GERDA, MAJORANA and LEGEND is given.

Chapter 2: The relevant physics for germanium detectors is summarized. This includes solid-state physics, especially the working principle of diode-based detectors and the physics of the relevant interactions of particles with matter.

Chapter 3: A detailed introduction of germanium detectors including an overview of the technicalities is given.

Chapter 4: The experimental test stand GALATEA used for the measurements presented in this thesis is introduced.

Chapter 5: An overview of the total simulation chain for germanium detector signals is given. The new pulse-shape simulation software *SolidStateDetectors.jl* [18] is introduced. The development of *SolidStateDetectors.jl* was a major part of the work for this thesis.

Chapter 6: The general data taking and alignment procedures for germanium detectors in GALATEA are presented. In addition, the tuning of the parameters of the simulation by analyzing characterization measurements is demonstrated.

Chapter 7: The response of two germanium detectors, Super Siegfried and Siegfried III, to alpha and gamma particles is presented. The response of Super Siegfried is compared to its previous response before the detector became fully metallized.

Chapter 8: The response of Super Siegfried to beta particles is presented and compared to the response to alpha particles.

Chapter 9: First simulations of surface effects with *SolidStateDetectors.jl* are presented. This includes first models of a surface channel and trapping of charge carriers during the drift.

Chapter 1: Neutrinoless Double Beta Decay

The goal of the search for $0\nu\beta\beta$ is, besides observing a lepton number violating process, to learn something about neutrinos. The current knowledge on neutrinos is summarized briefly, the SM process $2\nu\beta\beta$ is described, and the beyond SM process $0\nu\beta\beta$ is discussed. An overview covering the current experimental approaches searching for $0\nu\beta\beta$ using ^{76}Ge is given. Alternative searches using Xenon and other isotopes are not discussed in detail, an overview can be found elsewhere [6].

1.1 Neutrinos

In the currently most accepted model, there are three types (flavors) of light neutrinos, ν_α, one for each leptonic family: the electron neutrino, ν_e, the muon neutrino, ν_μ, and the tau neutrino, ν_τ. They are quantum mechanical superpositions of three mass eigenstates, ν_i with $i \in [1, 2, 3]$,

$$|\nu_\alpha\rangle = \sum_{i=1}^{3} U_{\alpha i} |\nu_i\rangle \qquad , \tag{1.1}$$

where $U_{\alpha i}$ are elements of the lepton mixing matrix, the so-called Pontecorvo-Maki-Nakagawa-Sakata (PMNS) matrix:

$$U = \begin{bmatrix} c_{12}c_{13} & s_{12}c_{13} & s_{13}e^{-i\delta} \\ -s_{12}c_{23} - c_{12}s_{23}s_{13}e^{i\delta} & c_{12}c_{23} - s_{12}s_{23}s_{13}e^{i\delta} & s_{23}c_{13} \\ s_{12}s_{23} - c_{12}c_{23}s_{13}e^{i\delta} & -c_{12}s_{23} - s_{12}c_{23}s_{13}e^{i\delta} & c_{23}c_{13} \end{bmatrix} \times \begin{bmatrix} e^{i\alpha_1} & 0 & 0 \\ 0 & e^{i\alpha_2} & 0 \\ 0 & 0 & e^{i\delta} \end{bmatrix} \qquad , \tag{1.2}$$

where $c_{ij} = \cos\theta_{ij}$ and $s_{ij} = \sin\theta_{ij}$ represent the three neutrino mixing angles θ_{12}, θ_{23} and θ_{13}, δ is the CP violating Dirac phase, and α_1 and α_2 are the two Majorana phases, which do not exists if neutrinos are Dirac particles.

The mass eigenstates, ν_i, are eigenstates of the Hamiltonian of a free particle whereas the flavor states, ν_α, are eigenstates of the Hamiltonian describing their interactions. Neutrinos are produced and interact as their flavor eigenstates but propagate, in vacuum, as their mass eigenstates.

Neutrinos do not carry electric charge and interact only via the weak force; gravitation can in general be neglected in particle physics.

1.2 Neutrino Accompanied Double Beta Decay

Neutrino accompanied double beta decay, $2\nu\beta\beta$, is a second order nuclear decay where two neutrons decay into two protons and two electrons and two electron antineutrinos are emitted:

$$^{A}_{Z}\mathrm{X} \rightarrow {}^{\;\;A}_{Z+2}\mathrm{Y} + 2e^{-} + 2\bar{\nu}_e \qquad . \tag{1.3}$$

Here, X is the isotope with the atomic number A and Z protons. Y presents the corresponding daughter isotope.

The total energy released in the decay, Q, is divided between the four final state particles, resulting in a continuous spectrum for the sum of the energies of the two electrons. This is similar to the energy spectrum of the single electron emitted in "normal" beta decays. The spectrum is illustrated in Fig. 1.1.

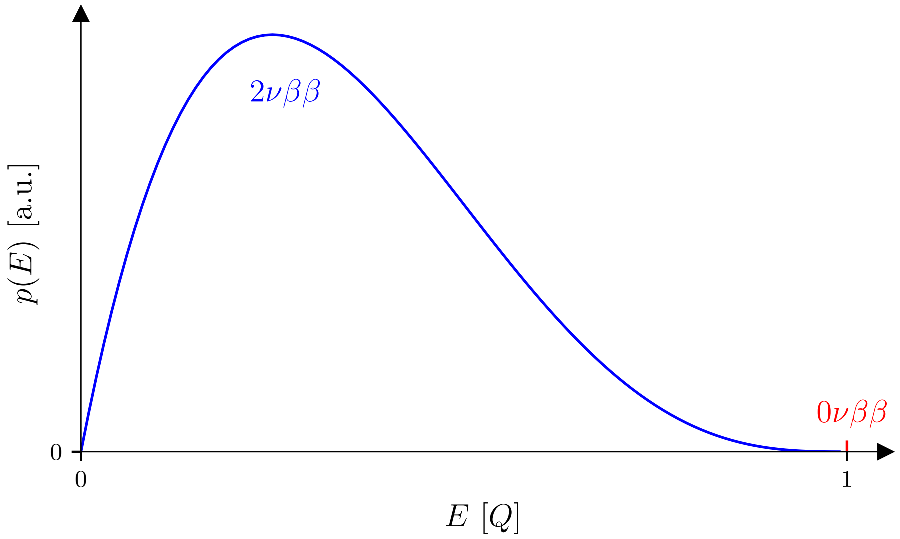

Figure 1.1.: Illustration of the energy spectra of $2\nu\beta\beta$ and $0\nu\beta\beta$ assuming perfect energy resolution. Not to scale.

Up to now, $2\nu\beta\beta$ has only been observed for certain isotopes where single beta decay is forbidden. This is, e.g., the case for isotopes where the binding energy of the daughter nucleus would be lower than that of the initial nucleus. In other words, where the daughter would be heavier than the initial nucleus. The mass of a nucleus and its binding energy can be calculated through a semi-empirical mass formula, the Bethe-Weizsäcker formula [19].

It turns out, as shown in Fig. 1.2, that single beta decay is forbidden for some isotopes with an even number of protons and an even number of neutrons. The daughter nucleus would have odd numbers, resulting in less binding energy, and thus, would be heavier than the initial nucleus.

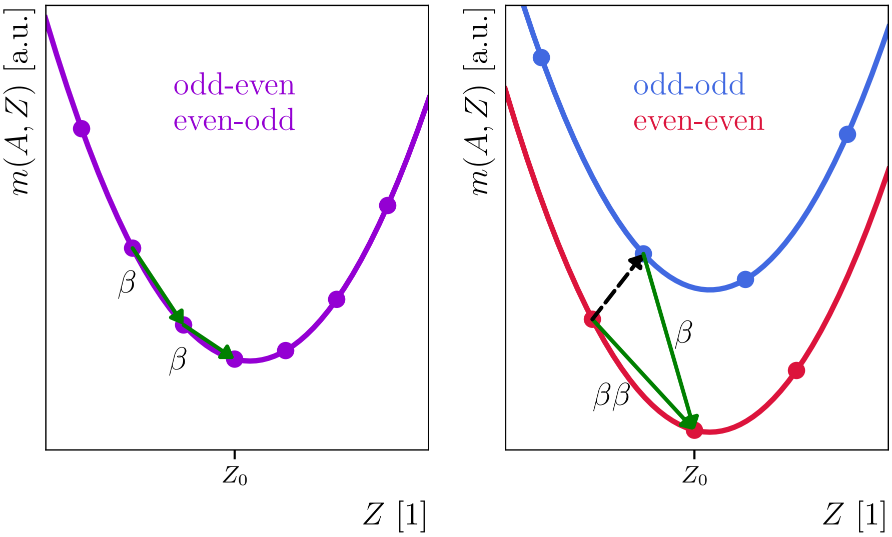

Figure 1.2.: The nucleon mass, $m(A,Z)$, for different combinations of even/odd numbers of protons/neutrons as a function of Z around the minimum at Z_0 for fixed A as calculated via the Bethe-Weizsäcker [19] formula. The green arrows indicate allowed decays, whereas the dashed black arrow indicates the forbidden beta decay.

The $2\nu\beta\beta$ process also occurs for isotopes where single beta decay is allowed. However, $2\nu\beta\beta$ is a second order process and, thus, it happens much rarer than single beta decay which is an intrinsic background and hard to discriminate against as long as the electrons are not tracked. Measured $2\nu\beta\beta$ half-lifes, $T^{2\nu}_{1/2}$, range from 10^{18} y to 10^{24} y for different isotopes [20].

1.3 Neutrinoless Double Beta Decay

In the framework of Majorana neutrinos, the two electron antineutrinos, as being identical to neutrinos, could annihilate or equivalently one antineutrino would be absorbed as a neutrino. Thus, there could be $0\nu\beta\beta$ where only two electrons are emitted:

$$ {}^{A}_{Z}\mathrm{X} \rightarrow {}^{\;\;A}_{Z+2}\mathrm{Y} + 2e^{-} \qquad . \tag{1.4}$$

Due to the absence of the electron antineutrinos in the final state, the full decay energy is equally divided between the two electrons. Thus, the spectrum of the combined electron energies is a mono-energetic line at the Q-value. For the illustration in Fig. 1.1, a perfect energy resolution is assumed. This is quite reasonable for the case of germanium detectors. Like single beta decay is an intrinsic background for $2\nu\beta\beta$, $2\nu\beta\beta$ is an intrinsic background to $0\nu\beta\beta$.

The simplest Feynman diagram for $0\nu\beta\beta$ is depicted in Fig. 1.3. It should be mentioned that $0\nu\beta\beta$ could also be realized through other mechanisms and exchange particles. The one shown here represents the light neutrino exchange mechanism [21], which is assumed to be the driving mechanism for $0\nu\beta\beta$.

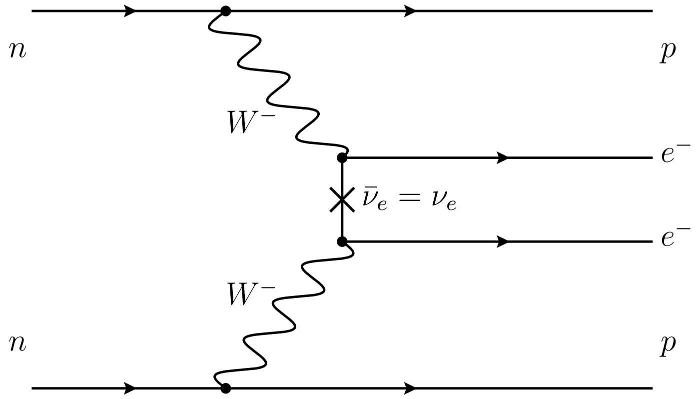

Figure 1.3.: Feynman diagram for neutrinoless double beta decay via the light neutrino exchange mechanism.

Experimentally, the half-life of $0\nu\beta\beta$, $T^{0\nu}_{1/2}$, is the important quantity. For the exchange of light neutrinos it can be calculated as

$$T^{0\nu}_{1/2} = \left(\mathcal{G}^{0\nu}(Q,Z) \cdot |\mathcal{M}^{0\nu}|^2 \cdot \frac{\langle m_{ee}\rangle^2}{m^2_{\nu_e}}\right)^{-1} \quad . \tag{1.5}$$

Here, $\mathcal{G}^{0\nu}$, is the phase space factor, which depends on the Q-value of the decay and the number of protons, Z, in the daughter nucleus, and $\mathcal{M}^{0\nu}$ is the nuclear matrix element (NME) for the given isotope, which describes the effects of the nuclear structure on the transition from the initial to the final state. Both, $\mathcal{G}^{0\nu}$ and $\mathcal{M}^{0\nu}$, can be calculated depending on the isotope. However, there are rather large uncertainties on the different NMEs. Different numerical approaches tend to result in different values of up to a factor of about three for $\mathcal{M}^{0\nu}$.

The effective electron neutrino mass, m_{ν_e}, is

$$m_{\nu_e} = \sqrt{\sum_{i=1}^{3} U^2_{ei} m^2_i} \tag{1.6}$$

and the so-called effective Majorana mass, $\langle m_{ee}\rangle$, is defined as the coherent sum of the masses, m_1, m_2, m_3, of the mass eigenstates ν_1, ν_2 and ν_3

$$\langle m_{ee} \rangle = \left| \sum_{i=1}^{3} m_i U_{\alpha i}^2 \right| = \left| c_{12}^2 c_{13}^2 e^{2i\alpha_1} m_1 + s_{12}^2 c_{13}^2 e^{2i\alpha_2} m_2 + s_{13}^2 m_3 \right| \qquad , \tag{1.7}$$

where $U_{\alpha i}$ are elements of the PMNS matrix from Eq. 1.2.

Information about the mass differences between the neutrino mass eigenstates are available from oscillation experiments [22]:

$$\begin{aligned} \Delta m_{12}^2 = m_2^2 - m_1^2 \quad &= 7.39_{-0.20}^{+0.21} \times 10^{-5}\ \mathrm{eV}^2 \qquad , \\ |\Delta m_{13}^2| = |m_3^2 - m_1^2| \quad &= \pm 2.528_{-0.031}^{+0.029} \times 10^{-3}\ \mathrm{eV}^2 \qquad . \end{aligned} \tag{1.8}$$

Thus, two of the m_i in Eq. 1.7 can be substituted and $\langle m_{ee} \rangle$ becomes a function of one mass, e.g. the lightest one, m_l.

However, oscillation experiments do not provide information on the sign of Δm_{13}. Thus, the ordering of the mass eigenstates is unknown. It could be $m_1 < m_2 < m_3$ or $m_3 < m_1 < m_2$. The first case is called normal ordering and the second case inverted ordering. This leads to different predictions for the possible parameter space $[m_l, m_{ee}]$ as shown in Fig. 1.4. The widths of the bands result from the uncertainties on the elements of the PMNS matrix. At higher values of m_l, the bands overlap since the small mass differences become negligible compared to the absolute scale. Fig. 1.4 also shows the probability densities for $\langle m_{ee} \rangle$ evaluated in a Bayesian global fit [23]. In addition, a second independent Bayesian global fit was performed with a similar result for the probability distributions [24].

Also indicated in Fig. 1.4 are the areas of the parameter space excluded by observations. Cosmological observations can set upper limits on the sum of the neutrino masses [25],

$$\Sigma = \sum_{i=1}^{3} m_i \qquad , \tag{1.9}$$

which can be translated through the known mass differences to an upper limit on the lightest neutrino mass, m_l; the PLANCK collaboration set an limit of $\Sigma < 0.6\,\mathrm{eV}$ [26]. Other cosmological constraints are more model dependent. The strongest limits quoted are around 0.15 eV [27].

Another limit is provided by direct searches for the influence of the electron neutrino mass, m_{ν_e}, on the electron energy spectrum from tritium decay. This can also be translated into an upper limit on m_l. The best limit has been published by the KATRIN collaboration which set an upper limit of $m_{\nu_e} < 1.1\,\mathrm{eV}$ [28]. The KATRIN collaboration started data taking in 2018 and their goal is to increase the sensitivity by about one order of magnitude within the next years. In this regime of absolute mass scale, the neutrino eigenstates have approximately the same masses. Thus, the following relation can be used: $m_1 \approx m_2 \approx m_3 \approx m_l \approx m_{\nu_e}$. If they are to measure the electron neutrino mass in this regime, the probability of Majorana neutrinos would be enormously reduced since

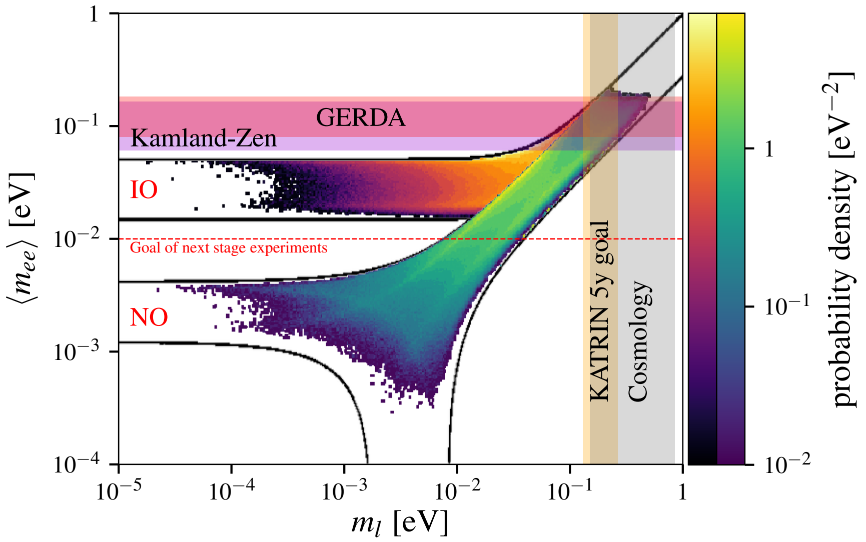

Figure 1.4.: Possible parameter space of the effective Majorana neutrino mass as a function of the lightest neutrino mass for inverted (IO) and normal (NO) ordering. The probability densities are taken from [23]. The widths of both bands originate from the uncertainties on the elements of the PMNS Matrix. Also shown are limits on $\langle m_{ee} \rangle$ from the GERDA and KamLAND-Zen Collaborations. In addition, limits from cosmological observations (e.g. from the PLANCK collaboration) on the lightest neutrino mass are shown. Also indicated is the desired sensitivity on m_l from the KATRIN Collaboration after five years of data taking.

the corresponding regime for $\langle m_{ee} \rangle$ is already mostly explored and ruled out by $0\nu\beta\beta$ searches, which provide direct constraints on the effective Majorana mass. Since $0\nu\beta\beta$ has not yet been observed, experiments only provide upper limits on the half-life, $T^{0\nu}_{1/2}$, which are converted into limits on $\langle m_{ee} \rangle$ via Eq. 1.5. The GERDA collaboration set the best germanium based limit of $\langle m_{ee} \rangle < 79 - 180\,\mathrm{meV}$ [10, 9, 11]. The best value based on Xenon, published by the KamLAND-Zen collaboration, is $\langle m_{ee} \rangle < 61 - 165\,\mathrm{meV}$ [29]. The large uncertainties on these limits are mainly due to the large uncertainties on the NMEs.

Next stage experiments are built to be sensitive to effective neutrino masses of $\approx 10\,\mathrm{meV}$. As shown in Fig. 1.4, this would exclude the possible parameter space for the case of inverted ordering and would cover a large part of the parameter space for the case of normal ordering.

As Eq. 1.5 can be used to convert a half-life limit into a limit on the effective Majorana mass, the equation can also be used to estimate the sensitivity and background level of a $0\nu\beta\beta$ experiment necessary to reach a certain discovery potential for a given $\langle m_{ee} \rangle$.

1.4 $0\nu\beta\beta$ Experimental Design Criteria

The search for $0\nu\beta\beta$ is basically the search for a line at the Q-value in the spectrum of double beta decay as depicted in Fig. 1.1. The energy of the two electrons has to be measured as accurately as possible. There are 35 isotopes [6] that are, theoretically, candidates. Out of these, isotopes with the smallest expected half-lifes for $0\nu\beta\beta$ and the hightest possible sensitivities should be chosen for experiments.

Equation 1.5 shows that the half-life, $T_{1/2}^{0\nu}$, decreases with increasing $\mathcal{G}^{0\nu}(Q,Z)$ and increasing $\mathcal{M}^{0\nu}$. As $\mathcal{G}^{0\nu}(Q,Z) \propto Q^5$ [6], isotopes with a high Q-value are preferred in that respect.

In presence of background, the sensitivity is proportional to

$$S_{T_{1/2}^{0\nu}} \propto a\epsilon\sqrt{\frac{Mt}{B\Delta E}} \quad , \tag{1.10}$$

where M is the total mass of the source material, a its isotopic abundance, ϵ the detection efficiency, t the measurement time, ΔE the energy resolution at the Q-value and B is the background index. The background index, B, is determined from the energy spectrum in a predefined window around the Q-value, e.g. $\approx Q \pm 50\Delta E$. This window is called the region of interest (ROI). The range, in which the signal is searched for is much smaller, $\approx Q \pm \Delta E$, and is called the signal window.

Not all of these parameters are determined by the choice of isotope, but are also influenced by the corresponding detector system.

The measurement time, t, increases the sensitivity not linearly but only with the square root of t because the neutrino mass enters in quadrature in Eq. 1.5. Hence, it does not help to just measure longer after some point in time. However, in the limit of no background, the sensitivity becomes directly proportional to t and, thus, increases linearly with time. Current and next stage $0\nu\beta\beta$ experiments are taking data over a few years. Thus, detector systems which are very stable, and do not need a lot of maintenance over such time scales, are needed.

Next stage $0\nu\beta\beta$ experiments are targeting M on the ton scale. Thus, the isotope and corresponding detector system should be scalable to such large masses. This also includes the availability of the isotope. Isotopes with low natural abundance are a priori not favourable since the enrichment process might be very expensive. However, within the overall budget, enrichment might not be the decisive cost factor.

In general, a high detection efficiency, ϵ, is reached for detector systems where the active detection material is also the source material. In this case, the probability is high that the electrons are detected and that their energy can be reconstructed correctly. If the source is not active, the electrons have to escape the source to reach the active detector. That always reduces ϵ. Some experiments use compounds as a compromise.

A very good energy resolution, small ΔE, does not only increases the sensitivity. It also reduces the unavoidable intrinsic background of the $2\nu\beta\beta$ decay of the isotope. Even if the probability that the electrons carry almost all the energy of the Q-value is very small, it is still not negligible since $T_{1/2}^{2\nu}$ is several orders of magnitude shorter than the half-life of $0\nu\beta\beta$. This background, as well as the others, is reduced for detectors with very good energy resolution because the signal window can be narrower.

This leads to the last remaining parameter in Eq. 1.10, the background index, B, usually given in units of cts/(keV $\cdot$ kg $\cdot$ yr). There are various sources of background radiation which can be reduced through passive and active shielding techniques. The different isotopes, or actually their detector systems, have different shielding techniques against the different kinds of background.

The sources of backgrounds and the general (passive) measures against them are:

- $2\nu\beta\beta$ decay events: As just mentioned above, detectors with a very good energy resolution have a good background suppression against $2\nu\beta\beta$.
- Natural radioactivity: Radiation from radioactive decays is always present and can deposit energy close to the Q-value in a detector and, thus, fake an $0\nu\beta\beta$ event. In order to reduce this source of background the detector and its surroundings are made out of radiopure material and are shielded as good as possible during the fabrication. Also, an isotope with a high Q-value is favourable since it reduces the amount of possible decays which could fake a $0\nu\beta\beta$ event.
  Especially important for germanium detector based systems are radioactive decays on the surface of the detector. They can come from contaminations deposited during detector fabrication or deposited on the surface during detector operation. Alpha or beta radiation on the surface can produce background events which are particularly difficult to identify.
- Radiation from cosmic rays: When high energy particles, mostly protons, hit the earth atmosphere, large particle showers are created. High energy muons are one component of such showers and can penetrate deep into the earth and reach a detector. These muons can produce showers in the vicinity of the experiment and might also accidentally fake $0\nu\beta\beta$ events. In addition, they can activate the material close or inside the detector, and thus, increase the level of natural radioactivity. In order to minimize backgrounds due to cosmic rays the experiments are build in deep underground laboratories.

Depending on the detector system, there are further (active) techniques for discrimination against background events. However, since this thesis is about germanium detectors, the reader is referenced to review papers like [6] and [30] for more detailed information about non germanium based $0\nu\beta\beta$ experiments. In the next part of this chapter, it is explained why germanium is suitable for the search after $0\nu\beta\beta$ and an overview of the germanium based experiment GERDA and the followup experiment LEGEND is given.

1.5 Germanium Based Experiments

The isotope ^{76}Ge is one of the best candidates to search for $0\nu\beta\beta$. The Q-value is $Q_{\beta\beta} = 2039.061 \pm 0.007\,\mathrm{keV}$. As a semiconductor, germanium itself can be used as a particle detector featuring a very high detection efficiency as well as an excellent energy resolution at the permille level.

1.5.1 The GERDA Experiment

The GERDA experiment [8, 10, 11] was located at the underground *Laboratori Nazionali del Gran Sasso* (LNGS) in Italy. The laboratory has a rock overburden of $\approx 3500\,\mathrm{m\,w.e.}$, reducing the flux of cosmic muons to $\approx 1.25\,\mathrm{m^{-2}h^{-1}}$. The LNGS setup is illustrated in Fig. 1.5. The experiment itself is illustrated in Fig. 1.6 and Fig. 1.7. It took data from November 2011 to the end of 2019.

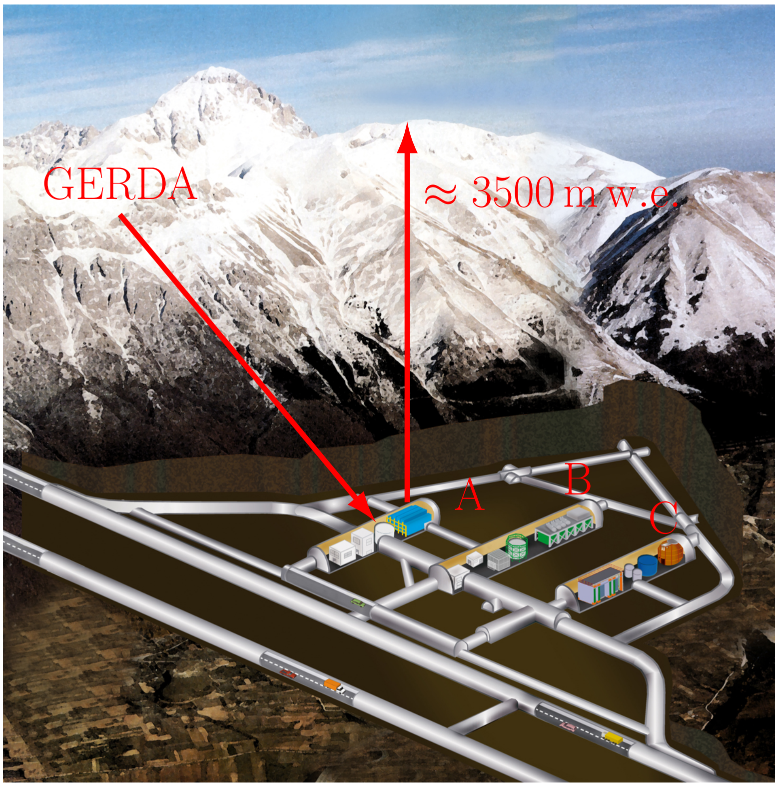

Figure 1.5.: Illustration of the LNGS taken and adapted from [31]. The GERDA experiment is located in Hall A.

The core of the experiment[1] were 40 ^{76}Ge enriched ($\approx 87\,\%$) high purity germanium (HPGe) detectors with a combined mass of 35.6 kg. They were arranged in 7 strings forming the detector array.

---

[1] The GERDA collaboration upgraded the experiment in 2015. The described setup and stated values in this chapter refer to this upgrade: GERDA Phase II [32].

The array was hanging in a cryostat which was filled with 64 m^3 purified liquid argon (LAr). The LAr was not only cooling the detectors, but it also acted as a shield against background gamma-radiation. The LAr also acted as a photon detector. When a particle deposits energy inside LAr, the LAr scintillates. The light was transported through wavelength shifting fibers to Silicon-Photomultipliers (SiPMs) at the top of the array. The fibers were located closely around and in the middle of the array increasing the efficiency of the LAr detector. This system is called the LAr veto in GERDA since it is used to identify background originating from gamma interactions only partially contained in the germanium detectors. [33, 34].

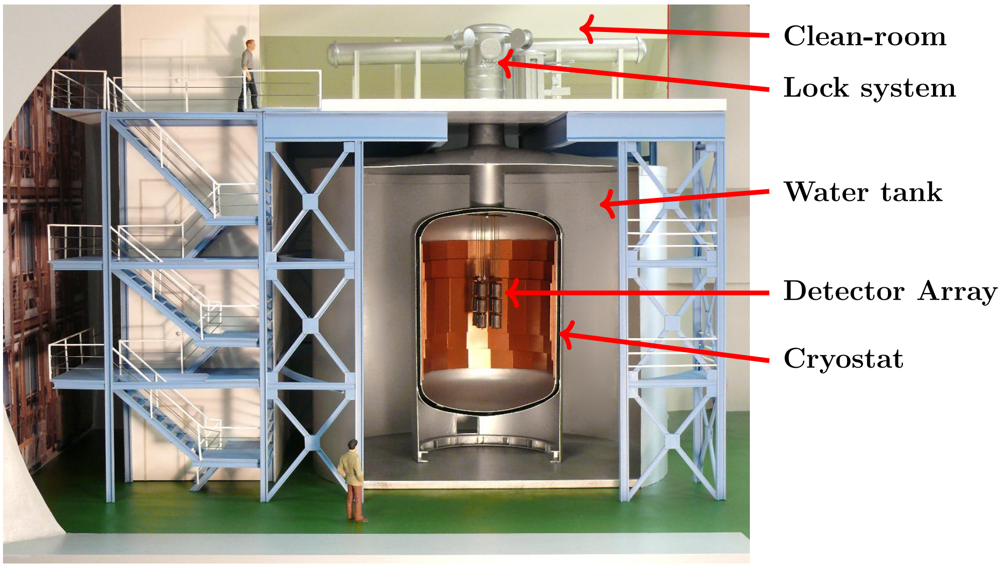

Figure 1.6.: Illustration of the GERDA experiment inside the LNGS, taken and adapted from [35]. The detector array is not to scale.

The whole cryostat was surrounded by a tank filled with 590 m^3 of ultra-pure water which acted as a passive shield against external photons and neutrons. In addition, there were 66 PMTs at the walls of the water tank to detect Cherenkov light produced in the water by charged particles. This was used as a muon veto system. A clean-room was located on top of the water tank. The detector array was prepared in the clean-room and lowered through the access pipe into the LAr volume. On top of the clean-room, there were plastic scintillator panels which acted as a veto system against vertical muons.

Whenever any of the veto systems detected a particle at the same time as a germanium detector recorded an event, the event was rejected. In addition, the germanium array itself acted as a veto system. If two or more detectors registered an event, they were rejected. This was called the anti-coincidence veto.

The plastic scintillator panels and the water Cherenkov veto mainly shielded against background due to cosmic rays. The LAr and the anti-coincidence veto mainly shield against radiation predominantly originating from radioactivity in the structural materials close to the germanium detectors.

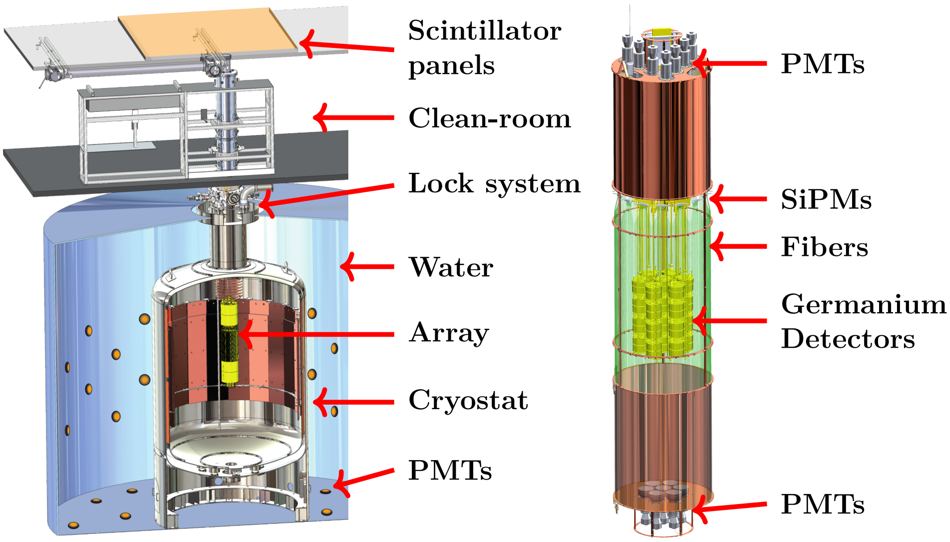

Figure 1.7.: On the left: Schematic view of the GERDA detector array inside the LAr cryostat surrounded by water and the clean-room on top. On the right: Illustration of the detector array. Illustrations taken and adapted from [32].

However, additional sources of background were identified, for which none of the veto systems provided a reduction. One specific source was the LAr itself [36]. The disadvantage of LAr is the presence of ^{42}Ar, which decays to ^{42}K. The Q-value is way below the Q-value of $0\nu\beta\beta$ and, thus, this decay does not matter in itself. However, the ^{42}K is positively charged and may by attracted by one of the germanium detectors through its electric field and drifts towards its surface. ^{42}K is unstable and decays via beta-decay to ^{42}Ca. The Q-value is 3.5 MeV and, therefore, these decays can create background events, if not all the energy is recorded for these surface events. To minimize this source of background, a physical barrier in form of a transparent nylon shroud was installed around each detector string.

Another contribution originated from radioactive surface contaminations of the germanium detectors. The isotopes ^{210}Po, ^{226}Ra, ^{222}Rn and ^{218}Po [16] were identified. They produce alpha particles with energies above $Q_{\beta\beta}$ at the surface of a detector, which can create background events, if not all the energy is recorded.

Surface events were one of the limiting factors for GERDA. Thus, the investigation of surface events is extremely important for future experiments with larger exposures.

Background events not rejected by the veto systems were identified through so-called pulse shape analysis (PSA). For this, the signal pulses of the germanium detectors are analysed in detail. This kind of background identification is called pulse shape discrimination (PSD) and requires precise knowledge of the detectors and their response to certain kind of events including surface events. This motivates the studies presented in this thesis.

There are two kind of events which are rejected due to PSD [15, 37]:

1 Multi-site events (MSE): A $0\nu\beta\beta$ decay inside a germanium detector would create free charge carriers in form of a small charge cloud at one single position inside the germanium. Such events are called single-site events (SSE). In most cases, the electric pulse of a SSE is very distinguishable from the one of a MSE. Events classified as a MSE are rejected as background. They are predominantly Compton scattered photons.

2 Surface events: Surface events often feature very characteristic pulse shapes, which can be used to discriminate them against bulk events. Even though $0\nu\beta\beta$ could also appear at the surface of a detector, events at the surface are most likely background events due to alpha or beta particles, since they do not penetrate far into solid matter. Hence, rejecting surface events increases the sensitivity, even though the active mass is reduced.

The different kinds of background and the different veto techniques against them are illustrated in Fig. 1.8.

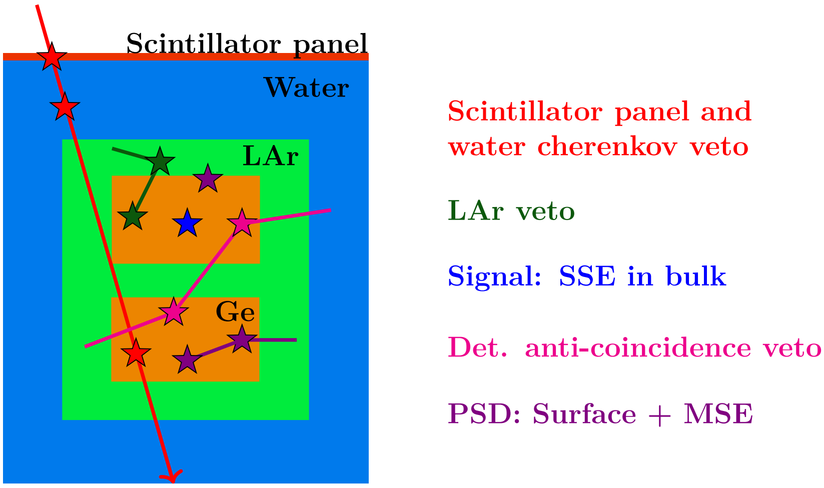

Figure 1.8.: Schematic view of the topological sources of background to $0\nu\beta\beta$ in the GERDA experiment.

The GERDA collaboration finished data taking at the end of 2019 and achieved an energy resolution, defined as full width at half maximum (FWHM), at $Q_{\beta\beta}$ of FWHM = 3.3 keV and a background index of 5.2×10^{-4} cts/(keV · kg · y) and set a limit of $T_{1/2}^{0\nu\beta\beta} > 1.8 \times 10^{26}$ y [9, 10, 11].

1.5.2 The MAJORANA Experiment

The MAJORANA experiment [38, 39, 40] was located in the Sanford Underground Laboratory and started data taking in 2015. The laboratory has an overburden of ≈ 5000 m w.e.. In this thesis, the experiment is not described in detail, but only the key differences with respect to the GERDA experiment are summarized.

The main difference was the shielding technique against incoming radiation. The 44 kg of germanium detectors were located inside two vacuum cryostats made out of ultra clean materials. The cryostats were surrounded by an inner copper shield and a massive lead castle. Both acted as passive shields. It turned out that GERDAs shielding approach resulted in a better background suppression. MAJORANA achieved a better energy resolution, FWHM = 2.5 keV, by using front-end electronics very close to the detectors [41], which, however, could not compensate for the higher background.

The MAJORANA collaboration finished data taking in 2020 and achieved a background index of $4.7 \times 10^{-3}\,\mathrm{cts/(keV \cdot kg \cdot y)}$ and set an limit of $T_{1/2}^{0\nu\beta\beta} > 2.7 \times 10^{25}\,\mathrm{y}$ [42].

1.5.3 The LEGEND Experiment

In order to be sensitive to effective Majorana masses as low as $\approx 10\,\mathrm{meV}$, the GERDA and MAJORANA collaborations together with other groups, formed a new collaboration in 2017, the Large Enriched Germanium Experiment for Neutrinoless double beta Decay (LEGEND) collaboration [13].

The final goal of the collaboration is a ton-scale experiment increasing the exposure, $M \cdot t$, to 5–10 $\mathrm{t \cdot y}$ while preserving the excellent energy resolution and reducing the background level below $5 \times 10^{-5}\,\mathrm{cts/(keV \cdot kg \cdot y)}$ [13].

The baseline approach to reach this is to use the shielding technique and background identification capability of LAr and water as in GERDA and the very good energy resolution due to the front-end electronics of MAJORANA. The experiment is planned to be realized in two phases: LEGEND 200 and LEGEND 1000.

LEGEND 200

LEGEND 200 is basically a major upgrade of the GERDA experiment in the LNGS, using the existing cryostat and GERDA infrastructure. The upgrade started in 2020. The lock on top of the cryostat is going to be enlarged such that more strings, with more detectors, can be inserted. The detectors from MAJORANA are going to be added to the GERDA detectors. In addition, new detectors are being produced in order to reach a total mass of $\approx 200\,\mathrm{kg}$. The detectors were built at different times and are categorized in different types mainly based on their geometry: Coaxial (COAX), broad energy germanium (BEGe) [43], p-type point contact (PPC) and inverted coaxial (IVC) [44] detectors. The latter three have a better MSE recognition capability compared to the COAX detectors. PPC and BEGe detectors have the best energy resolution.

LEGEND 1000

The COAX detector type is not going to be considered anymore for LEGEND 1000. The IVC detector type is promising and might be the most common design for LEGEND 1000 since individual detectors can be made larger and, thus, the surface to volume ratio is reduced resulting in less background from surface events. Currently, intensive research and development (R&D) is ongoing in order to improve the detectors with respect to energy resolution and background identification. In addition, their is R&D on the holding structures, electronics and surrounding veto systems [45]. In order to reduce the background from the ^{42}Ar, there is a plan to use 42-depleted Argon. However, so far it has not been established what level of purification can be reached.

To house $\approx 1\,\mathrm{t}$ of germanium detectors the GERDA cryostat is not big enough. Thus, a new one has to be build. Currently, the baseline design for the new cryostat has several locks at the top such that several detector arrays can be inserted, where each one of them would have roughly the size of the array in LEGEND 200. The experiment is most likely not going to be at LNGS, since the challenging goal of such a low background is easier to accomplish in an even deeper laboratory. It should be said that the general design is not fixed yet. The results of current R&D and the experience gained from LEGEND 200 will be the basis of final decisions [46].

Chapter 2: Solid-State Physics

Germanium is a semiconductor very similar to silicon. It can be turned into an electronic component such as a diode, which can be used as particle detector. Actually, the first transistor was made out of germanium [47]. In this chapter, a summary about the solid-state physics of semiconductors relevant for germanium detectors and the simulations developed for this thesis is given. For more details, the reader is referred to further literature like [48].

2.1 Crystal Structure

A crystal is a many-particle system of N_e electrons and N_N nuclei arranged in a lattice. The periodic pattern of the lattice can be described through a so-called unit cell. The shape of the cell is defined through three vectors, $\mathbf{a_1}$, $\mathbf{a_2}$ and $\mathbf{a_3}$, which are called primitive vectors. Any integer linear combination of the primitive vectors define the lattice points, $\mathbf{R}_{hkl}$ where $h, k, l \in \mathbb{Z}$. In case of germanium, one possible unit cell has a cubic shape, thus, the primitive vectors all have equal length, a, and are orthogonal to each other. Additional information is needed to describe the exact structure of the lattice, i.e., the number and arrangement of the nuclei inside the unit cell. This is described through the so-called basis and their positions. For germanium, each basis is made out of two germanium nuclei separated through $(\mathbf{a_1} + \mathbf{a_2} + \mathbf{a_3})/4$. The bases are placed at the centers of the faces and at the corners of the cube. This is called the face-centered cubic (fcc) structure, which is one of the 14 so-called Bravais lattices, which are the set of cells classifying all possible crystallographic lattice structures. The fcc structure for germanium is shown in Fig. 2.1.

Different unit cells can describe the same crystal structure. Unit cells with the smallest volume are called primitive volume cells. Primitive cells also have the property that they only contain one lattice point. If lattice points are on a face (corner) of the cell, they are only counted with 1/2 (1/8). A special type of primitive cells are the Wigner-Seitz cells, where the one lattice point is located exactly in the middle of the cell.

The direction of the primitive vectors are often expressed via the "Miller indices" notations. The $[hkl]$-notation denotes the direction equivalent to $h\mathbf{a_1} + k\mathbf{a_2} + l\mathbf{a_3}$ where $h, k, l \in \mathbb{Z}^+$. In case of directions with negative indices, the indices are written with a bar, e.g. $[\bar{h}kl]$. The $\langle hkl \rangle$-notation denotes a set of directions which are equivalent by symmetry. E.g., in case of the fcc structure [100], [010] and [001] are included in $\langle 100 \rangle$ and all 12 edges of the cube belong to $\langle 100 \rangle$.

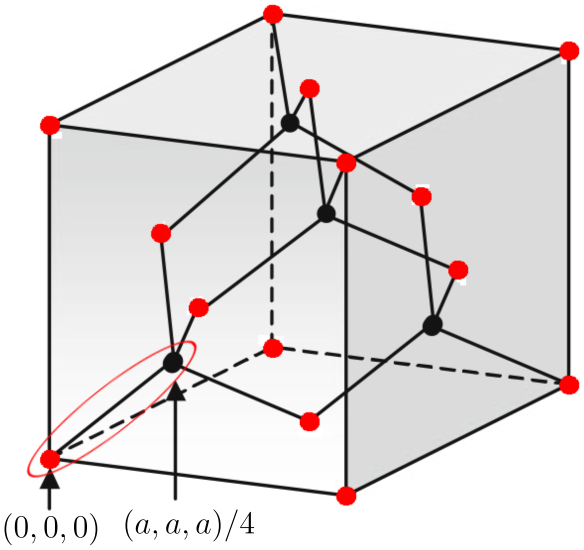

Figure 2.1.: Face-centered cubic structure of germanium, adapted from [48]. The red ellipsoid outlines one basis which consists of two germanium atoms. The red points mark the origin of all bases.

2.2 Electrons in a Crystal

The electric properties of a crystal are determined trough the electrons inside the crystal, or more precisely, how they are bound in the many-particle system. Only electromagnetic interactions are considered between the electrons and nuclei. The fundamental equation describing the system is the many-particle Schrödinger equation

$$\mathcal{H}_\mathrm{E}\psi = i\hbar\frac{\delta\psi}{\delta t} \qquad , \tag{2.1}$$

where $\mathcal{H}_\mathrm{E}$ is the electrostatic Hamiltonian, $\psi = \psi(\mathbf{r}_k, \mathbf{R}_l, t)$ is the wave function of N_e electrons and N_N nuclei at their respective coordinates $\mathbf{r}_k$, $k \in 1, 2, ..., N_e$, and $\mathbf{R}_l$, $l \in 1, 2, ..., N_\mathrm{N}$, at the time t, $\hbar$ is Planck's constant and i is the imaginary unity.

The electrostatic Hamiltonian is

$$\begin{aligned}\mathcal{H}_\mathrm{E} = &-\sum_{k=1}^{N_e}\frac{\hbar^2}{2m_e}\nabla_k^2 - \sum_{l=1}^{N_\mathrm{N}}\frac{\hbar^2}{2M_l}\nabla_l^2 + \frac{1}{2}\sum_{\substack{k=1,k'=1\\k\neq k'}}^{N_e,N_e}\frac{e^2}{4\pi\epsilon_0|\mathbf{r}_k-\mathbf{r}_{k'}|}\\ &-\sum_{k=1,l=1}^{N_e,N_\mathrm{N}}\frac{e^2 Z_l}{4\pi\epsilon_0|\mathbf{r}_k-\mathbf{R}_l|} + \frac{1}{2}\sum_{\substack{l=1,l'=1\\l\neq l'}}^{N_\mathrm{N},N_\mathrm{N}}\frac{e^2 Z_l Z_{l'}}{4\pi\epsilon_0|\mathbf{R}_l-\mathbf{R}_{l'}|} \qquad ,\end{aligned} \tag{2.2}$$

where the first two terms describe the kinetic energy of the electrons, T_e, and nuclei, T_N, and the last three terms describe the Coulomb interaction between the electrons, electrons and nuclei, and the nuclei. Here, M_l is the mass of the nuclei l with Z_l protons, m_e is the electron mass, e the elementary charge and ϵ_0 is the dielectric constant of the vacuum.

Several approximations have to be made in order to solve this equation. Note that already in choosing Eq. 2.1 as the fundamental equation, the spins of the electrons and nuclei (and their internal structure) were neglected. In the framework of this thesis, the basic and most important approximations are:

- Born-Oppenheimer approximation: The masses of the nuclei are much larger than m_e: $M_l \gg m_e$. Thus, their kinetic energy is much smaller, $T_\mathrm{N} \ll T_e$. As a consequence, the nuclei are basically stationary (in the coordinate system of the electrons). This leads to the assumption that the wave function, ψ, can be factorised into two wave functions, one for the electrons, ψ_e, and one for the nuclei, ψ_N: $\psi = \psi_e \cdot \psi_\mathrm{N}$. Hence, Eq. 2.1 can be splitted into two equations, one for the electrons and one for the nuclei.

- An infinitely large crystal is assumed to allow the next two approximations.

- Reduction to a one-electron problem via mean-field approximation: The Born-Oppenheimer approximation still leaves a many-particle problem. In order to find the wave function for a single electron i, $\psi_{e,i}$, the usual approach is to also factorise the wave function for all electrons, $\psi_e = \psi_{e,1} \cdot \ldots \cdot \psi_{e,N_e}$, and average the electron-electron interaction by assuming a time-independent electron density.

- Periodicity of the crystal lattice: The fourth term in Eq. 2.1 describes the potential off all nuclei on one electron. It can be simplified to one single periodic potential by assuming a perfectly periodic alignment of the nuclei.

Bloch's Theorem states that the wave function in a periodic potential is a periodic function. Thus, the wave function of a single electron in a crystal can be expressed through

$$\psi_{n,\mathbf{k}}(\mathbf{r}) = e^{i\mathbf{k}\cdot\mathbf{r}} u_{n,\mathbf{k}}(\mathbf{r}) \qquad , \tag{2.3}$$

where $u_{n,\mathbf{k}}(\mathbf{r})$ is a function with the same periodicity as the crystal, n is a quantum number for the energy and $\mathbf{k}$ is any vector of the reciprocal lattice. The reciprocal lattice is the Fourier transformation of the position lattice, thus, it presents the momentum space. As the lattice is periodic, also the reciprocal lattice is periodic and $\mathbf{k}$ can be restricted to be within the first Brillouin zone as larger $\mathbf{k}$ can be translated back into the first Brillouin zone, which is the Wigner-Seitz cell in the reciprocal space. For the fcc lattice this first Brillouin zone is shown in Fig. 2.2.

For every n, the corresponding Eigenvalue, $E_n(\mathbf{k})$, is a function of $\mathbf{k}$ forming bands of possible states for the electrons of a crystal in the reciprocal space. These bands form the so-called band structure of a crystal.

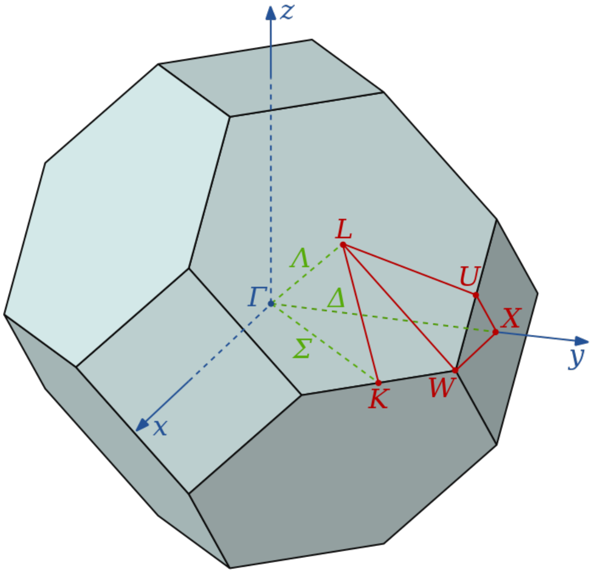

Figure 2.2.: First Brillouin zone of the fcc lattice, taken from [49]. Γ, X, L, K, U, W are sets of characteristic points of the geometry whereas Λ, Σ, Δ are sets of all $\mathbf{k}$ vectors starting from Γ and pointing in the directions of L, K, X. Elements of Λ, Σ, Δ are parallel to the Miller indices $\langle 111 \rangle$, $\langle 110 \rangle$ and $\langle 100 \rangle$.

2.3 Electronic Band Structure

As electrons are fermions, the Pauli principle prohibits two or more electrons to be in the same state. Thus, the electrons fill up all possible states in the different bands starting with the state with the lowest corresponding energy $E_n(\mathbf{k})$.

Fermi Energy

One of the quantities describing the system is the so-called Fermi energy, E_F, which is defined as the difference between the energies of the highest and lowest state filled at the temperature of $0\,\mathrm{K}$.

The band structure of germanium around its Fermi energy is shown in Fig. 2.3. There are many more bands than shown in the figure. However, for the electric properties of the crystal, only the bands around the Fermi energy are of importance as the electrons in these states are not as tightly bound as the electrons in the lower states.

Valence and Conduction Band

There are two special bands: the conduction band and the valence band. The band just above E_F is the conduction band, $E_\mathrm{C}(\mathbf{k})$, whereas the band just below E_F is the valence band, $E_{\mathrm{V}}(\mathbf{k})$. The states just below E_{F} are the states of the valence electrons of the atoms, hence, the name valence band. The electrons filling these states are fixed in place as they are part of valence bonds in the molecular picture. Electrons inside the conduction band, however, are not bound to a fixed molecule. Their energy exceeds the potential barrier to the nearest neighbor. They are quasi-free particles which are free to move through the crystal but cannot leave it. Electrons in the conduction band are also referred to as conduction electrons.

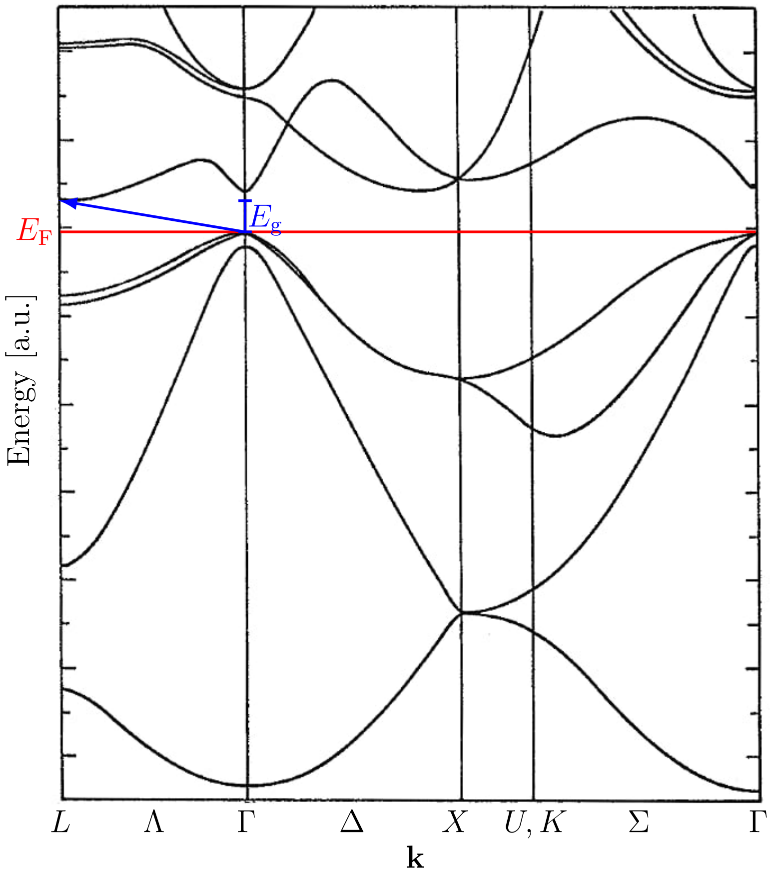

Figure 2.3.: Band Structure of Germanium, adapted from [50]. Γ, X, L, U, W and Λ, Σ, Δ are as shown in Fig. 2.2. The black lines present the different bands $E_n(\mathbf{k})$ around the Fermi Energy, E_{F}, shown by the red line. The band just above (below) the red line is the conduction (valence) band. The blue arrow shows the indirect band gap transition from the valence into the conduction band with the band gap energy, E_{g}.

Band Gap

Another important feature of the band structure is the so-called band gap also shown in Fig. 2.3. It is defined as the energy difference, E_{g}, between the highest energy of the valence band, $E_{\mathrm{V,max}}$, and the lowest energy of the conduction band, $E_{\mathrm{C,min}}$. However, the excitation of an electron from the valence into the conduction band with the minimal energy, E_g, requires a change in $\mathbf{k}$. Such a transition (excitation) is called an indirect transition in contrast to a direct transition where there is no change in $\mathbf{k}$. Materials with a direct (indirect) band gap transition are often said to have a direct (indirect) band gap. Germanium has an indirect band gap of $E_\mathrm{g} = 0.74\,\mathrm{eV}$.

The size of the band gap also classifies materials as insulators, semiconductors or conductors. For conductors, the band gap is actually negative, thus, both bands overlap. For semiconductors, the band gap is around 1 eV, whereas for insulators it is usually above 5 eV.

Phonons

The wave function of an electron in a crystal, Eq. 2.3, is a wave with $\mathbf{k}$ being its wave vector. The relation $\mathbf{p} = \hbar\mathbf{k}$ translate the wave vector into a quasi-momentum of the electron. Thus, an indirect transition also requires a momentum transfer. The momentum is transferred to (or from) the nuclei of the crystal, i.e., to (or from) the lattice. In the derivation of Eq. 2.3, it was assumed that the nuclei are at fixed positions and do not move. However, if some momentum is transferred to a nucleus it starts oscillating in the Coulomb potential of the surrounding atoms. This oscillations also excites neighbouring nuclei due to the Coulomb interaction between them and propagates through the crystal. This propagation can also be expressed as waves which can be seen as quasi-particles and are called phonons.

There are two kind of phonons: acoustic and optical phonons. Acoustic phones can occur in any crystal, whereas optical phonons can only exist in crystals where the basis of the primitive cell consists out of at least two atoms. The difference is, that for acoustic phonons the atoms of a base move coherently, whereas for optical phonons the atoms of a base move in opposite directions. Then, in ionic crystals, e.g. in NaCl, where the atoms are ionised and the crystal bonds between them are ionic, the oscillation amplitude of the nuclei result in an oscillating electric field, an electromagnetic wave. Thus, an optical phonon in an ionic crystal can directly interact with photons. Since the bonds between the germanium atoms are covalent, the optical phonons in germanium, however, cannot interact with photons directly. Acoustic phonons can, in general, not interact with photons. Thus, direct photon-phonon interactions do not have to be considered in germanium.

Also, phonons influence the electric charge transport in crystals, as will be introduced later, and, thus, have to be considered in the simulation of germanium detectors.

Effective Masses

The conduction band, $n = \mathrm{C}$, can be approximated around its local minima, e.g. at $\mathbf{l} \in L$ (see Fig. 2.3), as

$$E_{\mathrm{C}}(\mathbf{l} + \mathbf{k}') = E_{\mathrm{C,min}} + \frac{\hbar^2 \mathbf{k}'^2}{2m^*_{\mathrm{C},\mathbf{l},\mathbf{k}'}} \qquad , \tag{2.4}$$

where $m^*_{\mathrm{C},\mathbf{l},\mathbf{k}'}$ is a specific effective electron mass describing the curvature of the conduction band around the minimum $\mathbf{l}$ in direction of $\mathbf{k}'$. The reference to mass comes from the fact that the second term in Eq. 2.4 looks like the kinetic energy of a free particle with mass $m^*_{C,\mathbf{l},\mathbf{k}'}$.

In general, for band n, the effective mass is a 3 × 3 tensor with elements

$$\left(m^*_{n,\mathbf{l}}\right)_{ij} = \mathrm{inv}\left(\frac{1}{\hbar^2} \left.\frac{\delta^2 E_n(\mathbf{k})}{\delta k_i \delta k_j}\right|_{\mathbf{l}}\right) \tag{2.5}$$

and the scalar $m^*_{n,\mathbf{l},\mathbf{k}'}$ is defined as

$$m^*_{n,\mathbf{l},\mathbf{k}'} = \mathbf{k}'^{\mathsf{T}}/|\mathbf{k}'| \cdot \left(m^*_{n,\mathbf{l}}\right)_{ij} \cdot \mathbf{k}'/|\mathbf{k}'| \tag{2.6}$$

for $|\mathbf{k}'| > 0$.

Holes

When an electron is excited from the valence band into the conduction band, it leaves a vacancy in the valence band. This vacancy is called an electron hole, or just hole. It is not a real particle but can be seen as a quasi-particle. Since the excited electron carries away one negative elementary charge, a hole has a positive elementary charge. Holes are also quasi-free as they are bound to the crystal but are free to move through it. The movement of a hole is actually the collective movement of electrons. However, these electrons are in the valence band and their movement is easier to understand in the molecular picture: a valence electron of a neighbouring atom fills the vacancy but leaves, consequently, a vacancy at the neighbouring nucleus. As a result, the hole moved by one crystal atom. This way, the hole can move through the crystal.

Effective masses can also be assigned to holes. The approximation described above for the conduction band can also be made for the valence band with the only difference that one has to look at the local maxima instead of the local minima. Since the curvature at a maximum is negative, so are the effective masses of holes. However, masses are to be positive, thus, when talking about holes the summation in Eq. 2.4 is changed into a subtraction.

Fermi Level and Fermi-Dirac Distribution

The Fermi energy, E_F, has a fixed value for a material as it is defined for the temperature of 0 K, at which the conduction band is completely empty. A non-zero temperature, however, provides some energy to excite some of the electrons from the valence into the conduction band. Thus, also some states above the Fermi energy are occupied. As electrons are fermions, the probability density for a state of energy E to be occupied is given through the Fermi-Dirac distribution:

$$f(E,T) = \frac{1}{e^{(E-\mu)/(k_\mathrm{B}T)}+1} \qquad , \tag{2.7}$$

where T the temperature of the crystal, k_B is the Boltzmann constant and μ is the Fermi level, or electric potential. The Fermi level is defined as the energy at which $f(\mu,T) = 1/2$ is fulfilled. For $T = 0\,\mathrm{K}$ the Fermi level equals the Fermi energy, $\mu = E_\mathrm{F}$.

Density of Conduction Electrons at Non-Zero Temperatures

The macroscopic electric properties of a solid-state material depend on the density of the conduction electrons, which is

$$n_{ce}(T) = \int\limits_{E_\mathrm{C,min}}^{\infty} D(E) f(E,T) \mathrm{d}E \qquad , \tag{2.8}$$

where $D(E)$ is the density of states. Using the approximation from Eq. 2.4 and assuming that the effective mass, $m^*_{\mathrm{C},\mathbf{l},\mathbf{k}'}$, is isotropic in $\mathbf{k}'$ at $\mathbf{l}$ ($\rightarrow m^*_{\mathrm{C},\mathbf{l},\mathbf{k}'} = m^*_{\mathrm{C},\mathbf{l}}$) see [48], the density of states just above $E_\mathrm{C,min}$ can be approximated through

$$D_\mathbf{l}(E) = \frac{1}{2\pi^2}\left(\frac{2m^*_{\mathrm{C},\mathbf{l}}}{\hbar^2}\right)^{3/2}\sqrt{E-E_\mathrm{C,min}} \qquad . \tag{2.9}$$

The function $f(E,T)$ is approximated as

$$f(E,T) = \exp\left(-\frac{E-\mu}{k_\mathrm{B}T}\right) \qquad . \tag{2.10}$$

This is justified because, at room temperature, $k_\mathrm{B}T$ is about 0.025 eV. For semiconductors the band gap is around 1 eV and, since $E_\mathrm{g} \gg k_\mathrm{B}T$, the fermi level can be assumed to be in the middle between the bands: $\mu = E_{V,\mathrm{max}} + E_\mathrm{g}/2$. Hence, $E - \mu \gg k_\mathrm{B}T$ for $E \geq E_{C,\mathrm{min}}$.

With this approximation, the integral in Eq. 2.7 can be solved and n_{ce} becomes

$$n_{ce}(T) = 2\left(\frac{m^*_{\mathrm{C},L}k_\mathrm{B}T}{2\pi\hbar^2}\right)^{3/2}\exp\left(-\frac{E_\mathrm{g}}{2k_\mathrm{B}T}\right) \qquad . \tag{2.11}$$

This dependency of the conduction electron density on the band gap determines the previously stated separation between insulators and semiconductors as for large band gaps the density is exponentially suppressed.

Crystal Defects: Donor and Acceptor Impurities

Up to now, a perfect crystal was assumed. However, in reality, perfect crystals do not exist. There are always some defects like impurities, missing atoms (vacancies in the lattice) or missarrangements of the atoms, e.g. dislocations. Their concentration in germanium is usually so low, that the macroscopic assumptions made so far are still valid. However, defects create additional states in the band structure. Two special types of them are donor and acceptor impurities, which create states between the valence and conduction band. A simplified band structure showing additional donor and acceptor states is shown in Fig. 2.4.

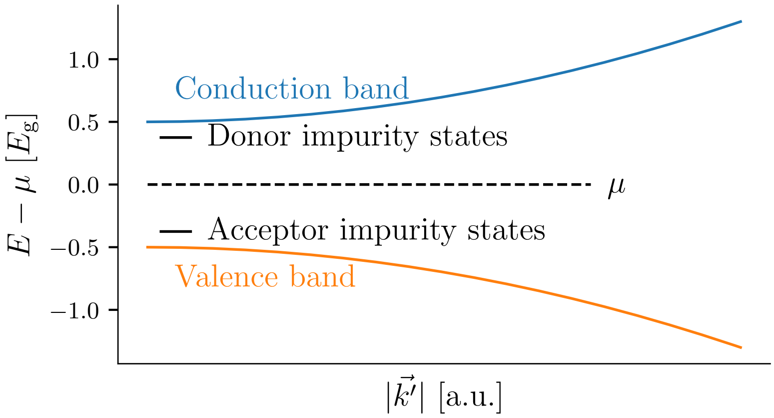

Figure 2.4.: Simplified band structure of a semiconductor around a local minimum. The minimum is assumed to be symmetric. Also shown is the Fermi level, μ, and two examples for impurity states, one for a donor and one for an acceptor impurity.

Donor and acceptor impurities create states in different regions of the band gap. Donor impurities create states close to the conduction band, whereas acceptor impurities create states close to the valence band. Another difference is that donor impurity states are filled, hence their name as they can donate an electron, whereas acceptor impurity states are empty, thus they can accept an electron.

Donor and acceptor impurities are called electrically active impurities since they influence the electric behavior of the material. There are also electrically inactive (or neutral) impurities which create donor (acceptor) states below (above) the valence (conduction) band and, thus, do not impact the electrical behavior.

Equation 2.11 shows that the density of thermally excited electrons is higher for smaller

E_g. However, the gap between donor states and the conduction state is smaller than E_g. Thus, donor electrons can be excited more efficiently to the conduction band. The same holds for the acceptor impurity states, to which electrons can be easily excited from the valence band leaving holes back in the valence band. Thus, at the same temperature, a crystal has many more conductive charge carriers when it has a lot of donor and or acceptor impurities than when the crystal has no such impurities.

Space Charges and Charge Carriers

It is important to distinguish between space charges and charge carriers in the crystal:

- Fixed space charges: They are fixed to a lattice point, i.e. they cannot move. These are electrons in the valence band and electrons or holes in any kind of impurity states.
- Free charge carriers: They can move through the crystal and, thus, contribute to a possible electric current. Free charge carriers are electrons in the conduction band (conduction electrons) and holes in the valence band.

It should be noted that the general charge density, $\rho(\mathbf{r})$, is still zero everywhere, since electrons and holes are always created in pairs, so-called electron-hole pairs. These can recombine, meaning that a free electron can fill a hole. In thermal equilibrium, the amount of electron-hole pair creation (due to thermal excitations) and the amount of recombination is equal.

2.4 Electrical Currents in Semiconductors

Free charge carriers inside a crystal move at a certain velocity depending on their kinetic energy and direction. The latter because their effective mass depends on the direction. However, they scatter frequently and change their direction randomly. Thus, the average velocity, $\mathbf{v}_\mathrm{d}$, is zero. Scattering centers are ionized impurities, neutral impurities, acoustic phonons, optical phonons and dislocations in the crystal lattice. In case an electric field, $\boldsymbol{\mathcal{E}}(\mathbf{r})$, is applied across the semiconductor, the free charge carriers get accelerated. Due to the scattering, their drift speed is limited and there is a terminal velocity. For large enough $\boldsymbol{\mathcal{E}}(\mathbf{r})$, the terminal velocity is instantaneously reached and, thus, the acceleration part can be neglected. The terminal velocity is also just called drift velocity, $\mathbf{v}_\mathrm{d}$, even though in special circumstances the actual drift velocity can be lower. The so-called drift field, $\mathbf{v}_\mathrm{d}(\mathbf{r})$, is defined as

$$\mathbf{v}_{\mathrm{d,e/h}}(\mathbf{r}, \boldsymbol{\mathcal{E}}(\mathbf{r}), T) = \pm_\mathrm{e}^\mathrm{h} \cdot \mu_{\mathrm{e/h}}(\mathbf{r}, \boldsymbol{\mathcal{E}}(\mathbf{r}), T) \cdot \boldsymbol{\mathcal{E}}(\mathbf{r}) \qquad , \tag{2.12}$$

where $\mu_{\mathrm{e/h}}(\mathbf{r}, \boldsymbol{\mathcal{E}}(\mathbf{r}), T)$ is the so-called (electron or hole) mobility tensor, which also depends on the electric field, $\boldsymbol{\mathcal{E}}(\mathbf{r})$, itself. It mainly comprises the contributions of the different scattering sources via Matthiessen's rule

$$\left(\frac{1}{\mu}\right)_{ij} = \left(\frac{1}{\mu_{\mathrm{Aco}}}\right)_{ij} + \left(\frac{1}{\mu_{\mathrm{Opt}}}\right)_{ij} + \left(\frac{1}{\mu_{\mathrm{Ion}}}\right)_{ij} + \left(\frac{1}{\mu_{\mathrm{Neu}}}\right)_{ij} + \left(\frac{1}{\mu_{\mathrm{Dis}}}\right)_{ij} \quad . \tag{2.13}$$

The first two contributions, μ_{Aco} and μ_{Opt}, are due to scattering on phonons and, thus, depend on the orientation of the crystal axes with respect to the electric field direction; they should be constant across the crystal. However, the contributions from ionised, μ_{Ion}, and neutral, μ_{Neu}, impurities as well as from dislocations, μ_{Dis}, are not constant across the crystal as these impurities and dislocation are not homogenously distributed. Thus, the mobility tensor also depends directly on the position of the charge carriers, $\mathbf{r}$. All the different contributions to μ are also dependent on the temperature, T, of the crystal.

2.5 Charge Trapping and Surface Effects

Charge carriers can get trapped during their drift through the crystal. This can happen at impurities or crystal defects: E.g. a conduction electron meets an empty donor impurity state and recombines or gets caught by an interstitial atom.

For drifts through the bulk (bulk drifts) this happens very rarely and, hence, it has a very small effect on the signals and the resolution of a germanium detector. However, this is different for drifts close to the surfaces of a crystal (surface drifts). There, the assumptions made in the calculation of the band structure fail and a variety of unknown states are produced. These additional states are possible trapping centers for the charge carriers and, as will be demonstrated later, have a huge impact on the signals seen in germanium detectors.

Such trapping centers close to the surface can create additional problems because they are likely to be at partially filled. As they are fixed locally, this might result in charged surface layers. In case of a positively (negatively) charged surface layer, electrons (holes) in the conduction (valence) band are attracted whereas holes (electrons) in the valence (conduction) band are repelled. Therefore, the density of occupied states of the conduction (valence) band would be higher at the surface whereas the density of occupied states in the valence (conduction) band would be smaller. Sometimes, these modified bands are called surface channels. On the one hand, this increased density of occupied states in the conduction (valence) band increases the electric conductivity for electron (holes) and decreases the conductivity of the holes (electrons). On the other hand, however, the conductivity in this layer is reduced by the additional amount of scattering centers.

It should be noted that these are only theoretical concepts. They are subject to ongoing research and also motivate this thesis.

2.6 Doping

The impurities inside a crystal actually dominate the electric behavior of a typical semiconductor. Therefore, impurities are added on purpose. This is called doping. Undoped semiconductors, which basically are not in use, are called intrinsic semiconductors whereas doped semiconductors, also called extrinsic, are widely used.

2.6.1 N-Type and P-Type

There are two different types of doping:

- n-type: The semiconductor is doped with donor impurities, adding states close to the conduction band and, thus, shifting the fermi level, μ, closer to the conduction band.
- p-type: The semiconductor is doped with acceptor impurities, adding states close to the valence band and, thus, shifting the fermi level, μ, closer to the valence band.

Here, also the terms of majority and minority charge carriers are introduced. In n-type materials the free charge carriers are mostly electrons, whereas in p-type material they are mostly holes. Thus, in n-type (p-type) materials the majority charge carriers are electrons (holes) and the minority charge carriers are holes (electrons).

2.6.2 P-N Junction and Diode

Monolithic n-type or p-type semiconductors are not particularly useful. Only in combination, they can be turned into useful electronic devices like diodes. This can be done by, e.g., taking an n-type crystal (the bulk) and turning one side (surface) into a layer of p-type material by substantially adding acceptor impurities. The interface where the acceptor impurity concentration equals the donator impurity concentration is called the p-n junction. Let the coordinate perpendicular to the junction be x. Along x, the material changes continuously from being n-type to being p-type. Consequently, the Fermi level is also changing continuously from being close to E_C (n-type side) to being close to E_V (p-type side) as illustrated in Fig. 2.5.

The majority charge carriers, electrons (holes), on the n-type (p-type) side can drift to the p-type (n-type) side and recombine. This results locally in a non-zero charge distribution, $\rho(x)$, since on the p-type (n-type) side the acceptor (donator) state is still filled. Thus, over time, the p-type (n-type) side close to the p-n junction charges up negatively (positively) and an electric potential, $\Phi(x)$, builds up due to Gauss law,

$$\frac{\mathrm{d}^2\Phi}{\mathrm{d}x^2} = -\frac{\rho(x)}{\epsilon} \qquad , \tag{2.14}$$

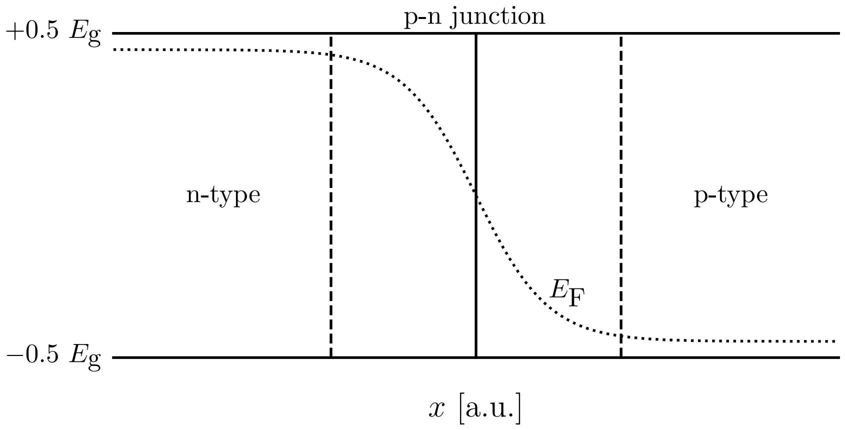

Figure 2.5.: Simplified band scheme of a p-n junction: The Fermi level, E_F, is plotted against the spatial coordinate x across the junction.

where ϵ is the dielectric constant of the medium. The resulting electric field,

$$\mathcal{E}(x) = -\frac{\mathrm{d}\Phi}{\mathrm{d}x} \qquad , \tag{2.15}$$

prevents further diffusion of the majority charge carriers.

The region where the charge density is non-zero around the p-n junction is called depleted as there are no free charge carriers left. Its thickness is d. The build-up of charge density, electric potential and electric field is illustrated in Fig. 2.6. The electric potential of the p-n junction, i.e. the difference in potential between the n-type and p-type sides, V_J, is usually of the order of the band gap energy: $V_J \approx E_g/e \approx 1\,\mathrm{V}$.

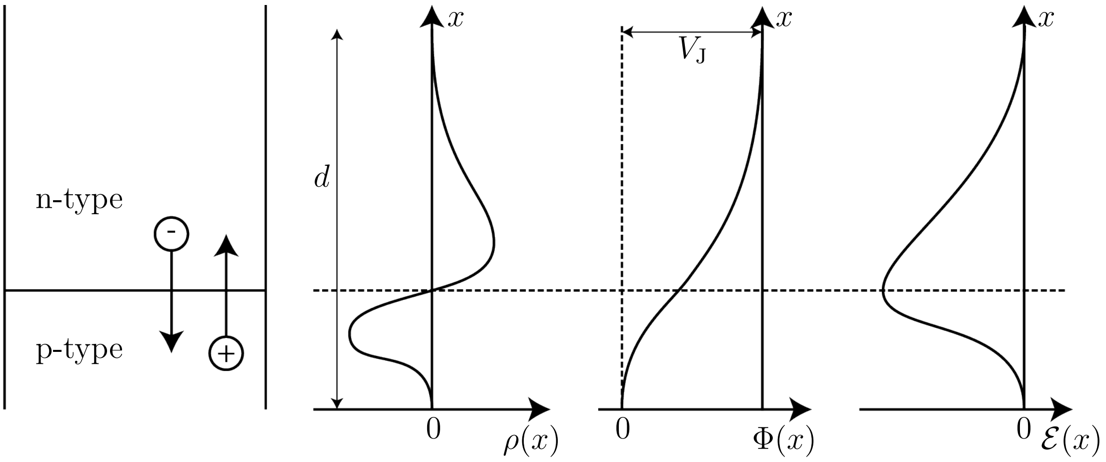

Figure 2.6.: Illustration of a p-n junction, adapted from [51]. Shown are the charge density, $\rho(x)$, potential, $\Phi(x)$, and electric field $\mathcal{E}(x)$ across the junction.

A diode is a p-n junction where an external voltage, called bias voltage V_B, is applied between the n-type and the p-type sides. If the potential on the n-type side is lower than the potential on the p-type side, current flows through the diode as soon as the bias voltage overcomes the voltage barrier of the junction: $V_\mathrm{B} > V_\mathrm{J}$.

If the applied potential on the n-type side is higher than on the p-type side, the depleted region increases and no current is flowing. This is called the reverse bias mode. The thickness of the depleted region can be approximated as

$$d \approx \sqrt{\frac{2\epsilon V_\mathrm{B}}{e N_\mathrm{D}}} \qquad , \tag{2.16}$$

where N_D is the (donor) impurity concentration of the bulk. This assumes that the p-type side is heavily doped and very thin, and thus, the depleted region mainly spreads into the bulk (n-type) of the crystal.

A fundamental property of a diode is its global charge neutrality. The over the total depleted volume, V_dep, integrated charge of a diode is zero:

$$\int_{V_\mathrm{dep}} \rho \, \mathrm{d}V = 0 \qquad . \tag{2.17}$$

2.7 Particle Interactions

Particles passing through germanium can create electron-hole pairs through interactions. Depending on the particle and its energy, different mechanism have to be considered. Here, only the most dominant and in the energy range for this thesis relevant important interactions are briefly summarized.

2.7.1 Photon Interactions

In matter, photons have a certain probability to interact with the material. The mean free path, $\overline{x}$, is the average distance a photon with a certain energy travels through a medium without any interaction. It is determined by

$$\overline{x} = (\rho_p \cdot \sigma)^{-1} \qquad , \tag{2.18}$$

where ρ_p is the density of the material and σ is the effective cross-section, which in general depends on the energy of the photon and the properties of the material. For a beam of photons of the same energy with intensity I_0, the attenuation of its intensity is given through Beer's Law

$$I(x) = I_0 \, e^{-x/\overline{x}} \qquad , \tag{2.19}$$

where $I(x)$ is the remaining intensity of the beam after a distance x.

There are three dominant processes in which photons interact with germanium. The energy of the photon determines which of the three is the most probable one.

Photoelectric Effect

The photon is completely absorbed from an electron, which gains all the energy of the photon exciting it into the conduction band or even higher bands. This process is dominant if the photon energy, E_γ, is below a few hundred keV.

Compton Scattering

Above a few hundred keV, Compton scattering becomes the dominant process. Here, the photon is not absorbed, but scattered and transfers only part of its energy to the electron on which it scatters.

Pair Production

Theoretically, this effect can appear above a photon energy of 1.022 MeV, i.e., two times the rest mass of an electron. Photons with energies above this threshold can convert into an electron and positron near a nucleus. This process becomes the most dominant process for photons with energies of several MeV.

2.7.2 Electromagnetic Interactions

In contrast to photons, charged particles, like alpha and beta particles, do interact with germanium in a continuous manner, i.e., they lose energy continuously when traveling through germanium. The strength at which energy is lost is called the stopping power,

$$S(E) = -\frac{\mathrm{d}E}{\mathrm{d}x} \qquad , \tag{2.20}$$

where E is the energy of the charged particle. The maximum penetration depth, x_d, is given through

$$x_\mathrm{d} = \int_{E_0}^{0} \frac{1}{S(E)} \mathrm{d}E \qquad . \tag{2.21}$$

Heavy Charged Particles

For heavy charged particles, like alphas, the stopping power is given through the Bethe-Bloch-Formula,

$$-\frac{\mathrm{d}E}{\mathrm{d}x} = \frac{4\pi n_\mathrm{e} Z^2}{m_\mathrm{e} c^2 \beta^2} \cdot \left(\frac{e^2}{4\pi\epsilon_0}\right) \cdot \left[\ln\left(\frac{2 m_\mathrm{e} c^2 \beta^2}{I_\mathrm{ex}(Z) \cdot (1-\beta^2)}\right) - \beta^2\right] \quad , \tag{2.22}$$

where $\beta = v/c$ is speed of the particle relative to the speed of light, E is the energy of the particle, Z is the atomic number of the material, ϵ_0 is the dielectric constant of the vacuum, e is the elementary charge, n_e is the electron density of the material, m_e is the mass of an electron and I_ex is the mean excitation potential which depends on Z.

Light Charged Particles

For light charged particles also the energy loss due to Bremsstrahlung has to be considered. For electrons, a good analytic expression does not exist and the stopping power for electrons in different materials are determined experimentally and stored in tables.

2.7.3 Ionization Energy

The energy which is lost by particles passing through a semiconductor is transferred into the semiconductor. However, not the total amount of transferred energy goes into the production of electron-hole pairs. Some part of the energy is converted into phonons or heat. The number of created electron-hole pairs is

$$N_\mathrm{pairs} = E_\mathrm{dep}/\epsilon_\mathrm{ion} \qquad , \tag{2.23}$$

where E_dep is the deposited energy and ϵ_ion is the so-called ionization energy. The ionization energy is a characteristic property of a semiconductor and is always larger than E_g. For germanium, ϵ_ion is 2.96 eV at 77 K.

Charge Cloud

The created electron-hole pairs spread over a finite volume which can be assumed to have a normal shape to a first approximation:

$$f(r,t) = \frac{1}{\sigma^2_\mathrm{cc}(t)\sqrt{2\pi}} \exp\left(-\frac{1}{2}\frac{r^2}{\sigma^2_\mathrm{cc}(t)}\right) \qquad , \tag{2.24}$$

where r is the radial variable and t is the time. Over time, the charge carriers diffuse and the size of the cloud grows. The initial size of the cloud, e.g. defined through $\sigma_\mathrm{cc}(t_0)$, depends on N_pairs and, thus, on the E_dep. In germanium, an energy deposition of 1 MeV results in an charge cloud size of approximately 0.5 mm.

Chapter 3: Germanium Detectors

A germanium detector is a diode in reverse bias mode where the active area of the detector is the depleted region, normally spanning the full volume. In principle, no current is flowing through the detector. Only when a particle deposits energy inside the crystal creating electron-hole pairs, the free charge carriers follow the electric field and a short current is measured. In this chapter a detailed view is presented, but the reader is referred to [14] for even more information.

3.0.1 Germanium Crystals

Germanium detectors are fabricated out of high purity germanium (HPGe) crystals which are created via zone refinement and subsequent Czochralski pulling: Germanium metal is melted and turned into a long cylindrical shaped ingot. Impurities are removed out of this ingot via zone refinement, i.e. heating coils move at a certain speed several times along the ingot, pushing the impurities to one end of the ingot. This end of the ingot is then cut off and the pure part can be melted again and the zone refining is repeated until the desired purity is reached. Then, the final crystal is pulled via the Czochralski-method: The pure germanium is melted again and a so-called seed crystal is dipped into it so that germanium atoms attach to the seed crystal in its fcc structure. The seed crystal is then slowly rotated and pulled upwards such that the germanium keeps attaching and a cylindrical ingot is formed [52]. The temperature of the germanium, the speed of the rotation and pulling defines the geometry of the ingot. Due to the cylindrical shape of the crystal, germanium detectors usually have a cylindrical base shape with a radius and length of a few centimeters.

High purity means, that the intrinsic net density of electrical active impurities is of the order of 10^9-$10^{10}\,\mathrm{cm}^{-3}$ (or even lower) and the dislocation density is of the order of $10^3\,\mathrm{cm}^{-2}$. This is extremely pure, which actually makes multi-centimeter dimensions for germanium detectors possible, see Eq. 2.16. However, it also makes the exact determination of the impurity profile extremely challenging. It should be noted, that their is a rather high uncertainty on these values. This is a known problem, since these are very important quantities because they impact the electric potential, see Eq. 2.14, of a detector and also the mobilities, see Eq. 2.13. This problem will be revisited later when simulation and data are compared.

Neutral impurities are even harder to determine, as they are electrically inactive. Usually, in HPGe, their concentration is assumed to be so low that they have no impact on the mobilities. However, this might not always be the case [53].

3.0.2 Doping and Contacts

Germanium crystals can be made n-type or p-type by adding the respective impurities to the molten germanium before or during pulling the crystal. The type of the bulk material defines whether a germanium detector is stated to be n-type or p-type.

In case of n-type detectors, one or more surfaces have to be turned into thin p-type layers by adding acceptor impurities. Usually, these are boron atoms inserted via ion implantation, i.e., ionized boron atoms are accelerated and targeted onto the desired surface of the detector. The energy of the ions determines how far they penetrate into the germanium. Usual thicknesses of the p-type layers are around 500 nm. The layers are usually substantially over-doped and, thus, do not fully deplete. Therefore, there is a conductive p-type layer which forms the so-called p^+-contact.

In case of p-type detectors one or more surfaces have to be turned into thin n-type layers by adding donor impurities. Usually, these are lithium atoms which are evaporated onto the surface and diffuse into it. Due to the different process, the lithium layers are thicker than the boron layers; they are around 0.5–1 mm thick. These layers are also substantially over-doped, such that a conductive n-type layer is present forming the n^+-contact.

Even though this is in principle enough to make a detector, also the respective other side is over-doped with the respective impurity type: an n^+-contact (p^+-contact) is created at a the n-type (p-type) side. This is done to create stable field conditions.

Since n^+-contact and p^+-contact are conductive, the applied bias voltage distributes evenly across these layers and there is no electric field inside them. Thus, they do not belong to the active detector material, but are so-called dead layers. The contacts can also be segmented in order to gain more information from one event. Usually, only either the n^+-contact or the p^+-contact is segmented.

The basic impurity and layer scheme of a germanium detector is illustrated in Fig. 3.1.

It should be noted that the exact processes of the detector fabrication and introduction of impurities are generally unknown. There are only very few companies world wide who are able to produce working germanium detectors and, thus, the exact details are kept confidential. This also applies to the next to subsections regarding metallization and passivation.

3.0.3 Metallization

Usually, the contact layers are metallized in order to secure that the applied potential is evenly distributed over the contact area. Mostly, aluminum, sometimes gold, is used and a thin layer is applied over the contacts. Typical thicknesses of the metallization are 10-300 nm.

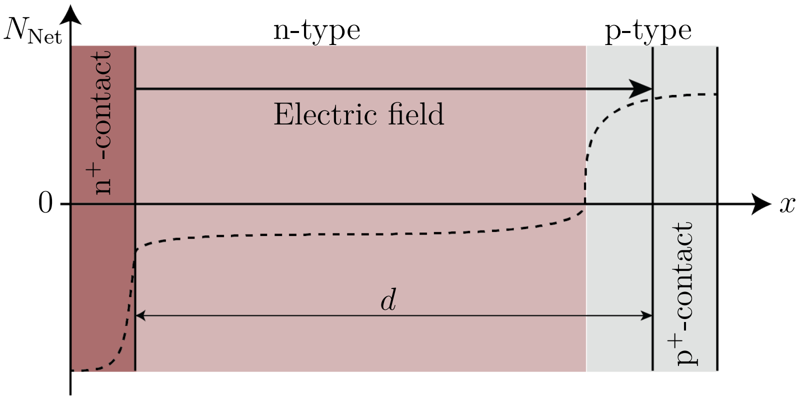

Figure 3.1.: Illustration (not to scale) of the basic impurity profile of an n-type germanium detector. The dashed line shows the net doping concentration N_{Net}. The electric field points from the n^{+}-contact to the p^{+}-contact and the depleted region extends almost over the whole crystal when biased. Adapted from [51].

Natural aluminum contains ^{26}Al, which is radioactive. Studies have shown that aluminum can be purified to an acceptable degree such that it does not contribute to much to the background in $0\nu\beta\beta$ experiments [54]. However, since in theory, the metallization should be redundant regarding the equal distribution of the potential, investigations were performed whether a reduced metallization has impact on the signal [51, 55]. This was investigated further in this thesis, see Ch. 7.

3.0.4 Passivation

Surfaces of the germanium detectors which are neither an n^{+}-contact nor a p^{+}-contact are called floating surfaces as the potential is not fixed there. These surfaces are usually passivated to protect the bare germanium, since germanium is a hygroscopic material.

For germanium detectors, typical passivations are silicon oxides, germanium oxides or amorphous germanium. The thicknesses vary from tenth of nanometer to micrometers, depending on technology. In general, detector manufacturers consider details on passivation technology proprietary.

The passivation layers also influence the band structure of the germanium just underneath. Similar to the situation at the end of a germanium crystal, see Sec. 2.5, the modified band structure can lead to a charged-up passivation layer and, thus, a modification of the density of occupied states in the germanium just underneath. How exactly these different kinds of passivation influence the detector response is yet unclear. The fact, that exact information about the passivation layers are often not available, makes it especially difficult to make predictions.

3.0.5 Operation Temperature and Leakage Current

Germanium detectors have to be operated at liquid nitrogen temperatures around $77 - 100\,\mathrm{K}$. At higher temperatures, the band gap is not large enough to suppress the thermal excitation of electrons sufficiently.

Theoretically, no current should flow through a reversely biased diode. In practice, however, there is a small current in the pA regime. This is usually dominated by surface currents flowing along the floating surfaces of a detector. These surface currents are due to the imperfect (modified) band structure and additional states close to the surface of a crystal. Reduced temperatures also suppress this leakage current.

Small bulk currents occur from thermal electron-hole pair production in the depleted region. At $T < 100\,\mathrm{K}$, they do not influence the operation.

3.1 Electric Potential and Field

In Sec. 2.6.2, the one dimensional Poisson equation was used to describe the electric potential of a p-n junction with an infinite diameter. However, real germanium detectors are finite and have an environment which influences the electric potential and the electric field. Therefore, the first Maxwell equation, also known as Gauss's law,

$$\nabla \cdot \mathbf{D}(\mathbf{r}) = \rho(\mathbf{r}) \qquad , \tag{3.1}$$

where $\mathbf{D}(\mathbf{r})$ is the electric displacement field and $\rho(\mathbf{r})$ is the charge density distribution, has to be used:

$$\begin{aligned} \mathbf{D}(\mathbf{r}) &= \epsilon_0 \epsilon_\mathrm{r}(\mathbf{r}) \boldsymbol{\mathcal{E}}(\mathbf{r}) \, , & (3.2) \\ \boldsymbol{\mathcal{E}}(\mathbf{r}) &= -\nabla \Phi(\mathbf{r}) \, , & (3.3) \end{aligned}$$

where $\boldsymbol{\mathcal{E}}(\mathbf{r})$ is the electric field, ϵ_0 is the dielectric constant of the vacuum and $\epsilon_\mathrm{r}(\mathbf{r})$ is the relative permittivity distribution. Eq. (3.1) becomes

$$\nabla \cdot (\epsilon_\mathrm{r}(\mathbf{r}) \cdot \nabla \Phi(\mathbf{r})) = -\frac{\rho(\mathbf{r})}{\epsilon_0} \; . \tag{3.4}$$

The relative permittivity of a material depends on the temperature and is influenced by doping. However, the typical doping levels of HPGe are so low that this influence can be neglected. Thus, the permittivity of germanium is assumed to be a constant between 77-300 K, $\epsilon_\mathrm{r}^\mathrm{Ge}(\mathbf{r}) = 16$ [14]. The total charge density, $\rho(\mathbf{r})$, can be separated into two distributions: $\rho = \rho_\mathrm{imp} + \rho_\mathrm{b}$. Here, ρ_imp is the part originating from the space charge density of the depleted region. Thus, it is given by the impurity density, N_imp: $\rho_\mathrm{imp} = e \cdot N_\mathrm{imp}$. This contribution depends on the bias voltage as it is only non-zero in depleted regions. The other contribution, ρ_b, is originating from the build-up of space charges, e.g. charged-up surfaces. Here, it is yet unclear how this distribution varies with the applied bias voltage.

The boundary conditions are the (fixed) potentials applied at the contacts. However, the floating surfaces do not provide fixed boundary conditions. Even if these surfaces are kept small, it means that also the environment of the detector has to be taken into account in the calculation of the electric potential as the electric flux through this floating surfaces might be non-zero. For example, there is a difference in the potential of the detector if the detector is in vacuum or immerged in LAr. Also, grounded material of the holding structure close to these surfaces influences the potential.

3.2 Charge Drift

As explained in Sec. 2.4, the charge carriers do not follow exactly the electric field but the drift field, $\mathbf{v}_{\mathrm{d,e/h}}(\mathbf{r}, \boldsymbol{\mathcal{E}}(\mathbf{r}), T)$, see Eq. 2.12, and the mobility tensor, $\mu_{\mathrm{e/h}}(\mathbf{r}, \boldsymbol{\mathcal{E}}(\mathbf{r}), T)$, consists out of several different contributions, see Eq. 2.13. As it depends on a number of different quantities (which are also hard to determine), the mobility tensor for germanium is not well understood yet. However, some models were developed to approximate the mobility tensor in HPGe.

3.2.1 Charge Drift Model

The drift model used in the simulations prepared for this thesis was first introduced by Canali [56], then extended by Mihailescu [57] and Bruyneel [58, 59].

It is assumed, that due to the very low impurity concentrations in HPGe, the contributions to μ from impurities, μ_{Ion}, μ_{Neu} and μ_{Dis} in Eq. 2.13, can be neglected. The scattering on phonons varies for different drift directions since the effective mass of the phonons depends on it as well, see Sec. 2.3. Therefore, the drift velocity is not parallel to the electric field in general. However, due to the symmetry of fcc structure, it should be parallel to it in case the electric field aligns with one of the crystal axes $\langle 100\rangle$, $\langle 110\rangle$ or $\langle 111\rangle$. These drift directions are labeled as longitudinal drifts and the respective mobility tensors, μ_{l}, become scalars and can be expressed through the empirical formula

$$\mu_{\mathrm{l}}(\mathcal{E}) = \frac{\mu_0}{\left(1 + (\mathcal{E}/\mathcal{E}_0)^{\beta}\right)^{1/\beta}} - \mu_n \qquad , \tag{3.5}$$

where μ_0, $\mathcal{E}_0$, β and μ_n are parameters, which are different for electrons and holes and also differ for the directions $\langle 100\rangle$, $\langle 110\rangle$ and $\langle 111\rangle$. The parameters are obtained through fits to appropriate data sets [58]. However, it was observed and discussed, [58], that these parameters are not the same for each detector. This implies that the assumption that the scattering on phonons is the dominant process is not entirely correct, and thus, that also the impurities have to be considered in a general model. But since it is not yet possible to determine those with an sufficient precision, the influence of the impurities cannot be modeled and the parameters of Eq. 3.5 have to be determined for each individual detector with appropriate characterization measurements.

Electron Drift

The conduction band has 8 global minima at $\mathbf{l}_f \in L$. If no electric field is applied, almost all conduction electrons are equally divided onto the eight corresponding valleys with an effective mass tensor of

$$\left(m^*_{\mathrm{C},\mathbf{l}_f}\right)_{ij} = \mathrm{inv}\left(\frac{1}{\hbar^2}\left.\frac{\delta^2 E_\mathrm{C}(\mathbf{l}_f)}{\delta k_i \delta k_j}\right|_{\mathbf{l}_f}\right) \qquad , \tag{3.6}$$

which can be approximated as a diagonal matrix with only two different parameters,

$$m^*_{\mathrm{C},L} = \begin{pmatrix} m_\mathrm{t}^{-1} & 0 & 0 \\ 0 & m_\mathrm{l}^{-1} & 0 \\ 0 & 0 & m_\mathrm{t}^{-1} \end{pmatrix} \qquad , \tag{3.7}$$

if the coordinates axes align with the crystal axes. The parameters $m_\mathrm{l} = 1.64\ m_\mathrm{e}$ (longitudinal) and $m_\mathrm{t} = 0.0819\ m_\mathrm{e}$ (transversal) were experimentally determined [60]. Through rotational transformations, R_i, the effective mass tensor of each individual valley, γ_i, is given as

$$\gamma_i = R_\mathrm{i}^\mathsf{T} \cdot m^*_{\mathrm{C},L} \cdot R_\mathrm{i} \qquad . \tag{3.8}$$

If an electric field is applied along $\boldsymbol{\mathcal{E}}/|\boldsymbol{\mathcal{E}}| = \boldsymbol{\mathcal{E}}_0 \in \langle 100 \rangle$, the electrons can be assumed to occupy equally only 4 of those valleys which have a positive scalar product: $\mathbf{l}_i \cdot \boldsymbol{\mathcal{E}}_0 > 0$. The relative population of each valley, n_i, is related to the direction of the electric field via [61]

$$n_i = \mathcal{R}(\mathcal{E}) \left(\frac{\sqrt{\boldsymbol{\mathcal{E}}_0^\mathsf{T} \gamma_i \boldsymbol{\mathcal{E}}_0}}{\sum\limits_{i=1}^{4} \sqrt{\boldsymbol{\mathcal{E}}_0^\mathsf{T} \gamma_i \boldsymbol{\mathcal{E}}_0}} - \frac{1}{4} \right) + \frac{1}{4} \qquad , \tag{3.9}$$

where $\mathcal{R}$ is a factor depending on the electric field strength, $\mathcal{E} = |\boldsymbol{\mathcal{E}}|$.

The resulting net velocity can be expressed via

$$\mathbf{v}_\mathrm{e}(\boldsymbol{\mathcal{E}}) = \mathcal{A}(\mathcal{E}) \sum_{i=1}^{4} n_i \frac{\gamma_i \boldsymbol{\mathcal{E}}_0}{\sqrt{\boldsymbol{\mathcal{E}}_0^\mathsf{T} \gamma_i \boldsymbol{\mathcal{E}}_0}} \qquad , \tag{3.10}$$

where $\mathcal{A}(\mathcal{E})$ is also a factor depending on the electric field strength.

The two factors $\mathcal{A}$ and $\mathcal{R}$ can be determined for a crystal by measuring the drift velocity along two directions: $\langle 100 \rangle$ and $\langle 111 \rangle$. For an electric field parallel to $\langle 100 \rangle$, $\mathcal{A}$ becomes

$$\mathcal{A}(\mathcal{E}) = \mathbf{v}_\mathrm{e}^{100}(\mathcal{E})/2.888 \tag{3.11}$$

and along $\langle 111 \rangle$ $\mathcal{R}$ can be calculated with Eq. 3.9 and Eq. 3.10:

$$\mathcal{R}(\mathcal{E}) = -1.182\ \mathbf{v}_{\mathrm{e}}^{111}(\mathcal{E})/\mathcal{A}(\mathcal{E}) + 3.161 \qquad . \tag{3.12}$$

The numbers only depend on the transversal and longitudinal effective masses. The two drift velocities, $\mathbf{v}_{\mathrm{e}}^{100}$ and $\mathbf{v}_{\mathrm{e}}^{111}$, are modeled with Eq. 3.5 and Eq. 2.12. Thus, the electron drift can be modeled with 8+2 parameters: m_{l}, m_{t}, $\mu_{0,\mathrm{e}}^{100}$, $\mathcal{E}_{0,\mathrm{e}}^{100}$, β_{e}^{100}, $\mu_{n,\mathrm{e}}^{100}$, $\mu_{0,\mathrm{e}}^{111}$, $\mathcal{E}_{0,\mathrm{e}}^{111}$, β_{e}^{111}, $\mu_{n,\mathrm{e}}^{111}$.

Hole Drift

The valence band has its global maximum at $\mathbf{k} = \Gamma$. Analytical descriptions of the valence band around Γ are more complicated, but the hole drift velocity, $\mathbf{v}_{\mathrm{h}} = (v_{\mathrm{r}}, v_{\varphi}, v_{\theta})^{\mathsf{T}}$, in spherical coordinates can be approximated via [58]:

$$\begin{aligned}
v_{\mathrm{r}}(\mathbf{k}) &= v_{\mathrm{h}}^{100}(\mathcal{E}) \left[1 - \kappa(k_{\mathrm{r}}) \left(\sin k_{\theta}{}^{4} \sin 2k_{\varphi}{}^{2} + \sin 2k_{\theta}{}^{2}\right)\right] \quad , & (3.13)\\
v_{\theta}(\mathbf{k}) &= v_{\mathrm{h}}^{100}(\mathcal{E})\Omega(k_{\mathrm{r}}) \left[2 \sin k_{\theta}{}^{3} \cos k_{\theta} \sin 2k_{\varphi}{}^{2} + \sin 4k_{\theta}\right] \quad , & (3.14)\\
v_{\varphi}(\mathbf{k}) &= v_{\mathrm{h}}^{100}(\mathcal{E})\Omega(k_{\mathrm{r}}) \sin k_{\theta}{}^{3} \sin 4k_{\varphi} \quad . & (3.15)
\end{aligned}$$

Here, $\mathbf{k} = (k_{\mathrm{r}}, k_{\varphi}, k_{\theta})^{\mathsf{T}}$ is the mean wave vector of the holes in spherical coordinates, which is assumed to be parallel to the applied electric field and $\kappa(k_{\mathrm{r}})$ and $\Omega(k_{\mathrm{r}})$ are two factors depending on the radial component of the wave vector, k_{r}. The dependence can be approximated as [58]:

$$\begin{aligned}
\kappa(k_{\mathrm{r}}) &= -0.01322\ k_{\mathrm{r}} + 0.41145\ k_{\mathrm{r}}^{2} - 0.23567\ k_{\mathrm{r}}^{3} + 0.04077\ k_{\mathrm{r}}^{4}\,, & (3.16)\\
\Omega(k_{\mathrm{r}}) &= +0.00655\ k_{\mathrm{r}} - 0.19946\ k_{\mathrm{r}}^{2} + 0.09859\ k_{\mathrm{r}}^{3} - 0.01559\ k_{\mathrm{r}}^{4}\,. & (3.17)
\end{aligned}$$

The relative velocity,

$$v_{\mathrm{rel}}(\mathcal{E}) = v_{\mathrm{h}}^{111}(\mathcal{E})/v_{\mathrm{h}}^{100}(\mathcal{E}) \quad , \tag{3.18}$$

which is the ratio between the absolute drift velocities for electric fields along $\langle 100 \rangle$ and $\langle 111 \rangle$, can be used to calculate the radial component, k_{r} [58]:

$$k_{\mathrm{r}}(v_{\mathrm{rel}}(\mathcal{E})) = 9.2652 - 26.3467\ v_{\mathrm{rel}}(\mathcal{E}) - 29.6137\ v_{\mathrm{rel}}(\mathcal{E})^{2} - 12.3689\ v_{\mathrm{rel}}(\mathcal{E})^{3}\,. \tag{3.19}$$

Both velocities, $v_{\mathrm{h}}^{100}(\mathcal{E})$ and $v_{\mathrm{h}}^{111}(\mathcal{E})$, can be modeled with Eq. 3.5 and the parameters can be determined in appropriate characterization measurements. Thus, the hole drift can be modeled with 8 parameters: $\mu_{0,\mathrm{h}}^{100}$, $\mathcal{E}_{0,\mathrm{h}}^{100}$, β_{h}^{100}, $\mu_{n,\mathrm{h}}^{100}$, $\mu_{0,\mathrm{h}}^{111}$, $\mathcal{E}_{0,\mathrm{h}}^{111}$, β_{h}^{111}, $\mu_{n,\mathrm{h}}^{111}$.

Temperature Dependence

So far, the drift models introduced for the electrons and holes do not have a temperature dependency. Therefore, a scaling factor is added to the drift model, $f_{\mathrm{T,e/h}}^{100/111}(T)$, which scales the longitudinal drift velocities:

$$\mathbf{v}_{\mathrm{e/h}}^{100/111}(T) = f_{\mathrm{T,e/h}}^{100/111}(T) \cdot \mathbf{v}_{T_{\mathrm{ref}},\mathrm{e/h}}^{100/111} \quad . \tag{3.20}$$

The previously introduced parameters, μ_0, $\mathcal{E}_0$, β and μ_n are determined at $T = T_{\mathrm{ref}}$ and determine $\mathbf{v}_{T_{\mathrm{ref}},\mathrm{e/h}}^{100/111}$. Different models for $f_{\mathrm{T,e/h}}^{100/111}$ were introduced [62, 63, 64]. In this thesis, a Boltzmann-like model is used [64],

$$f_{\mathrm{T,e/h}}^{100/111}(T) = \frac{1 + p_{1,\mathrm{e/h}}^{100/111} \cdot \exp\Big(-p_{2,\mathrm{e/h}}^{100/111}/T_{\mathrm{ref}}\Big)}{1 + p_{1,\mathrm{e/h}}^{100/111} \cdot \exp\Big(-p_{2,\mathrm{e/h}}^{100/111}/T\Big)} \quad , \tag{3.21}$$

adding 8 more parameters to the total drift model: $p_{1/2,\mathrm{e/h}}^{100/111}$.

Surface Drifts

If the introduced drift model parameters for a given detector are determined, the above model can describe bulk drifts quiet well. However, it fails so describe the drift correctly for surface drifts. As explained in Sec. 2.5, the electric conductivity, or respectively the mobility, is influence by the additional states at the surfaces.

So far, there is no sophisticated or realistic extension of the model to describe surface drifts. Later in this thesis, a modulation of the surface drift in simulations will be introduced to reproduce the effect seen in data.

3.3 Signal Generation

The charge carriers induce mirror charges on the contacts of the detector depending on their position within the detector. At the beginning, holes and electrons are at the same position and, thus, the net induced charge on contact i, Q_i, is zero.

As soon as they start drifting due to the electric field, electron and holes separate and Q_i becomes non-zero. The dependence of the net induced charge on the position of electrons and holes, $\mathbf{r}_\mathrm{e}$ and $\mathbf{r}_\mathrm{h}$, is given by the Shockley-Ramo theorem [65, 66]:

$$Q_i(\mathbf{r}_\mathrm{e}(t), \mathbf{r}_\mathrm{h}(t)) = Q_0 \left[\mathcal{W}_i(\mathbf{r}_\mathrm{h}(t)) - \mathcal{W}_i(\mathbf{r}_\mathrm{e}(t))\right] \quad , \tag{3.22}$$

where Q_0 is the absolute charge of the electrons and holes, $Q_0 = |Q_e| = Q_h$, and $\mathcal{W}_i$ is the so-called weighting potential of contact i.

3.3.1 Weighting Potentials

The weighting potential of contact i, $\mathcal{W}_i(\mathbf{r})$, defines the portion of a charge at position $\mathbf{r}$ which is induced on the contact. Hence, it is dimensionless and ranges from 0 to 1. It is calculated via Eq. 3.4, like the electric potential, but with different boundary conditions:

- The charge density $\rho(\mathbf{r})$ is set to zero everywhere.
- The weighting potential on the contact itself is fixed to 1.
- The weighting potential on all other contacts is fixed to 0.

Chapter 4: Experimental Test Stand

As discussed in the previous chapters, the surfaces of germanium detectors are critical areas. Low-range background radiation deposits its energy at these surfaces where the physics is not well understood as the model approximations are not valid at the boundaries of the crystal.

Therefore, a test facility was developed to address these problems by studying the response of germanium detectors to such surface events: the GermAnium LAser TEst Apparatus (GALATEA). It was especially designed to irradiate germanium detectors with alpha and beta radiation and LASER[1] light. Since its commissioning in 2011 [67], it has undergone several changes and improvements. The technical details can be found in [51, 67, 68, 69, 70, 71]. In this chapter, only the general setup and the last upgrades are summarized. All studies of germanium detectors presented in this thesis were performed in GALATEA.

4.1 GALATEA

The test stand is depicted in Fig. 4.1. In order to irradiate a germanium detector with alpha or beta radiation, the radioactive source and the detector have to be located together in one vacuum volume. Thus, the core of the setup is one big vacuum chamber, in which a germanium detector can be placed together with two independent radioactive sources. The inside of the vacuum chamber is shown in Fig. 4.2 and illustrated in Fig. 4.3. A pre-pump and a turbo pump connected to the chamber are able to create a vacuum with a pressure of about 10^{-6} mbar at room temperature.

All kind of germanium detectors can be studied in this setup. They only have to be mounted to the detector holder plate which fits on a cooling finger located in the center of the vacuum chamber. This cooling finger goes to the bottom of the chamber where a liquid nitrogen (LN2) tank is located. The cooling finger penetrates into the LN2 and, thus, cools the detector such that it can be operated ($\lesssim 100\,\mathrm{K}$). However, the cooling finger alone would not provide enough cooling power to do so. A silver coated copper "hat" is put over the detector and sits on the detector holder plate. Thus, the hat is also in indirect contact with the cooling finger and is cooled down. This hat is also called the infrared shield (IR shield), since it shields the detector against thermal radiation and, thus, radiation heating. In addition, to isolate the inner volume of the vacuum chamber thermally from the warm steel walls of the vacuum chamber, a special cryogenic multilayer foil "COOLCAT 2" is placed closed to the walls. The fill level of the

---

[1] A LASER has not yet been installed.

LN2 tank is monitored and the tank is automatically refilled through a connected LN2 dewar. This happens about every 24 h. While being cold, the interior of the chamber acts as cryo pump reducing the pressure to $\approx 10^{-8}$ mbar while the turbo pump is on.

During the operation of a germanium detector, the pre- and turbo pump have to be turned off as they introduce microphonics into the system and, thus, add noise to the signal of the detector. Therefore, a shutter is located between the pumps and the chamber. When the shutter is closed, the pressure rises but stabilizes between 10^{-5}-10^{-4} mbar and holds over several days or even weeks.

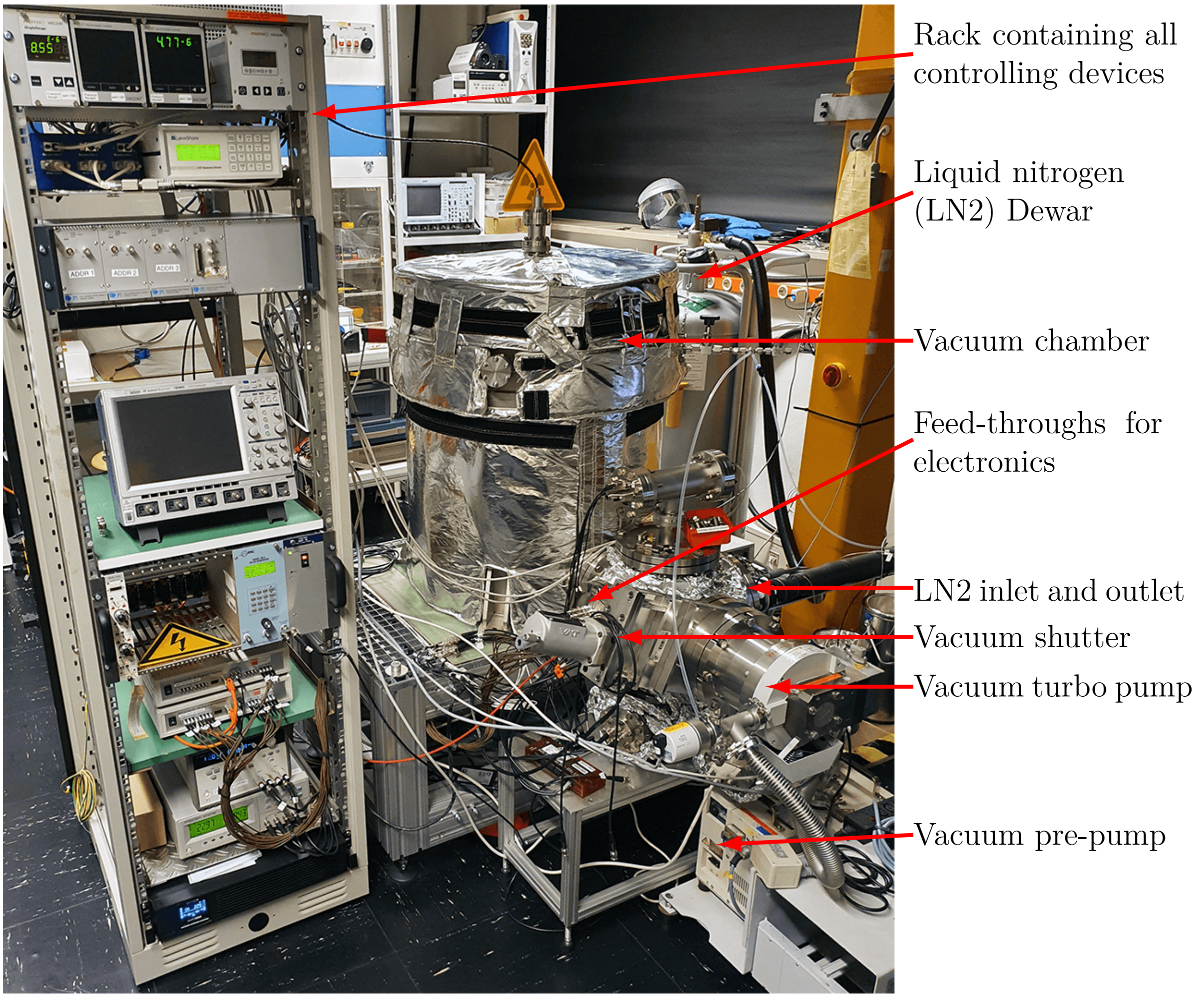

Figure 4.1.: Picture of GALATEA taken March 3, 2020. The most important parts are annotated.

Two sources of radiation can be mounted in two collimators called the horizontal and vertical collimators. The horizontal (vertical) collimator is attached to a linear motor which can move the collimator in horizontal (vertical) direction around the detector. The corresponding linear motors are also labeled horizontal and vertical. The collimators touch the hat on Murthfeldt sliders. Murthfeldt is a special material as it is electrically isolating while having very low friction coefficients. These properties are needed as the horizontal (vertical) collimator has to slide along the hat along a horizontal (vertical) slit on the side (top) of the hat. The slits allow low range radiation to pass through the hat such that it can reach the detector.

All these components, the vertical and horizontal motors and collimators and the hat sit on a stage. This stage can be rotated by a third motor, the rotational motor, by almost 360° around the detector. In order to perform a rotation, the hat has to be lifted a little bit such that is looses the contact to the detector holder plate. Three small linear actuators, called screws, which are also attached to the stage underneath the hat together with a screw (hat) positioning system (HPS), were installed for that purpose [51].

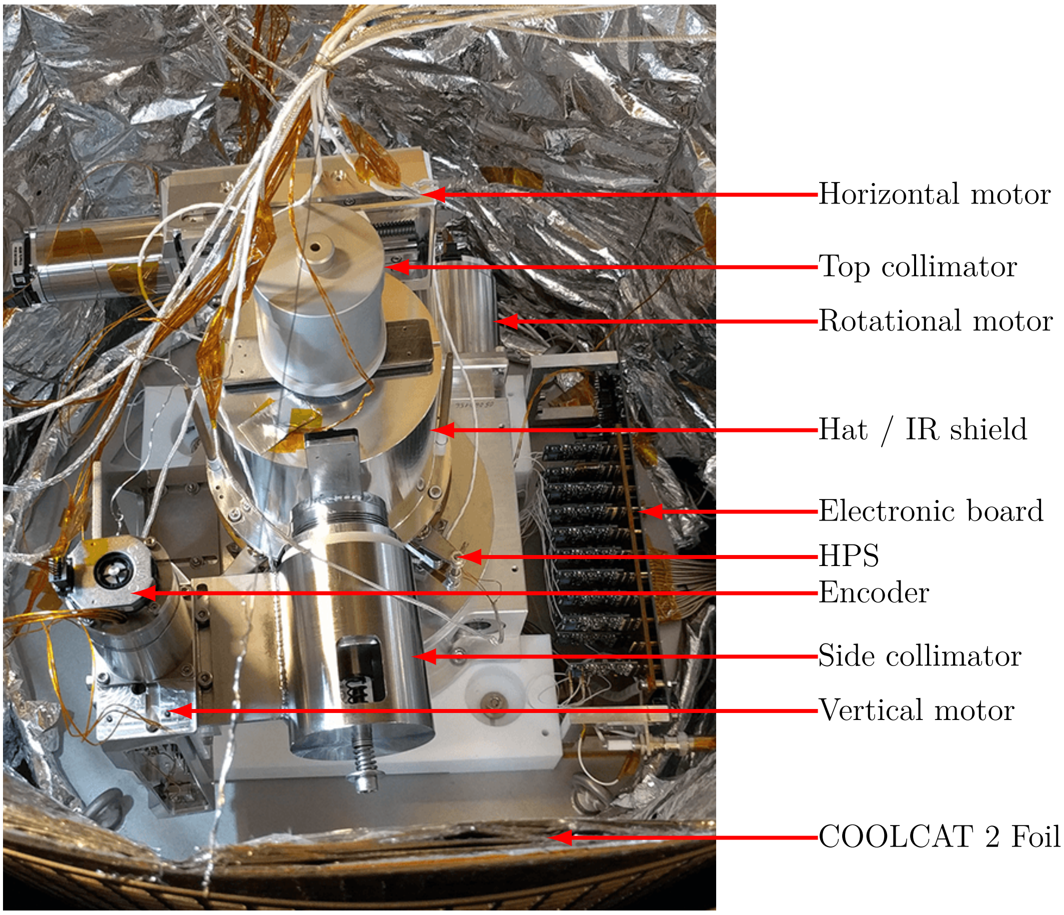

Figure 4.2.: Annotated picture of the inside of the vacuum chamber of GALATEA taken on July 19, 2017.

In combination, the three motors are able to move the two collimators around the detector, such that almost any point on the top surface or the mantle of a germanium detector can be irradiated with with particles emitted by the sources.

Each collimator consists internally of 7 segments, which have a cylindrical shape with an inner borehole. Individual segments with varied borehole size and material can be combined to alter the resulting beam-spot on the detector surface.

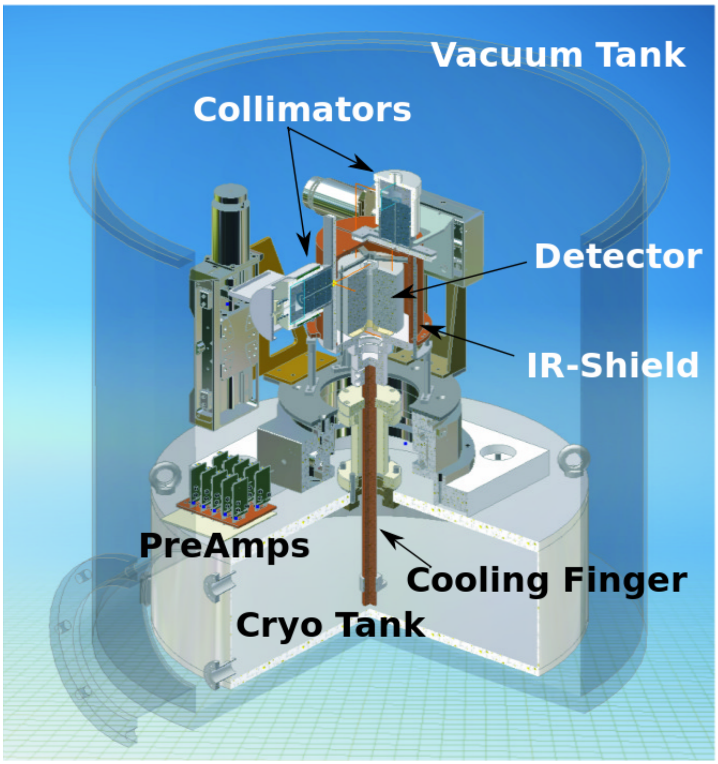

Figure 4.3.: Illustration of the inside of GALATEA. The most important parts are annotated.

4.1.1 New Motor Encoders

During data taking, a problem with the vertical motor occurred. Even though the stage and, thus, the motors were always thermally isolated from the LN2 tank, these components still cooled down to about 220 K and, sometimes, the vertical motor got stuck. Unfortunately the motor controller itself was not configured to recognize this. As a result, the information about the vertical motor position was lost. Therefore, the system was upgraded: encoders were attached to the spindle of each motor as shown in Fig. 4.4. These encoders are able to measure the distance the motor really moves by counting the number of rotations of the motor spindle. Thus, the information on the position of all motors now always reflects the real situation of the system.

4.1.2 Electronics

The electronic board, which is also visible in Fig. 4.2 and Fig. 4.3, is located on the bottom of the vacuum chamber. Up to 20 charge sensitive pre-amplifier boards can be attached. These pre-amplifiers amplify the charge signals, which are induced on the contacts of the detector.

Usually, one special contact is the "main" channel of the detector. In the case of seg-

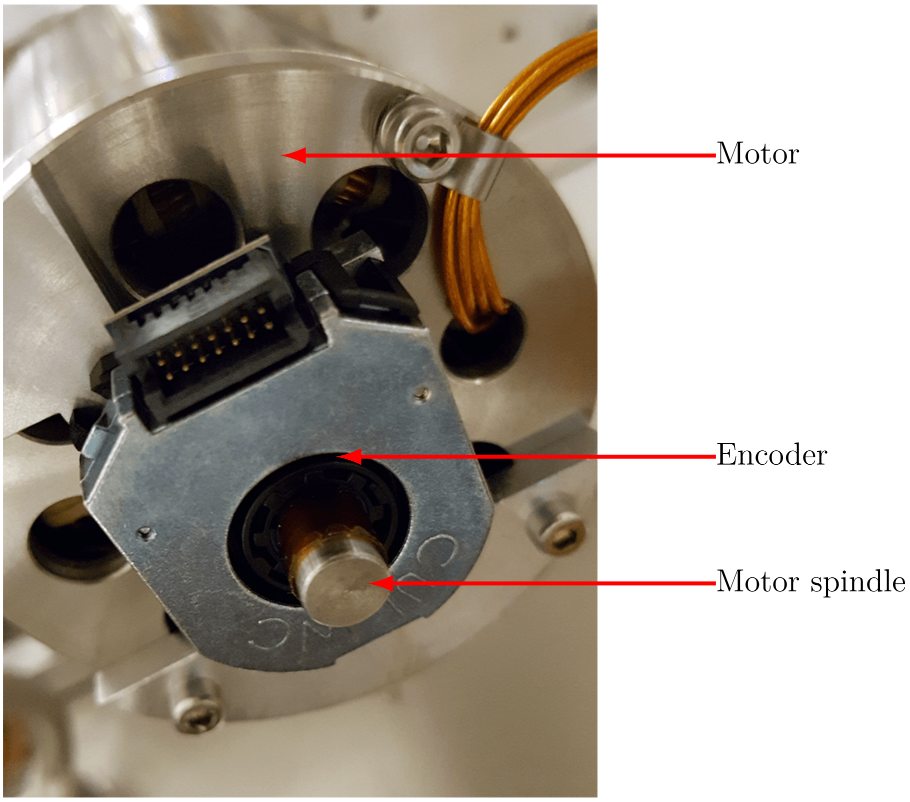

Figure 4.4.: One new motor encoder attached to one of the three motors in GALATEA. The encoder measures the rotation of the motor spindle, what can be translated into the distance the motor actually moved.

mented germanium detectors, this is the full volume contact, as, usually, only either the p-type or n-type side of a germanium detector is segmented. This channel is called the "core" throughout this thesis.

The general read-out configuration of GALATEA is show in Fig. 4.5. However, the details depend on the individual detector. In GALATEA, the pre-amplifier boards feature a field effect transistor (FET), which is the main amplification unit. In order to reduce the electronic noise in the core channel, its FET is moved from the pre-amplifier board onto a smaller board which is mounted very closely underneath the detector. Due to spacial limitations, this is not possible for all channels. The high (bias) voltage (HV) is applied to the core channel whereas the other channels are at ground. Therefore, the core channel is AC coupled to the FET such that the high frequency signals of the detector are transferred to the FET and not to the HV line. The other channels are DC coupled to their FETs. In addition, it is possible to feed a test pulse into the FET of the core channel.

The line for the test pulse, the HV line and all pre-amplified signal channels are accessible through feed-throughs. The signal feed-throughs are connected to a data acquisition unit (DAQ) located in the rack next to the vacuum chamber, see Fig. 4.1. The DAQ converts the analog signals into digital signals and stores them on disc.

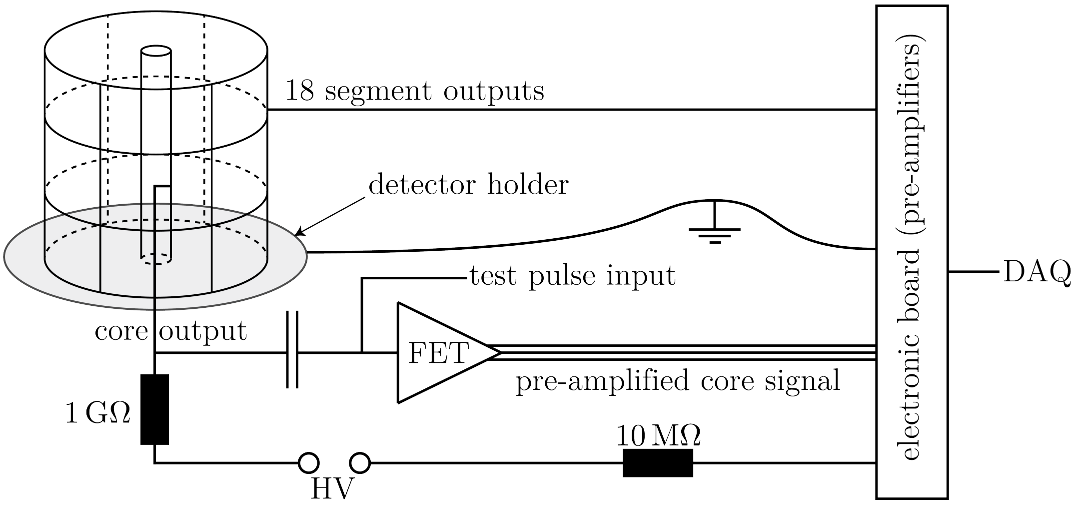

Figure 4.5.: Schematic of the electronics in GALATEA, taken from [51]. Here, the detector is a true coaxial segmented germanium detector, where the inner borehole is the core channel and the mantle is segmented into 18 segments.

4.1.3 New Data Acquisition Units

A new data acquisition system was installed for the measurements presented in this thesis: two SIS3316 units [72]. Each unit has up to 16 channels. The analog input signal of each channel is converted into 14-bit unsigned integers (Analog to Digital Counts (ADC)) with a sampling rate of 250 MHz. The number of samples per channel per event is 5000.

The DAQ uses a sliding trapezoidal filter as a trigger algorithm to recognize whether an event occurred in the detector which has to be stored.

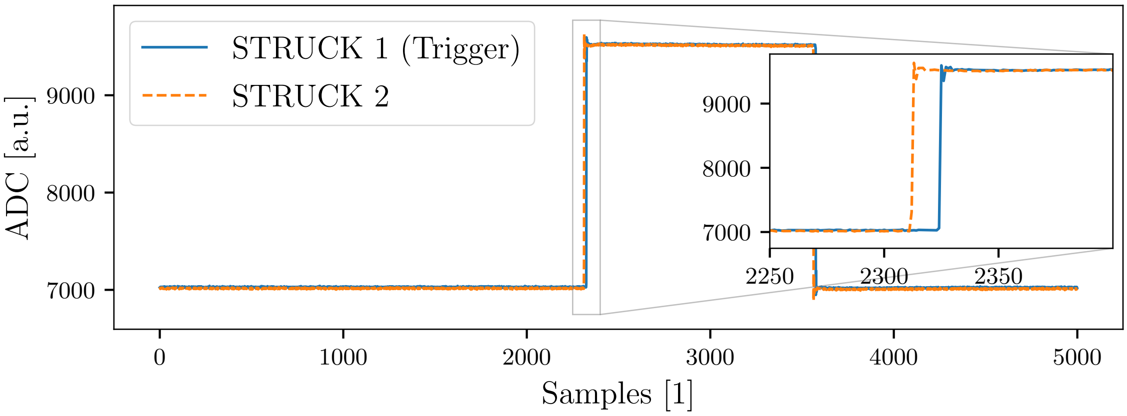

Figure 4.6.: Pulses recorded in the first channels of the two STRUCK units. The delay caused by the delayed trigger signal is visible in the subplot.

Usually, the DAQ system is configured to trigger only on the core channel as it registers the full volume energy. The core channel is connected to STRUCK module 1 and the trigger signal is forwarded to STRUCK module 2 via a short cable. As a result, there is a small constant time delay between the channels of the two STRUCK modules. This delay was measured and taken into account for offline.

4.1.4 Monitoring

Several operational parameters of GALATEA are monitored during operation. In order to monitor the pressure within the vacuum chamber, two pressure sensors are mounted on two flanges of the vacuum chamber. The temperature is monitored with several PT-100 sensors located inside and on the outside of the chamber.

All devices to operate GALATEA are located in the rack next to the vacuum chamber. This includes the HV module, the DAQ units, one motor controller, one controller for the screws, one controller for the HPS, the power supply for the electronic board, a test pulse generator, an LCR meter for the LN2 fill level, two controllers for the pressure sensors and two controllers to read out the PT-100 sensors. Figure. 4.7 shows some quantities monitored in GALATEA over a few days.

4.1.5 Scans and Measurements

All devices are controlled and monitored via one software package, which allows for automated scans. A scan is a set of measurements, where a measurement is a set of events recorded over a certain period of time, e.g. 30 min. During one measurement the collimators with the sources are in fixed positions. Thus, also the center of both beam-spots are fixed. They are given by 3 (4) parameters: r_m, $\varphi^\mathrm{s}_\mathrm{m}$ ($\varphi^\mathrm{t}_\mathrm{m}$) and z_m, which are are cylindrical coordinates in the coordinate system of the detector. (r_m, $\varphi^\mathrm{t}_\mathrm{m}$) are polar coordinates of the center of the beam-spot of the top source on the top surface of the detector and ($\varphi^\mathrm{s}_\mathrm{m}$, z_m) are the mantle coordinates of the beam-spot of the side source on the side (mantle) surface. The top and side collimator are always separated by 90°: $\varphi^\mathrm{t}_\mathrm{m} = \varphi^\mathrm{s}_\mathrm{m} + 90°$. Thus, a cylindrical vector can be assigned: $\mathbf{r}_\mathrm{m} = (r_\mathrm{m}, \varphi^\mathrm{s}_\mathrm{m}(\varphi^\mathrm{t}_\mathrm{m}), z_\mathrm{m})$ to each measurement.

4.1.6 Alignment: Systematic Uncertainties

The motors, in combination with the encoders, have a very good spatial resolution, on the μm level. However, a larger systematic uncertainty results from alignment uncertainties concerning the position of the detector with respect to the coordinate system of the motors. A general systematic uncertainty of 0.5 mm was estimated for the radial and vertical positions due to a possible shift and tilt of the detector. For a typical detector radius of $30-40$ mm, this translates to a systematic uncertainty of up to 1° for the polar angle.

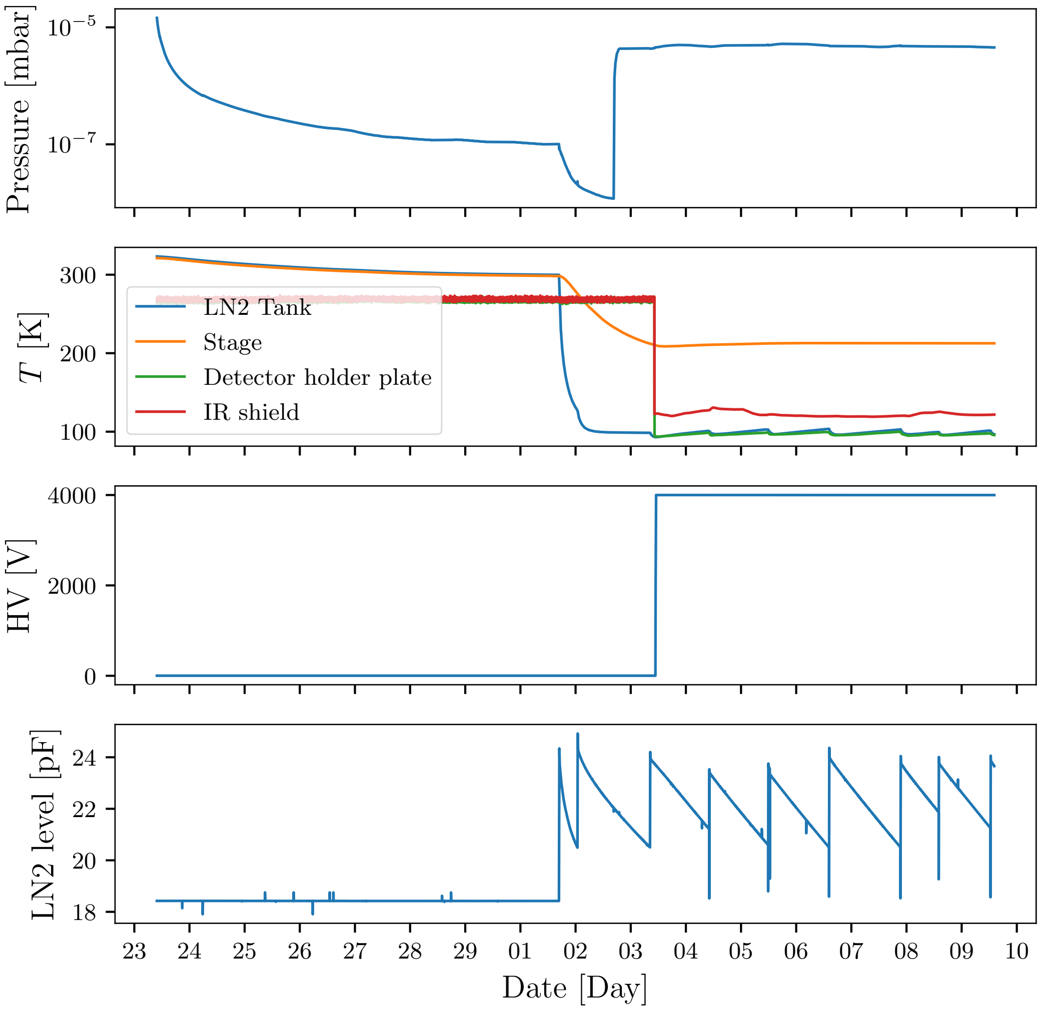

Figure 4.7.: Selected quantities as monitored in GALATEA during operation starting on February 23, 2020. Until first of March, GALATEA was only pumped. Then, the automated filling of the LN2 tank was started, cooling the chamber and reducing the pressure further. On March 2, the shutter was closed and the pumps were switched off. Hence, the pressure went up to 10^{-5} mbar. On March 3, the electronic board was switched on which also read-outs the detector and PT-100's on the IR shield. In addition, the high voltage was ramped up.

Chapter 5: Detector Simulation

As pointed out in Ch. 1.5, pulse shape analysis (PSA) is a tool to discriminate signal from background events in the search for $0\nu\beta\beta$. Thus, it is very important to understand how the signals in a germanium detector are generated. Even if a germanium detector is, in principle, only a diode operated in reverse bias mode, the exact drift of the charge carriers and, thus, the induced signals depend on a large number of different parameters. Therefore, pulse shape simulation (PSS) is very important to understand the signals of all kinds of events recorded in the experiment to verify the background discrimination techniques based on PSA.

In addition, PSS enables the study of new detector types, e.g. new special geometries, without the need of costly producing and testing them in the laboratory. Thus, many detector types, which might have beneficial features with regard to PSA, can be studied.

The total simulation chain to obtain germanium detector data can be separated into three different parts as shown in Fig 5.1.

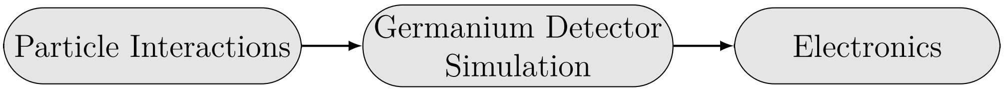

Figure 5.1.: Simulation chain for germanium detectors in a test stand or experiment.

5.1 Simulation of Particle Interactions - Geant-4

In the first part, the interaction of particles and radiation in matter is simulated. The result is a list of hits indicating where and how much energy was deposited in the germanium detector. For low background experiments, events induced by cosmic radiation and environmental radioactivity are important. However, in the case of test setups like GALATEA, such external sources can be neglected and only events due to the radiation from the radioactive sources have to be simulated.

In GALATEA, the germanium detector under study is irradiated with alpha, beta or gamma particles, produced by two collimated sources. The particles are emitted isotropically and the majority of them are absorbed in the collimators. The fraction, which passes through the boreholes of the collimator segments reach the detector and form the vast majority of the events. The shape and the density of the beam-spot depend on the geometry and material of the collimator segments and the strength of the source. Some particles not emitted towards the borehole also reach the detector due to scattering of the primaries in the collimators. The distribution of such events also needs to be studied.

The standard software package to simulate the passage and interaction of particles through matter is Geant-4 [73, 74, 75], which was also used for the studies presented in this thesis. The implementation of the geometry of GALATEA in Geant-4 considering only the top collimator is shown in Fig. 5.2. Only the germanium detector and its close environment, the IR shield, detector holder plate and collimators were implemented. The germanium detector and the configuration of the collimator segment can be replaced or modified in the simulation.

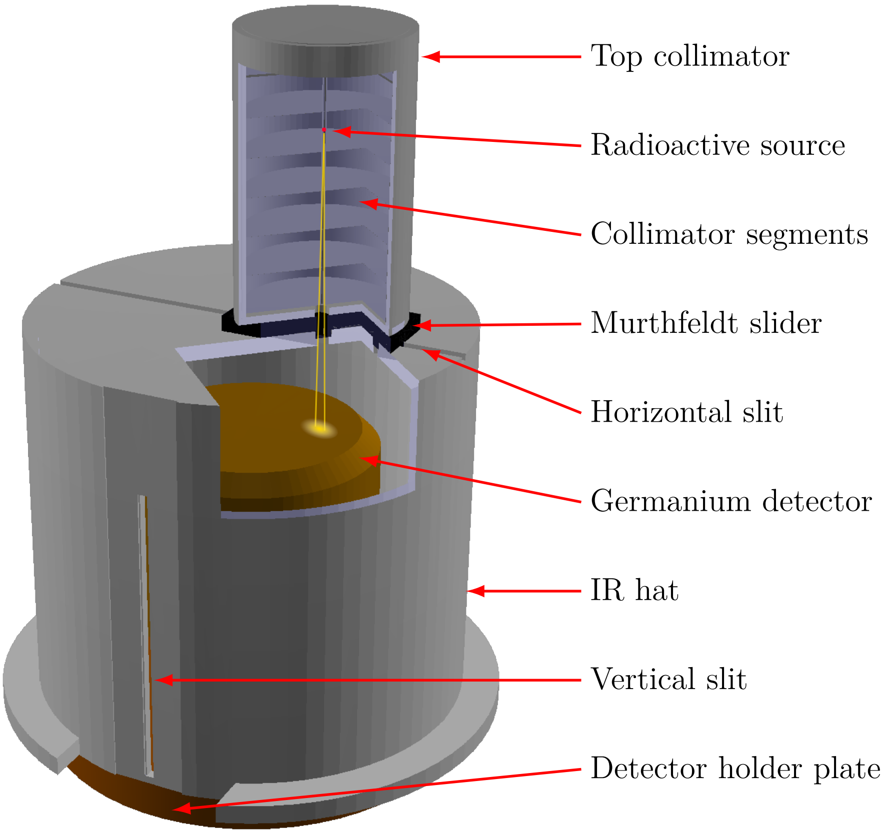

Figure 5.2.: Visualization of the Geant-4 implementation of GALATEA. The different parts are annotated. The particle beam passes through the boreholes of the collimator segments and the slit in the IR hat. The resulting beam-spot on the detector surface is illustrated in yellow. The side collimator was left out in this visualization for better visibility.

5.2 Pulse-Shape Simulation: SolidStateDetectors.jl

The locations and amounts of deposited energy, i.e. the output of Geant-4, are the input for the next part of the simulation. In this stage, the energy is converted into electron-hole pairs. Their drift paths through the germanium are simulated and the predicted signals calculated accordingly.

A new pulse-shape simulation package was developed by the LEGEND group at the Max Planck Institute for Physics in Munich: *SolidStateDetectors.jl* (SSD)[18]. As the name implies, SSD is not restricted to germanium detectors, but any detector based on a solid-state diode can be simulated, e.g., also silicon detectors. As there are already other software packages available for the PSS of germanium detectors, like the Field Generation and Signal Generation (FieldGen+SigGen) software [76] and the AGATA Detector Library (ADL) [59], the question arises why yet another software was developed. There were several good reasons:

- Arbitrary detector and environmental geometries in 3D: The need to simulate any detector geometry without any restriction to certain hard-coded detector geometries. The need to simulate detectors with any kind of segmentation. In addition, also the surrounding of a detector should be considered in the simulation as it impacts the electric field and the weighting potentials. This not only affects the geometry itself, it also affects the boundary conditions like fixed potentials of certain materials, like grounded holding structures and variable impurity profiles for the crystal.

- Modular structure: The software should be written in a modular fashion such that it is easy to exchange and modify individual parts without disturbing other segments of the simulation. For example, it should be easy to exchange the charge drift model with a different (user defined) model.

- Open Source: The package should be open source and documented. This enables other groups to use the software and also contribute to it. It also simplifies the ultimate goal to combine all features of all the different simulation software packages from different groups in one single package.

- Fast simulation: As the final simulated signals depend on a large number of different parameters, the whole simulation should be as fast as possible in order to test the impact of certain parameters. A very fast simulation chain even enables the fitting of certain parameters to real data.

To address these points, and, as physicists are usually not well-trained programmers, an easy to learn and use programming language was chosen: Julia. All the desired goals listed above were achieved in the new open source Julia package *SolidStateDetectors.jl* (SSD), which is available and documented on [77].

5.2.1 The new Programming Language: Julia

Since Julia is a very new language, a short introduction (advertisement) is provided.

Julia is a young dynamic general-purpose programming language [78, 79]. Its development started in 2009 and the first open source version was released in February, 2012. The first long term stable version, v1.0, was released in August, 2018. Even though it is a general purpose language, it targets especially statistical, numerical and computational science and was developed to solve the "two language problem". Thus, the slogan of Julia is: As fast as C, as easy as Python.

Julia offers multiple dispatch and can be used interactively like Python. The user does not have to care about types of variables as is needed in C. However, the option to define variable types and write type stable code exists, increasing the execution speed due to Julia code being compiled before execution by a just-in-time (JIT) compiler. Julia also offers in-built tools to analyze the code and check for, e.g. type instabilities, which actually helps a lot in learning Julia and programming in general.

Julia also offers a very good interface for parallel computing. This addresses not only the usage of all the threads on a local machine, but also the distribution of calculations over a cluster of machines or, also easily and efficiently, over hundreds of cores on a supercomputer. For example, a peak rate of 1.54 petaFLOPS (10^{15} floating point operations per second) was achieved by the Celeste project on the supercomputer Cori in the analysis of astronomical images using 1.3 million threads [80]. In addition, there are also simple interfaces to make use of GPUs.

The are two disadvantages of the language which should also be mentioned. The ecosystem is not yet as big as Python's as it is a very new language and, as the code is just-in-time compiled, the first call to a function needs additional time. However, both problems become naturally insignificant with time.

It is also possible to directly call C and Fortran functions out of the many existing and matured high-quality libraries. Thus, even if the code could be rewritten in fast Julia code this is not really necessary. In addition, the entire Python ecosystem can also be used as Python code can also be called from inside Julia.

It should be noted, that the software controlling and monitoring GALATEA as well as the data acquisition software and the data analysis software is entirely implemented in Julia.

5.2.2 Calculation of the Electric Potential

The first step in the simulation of the detector is the calculation of its electric potential by solving Gauss' law, see Eq. 3.4. As this is a time independent problem, SSD calculates the electric potential only once via successive over-relaxation (SOR) on a 3-dimensional adaptive grid.

SOR is a faster variant of the Gauss-Seidel method, which is often used to solve a system of linear equations. The basic idea is that the potential on each grid point only depends on its direct neighbors and the local charge around the grid point. Thus, the initial state, which is defined through the fixed boundary conditions, is used to initialize the grid. Then, the values of the potential on each grid point are updated by iterating over all grid points until an equilibrium is reached, i.e., the potential on each grid point does not change anymore beyond a preset criterion.

An adaptive grid is modified during the calculation. At the beginning, the grid is very coarse and the equilibrium is reached very quickly. Then, the grid is refined in areas where the neighbouring grid points have potentials which differ by more than a certain limit. Afterwards, the potential is again updated on the refined grid until it has converged again. This can be repeated several times until a desired precision, which can be defined by the user, is reached.

In addition, the grid points are divided into two groups, where each point in a group only depend on its six nearest neighbors which are part of the other group. Thus, the grid points in each group are independent from each other. This is often called red-black or even-odd division and allows for parallelization. SSD makes use of this and is able to calculate the electric potential using multiple threads for even faster convergence. Furthermore, the calculation to update the potential of a grid point can be reduced to specific additions and multiplications. Modern CPUs have special processing units to perform so-called "single instruction, multiple data" (SIMD) operations. These are also called vectorized operations. These units can perform addition and multiplication in parallel if the exact same operations (single instruction) are to be performed on different bytes (multiple data). This is the case here. Thus, a single CPU thread can update several grid points at once. SSD also makes use of this.

Considering all this, the equation to update the potential on a grid point has to be derived from Eq. 3.4 for cylindrical coordinates. For a 2-dimensional regular grid, it has been shown in [81] how to express the problem in a system of linear equations. In the following, it is shown for the 3-dimensional problem at hand.

Grid

The system to simulate, e.g. a cryostat with a detector inside, is called "the world". In cylindrical coordinates, the world is a cylinder ranging from $r_\mathrm{l} = 0\,\mathrm{m}$ to r_r in r, φ_l to φ_r in φ and z_l to z_r in z. This world is divided into a set of discrete points, i.e. each axis is divided into a discrete number of points: N_r, N_φ, N_z. The linear combinations of those points form the set of all $N_{\text{gp}} = N_r \times N_\varphi \times N_z$ grid points

$$\mathbf{r}_{i,j,k} = \begin{pmatrix} r_i \\ \varphi_j \\ z_k \end{pmatrix} \qquad i \in 1,\dots,N_r;\ j \in 1,\dots,N_\varphi;\ k \in 1,\dots,N_z\ . \tag{5.1}$$

The calculations also depend on the mid-points along each axis:

$$r_{mp,i} = r_i\ + 0.5 \cdot (r_{i+1}\ - r_i) \quad , \tag{5.2}$$

$$\varphi_{mp,j} = \varphi_j + 0.5 \cdot (\varphi_{j+1} - \varphi_j) \quad , \tag{5.3}$$

$$z_{mp,k} = z_k\ + 0.5 \cdot (z_{k+1}\ - z_k) \quad . \tag{5.4}$$

One grid point and its direct neighbors are shown in Fig. 5.3. Also shown is the volume around the grid point and its surfaces which are also needed in the calculations. The volume is a sector of a tube ranging from the midpoints between the grid point and its direct neighbors. A cross-section in r and z is shown in Fig. 5.4, where also the red-black division of the grid is indicated. The black points are defined as the points for which the sum of the indices $(i + j + k)$ is even whereas red points have $i + j + k$ uneven.

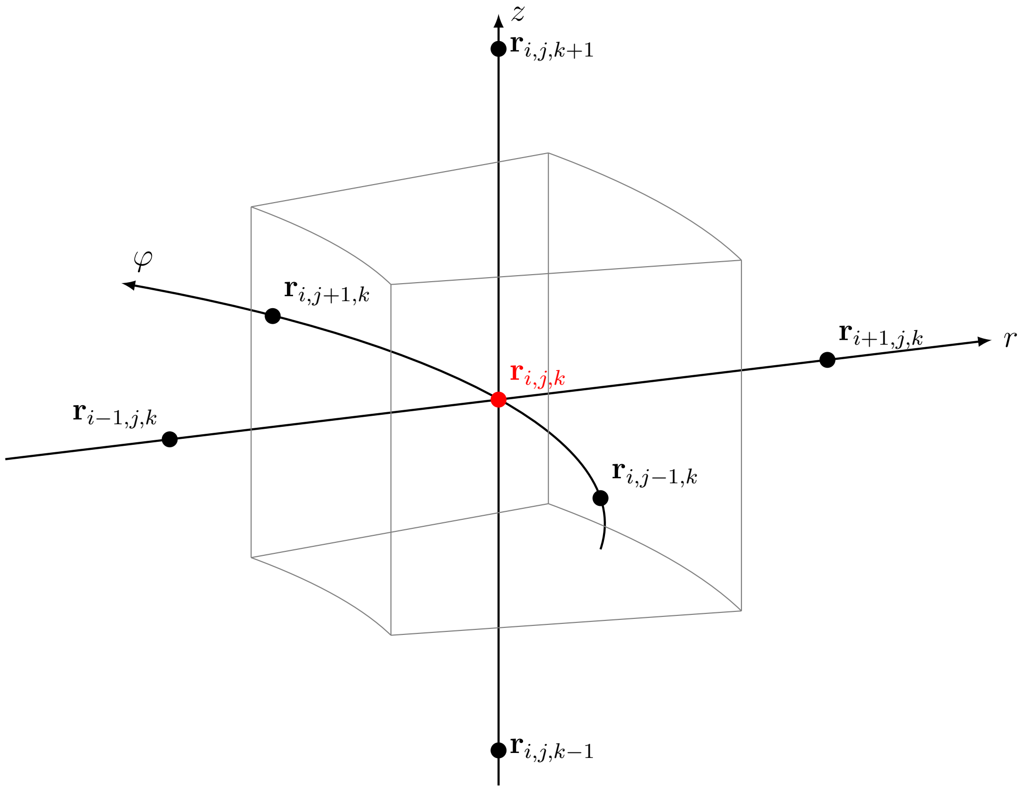

Figure 5.3.: A grid point (in red) and its direct neighbors (in black). The boundaries of the volume belonging to the red grid point are shown as a sector of a tube.

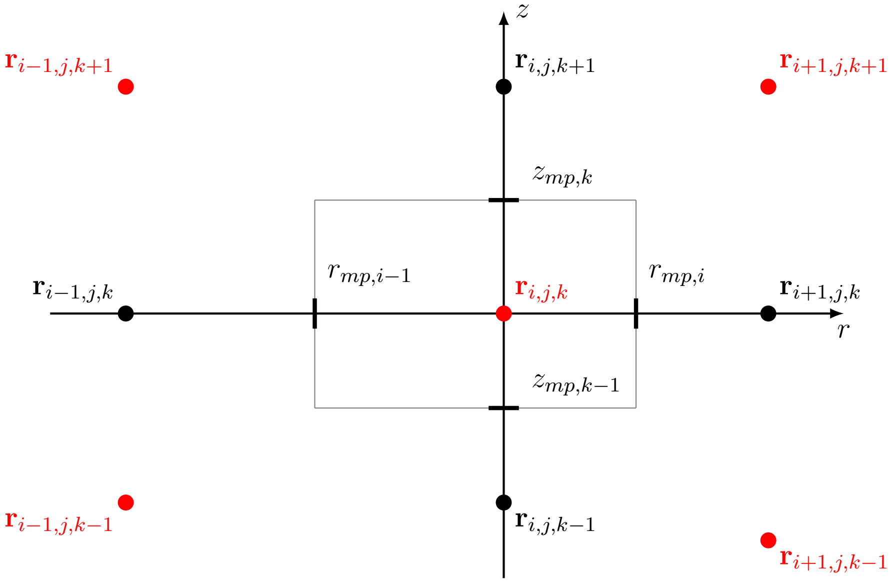

Figure 5.4.: Two dimensional cross-section in r and z at φ_j of Fig. 5.3. Also shown are the midpoints and diagonal (red) neighbors. The red-black division represents the separation of points used in the computation.

Calculation of the Potential on an Individual Grid Point

In the following, the equation to calculate the potential of an individual grid point is derived.

Equation 3.4 is in differential form, but for the derivation, the integral form

$$\iiint_V \nabla \cdot (\epsilon_r(\mathbf{r}) \cdot \nabla\Phi(\mathbf{r}))\ dV = \iiint_V -\frac{\rho(\mathbf{r})}{\epsilon_0}\ dV \tag{5.5}$$

is preferable because the divergence theorem can be applied to remove one differential operator

$$\oint\!\!\!\oint_S (\epsilon_r(\mathbf{r}) \cdot \nabla\Phi(\mathbf{r})) \cdot d\mathbf{S} = -\iiint_V \frac{\rho(\mathbf{r})}{\epsilon_0}\ dV\ , \tag{5.6}$$

where the nabla operator, ∇, for cylindrical coordinates is

$$\nabla = \left(\frac{\partial}{\partial r}, \frac{1}{r}\frac{\partial}{\partial \varphi}, \frac{\partial}{\partial z}\right)\ . \tag{5.7}$$

Eq. 5.6 becomes

$$\oint\!\!\!\oint_S \epsilon_r(\mathbf{r}) \cdot \left(\frac{\partial}{\partial r}, \frac{1}{r}\frac{\partial}{\partial \varphi}, \frac{\partial}{\partial z}\right) \Phi(\mathbf{r}) \cdot d\mathbf{S} = -\iiint_V \frac{\rho(\mathbf{r})}{\epsilon_0}\ dV\ . \tag{5.8}$$

On the right side, there is a volume integral, and, on the left side, there is an integral over the surface of this volume.

For grid point $\mathbf{r}_{i,j,k}$, this volume is a sector of a tube defined through the midpoints between the point and it direct neighbors as shown in Fig. 5.3 and Fig. 5.4. The right side of Eq. 5.8, the volume integral, becomes

$$\begin{aligned}
-\iiint\limits_V \frac{\rho(\mathbf{r})}{\epsilon_0}\,dV &= -\int\limits_{r_{mp,i-1}}^{r_{mp,i}}\int\limits_{\varphi_{mp,j-1}}^{\varphi_{mp,j}}\int\limits_{z_{mp,k-1}}^{z_{mp,k}} r\cdot\frac{\rho(\mathbf{r})}{\epsilon_0}\,dz\,d\varphi\,dr && (5.9)\\
&= -\frac{\rho_w(\mathbf{r}_{i,j,k})}{\epsilon_0}\int\limits_{r_{mp,i-1}}^{r_{mp,i}}\int\limits_{\varphi_{mp,j-1}}^{\varphi_{mp,j}}\int\limits_{z_{mp,k-1}}^{z_{mp,k}} r\,dz\,d\varphi\,dr\\
&= -\frac{\rho_w(\mathbf{r}_{i,j,k})}{\epsilon_0}\cdot\frac{1}{2}(r^2_{mp,i}-r^2_{mp,i-1})(\varphi_{mp,j}-\varphi_{mp,j-1})(z_{mp,k}-z_{mp,k-1})\\
&= -\frac{\rho_w(\mathbf{r}_{i,j,k})}{\epsilon_0}\cdot V_{i,j,k} \coloneqq Q^{\text{eff}}_{i,j,k} \quad , && (5.10)
\end{aligned}$$

with $\rho_w(\mathbf{r}_{i,j,k})$ being the geometrically weighted mean of the charge density over the volume, which is than assumed to be constant for the integration. The charge density is evaluated at the 8 corners of the integration volume, e.g. $\rho(r_{mp,i-1},\varphi_{mp,j-1},z_{mp,k-1})$, to determine the weighted mean $\rho_w(\mathbf{r}_{i,j,k})$.

Thus, the right side of Eq. 5.8 becomes a constant, an effective charge $Q^{\text{eff}}_{i,j,k}$:

$$\oiint\limits_S (\epsilon_r(\mathbf{r})\cdot\nabla\Phi(\mathbf{r}))\cdot d\mathbf{S} = Q^{\text{eff}}_{i,j,k} \quad . \tag{5.11}$$

The left side of Eq. 5.8, the surface integral, can be divided into 6 parts representing the surfaces of the sector as shown in Fig. 5.3:

$$\begin{aligned}
\oiint\limits_S (\epsilon_r(\mathbf{r})\nabla\Phi(\mathbf{r}))\cdot d\mathbf{S} &= \iint_{r^+} + \iint_{r^-} + \iint_{\varphi^+} + \iint_{\varphi^-} + \iint_{z^+} + \iint_{z^-} && (5.12)\\
\iint_{r^+} &= \int\limits_{z_{mp,k-1}}^{z_{mp,k}}\int\limits_{\varphi_{mp,j-1}}^{\varphi_{mp,j}} +\epsilon_r(\mathbf{r})\,(\nabla\Phi(\mathbf{r}))\; r_{mp,i}\,\mathbf{e}_r\,d\varphi\,dz && (5.13)\\
\iint_{r^-} &= \int\limits_{z_{mp,k-1}}^{z_{mp,k}}\int\limits_{\varphi_{mp,j-1}}^{\varphi_{mp,j}} -\epsilon_r(\mathbf{r})\,(\nabla\Phi(\mathbf{r}))\; r_{mp,i-1}\,\mathbf{e}_r\,d\varphi\,dz && (5.14)\\
\iint_{\varphi^+} &= \int\limits_{r_{mp,i-1}}^{r_{mp,i}}\int\limits_{z_{mp,k-1}}^{z_{mp,k}} +\epsilon_r(\mathbf{r})\,(\nabla\Phi(\mathbf{r}))\;\mathbf{e}_\varphi\,dz\,dr && (5.15)
\end{aligned}$$

$$\iint_{\varphi^-} = \int\limits_{r_{mp,i-1}}^{r_{mp,i}} \int\limits_{z_{mp,k-1}}^{z_{mp,k}} -\epsilon_r(\mathbf{r})\,(\nabla\Phi(\mathbf{r}))\;\mathbf{e}_\varphi\,dz\,dr \tag{5.16}$$

$$\iint_{z^+} = \int\limits_{r_{mp,i-1}}^{r_{mp,i}} \int\limits_{\varphi_{mp,j-1}}^{\varphi_{mp,j}} +\epsilon_r(\mathbf{r})\,(\nabla\Phi(\mathbf{r}))\;r\,\mathbf{e}_z\,d\varphi\,dr \tag{5.17}$$

$$\iint_{z^-} = \int\limits_{r_{mp,i-1}}^{r_{mp,i}} \int\limits_{\varphi_{mp,j-1}}^{\varphi_{mp,j}} -\epsilon_r(\mathbf{r})\,(\nabla\Phi(\mathbf{r}))\;r\,\mathbf{e}_z\,d\varphi\,dr\ . \tag{5.18}$$

Here, $\mathbf{e}_r$, $\mathbf{e}_\varphi$ and $\mathbf{e}_z$ are the unit vectors of the coordinate surface and are also the normal vectors of the corresponding surfaces multiplied by ±1, indicated through the sign in the subscript of each surface integration part, to point out off the volume.

These 6 surface integrals can be approximated and further simplified. This is shown for $\iint_{\varphi^+}$:

$$\iint_{\varphi^+} = \int\limits_{r_{mp,i-1}}^{r_{mp,i}} \int\limits_{z_{mp,k-1}}^{z_{mp,k}} +\epsilon_r(\mathbf{r})\,(\nabla\Phi(\mathbf{r}))\;\mathbf{e}_\varphi\,dz\,dr \tag{5.19}$$

$$= \int\limits_{r_{mp,i-1}}^{r_{mp,i}} \int\limits_{z_{mp,k-1}}^{z_{mp,k}} \epsilon_r(\mathbf{r})\frac{1}{r_i}\frac{\partial}{\partial\varphi}\Phi(\mathbf{r})\,dz\,dr \tag{5.20}$$

$$= \int\limits_{r_{mp,i-1}}^{r_{mp,i}} \int\limits_{z_{mp,k-1}}^{z_{mp,k}} \epsilon_r(\mathbf{r})\frac{\Phi_{i,j+1,k}-\Phi_{i,j,k}}{r_i\cdot(\varphi_{j+1}-\varphi_j)}\,dz\,dr \tag{5.21}$$

$$= \frac{\Phi_{i,j+1,k}-\Phi_{i,j,k}}{r_i\cdot(\varphi_{j+1}-\varphi_j)}\cdot \int\limits_{r_{mp,i-1}}^{r_{mp,i}} \int\limits_{z_{mp,k-1}}^{z_{mp,k}} \epsilon_r(\mathbf{r})\,dz\,dr \tag{5.22}$$

$$= \frac{\Phi_{i,j+1,k}-\Phi_{i,j,k}}{r_i\cdot(\varphi_{j+1}-\varphi_j)}\cdot \epsilon^{w,\varphi^+}_{i,j,k}\cdot \int\limits_{r_{mp,i-1}}^{r_{mp,i}} \int\limits_{z_{mp,k-1}}^{z_{mp,k}} dz\,dr \tag{5.23}$$

$$= \frac{\Phi_{i,j+1,k}-\Phi_{i,j,k}}{r_i\cdot(\varphi_{j+1}-\varphi_j)}\cdot \epsilon^{w,\varphi^+}_{i,j,k}\cdot (r_{mp,i}-r_{mp,i-1})(z_{mp,k}-z_{mp,k-1}) \tag{5.24}$$

$$= \frac{\Phi_{i,j+1,k}-\Phi_{i,j,k}}{r_i\cdot(\varphi_{j+1}-\varphi_j)}\cdot \epsilon^{w,\varphi^+}_{i,j,k}\cdot A^{\varphi^+}_{i,j,k}\quad . \tag{5.25}$$

$$\tag{5.26}$$

The derivative is approximated using the finite-difference method. This means, that the dependence on the value of the potential of the neighboring point in positive φ-direction, $\Phi_{i,j+1,k}$, is assumed to be linear. In addition, the dielectric distribution, $\epsilon_r(\mathbf{r})$, is approximated like the charge distribution, by using the geometrically weighted mean of the dielectric distribution evaluated at the 4 corners of the surface:

$$\begin{aligned}\epsilon^{w,\varphi^+}_{i,j,k} = & + \frac{r_i - r_{mp,i-1}}{r_{mp,i} - r_{mp,i-1}} \cdot \frac{z_k - z_{mp,k-1}}{z_{mp,k} - z_{mp,k-1}} \cdot \epsilon_r\big(r_{mp,i-1}, \varphi_{mp,j}, z_{mp,k-1}\big) \\ & + \frac{r_{mp,i} - r_i}{r_{mp,i} - r_{mp,i-1}} \cdot \frac{z_k - z_{mp,k-1}}{z_{mp,k} - z_{mp,k-1}} \cdot \epsilon_r\big(r_{mp,i}, \varphi_{mp,j}, z_{mp,k-1}\big) \\ & + \frac{r_i - r_{mp,i-1}}{r_{mp,i} - r_{mp,i-1}} \cdot \frac{z_{mp,k} - z_k}{z_{mp,k} - z_{mp,k-1}} \cdot \epsilon_r\big(r_{mp,i-1}, \varphi_{mp,j}, z_{mp,k}\big) \\ & + \frac{r_{mp,i} - r_i}{r_{mp,i} - r_{mp,i-1}} \cdot \frac{z_{mp,k} - z_k}{z_{mp,k} - z_{mp,k-1}} \cdot \epsilon_r\big(r_{mp,i}, \varphi_{mp,j}, z_{mp,k}\big) \quad . \end{aligned} \tag{5.27}$$

The other 5 surface integrals are solved (approximated) in the same way and Eq. 5.8 becomes

$$\oiint_S \left(\epsilon_r(\mathbf{r})\nabla\Phi(\mathbf{r})\right) \cdot d\mathbf{S} = + \iint_{r^+} + \iint_{r^-} + \iint_{\varphi^+} + \iint_{\varphi^-} + \iint_{z^+} + \iint_{z^-} \tag{5.28}$$

$$\begin{aligned} = & + \frac{\Phi_{i+1,j,k} - \Phi_{i,j,k}}{r_{i+1} - r_i} \cdot \epsilon^{w,r^+}_{i,j,k} \cdot A^{r^+}_{i,j,k} \\ & - \frac{\Phi_{i,j,k} - \Phi_{i-1,j,k}}{r_i - r_{i-1}} \cdot \epsilon^{w,r^-}_{i,j,k} \cdot A^{r^-}_{i,j,k} \\ & + \frac{\Phi_{i,j+1,k} - \Phi_{i,j,k}}{r_i \cdot (\varphi_{j+1} - \varphi_j)} \cdot \epsilon^{w,\varphi^+}_{i,j,k} \cdot A^{\varphi^+}_{i,j,k} \\ & - \frac{\Phi_{i,j,k} - \Phi_{i,j-1,k}}{r_i \cdot (\varphi_j - \varphi_{j-1})} \cdot \epsilon^{w,\varphi^-}_{i,j,k} \cdot A^{\varphi^-}_{i,j,k} \\ & + \frac{\Phi_{i,j,k+1} - \Phi_{i,j,k}}{z_{k+1} - z_k} \cdot \epsilon^{w,z^+}_{i,j,k} \cdot A^{z^+}_{i,j,k} \\ & - \frac{\Phi_{i,j,k} - \Phi_{i,j,k-1}}{z_k - z_{k-1}} \cdot \epsilon^{w,z^-}_{i,j,k} \cdot A^{z^-}_{i,j,k} \quad = Q^{\text{eff}}_{i,j,k} \quad . \end{aligned} \tag{5.29, 5.30}$$

As this is just a linear equation, it can be solved as

$$\begin{aligned}\Phi_{i,j,k} = a^0_{i,j,k}\,[\,Q^{\text{eff}}_{i,j,k} \; & + \; a^{r^+}_{i,j,k} \cdot \Phi_{i+1,j,k} + a^{r^-}_{i,j,k} \cdot \Phi_{i-1,j,k} \\ & + \; a^{\varphi^+}_{i,j,k} \cdot \Phi_{i,j+1,k} + a^{\varphi^-}_{i,j,k} \cdot \Phi_{i,j-1,k} \\ & + \; a^{z^+}_{i,j,k} \cdot \Phi_{i,j,k+1} + a^{z^-}_{i,j,k} \cdot \Phi_{i,j,k-1}\,] \quad , \end{aligned} \tag{5.31}$$

where $a^0_{i,j,k}$, $a^{r^+}_{i,j,k}$, $a^{r^-}_{i,j,k}$, $a^{\varphi^+}_{i,j,k}$, $a^{\varphi^-}_{i,j,k}$, $a^{z^+}_{i,j,k}$ and $a^{z^-}_{i,j,k}$ are coefficients which are constant for a given grid and fixed dielectric distribution. The effective charge, $Q^{\text{eff}}_{i,j,k}$, is also fixed for a given grid and fixed charge distribution.

By changing from 3- to 1-dimensional indexing, $(i, j, k) \rightarrow 1, \ldots, N_{\mathrm{gp}}$, Eq. 5.31 can be written as a matrix equation for all grid points:

$$\begin{pmatrix} \Phi_1 \\ \Phi_2 \\ \vdots \\ \Phi_{N_{\mathrm{gp}}} \end{pmatrix} = \begin{pmatrix} a_{1,1} & a_{1,2} & \cdots & a_{1,N_{\mathrm{gp}}} \\ a_{2,1} & \ddots & \ddots & \vdots \\ \vdots & \ddots & \ddots & \vdots \\ a_{N_{\mathrm{gp}},1} & \cdots & \cdots & a_{N_{\mathrm{gp}},N_{\mathrm{gp}}} \end{pmatrix}^{N_{\mathrm{gp}} \times N_{\mathrm{gp}}} \cdot \begin{pmatrix} \Phi_1 \\ \Phi_2 \\ \vdots \\ \Phi_{N_{\mathrm{gp}}} \end{pmatrix} + \begin{pmatrix} a_1^0\, Q_1^{\mathrm{eff}} \\ a_2^0\, Q_2^{\mathrm{eff}} \\ \vdots \\ a_{N_{\mathrm{gp}}}^0\, Q_{N_{\mathrm{gp}}}^{\mathrm{eff}} \end{pmatrix} \quad , \tag{5.32}$$

$$\mathbf{\Phi} = \mathbf{A} \cdot \mathbf{\Phi} + \mathbf{Q} \quad . \tag{5.33}$$

Most of the elements of the $N_{\mathrm{gp}} \times N_{\mathrm{gp}}$ matrix $\mathbf{A}$, $a_{m,n}$, are 0. It is a sparse matrix with only 6 elements in each row being non-zero. These non zero elements belong to the neighboring grid points.
The matrix $\mathbf{A}$ and the vector $\mathbf{Q}$ contain fixed parameters whereas the unknown variables are the potential values in $\mathbf{\Phi}$. This can be solved in an iterative manner through the Gauss-Seidel method:

$$\mathbf{\Phi}^{t+1} = \mathbf{A} \cdot \mathbf{\Phi}^{t} + \mathbf{Q} \quad , \tag{5.34}$$

where $t \in 0, 1, 2, \ldots, \infty$ is the iteration index. The initial vector $\mathbf{\Phi}^0$ is defined by the boundary conditions and contains mostly zeros. Only the grid points which have fixed potentials, e.g. the grid points on the contact electrodes, have the corresponding potential assigned while their corresponding coefficients in $\mathbf{A}$ and $\mathbf{Q}$ are set to 0. The solution, the final state $\mathbf{\Phi}^{\mathrm{final}}$, is reached when the potential values do not change anymore:

$$|\Phi_i^{t+1} - \Phi_i^{t}| < \Phi_{\mathrm{threshold}} \qquad \forall \quad i \in 1, \ldots, N_{\mathrm{gp}} \quad , \tag{5.35}$$

where $\Phi_{\mathrm{threshold}}$ is a threshold, e.g. $V_{\mathrm{B}}/10^6$, which can be set by the user.

In this method, the new values in each step only depend on the values on the neighboring grid points. Thus, Eq. 5.34 can be divided into two lower dimensional matrix equations by the red-black division:

$$\mathbf{\Phi}_R^{t+1} = \mathbf{A}_R \cdot \mathbf{\Phi}_B^{t} + \mathbf{Q}_R \quad , \tag{5.36}$$

$$\mathbf{\Phi}_B^{t+1} = \mathbf{A}_B \cdot \mathbf{\Phi}_R^{t+1} + \mathbf{Q}_B \quad , \tag{5.37}$$

where the index R indicates the red points and the index B indicates the black points. The dimension of the matrices $\mathbf{A}_R$ and $\mathbf{A}_B$ is only $N_{\mathrm{gp}}/2 \times N_{\mathrm{gp}}/2$. Through this reduction, the final state is reached faster as the set of values $\mathbf{\Phi}_R^{t+1}$ are used directly to compute $\mathbf{\Phi}_B^{t+1}$ without the need to store a complete set of values $\mathbf{\Phi}^t$ at any time.

Successive Over-Relaxation

As already mentioned, SSD uses the SOR method instead of the basic Gauss-Seidel method in order to achieve faster convergence. As the diagonal elements of the matrix $\mathbf{A}$ are zero, the SOR method can be written as

$$\begin{aligned} \mathbf{\Phi}^{t'} &= \mathbf{A} \cdot \mathbf{\Phi}^{t} + \mathbf{Q} \quad , \quad (5.38) \\ \mathbf{\Phi}^{t+1} &= \mathbf{\Phi}^{t} + \omega_{\mathrm{SOR}} \cdot (\mathbf{\Phi}^{t'} - \mathbf{\Phi}^{t}) \quad , \quad (5.39) \end{aligned}$$

where ω_{SOR} is the so-called SOR-constant which has to be in the interval $]0, 2[$ in order to guarantee convergence. If $\omega_{\mathrm{SOR}} = 1$, SOR reduces to the basic Gauss-Seidel method. The red-black division used in SSD is also effective for SOR.

Grid Boundary Condition

So far, the influence of the final size of the grid has not been accounted for. On the boundary, grid points exist which do not have 6 neighbors. To solve this problem efficiently, SSD extends the grid in each of the 6 direction $(\pm r, \pm\varphi, \pm z)$ by one grid point, but only iterates over the inner grid points which now all have 6 neighbors. After each iteration over the grid points, the potential values of the outer grid points have to be updated according to the chosen boundary condition. In SSD, possible grid boundary conditions are periodic, reflecting, fixed or an approximation for a potential decaying towards 0. These boundary conditions are always labeled "grid boundary condition" to separate them from "normal" boundary conditions.

Boundary Conditions - Geometry and Configuration Files

In addition to the grid boundary condition, there are also the boundary conditions of the differential equation (Gauss law: Eq. 3.4). These are the charge density and dielectric distributions, which were already addressed in Sec. 3.1. The dielectric distribution is defined by the objects in the world, i.e., through their material and their geometry. Both distributions, together with the grid, are than used to calculated the elements of $\mathbf{A}$ and $\mathbf{Q}$.

The package uses constructive solid geometry (CSG) to define the objects in the world. They can be defined in human readable JSON configuration files. The impurity distribution, which translates into an impurity charge distribution, ρ_{imp}, is assigned to the objects within this configuration file. Also, virtual volumes with build-up space charges, ρ_{b}, can be defined.

The remaining boundaries conditions are the fixed values of the potential on the contacts of the detector or of other objects, e.g. of grounded material around the detector. The geometry of all the contacts is also defined in the configuration file. A fixed potential is assigned to all contacts. This can also be done for world objects.

Each grid point not only has a value for the potential assigned, but also a point type, which is internally a single byte named point type. In this byte, the information whether the point is at fixed potential and whether it belongs to a semiconductor volume or not is stored. If the point is part of a semiconductor volume, the information whether it is in a depleted or undepleted region of the detector is also available.

If the simulated system has a certain symmetry, like periodicity or mirrorability, this can be specified in the configuration file by specifying the appropriate grid boundary conditions. This can reduce the necessary size of the world and, thus, the size of the grid. It can be specified whether a cylindrical or cartesian coordinate system should be used. The optimal choice depends on the symmetry of the system.

Undepleted Detectors

So far, it was assumed that the impurity density induces a well defined charge density ρ_{imp}. However, this is only true for depleted regions. In undepleted regions, ρ_{imp} is zero. Thus, the boundary condition are unclear and it is necessary to calculate where the detector is actually depleted for a given bias voltage. In general, this could be done by making the field calculation time dependent and calculating the time evolution starting from an unbiased detector and increasing the bias voltage over time. But such calculations would be resource intensive. Therefore, a trick is used in the time independent calculation of the electric potential.

Even for an only partially depleted detector, the final state is a steady state, in which the potential should be constant within any undepleted region. Thus, along a field line from a n^+- to a p^+-contact, there should not be any extrema: the potential should decrease monotonically. Therefore, the potential of a grid point cannot be smaller (bigger) than the minimum (maximum) of the potentials of the neighboring grid points.

This can[1] be used in SSD: The field calculation is started with the assumption that the detector is fully depleted and in each iteration the new potential for any grid point is calculated as described in Eq. 5.39. But, in addition, in each iteration a check is performed whether the new value is smaller (bigger) than the minimum (maximum) of the potentials of the neighboring grid points. If this is the case, the part coming from the effective charge is subtracted as the detector should not be depleted at this region and the charge should be actually zero. In addition, this point is marked as undepleted by updating its point type.

---

[1] Depletion handling is optional as it slows down the calculations.

5.2.3 Calculation of Weighting Potentials

All weighting potentials, $\mathcal{W}_i(\mathbf{r})$, are calculated using the same algorithm as used to calculate the electric potential. Only the boundary conditions change as described in Sec. 3.3.1. It should be noted, that the geometric symmetries used in the calculations for the electric potential might not be valid for the weighting potential of certain contacts. Thus, the symmetries for each weighting potential need to be defined individually.

5.2.4 Electric Field

The electric field is the negative gradient of the potential, $\boldsymbol{\mathcal{E}}(\mathbf{r}) = -\nabla\Phi(\mathbf{r})$, and is calculated for each grid point:

$$\boldsymbol{\mathcal{E}}^{i,j,k} = \left(\mathcal{E}_r^{i,j,k}, \mathcal{E}_\varphi^{i,j,k}, \mathcal{E}_z^{i,j,k}\right)^{\mathsf{T}} \quad , \tag{5.40}$$

where the elements are the means of the electric field in each direction calculated as finite differences:

$$\begin{aligned}
\mathcal{E}_r^{i,j,k} &= \frac{1}{2}\left(\frac{\Phi_{i+1,j,k} - \Phi_{i,j,k}}{r_{i+1} - r_i} + \frac{\Phi_{i,j,k} - \Phi_{i-1,j,k}}{r_i - r_{i-1}}\right) \quad , && (5.41)\\
\mathcal{E}_\varphi^{i,j,k} &= \frac{1}{2r_i}\left(\frac{\Phi_{i,j+1,k} - \Phi_{i,j,k}}{\varphi_{j+1} - \varphi_j} + \frac{\Phi_{i,j,k} - \Phi_{i,j-1,k}}{\varphi_j - \varphi_{j-1}}\right) \quad , && (5.42)\\
\mathcal{E}_z^{i,j,k} &= \frac{1}{2}\left(\frac{\Phi_{i,j,k+1} - \Phi_{i,j,k}}{z_{k+1} - z_k} + \frac{\Phi_{i,j,k} - \Phi_{i,j,k-1}}{z_k - z_{k-1}}\right) \quad . && (5.43)
\end{aligned}$$

5.2.5 Detector Capacity

A germanium detector effectively is a capacitor, where the contacts are the plates of the capacitor. The capacity can be calculated as

$$C = 2\, W_{\boldsymbol{\mathcal{E}}} \,/\, V_{\mathrm{B}}^2 \quad , \tag{5.44}$$

where $W_{\boldsymbol{\mathcal{E}}}$ is the energy stored in the electric field created in the detector by the bias voltage V_{B}:

$$W_{\boldsymbol{\mathcal{E}}} = \frac{1}{2}\epsilon_0 \int\limits_V \epsilon_r(\mathbf{r}) |\boldsymbol{\mathcal{E}}(\mathbf{r})|^2 \, dV \quad . \tag{5.45}$$

The integral is approximated by a sum over all grid points. Typically, the capacities of germanium detectors are in the pF regime. It is desirable to minimize the capacity of a detector as the electronic noise increases with increasing capacity, which in turn requires an increased readout threshold and leads to a worse energy resolution. SSD can support detector optimization by a fast computation of the capacitance for many different design options.

5.2.6 Drift Fields and Charge Drift

As described in Sec. 2.4 and in Sec. 3.2, two drift fields for the electrons and holes have to be computed from the electric field. At the time of writing, only the charge drift model described in detail in Sec. 3.2.1 was implemented in SSD. However, there is a user interface to define own charge drift models, e.g. for silicon detectors, for which there might be more sophisticated models available.

Using the drift fields, the drift paths are determined in steps for all charge carriers created in an event. The drift field is evaluated for every charge carrier at its current position at time t. The obtained drift vector is a velocity and multiplied with a small step in time δt, e.g. 1 ns. This yields a spatial translation, which is added to the current position. This is repeated until all charge carriers have reached a contact or a certain time limit is exceeded. This can be expressed as

$$\mathbf{r}(t + \Delta t) = \mathbf{r}(t) + \mathbf{v}_{\mathrm{d,e/h}}(\mathbf{r}(t)) \cdot \Delta t \quad . \tag{5.46}$$

At floating surfaces, the electric field and the drift fields can point out of the detector volume. However, the charge carriers cannot leave the crystal. If this happens, only the component of the drift vector is considered which is parallel to the surface. Thus, the charge drifts along the surface with reduced speed. This reduction of speed has, however, been insufficient to describe data where surface drifts are believed to have been observed. To further modulate the surface drift velocity, the user can pass an adapted function, which is internally called whenever a charge carrier drifts along the surface. This modulation is entirely up to the user.

In addition to the general drift model and the surface drift modulation, the drift can be modulated further in selected volumes. Such volumes can be defined in the configuration file as virtual volumes. If the charge drift enters such a volume, a modulation function acts on the drift vector. By default this is the identity function. This function can also be defined by the user. The modulation features can be used in R&D to develope and extend the general charge drift model and to accommodate special features of crystals.

5.2.7 Signal Generation

SSD generates the signal on the contacts as described in Sec. 3.3 by an implementation of Eq. 3.22. For each point in time during the drift, the signals induced on all contacts i are determined. These are the weighted sums of the signals induced by all charge carrier. The signals are determined as the values of the weighting potentials $\mathcal{W}_i$ evaluated at the current trajectory positions, $\mathbf{r}(t)$, times the respective charges.

For one created electron-hole pair, the induced charge on contact i is given by

$$Q_i(\mathbf{r}_\mathrm{e}(t), \mathbf{r}_\mathrm{h}(t)) = e\,[\mathcal{W}_i(\mathbf{r}_\mathrm{h}(t)) - \mathcal{W}_i(\mathbf{r}_\mathrm{e}(t))] \quad . \tag{5.47}$$

5.2.8 SSD Example: Inverted Coaxial (IVC) Detector

As an example for the whole detector simulation chain of SSD, the simulation of a fictional inverted coaxial (IVC) unsegmented p-type detector is presented in this section for demonstration purposes. As mentioned in Sec. 1.5.3, detectors of this type will be used in the LEGEND experiment.

The geometry of a detector is implemented in SSD via CSG. The geometry of an IVC detector is shown in Fig. 5.5. The core contact is the small p^+-contact at the bottom of the detector. This is often also called a point contact. The entire remaining surface, but for a ring on the bottom around the point contact, is the other contact (n^+).

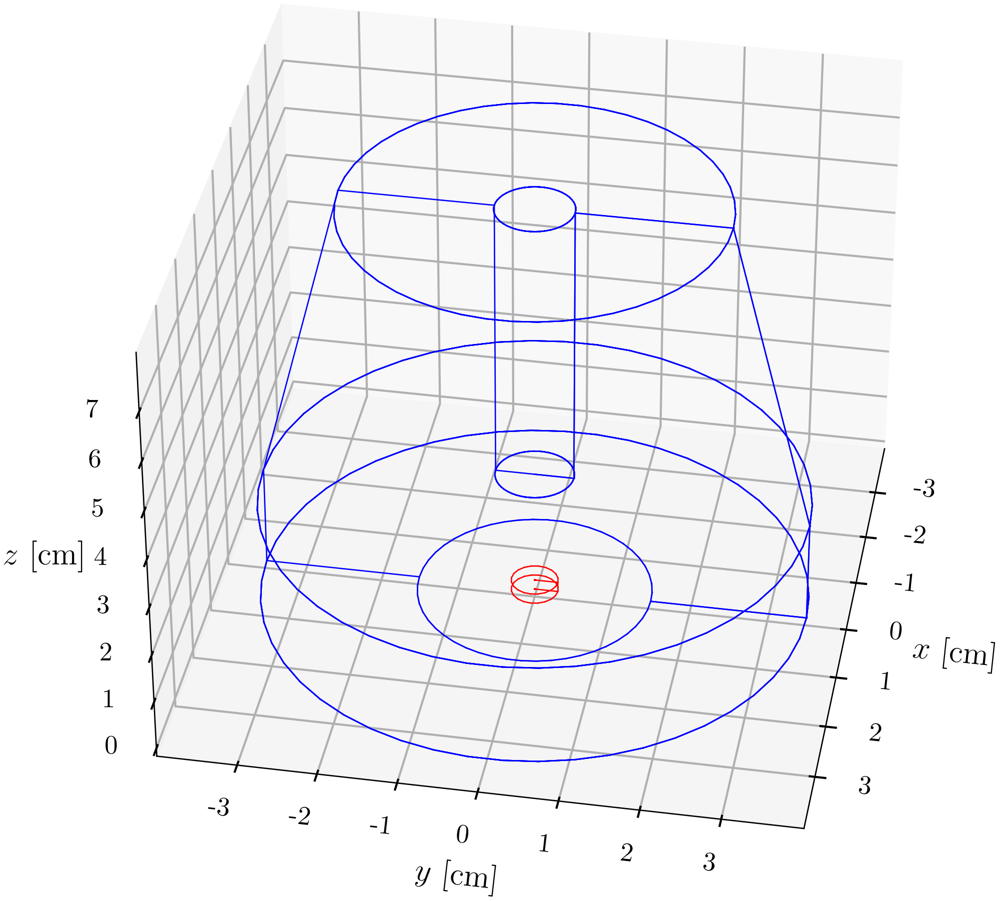

Figure 5.5.: Visualization of the geometry of an IVC germanium detector implemented in SSD via CSG. The core contact (p^+-contact), shown in red, is a point contact at the center of the bottom surface. Almost the entire remaining surface, but a ring between the red and blue circles on the bottom surface, is the other contact (n^+-contact) shown in blue.

The initial boundary conditions applied on a coarse grid are shown in Fig. 5.6. A typical linear impurity density profile along z was chosen.

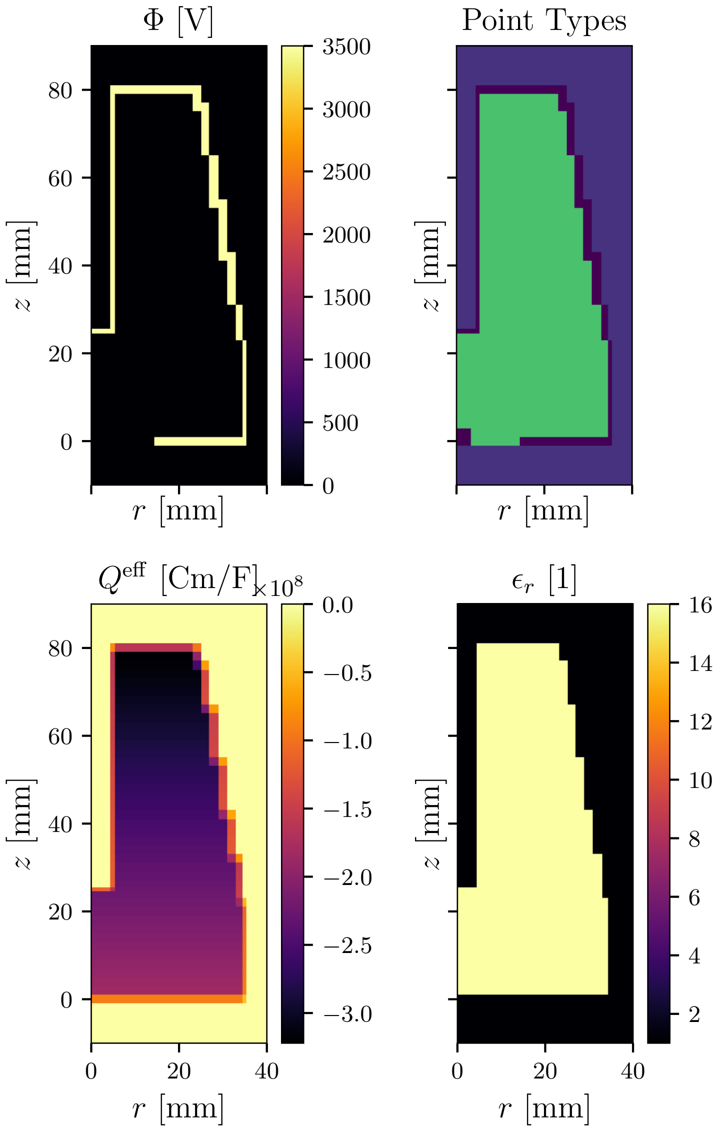

Figure 5.6.: Cross-sections in the r-z-plane of the initial boundary conditions for an IVC detector on a coarse grid. Top left: Electric Potential. Top right: Point types: the green area belongs to semiconductor material whereas the blue area does not. Black areas are at fixed potential. Bottom left: Effective charge distribution. Bottom right: Dielectric distribution.

The calculated electric potential on the initial coarse grid as well as on a finer grid are shown in Fig. 5.7. The calculated electric potential and point type map for a bias voltage of 1200 V are shown in Fig. 5.8. At this bias voltage, the detector is not fully depleted for the chosen impurity density.

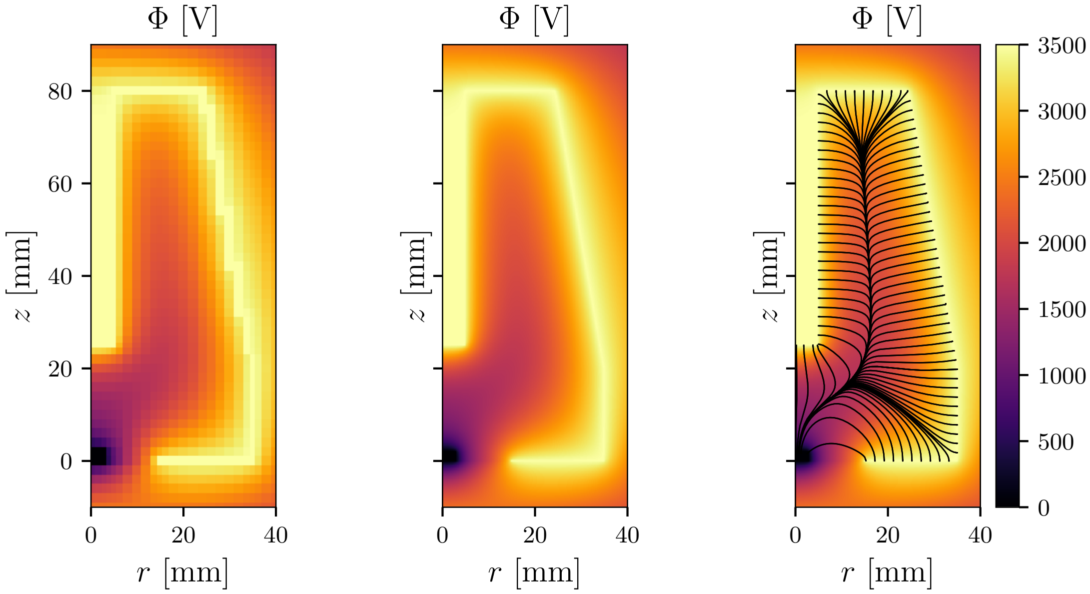

Figure 5.7.: Cross-sections in the r-z-plane of an IVC detector on (left) the initial coarse grid and for (center and right) the grid after 4 refinements. In the right plot, the electric field lines are also shown as black lines.

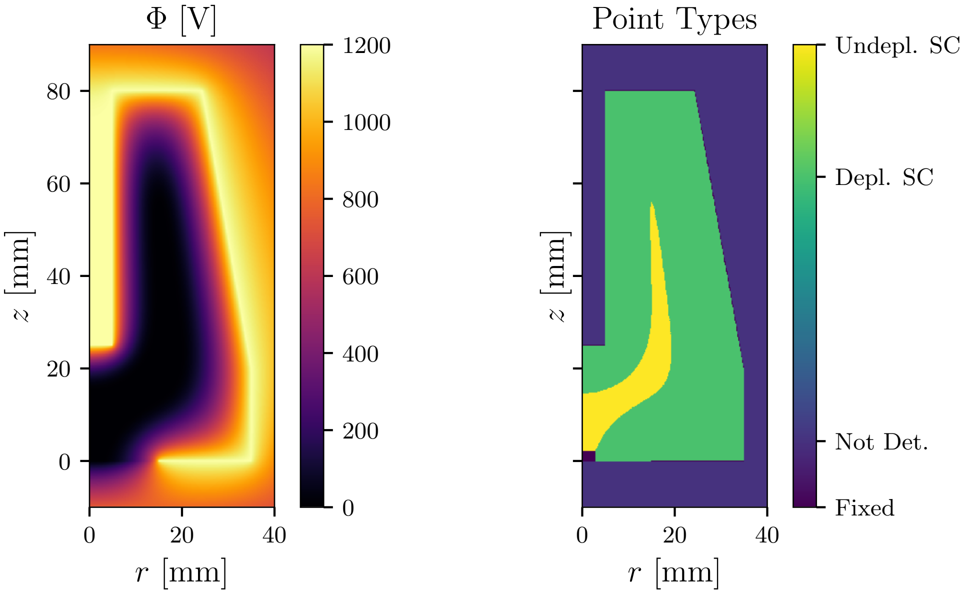

Figure 5.8.: Cross-sections in the r-z-plane of (left) the calculated electric potential and (right) the final point type map (right) for an IVC detector for a bias voltage of 1200 V and the unchanged impurity profile. Point types: the green area belongs to semiconductor material whereas the blue area does not. Black areas are at fixed potential. The yellow area represents the undepleted region.

A fictional multi-site event with only three electron-hole pairs, created at different positions was simulated and the calculated drift paths are shown in Fig. 5.9. In order to generate the signals on both contacts, the two weighting potentials are needed. Both are shown in Fig. 5.10. As the detector is not segmented and only a small part of the surface is floating, the two weighting potentials are almost perfect counterparts of each other:

$$\mathcal{W}_{\mathrm{Core}}(\mathbf{r}) + \mathcal{W}_{\mathrm{Mantle}}(\mathbf{r}) \approx 1 \quad . \tag{5.48}$$

This results in very similar signals in both channels, which are shown in Fig. 5.11.

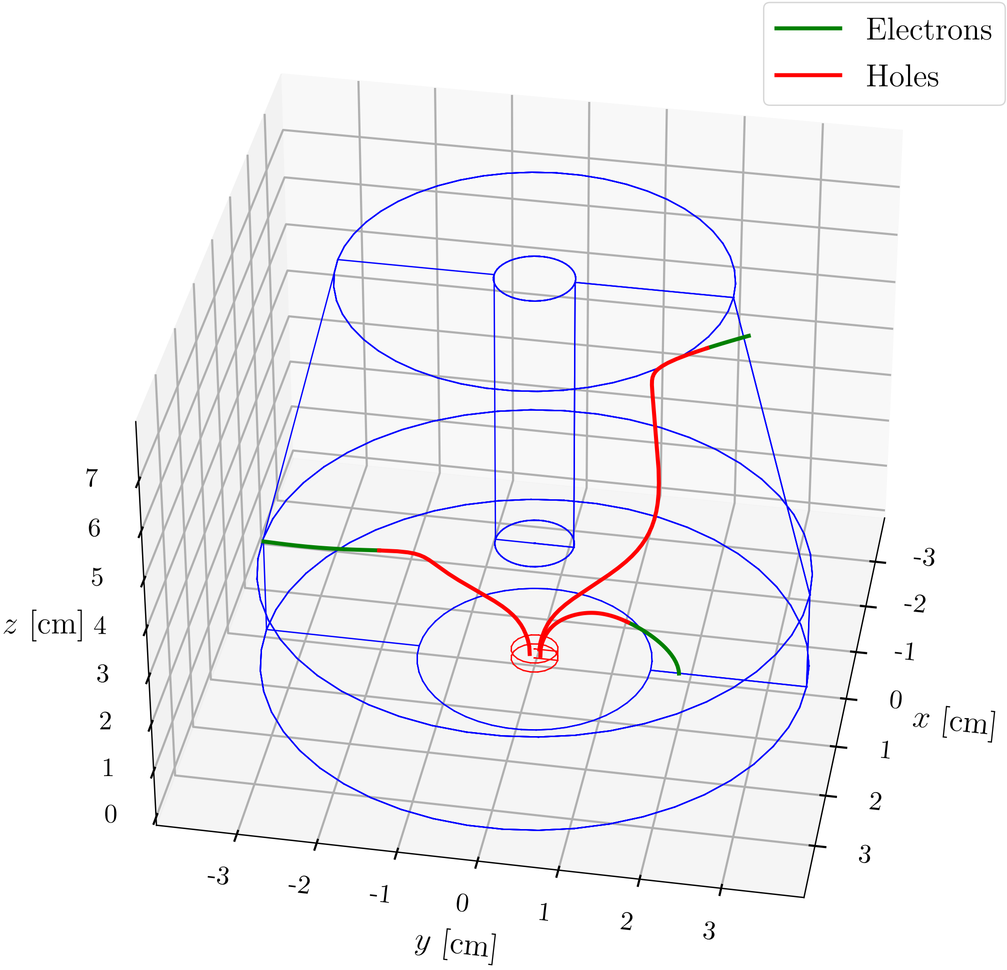

Figure 5.9.: Drift paths of an multi-site event (three charge depositions at three different locations) in the IVC detector as defined in Fig. 5.5. Electron drift is plotted in green and hole drift in red.

The shape of the signals reveal why this type of detector has a very good MSE identification capability. The induced signals mainly change when charge carriers drift through a region where the gradient of the weighting potential is large. This is the case near the core contact, see Fig. 5.10. As the three charge depositions are located in different places, the respective charge carriers (electrons, holes or both), drift though this region at different times. The charge drift in this region causes a rapid change in the induced signal, which is clearly visible in Fig. 5.11 at three values of time. It has to be noted that there are also multi-site events where this is not as clear as in this example, especially, since the detector is symmetric in φ.

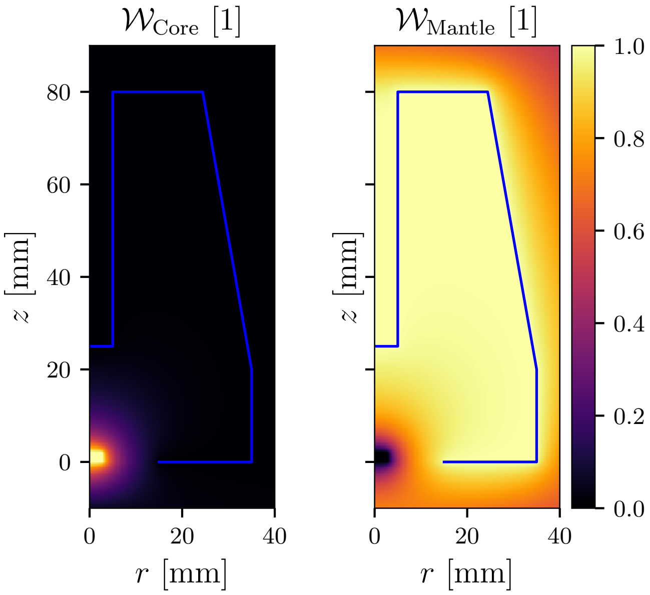

Figure 5.10.: Weighting Potentials for the core (left) and the mantle (right) of the IVC detector described in Fig. 5.11.

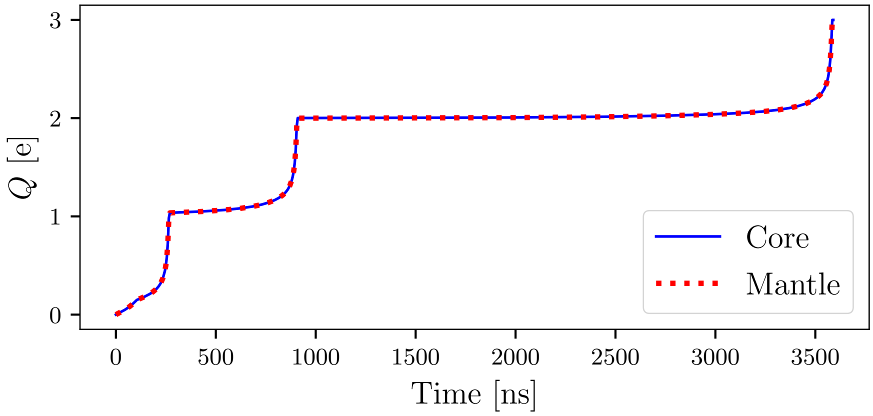

Figure 5.11.: Signals generated for the multi-site event shown in Fig. 5.9 for both channels. The signal of the mantle channel is shown inverted.

5.2.9 Validation: Comparison to Analytically Solvable Problems

The numerical calculations can only be validated analytically for certain geometries, for which the corresponding detectors do not exist. Two such geometries are used to validate the calculations in SSD: An infinitely long coaxial capacitor (detector) and a parallel plate capacitor (detector) with an infinite plate area.

The coaxial detector has a cylindrical shape with an outer radius of $r_\mathrm{o} = 3.5\,\mathrm{cm}$ and a borehole with a radius of $r_\mathrm{i} = 0.5\,\mathrm{cm}$, which contains no material. The electric potential is fixed at r_i to $V_\mathrm{i} = 0\,\mathrm{V}$ and at r_o to $V_\mathrm{o} = 10\,\mathrm{V}$. A quadratic charge density is assumed in the germanium:

$$\rho(r) = \begin{cases} ar^2 & \text{if } r_\mathrm{i} \leq r \leq r_\mathrm{o} \\ 0 & \text{elsewhere} \end{cases} \quad , \tag{5.49}$$

where a is $\rho_0/(\epsilon_r\epsilon_0)$ with ρ_0 chosen to be $-2.56 \times 10^{-3}\,\mathrm{Cm^{-5}}$. The analytic solution for the potential in the germanium is

$$\Phi_A(r) = \frac{ar^4}{16} - c_1 \log(r/\mathrm{m}) + c_2 \quad , \tag{5.50}$$

with

$$c_1 = \frac{1}{\log(r_\mathrm{o}/r_\mathrm{i})} \left[\frac{a}{16}(r_\mathrm{o}^4 - r_\mathrm{i}^4) - (V_\mathrm{o} - V_\mathrm{i}) \right] \quad , \tag{5.51}$$

and

$$c_2 = V_\mathrm{o} + c_1 \log(r_\mathrm{o}/\mathrm{m}) - \frac{ar_\mathrm{o}^4}{16} \quad . \tag{5.52}$$

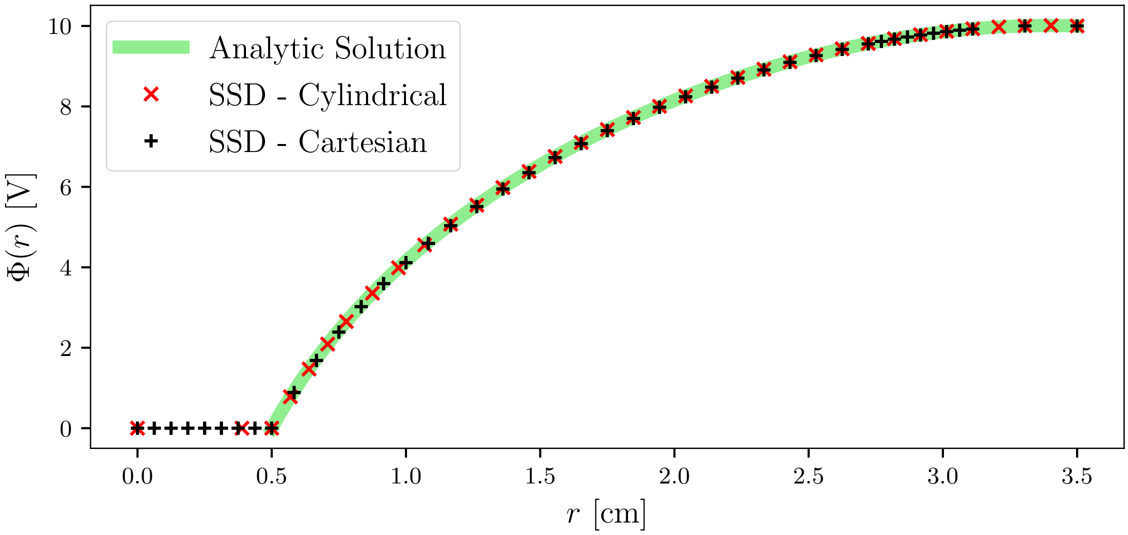

Figure 5.12.: Comparison of the electric potentials of an infinitely long coaxial detector as calculated numerically with SSD and analytically.

For this infinitely long coaxial detector, the numerical solutions for both coordinate systems as well as the analytic solution are shown in Fig. 5.12. The results are in very good agreement.

The capacity can also be used for validation. For the infinite coaxial capacitor the capacity is infinite. Thus, the capacity density, $C_{\mathrm{A}}^{\mathrm{coax}}/L$, is used, where L is a finite length. The capacity density is given by

$$C_{\mathrm{A}}^{\mathrm{coax}}/L = 2\pi\epsilon_r\epsilon_0/\log(r_{\mathrm{o}}/r_{\mathrm{i}}) \quad . \tag{5.53}$$

The capacity of the infinite parallel plate capacitor is also infinite. Thus, again, the capacity density, $C_{\mathrm{A}}^{\mathrm{plate}}/A$, is used, where A is a finite area. The distance between the plates of the capacitor is d. The capacity density is given by

$$C_{\mathrm{A}}^{\mathrm{plate}}/A = \epsilon_r\epsilon_0/d \quad . \tag{5.54}$$

The comparison to the values calculated with SSD yield

$$C_{\mathrm{cyl}}^{\mathrm{coax}}/C_{\mathrm{A}}^{\mathrm{coax}} = 0.9997 \quad , \tag{5.55}$$

$$C_{\mathrm{car}}^{\mathrm{coax}}/C_{\mathrm{A}}^{\mathrm{coax}} = 1.01 \quad , \tag{5.56}$$

$$C_{\mathrm{car}}^{\mathrm{plate}}/C_{\mathrm{A}}^{\mathrm{plate}} = 1.006 \quad . \tag{5.57}$$

Here, "cyl" and "car" indicate the coordinate system used by SSD to calculated the capacity. These values depend on the grid. As the grid becomes finer, these values become closer to 1. These comparisons are part of the automatic tests of SSD, which are always performed when a new release is going to be published.

5.3 Electronics

In the last stage of a simulation, the influence of the read-out electronics on the signals is simulated. This is usually very setup dependent. Thus, it is separated from the previous stage and not part of SSD.

In GALATEA, a test pulse can be fed directly into the pre-amplifier of the core channel. The recorded response can be used to create filters which reproduce the effect of the electronics onto the test pulse. The electronic responses for the segment channels have to be determined from comparison of data and simulations. These filters can be applied to the simulated pulses, see Fig. 5.11. The resulting pulses can be compared directly to data. This will be shown in the next chapter.

Chapter 6: Detector Alignment and Simulation Tuning

Before the response to alpha and beta irradiation of a detector can be studied, the detector orientation in respect to the coordinate system of the collimators in GALATEA has to determined. Also, the impurity model of the semiconductor as well as the parameter for the drift model and the electronic response functions have to be determined in order to tune the simulation. In this chapter, this is presented exemplarily for the detector Super Siegfried, while for the other detector Siegfried III presented in this thesis, this is done in a similar way.

6.1 The Super Siegfried Detector

The detector is depicted in Fig. 6.1 and its geometry as implemented in SSD is shown in Fig. 6.2. The detector has a cylindrical shape with a height of 70 mm and an outer radius of 37.5 mm. The borehole penetrates the full height and has a radius of 5 mm. At the top and the bottom, the borehole widens to a radius of 10 mm within about 3 mm. Super Siegfried is n-type. The surface of the inner borehole, without the area of the widening, is the only n^+-contact and, thus, the core. It was over-doped via Li-drift. The outer mantle of the detector was segmented into 19 p^+-contacts via Boron implantation. The 18 lower segments are ordered in a 6×3 geometry in φ and z as visible in Fig. 6.2 and Fig. 6.3. In φ, each of these segments spans 60° and the three rows are called bottom, middle and top row. The segments of the bottom and middle row have a height of ≈ 23.33 mm, while the segments of the top row have a height of ≈ 18.34 mm. The 19th segment with a height of ≈ 5 mm is located above the top row. It is not segmented in φ, but it is a complete ring around the mantle.

All 19 segments were fully metallized with aluminum for all measurements performed for this thesis. Previously published data [70, 71, 55, 82] were taken when the segments were not fully metallized, i.e. when each segment only featured a small metallized dot to facilitate a good contact to the cable.

The top and bottom surfaces, including the areas of the widening borehole, are passivated with silicon dioxide with a thickness of about $2\,\mu$m.

The impurity density, as stated by the manufacturer of the crystal, is $0.44 \times 10^{10}\,\mathrm{cm}^{-3}$ at the top and $1.3 \times 10^{10}\,\mathrm{cm}^{-3}$ at the bottom. The operation voltage is 3000 V. It is applied to the core, whereas the segments are kept at ground.

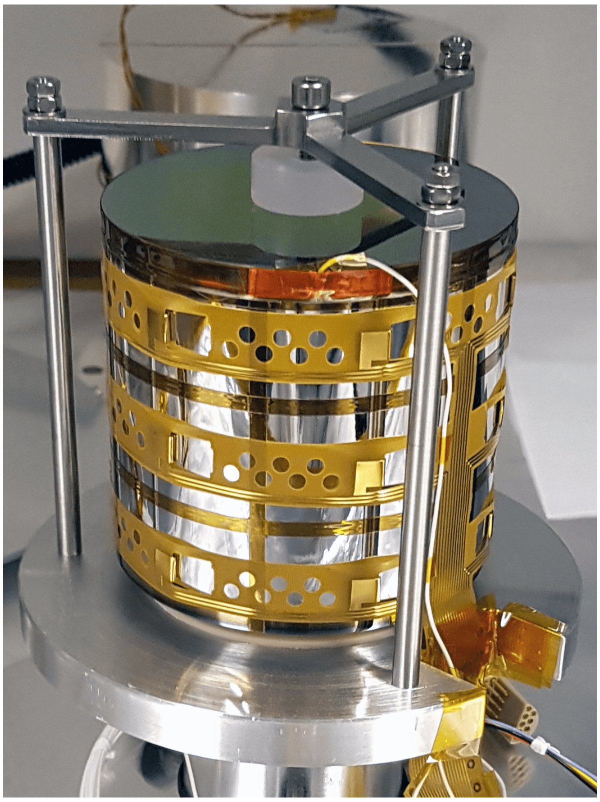

Figure 6.1.: Picture of Super Siegfried. The detector is mounted in its holder, which fits on top of the GALATEA cooling finger. Also visible is the Kapton printed-circuit-board (PCB) wrapped around the mantle, which is used to read out 18 segments. The 19th segment is read out with a separate white wire, which is also visible.

All scans of Super Siegfried are listed in Appx. A.2

6.2 Pulse Preprocessing, Calibration and Cross-talk Correction

The raw data of one single event recorded for Super Siegfried in GALATEA comprise 20 pulses, $p_i^{\mathrm{raw}}(k)$, with 5000 samples each, $k \in [1, \ldots, 5000]$. As the sampling rate of the DAQ is 250 MHz, see 4.1.3, the time between each sample is 4 ns. The trigger, a trapezoidal filter, is configured such that each pulse has a baseline of 1800 samples.

In order to calculate the deposited energies, E_i, for all channels $i \in [0, \ldots, 19]$, these raw pulses are processed in several steps which are described in detail in [51]. Here, they are only summarized:

1. Baseline subtraction: The DAQ digitizes the analog signal to unsigned integers. The analog signal can be negative or positive. Thus, an offset is configured for conversion. This offset is calculated from the baseline of each pulse and subtracted

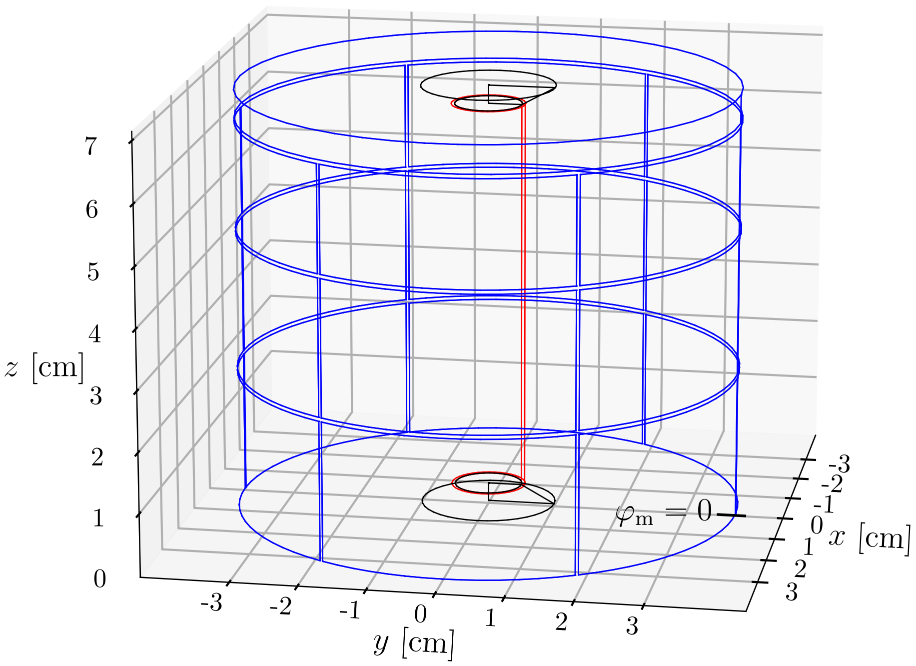

Figure 6.2.: Visualization of Super Siegfried in SSD. The p^+-segments are shown in blue and the n^+-contact (core) is shown in red. The widening of the borehole is shown in black.

from each sample.

2. Decay correction: The pre-amplifiers used in GALATEA have a decay constant of about 50 μs. Thus, any signal decays as soon as it is generated. This decay is filtered out. The decay constants for all channels were determined from single-site environmental background events. Fig. 6.4 illustrates steps 1 and 2, i.e. the path from the raw pulse, $p_0^{\mathrm{raw}}(k)$, to the background subtracted and decay time corrected pulses, $p_0^{\mathrm{bls}}(k)$ and $p_0^{\mathrm{tdc}}(k)$.

3. Calibration & cross-talk correction: The signal, the amplified induced charge, is proportional to the number of created electron-hole pairs and, thus, to the amount of deposited energy. The calibration factor for each channel is assumed to be constant for all energies. But, there is also cross-talk present. The calibration and cross-talk correction is done in one step for each individual measurement. For this, only linear cross-talk is considered. The cross-talk model allows for different cross-talk coefficients from the core to the segments, but the cross-talk from all segments to the core is assumed to be of equal strength. This assumption is made because in GALATEA, the cross-talk is dominated by the cabling and the core signal is already amplified before its cables gets close to the segment cables, see Sec. 4.1.2.

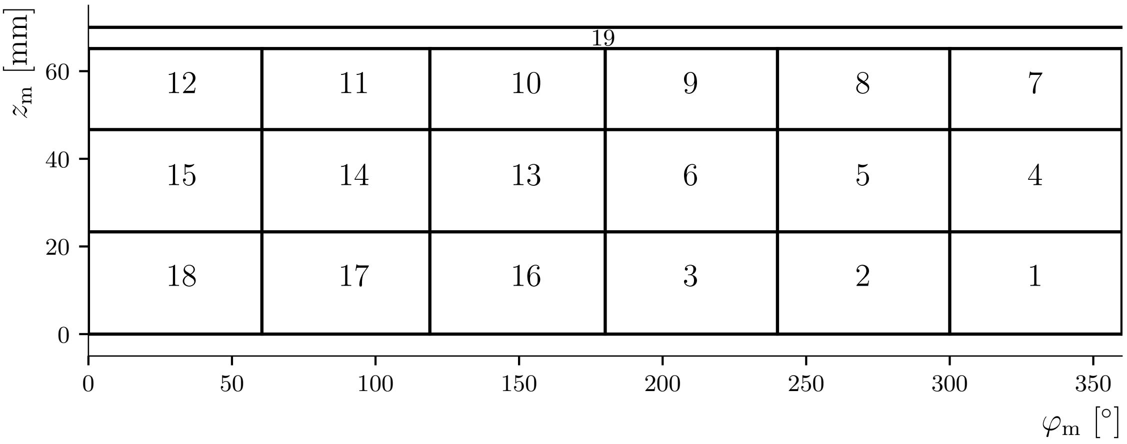

Figure 6.3.: Segment labeling of Super Siegfried.

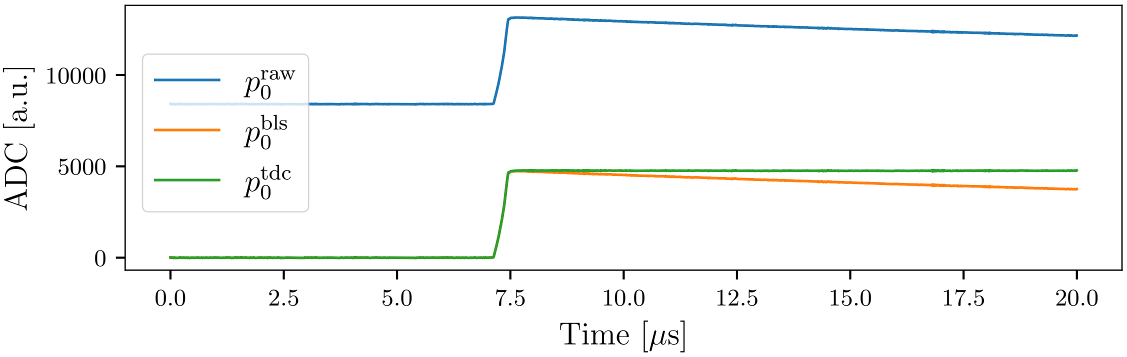

Figure 6.4.: Preprocessing of a core pulse recorded in Super Siegfried in GALATEA.

The energy in each channel is determined by the mean of the tail of the corrected pulse[1]. The energy windows which are used are illustrated in Fig. 6.5.

The energy spectra of a background measurement are shown in Fig. 6.6. As the core is the only n^+-contact, the core always detects the whole energy of an event. In contrast, the individual segments, as shown here for segment 1, only register the energy which is deposited in the respective volume of the detector where the holes drift towards the segment. For MSE, the energy can be deposited in different segments. However, the sum of all segment energies recorded for an event should equal the energy recorded in the core. Fig. 6.6 demonstrates this, even though the sum of the segment energies has a slightly worse resolution.

---

[1] For improved energy resolution there are more sophisticated methods to reconstruct the energy. However, for the analysis in this thesis, this is not necessary.

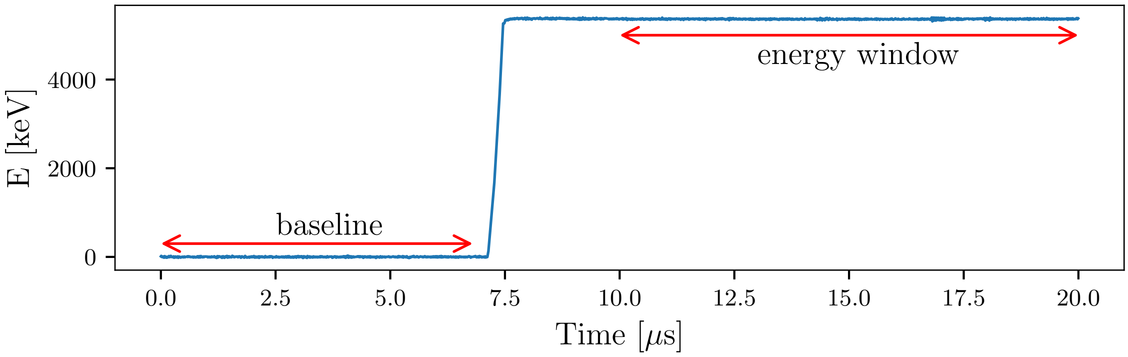

Figure 6.5.: Recorded pulse in the core channel after calibration and cross-talk correction.

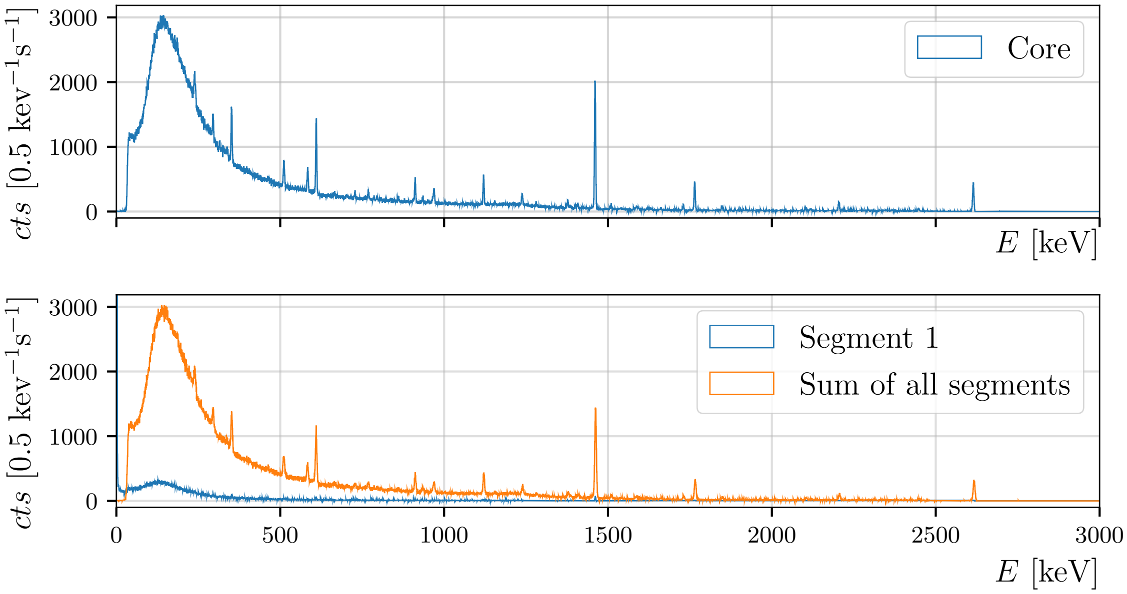

Figure 6.6.: Spectra of a background measurement. Top: the core channel of Super Siegfried. Bottom: Spectrum of segment 1 (blue) and the spectrum of the summed energies of all segments (orange).

6.3 Radioactive Source Americium: ^{241}Am

The isotope ^{241}Am is one of the sources used in GALATEA. It alpha decays into ^{237}Np and some excited states of ^{237}Np gamma decay. The branching ratios (BR) end decay energies, Q, of the most dominate decays of ^{241}Am are [83]

$$Q_{\alpha_1} = 5485.56 \pm 0.12\,\mathrm{keV} \qquad (\mathrm{BR} = 84.5 \pm 1.0\,\%)\ , \tag{6.1}$$

$$Q_{\alpha_2} = 5442.80 \pm 0.13\,\mathrm{keV} \qquad (\mathrm{BR} = 13.0 \pm 0.6\,\%)\ , \tag{6.2}$$

$$Q_{\alpha_3} = 5388.23 \pm 0.13\,\mathrm{keV} \qquad (\mathrm{BR} = 1.6 \pm 0.2\,\%)\ , \tag{6.3}$$

$$Q_{\gamma}^{\mathrm{Np}} = 59.5412 \pm 0.0002\,\mathrm{keV} \qquad (\mathrm{BR} = 35.9 \pm 0.4\,\%)\ . \tag{6.4}$$

The alphas have rather high energies but as they are strongly ionizing particles, they lose their energy within 20 μm of germanium and create events directly underneath the surface of a detector. Since the energy of the gammas is rather low, they only penetrate slightly deeper into the germanium and predominantly create events within ≈ 2 mm below the surface, see Sec. 2.7.

The two open ^{241}Am sources used were newly acquired for this thesis. Their performance is in contrast to the encapsulated ^{241}Am sources used in previous studies [51, 55, 70, 71, 82], which released alphas with energies reduced by ≈ 1 MeV [51].

6.4 Detector Alignment

In GALATEA, the three motors are used to move the collimators around the detector and irradiate the detector from different angles. Thus, the first step in the analysis is the determination of the conversion function of the positions of the motors, into the position of the center of the beam-spots created on the detector top surface, $\mathbf{r}_\mathrm{m}^\mathrm{t} = (r_\mathrm{m}, \varphi_\mathrm{m}^\mathrm{t})$, and on the detector mantle, $\mathbf{r}_\mathrm{m}^\mathrm{s} = (\varphi_\mathrm{m}^\mathrm{s}, z_\mathrm{m})$.

6.4.1 Beam-Spot on Mantle

As the detector is segmented, the segment boundaries can be used as reference to determine the position of the beam-spot on the side surface. In order to do so, scans over boundaries between two segments were performed and the relative number of detected events in both segments were used to determine the central position of the beam-spot: When the beam-spot is completely contained in one segment, all events created by the source are detected in this segment, whereas all other segments show only background events. If the collimator is moved and the beam shines onto the boundary between the two segments i and j, source events are detected in both segments. The relative difference between the amount of detected source events in both segments depends on the part of the beam-spot which illuminates the respective segment.

The 59.54 keV-gammas of ^{237}Np were used for the boundary determination. The alphas could not be used as the segment boundaries are covered with Kapton tape, see in Fig. 6.1. The Kapton tape is thick enough to absorb all alphas from ^{241}Am, but most of the gammas reach the detector.

Only the determination of the vertical segment boundary between segments 14 and 15, $\mathcal{B}_{14,15}$, is shown as the procedure is conceptional the same for all other boundaries. The scan SSAmRotMid was used to determine this boundary. It is illustrated in Fig. 6.7. It is a rotational scan where the beam-spot of the collimator was always completely contained in the mid row of segments. The scan consists of 48 measurements covering 180° in $\varphi^{\mathrm{s}}_{\mathrm{m}}$ for constant z_{m}. However, only 19 measurements (indexed with $i_m \in [1, 19]$) around the boundary were used in one bayesian fit with 249 parameters to determine $\mathcal{B}_{14,15}$. The fit was performed with the Bayesian Analysis Toolkit (BAT), implemented in Julia [84], using a Hamiltonian Monte Carlo (HMC) sampling algorithm [85].

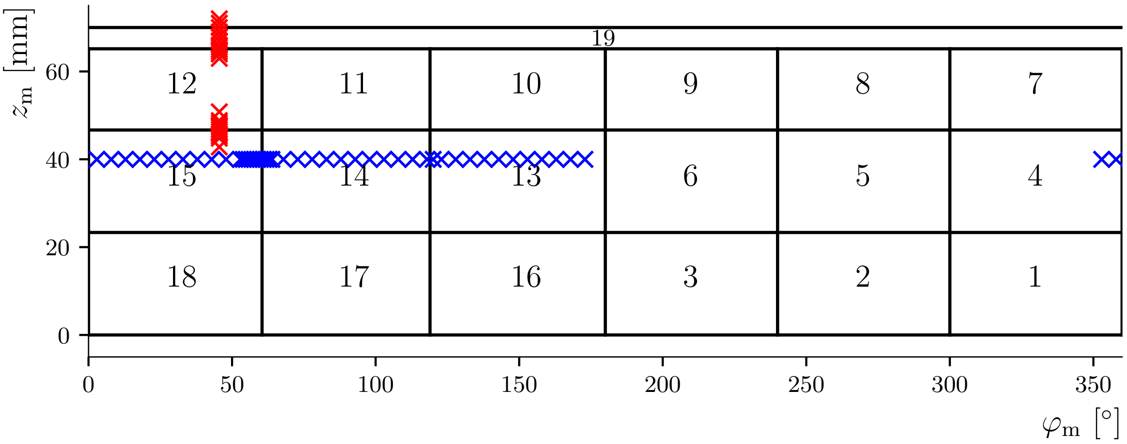

Figure 6.7.: Map of the measurements of the two scans SSAmRotMid (blue) and SSAmVert (red).

Data: The corresponding data are 57 (19 measurements × 3 channels: core and segment 14 and 15) energy histograms around the 59.54 keV gamma line ($48 - 72$ keV, bin width $= 1$ keV) filled only with single segment 14 and single segment 15 events. A single segment i event is an event where the energy recorded in segment i is approximately (here ±3 keV) the same as the energy detected in the core. Selected spectra are shown in Fig. 6.8.

Likelihood: The likelihood is given by the product of all likelihoods evaluated for each bin of the 57 histograms. The entry of each bin is a discrete number of events in the corresponding energy interval. Thus, the underlying distribution is the Poisson distribution. The expectation value for each bin is given through the "local" model function $\mathcal{G}_i^{i_m}(E)$, which was chosen to be a Gaussian on top of a linear function to describe the peak and the background. This local model has 5 parameters:

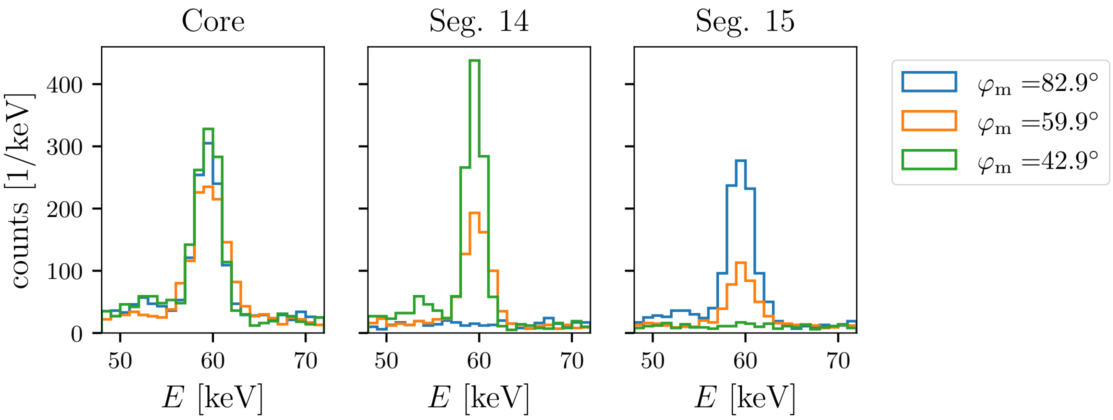

Figure 6.8.: Energy histograms of 3 of the 19 measurements used for the boundary determination. For the measurement shown in green, the beam-spot was fully contained in segment 14, whereas for the measurement in blue, it lies entirely in segment 15. For the measurement in orange, the beam-spot illuminates the boundary.

- The amplitude of the Gaussian, $\mathcal{A}_i^{i_m}$.
- Its standard deviation, $\sigma_i^{i_m}$, which is a measure for the energy resolution of the channel at $\sim 60\,\mathrm{keV}$.
- Its mean value, $\mu_i^{i_m}$, which might not exactly be 59.54 keV due to uncertainties in the energy calibration.
- The background density on the left, $bgl_i^{i_m}$.
- The background density on the right, $bgr_i^{i_m}$.

The formula of the local model (for the given histograms) is

$$\mathcal{G}_i^{i_m}(E) = \frac{\mathcal{A}_i^{i_m}}{\sigma_i^{i_m}\sqrt{2\pi}} \exp\left\{-\frac{(E-\mu_i^{i_m})^2}{2{\sigma_i^{i_m}}^2}\right\} + bgl_i^{i_m} + \frac{bgr_i^{i_m} - bgl_i^{i_m}}{23\,\mathrm{keV}} \cdot (E - 48.5\,\mathrm{keV}) \ . \quad (6.5)$$

Only in the core spectra, the amplitude is a free parameter. For each measurement i_m and, thus, each polar position $\varphi_\mathrm{m}^{\mathrm{s},i_m}$, the amplitudes for the two segment spectra are determined by the corresponding amplitude in the core channel by

$$\mathcal{A}_{14}^{i_m} = \frac{1}{2}\mathcal{A}_\mathrm{core}^{i_m}(\varphi_\mathrm{m})\left\{\mathrm{erf}\left(-\mathcal{S}_\mathrm{side}\cdot(\varphi_\mathrm{m}^{\mathrm{s},i_m} - \mathcal{B}_{14,15})\right) + 1\right\} \ , \quad (6.6)$$

$$\mathcal{A}_{15}^{i_m} = \frac{1}{2}\mathcal{A}_\mathrm{core}^{i_m}(\varphi_\mathrm{m})\left\{\mathrm{erf}\left(+\mathcal{S}_\mathrm{side}\cdot(\varphi_\mathrm{m}^{\mathrm{s},i_m} - \mathcal{B}_{14,15})\right) + 1\right\} \ , \quad (6.7)$$

where $\mathcal{B}_{14,15}$ is the position of the boundary and $\mathcal{S}_\mathrm{side}$ is a parameter which is correlated to the shape of the beam-spot and is constant for a given source and collimator configuration.

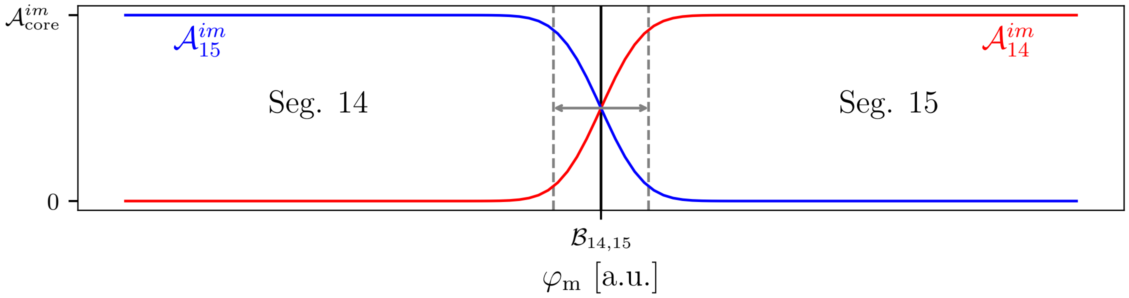

Figure 6.9.: Expected segment amplitudes depending on φ_{m} and $\mathcal{A}^{i_m}_{\text{core}}$. The size of the beam-spot corresponds roughly to the range marked in grey.

The beam-spot is assumed to be of Gaussian shape due to the geometrical configuration of the collimator. As the integral of a normal distribution is an error-function, the error-function was chosen to describe the drop (increase) of the ratio of detected events in the segments, which is illustrated in Fig. 6.9.

Prior: Flat priors were used for all 249 parameters. As this is a very high-dimensional problem, the intervals of the 247 parameters of the peak plus background model functions, Eq. 6.5, were restricted to the 99.7 % central intervals (3σ) of the marginal posterior distributions of smaller (5 parameters) bayesian fits of $\mathcal{G}^{i_m}_i(E)$ on each individual histogram, see Fig. 6.10. The interval for the flat prior for $\mathcal{B}_{14,15}$ was chosen to be ±3° around a guess (by eye) for $\mathcal{B}_{14,15}$. For $\mathcal{S}_{\text{side}}$]0,2] was chosen. In the fits of the other vertical segment boundaries, an approximated truncated normal distribution of the marginalized posterior distribution of $\mathcal{S}_{\text{side}}$ was taken as prior distribution, since for the other segment boundaries fewer measurements over the respective boundary were taken and the beam-spot was identical.

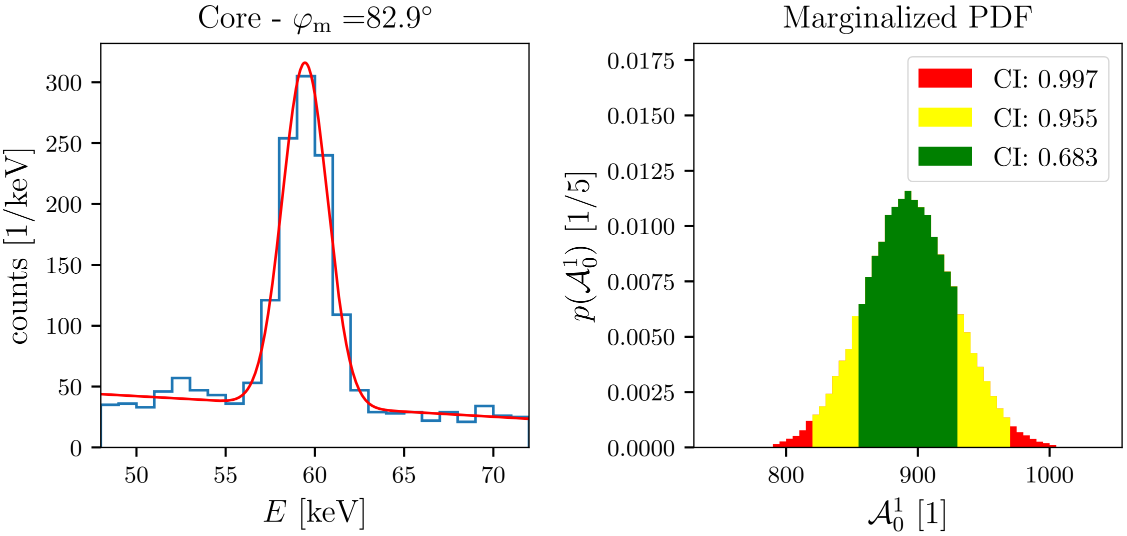

Figure 6.10.: Left: Input core spectrum (blue) of the measurement $i_m = 1$ ($\varphi_{\text{m}} = 82.9°$) and $\mathcal{G}^1_0$ (red) as obtained from the prefit. Right: Marginalized posterior distribution of the prefit for $\mathcal{A}^1_{\text{core}}$, used as input for the global fit, for details see text.

Posterior: Most of the parameters are not of particular interest and there are too many to be visualized here. Only the marginalized posteriors of the two parameters $\mathcal{B}_{14,15}$ and $\mathcal{S}_{\text{side}}$ are shown in Fig. 6.11. The local mode of the marginalized posterior of $\mathcal{B}_{14,15}$, 60.44°, was taken as the position of the segment boundary.

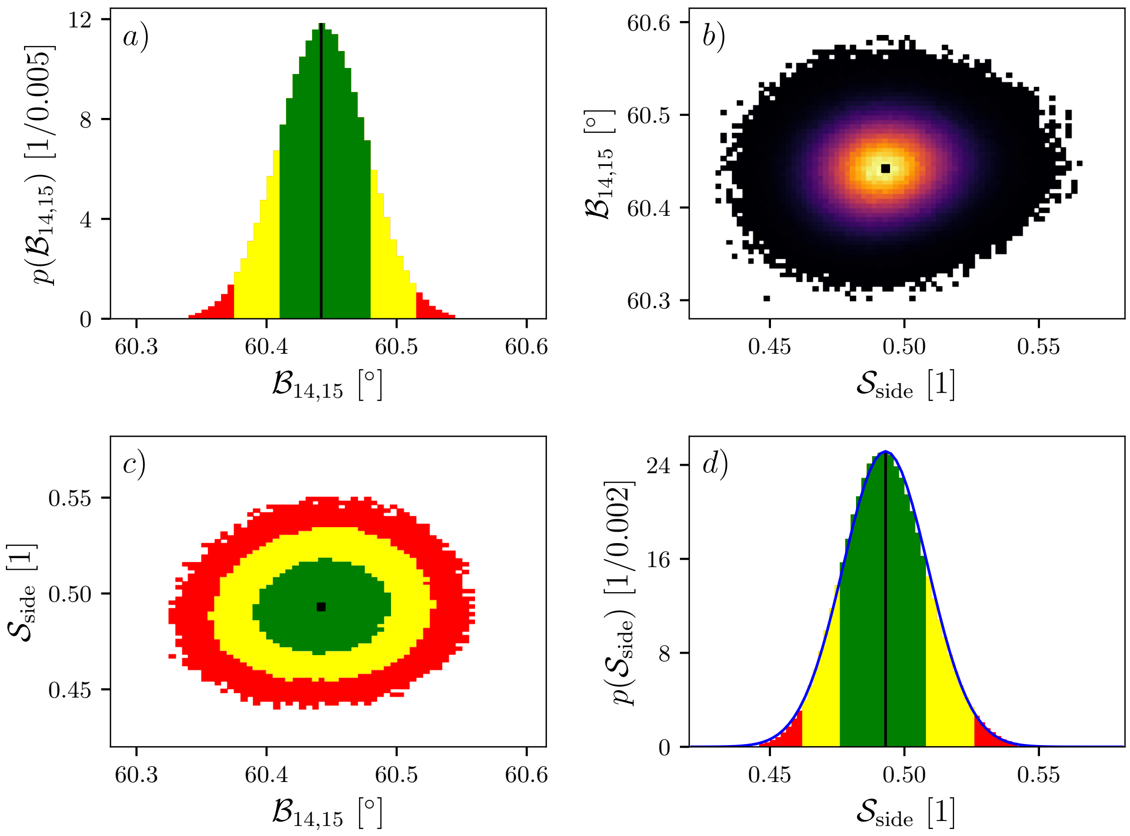

Figure 6.11.: Marginalized posterior distributions of the two parameters (a) $\mathcal{B}_{14,15}$ and (d) $\mathcal{S}_{\text{side}}$. The green, yellow and red colors represent the 68.3%, 95.5% and 99.7% smallest credibility intervals. The 2d marginalizations of the two parameters are shown in (c) in form of credibility intervals and in (b) as a heatmap. The black dots and black lines are the local modes. (d): Also the normal distribution approximating the marginalized posterior distribution of $\mathcal{S}_{\text{side}}$ is shown in blue, which is used as prior distribution for the determination of the other vertical segment boundaries.

Uncertainties: The credibility intervals of the marginalized posteriors of $\mathcal{B}_{14,15}$ are very small ($\sim 0.2°$). However, as described in Sec. 4.1.6, there is a larger systematic uncertainty, duo to the alignment of the detector in GALATEA.

The positions and uncertainties of all segment boundaries are summarized in Table 6.1. For the horizontal boundaries the vertical scan SSAmVert, see Fig. 6.7, was used. The coordinate system was chosen such that the segment boundary $\mathcal{B}_{4,15}$ is at 0° and the bottom of the detector is at 0 mm.

	$\mathcal{B}_{i,j}$ + sta. unc.	Sys. unc.	
$\mathcal{B}_{4,15}$	$0.00 \pm 0.14°$	$\pm 1°$	vertical
$\mathcal{B}_{14,15}$	$60.44 \pm 0.04°$	$\pm 1°$	vertical
$\mathcal{B}_{13,14}$	$118.95 \pm 0.07°$	$\pm 1°$	vertical
$\mathcal{B}_{12,15}$	$46.67 \pm 0.04\,\mathrm{mm}$	$\pm 0.5\,\mathrm{mm}$	horizontal
$\mathcal{B}_{12,19}$	$65.16 \pm 0.04\,\mathrm{mm}$	$\pm 0.5\,\mathrm{mm}$	horizontal

Table 6.1.: Positions as determined for the segment boundaries of Super Siegfried.

6.4.2 Beam-Spot on Top

In order to validate the position of the top beam-spot, the position of the edge of the detector at a radius of 37.5 mm was determined in four radial scans at different $\varphi^{\mathrm{t}}_{\mathrm{m}}$. The radial top scans SSAmRad1, SSAmRad23, SSAmRad136 and SSAmRad181 were used, see Fig 6.12. The procedure is not described in detail as it is very similar to the procedure used to determine the segment boundaries. The only difference is that only the decrease of the number of events in the core channel is used to determine the edge. Thus, only the core spectra filled with single segment 19 events were used. The global fit function, which predicts the amplitude of the peak for different radial positions, is

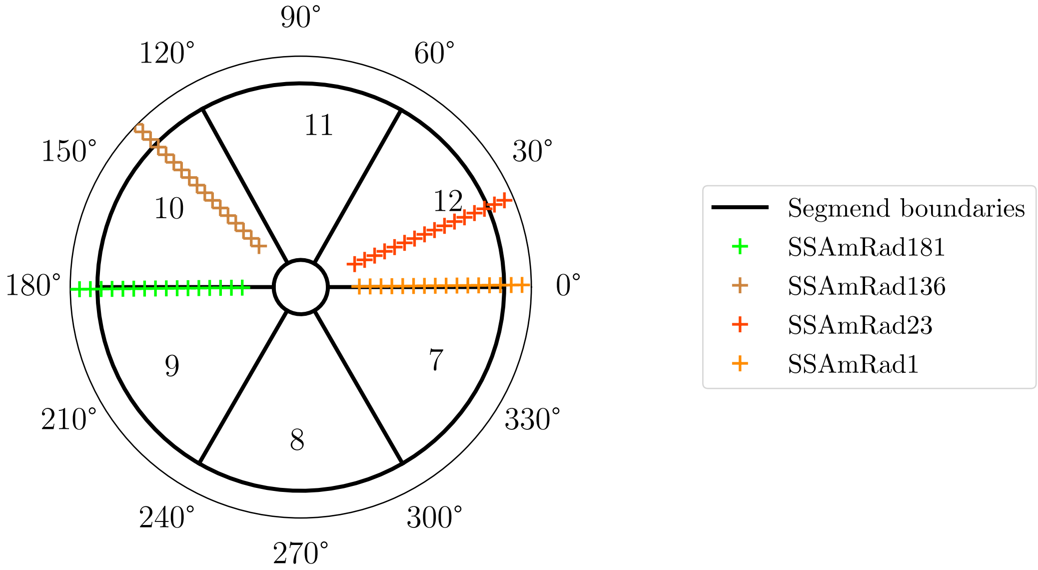

Figure 6.12.: Map of the measurements of the four scans used to align the top collimator. The numbers indicate the six segments underneath the top segment, i.e. segment 19.

$$\mathcal{A}^{im}_{\mathrm{core}} = \frac{1}{2}\mathcal{A}_{\mathrm{top}} \left\{ \mathrm{erf}\left(-\mathcal{S}^{r}_{\mathrm{top}} \cdot \left(r^{im}_{\mathrm{m}} - \mathcal{R}^{im}_{\mathrm{mantle}} \right) \right) + 1 \right\} \ , \tag{6.8}$$

where $\mathcal{A}_{\mathrm{top}}$ is the amplitude, which should be constant for a given source and collimator configuration. $\mathcal{S}^{r}_{\mathrm{top}}$ is the slope parameter, which is also constant for a given source and collimator configuration. It describes the shape of the top beam-spot in radial direction. $\mathcal{R}^{i_m}_{\text{mantle}}$ is the position of the edge of the mantle and $r^{i_m}_{\text{m}}$ is the radial position as determined from measurement i_m. This function is shown in Fig. 6.13 for the scan SSAmRad136.

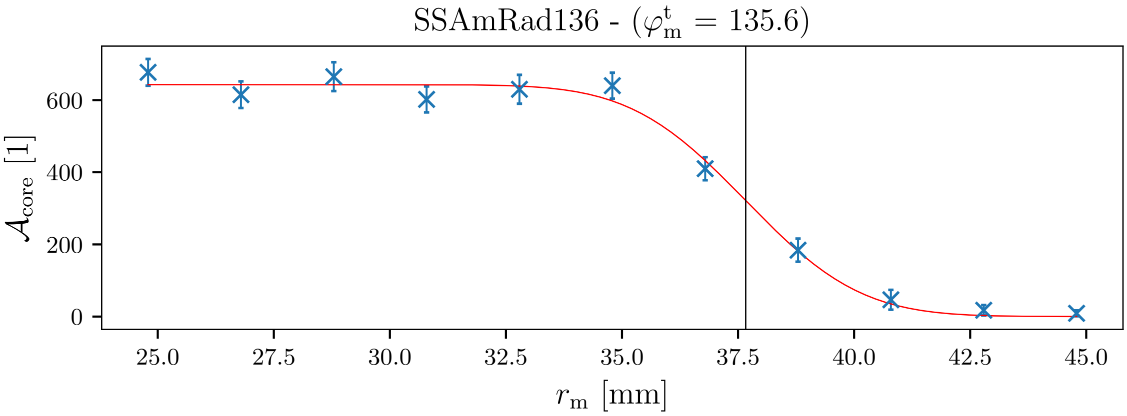

Figure 6.13.: Red: Global model for the outer edge of the detector, which predicts the number of counts in the core for the scan SSAmRad136. The local modes are used as parameters of the model. Blue crosses: Local modes of the amplitude parameter, $\mathcal{A}^{i_m}_{\text{core}}$, of the local pre-fits of the peak in the core spectra. The error bars represent the 68.8 % central confidence interval of $\mathcal{A}^{i_m}_{\text{core}}$. Black line: Local mode of the marginalized posterior distribution of $\mathcal{R}^{i_m}_{\text{mantle}}$.

The positions of the edge, $\mathcal{R}^{i_m}_{\text{m}}$, determined from the four scans are summarized in Table 6.2. The center of the detector and the center of the motor coordinate system are offset by (0.42 mm, 203.3°) (polar vector), assuming that the detector is not tilted. This is within the determined systematic uncertainty due to the alignment as determined in Sec. 4.1.6.

$\varphi^{\text{t}}_{\text{m}}$	$\mathcal{R}^{i_m}_{\text{m}}$ + sta. unc.	Sys. unc.
180.6°	37.11 ± 0.17 mm	±0.5 mm
135.6°	37.67 ± 0.19 mm	±0.5 mm
23.1°	37.87 ± 0.23 mm	±0.5 mm
0.6°	37.37 ± 0.17 mm	±0.5 mm

Table 6.2.: Positions and uncertainties of the edge $\mathcal{R}^{i_m}_{\text{mantle}}$ of Super Siegfried for different polar angles $\varphi^{\text{t}}_{\text{m}}$ as determined from the scans depicted in Fig. 6.12. The systematic uncertainties were estimated in Sec. 4.1.6

6.4.3 Position of "Mercedes Bar"

The holding structure of Super Siegfried, see Fig. 6.1, consists of three metal rods with a distance of 120° to each other around the detector. They are connected at the top with one metal piece, which has the shape of a mercedes star. In the center, the mercedes star presses a teflon piece slightly onto the detector to hold the detector in place. The three rods and the three bars of the mercedes star block particles when the collimator are in the respective positions. The scan SSAmRotMid, see Fig. 6.14, was used to determine the position of one of the three bars on top, $\varphi_{\mathcal{MB}}$. The procedure is, again, similar to the procedure to determine the segment boundaries.

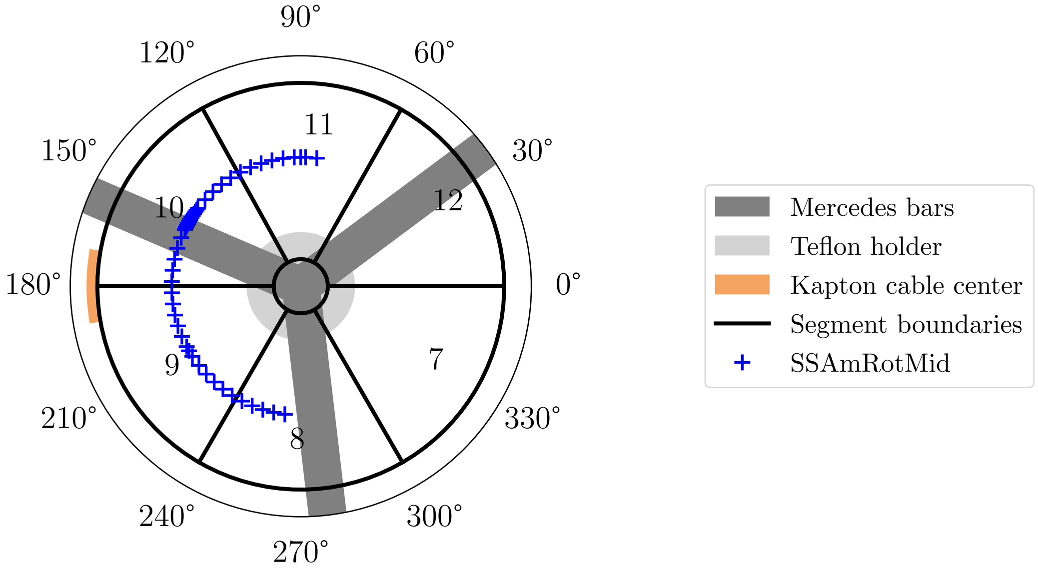

Figure 6.14.: Map of the top beam-spot positions of the scan SSAmRotMid used to determine the position of the mercedes star.

The global function,

$$\mathcal{A}^{im}_{\text{core}} = \frac{1}{2}\mathcal{A}_{\text{top}}\left\{\text{erf}\left(-\mathcal{S}^{\varphi}_{\text{side}}\cdot\left(\varphi^{\text{t},im}_{\text{m}}-\varphi_{\mathcal{MB}}+w_{\mathcal{MB}}\right)\right)+1\right\} \tag{6.9}$$

$$+ \frac{1}{2}\mathcal{A}_{\text{top}}\left\{\text{erf}\left(+\mathcal{S}^{\varphi}_{\text{side}}\cdot\left(\varphi^{\text{t},im}_{\text{m}}-\varphi_{\mathcal{MB}}-w_{\mathcal{MB}}\right)\right)+1\right\} , \tag{6.10}$$

predicts the number of 59.54 keV photons in the core spectrum, which was only filled with single segment 19 events. Here, $w_{\mathcal{MB}}$ is the width of the metal bar at the radius of the scan and, thus, is constant. $\mathcal{S}^{\varphi}_{\text{top}}$ is the slope parameter which describes the shape of the beam-spot in φ_{m} direction. The center of the mercedes bar shown in Fig. 6.14 was determined to be

$$\varphi_{\mathcal{MB}} = 156.7 \pm 1.3° \quad . \tag{6.11}$$

The global function, with local modes as parameters, is shown in Fig. 6.15.

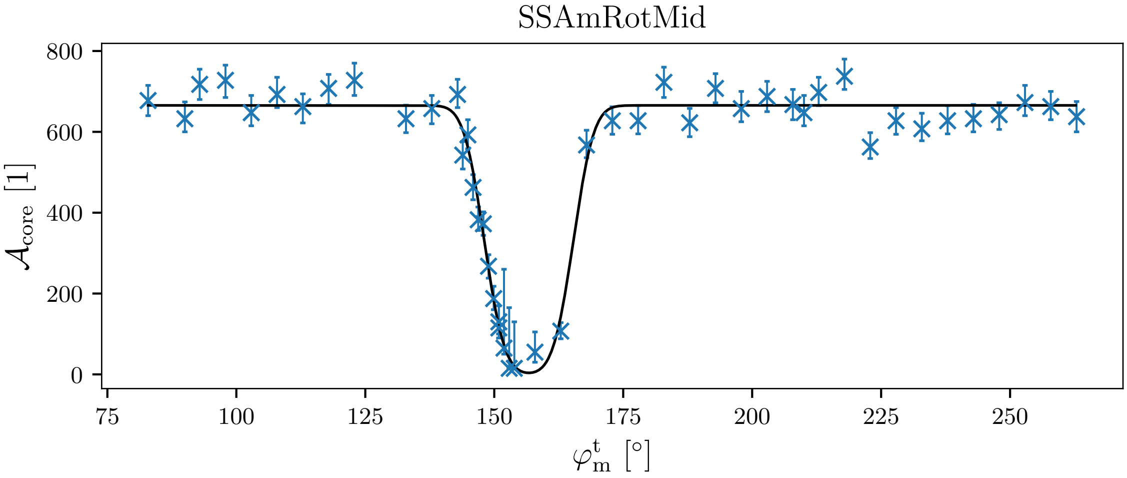

Figure 6.15.: Black: Global fit function, Eq. 6.10, with the local modes as parameters. Blue markers: Local modes of the amplitude parameter of the 59.54 photon peak pre-fits of the individual core spectra of the scan SSAmRotMid. The error bars represent their 68.7 % confidence intervals of their marginalized posterior distributions.

6.5 Crystal Axes Determination

The last step regarding alignment is the determination of the orientation of the crystal. As the axes influence the drift and the signals, it is important to know their orientation in order to compare events at different locations as well as to compare data to simulation. The axes $\langle 100 \rangle$, $\langle 010 \rangle$ and $\langle 001 \rangle$ are called fast axis and <110>, <011>, <101> are called slow axes throughout this thesis, because charge carriers drift faster and slower along these axes, respectively.

Germanium crystals are normally pulled with the $\langle 001 \rangle$ direction parallel to the z axis of the detector. Therefore, the other axes are in the r-φ plane. The oscillation of the duration of pulses from surface events on the mantle at fixed z over varying φ_{m} provides the information to determine the orientation of $\langle 100 \rangle$, $\langle 110 \rangle$, $\langle 010 \rangle$ and, thus, all other axes.

Events induced by alphas entering from the side of the rotational scan SSAmRotMid, see Fig. 6.7, were used for this purpose. As they have high energies, see Sec. 6.3, they can simply be selected by energy since, at these energies, the background is negligible. This is demonstrated in Fig. 6.16. Also shown in this figure is the local mode of the fit of the three alpha peaks. This fit was performed for every measurement of the scan SSAmRotMid in order to determine the energy window to select alpha events, which was chosen to be the 1-σ window around the dominant alpha peak.

In the next step, the drift duration of all these alpha events was determined. The duration of a pulse is often quantified as the so-called rise times, $\mathcal{T}_{x-y}$, which are the

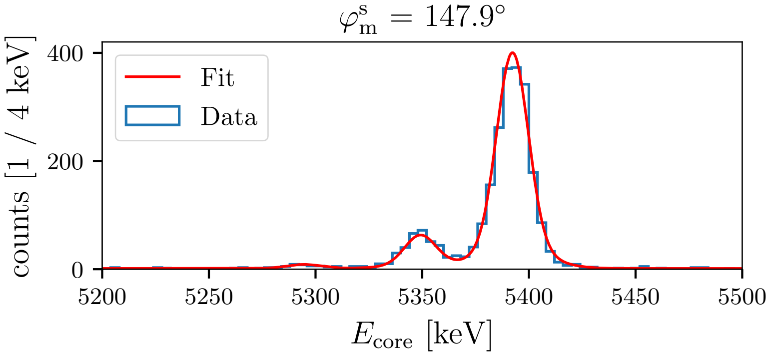

Figure 6.16.: Blue: Histogram of the core energies of single segment 13 events of the measurement of the scan SSAmRotMid, see Fig. 6.7, at $\varphi_{\mathrm{m}}^{\mathrm{s}} = 147.9°$. In red: Fit of the 3 alpha peaks due to ^{241}Am.

times in which the pulse rises from $x\%$ to $y\%$ of its maximum. This is illustrated in Fig. 6.17.

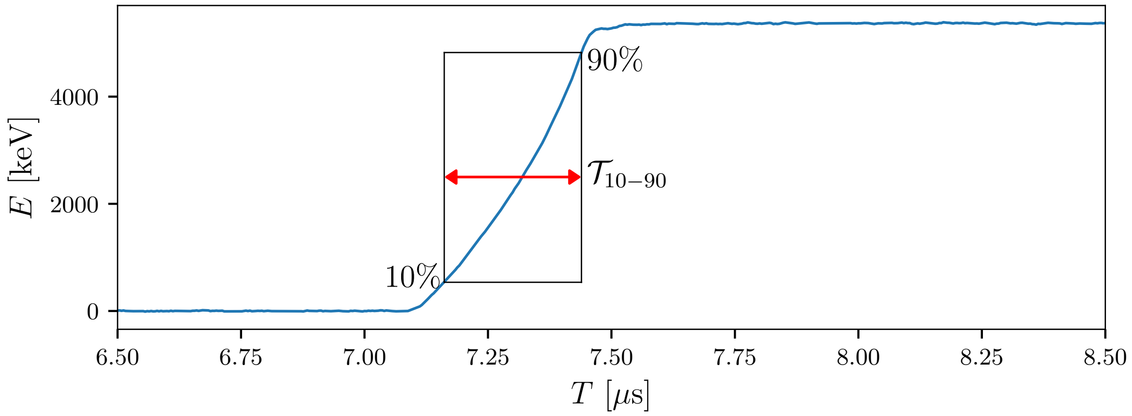

Figure 6.17.: Visualization of the rise time $\mathcal{T}_{10-90}$ via the red arrow. Blue: Core pulse of a typical alpha event.

For each measurement, a scaled normal distribution was fitted to the distribution of the rise time $\mathcal{T}_{10-90}$ of the selected alpha events. This is shown in Fig. 6.18 as well as the marginalized posterior distribution of the μ parameter of the scaled normal distribution.

Normal distributions were fitted to these marginalized posterior distributions and their standard deviations were added to an estimated systematic uncertainty of 6 ns (1 σ) which is due to the variation of crystal temperature in GALATEA due to the refilling of the LN2 tank. The uncertainties in form of one standard deviation, together with the local mode as the mean parameter form a normal distribution, which was taken as prior distribution and likelihood for the rise time at the corresponding $\varphi_{\mathrm{m}}^{\mathrm{s}}$ in the final fit of the oscillation of the rise time over φ_{m}. The oscillation is modeled as

$$\mathcal{T}_{10-90}(\varphi_{\mathrm{m}}^{\mathrm{s}}) = \Delta\mathcal{T}_{10-90} \cdot \sin(4(\varphi_{\mathrm{m}}^{\mathrm{s}} - \varphi_{\mathrm{fa}} - 45°/2)) + \mathcal{T}_{10-90}^{0} \quad , \tag{6.12}$$

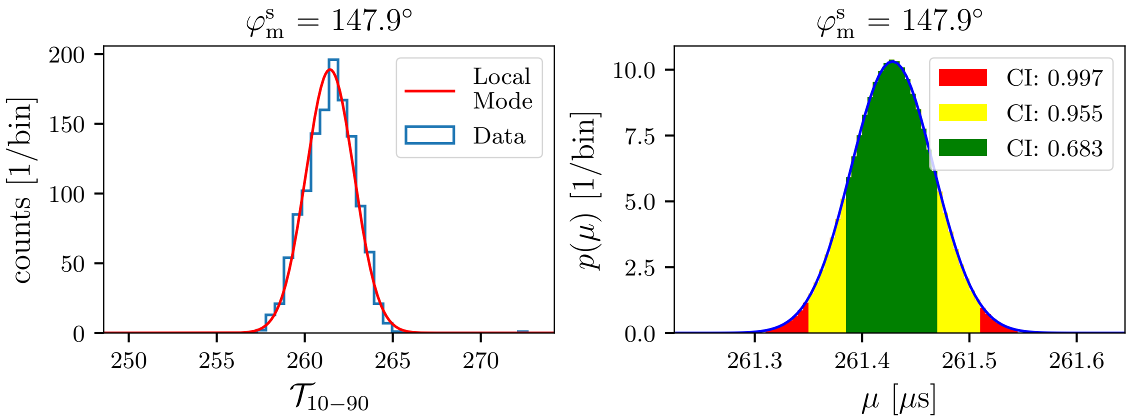

Figure 6.18.: Left: Histogram of $\mathcal{T}_{10-90}$ of all selected alpha events and a scaled normal distribution fitted to the histogram (red). Right: Marginalized posterior distribution of the μ parameter of the normal distribution fitted to the histogram on the left and the normal distribution fitted to the marginalized posterior distribution (blue).

where $\Delta\mathcal{T}_{10-90}$ is the amplitude of the oscillation, φ_{fa} is the position of the fast axis and $\mathcal{T}_{10-90}^{0}$ is the average rise time. The rise times and the modulation function with the local mode as parameters are shown in Fig. 6.19. The orientation of one of the fast axis was determined to be

$$\varphi_{\mathrm{fa}} = 45.4 \pm 1.0(\mathrm{sys}) \pm 1.4(\mathrm{stat})° \quad . \tag{6.13}$$

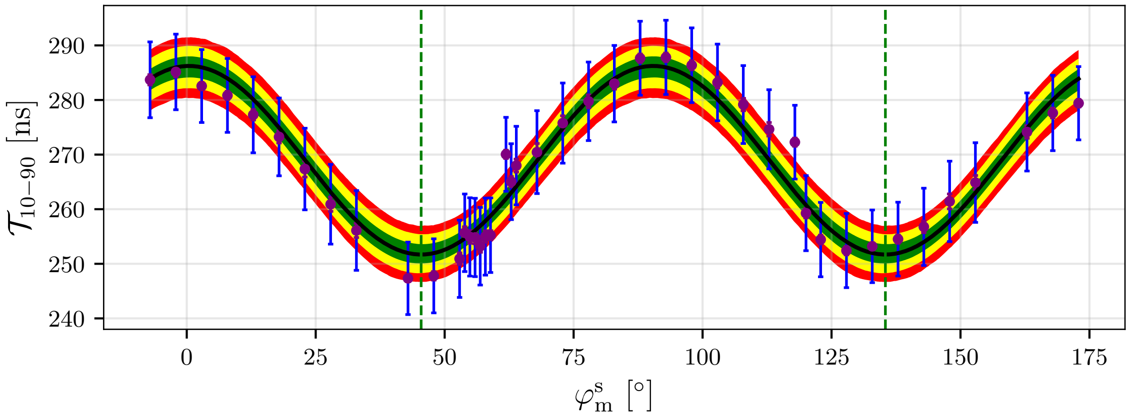

Figure 6.19.: Rise time $\mathcal{T}_{10-90}$ for all measurements of the scan SSAmRotMid (purple dots). The statistical uncertainty ranges are barely visible as they are very small. The assumed systematic uncertainty is shown in blue. The model function, Eq. 6.13, describing the oscillation of the rise time with the local mode as parameters is shown as a solid black line. The position of the fast axes are indicated in dashed green lines. The green, yellow and red areas show the 68.3%, 95.5% and 99.7% credibility intervals of the rise time.

6.6 Electronic Response of the Core Channel

In order to compare simulation to data, the response of the electronics has to be included in the simulation as discussed in Sec. 5.3. Another possibility would be to filter the effect of the electronic out of the data, but, for this thesis, the electronic response was folded into the simulated raw pulses.

GALATEA features a test input channel to the FET of the core channel, see Sec. 4.1.2. Rectangular pulses with different amplitudes, PGA, of 50 meV, 60 meV and 80 meV were fed into the core FET to obtain the electronic response of the core channel of Super Siegfried.

The energy spectra of the three measurements with the test pulses are shown in Fig. 6.20 a). Clearly visible are the peaks originating from these pulses. The different amplitudes of the pulses result in different reconstructed energies. The mean of all three peaks was determined through Gaussian fits, shown in the plots in Fig. 6.20 b), c) and d). These values were used to validate the voltage to energy linearity of the electronics, which is shown in Fig. 6.20 e).

For further analysis, pulses were selected by energy ($\pm 1\sigma$). These are shown in Fig. 6.21 a). The slowly rising pulses are background events, i.e. events induced by environmental radioactivity. These were removed by a cut based on their very different pulse shape. The remaining events are shown in Fig. 6.21 b). Three so-called superpulses were formed from these events. These superpulses are also shown in Fig. 6.21 b). A superpulse is the simple average of multiple individual pulses. This reduces the noise with respect to individual events.[2]

The superpulses were used to extract an electronic response function, which transforms rectangular pulses into the observed superpulses. The final filter is a combination of several "BiQuad" filters. The pre-ringing was achieved through one of those BiQuads being applied in reversed direction. A BiQuad filter is defined through 5 parameters b_0, b_1, b_2, a_1 and a_2. Through different combinations ot those parameters, the filter can be turned into common filters, such as low- or high-pass filters. The filters are applied on the pulse samples, $p(k)$:

$$p_f(k) = b_0 p(k) + b_1 p(k-1) + b_2 p(k-2) - a_1 p_f(k-1) - a_2 p_f(k-2) \quad , \tag{6.14}$$

where $p_f(k)$ is the filtered output. The extracted filter and the corresponding coefficients are given in Appx. B.

The determined filter output, as well as the input and one of the normalized superpulses are shown in Fig. 6.21 c).

---

[2] All core pulses in GALATEA were ringing during the relevant data taking period. The source could not be identified, an antenna effect is suspected. As the ringing was very regular, it does not hinder the analysis.

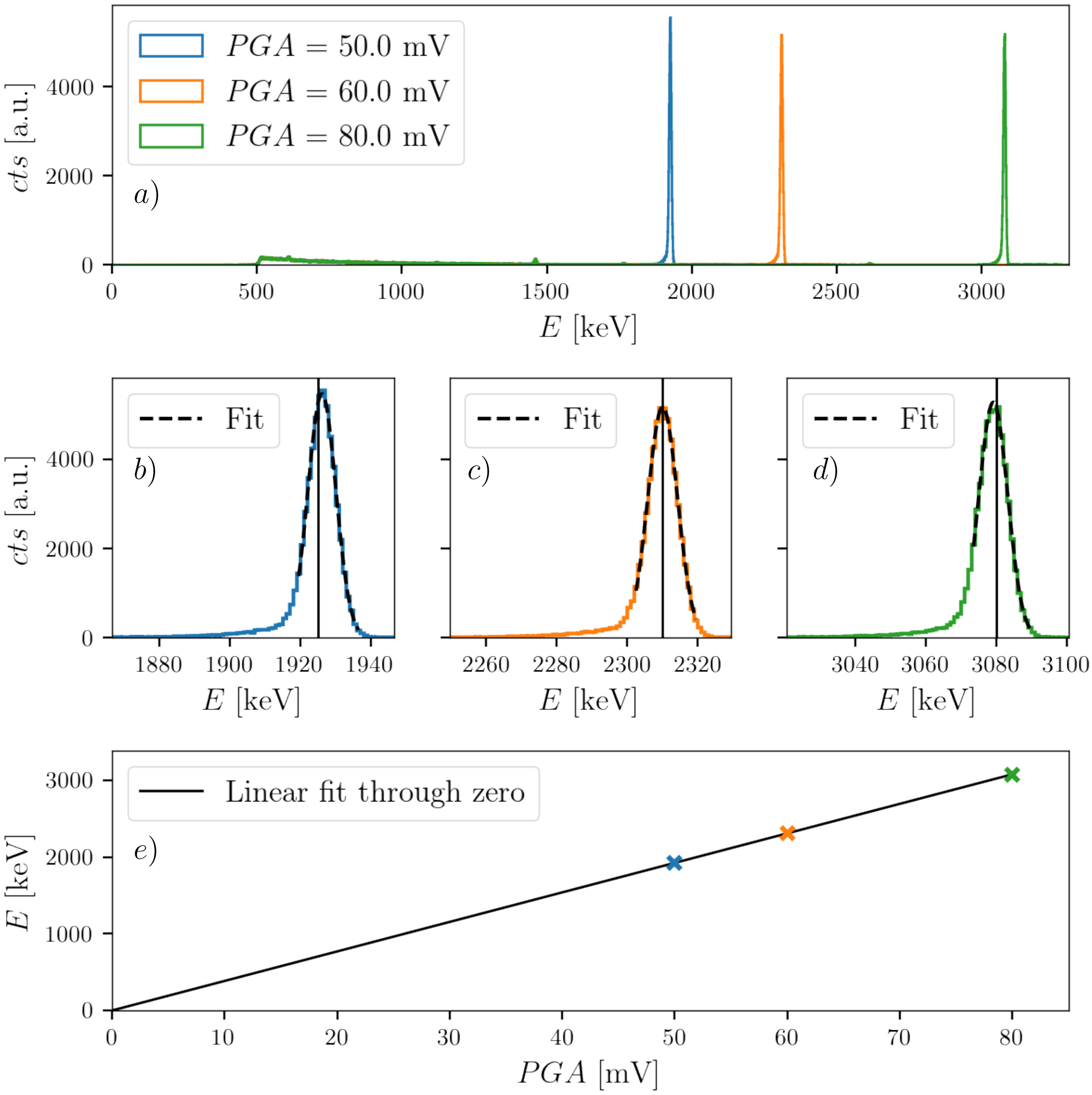

Figure 6.20.: (a): Energy spectra of the core for the 3 measurements with the test pulser. (b,c,d): Zoom onto the 3 peaks of the events from the test pulser. The black lines show the expected position of the peaks determined from the linear function fitted to the measured peak positions (mean of the Gaussians fitted to the individual peaks (dashed black lines)), which is shown in the bottom plot (e). The linear function is fixed to go through the origin. The uncertainties on the peak positions as obtained from the fits are to small too be seen.

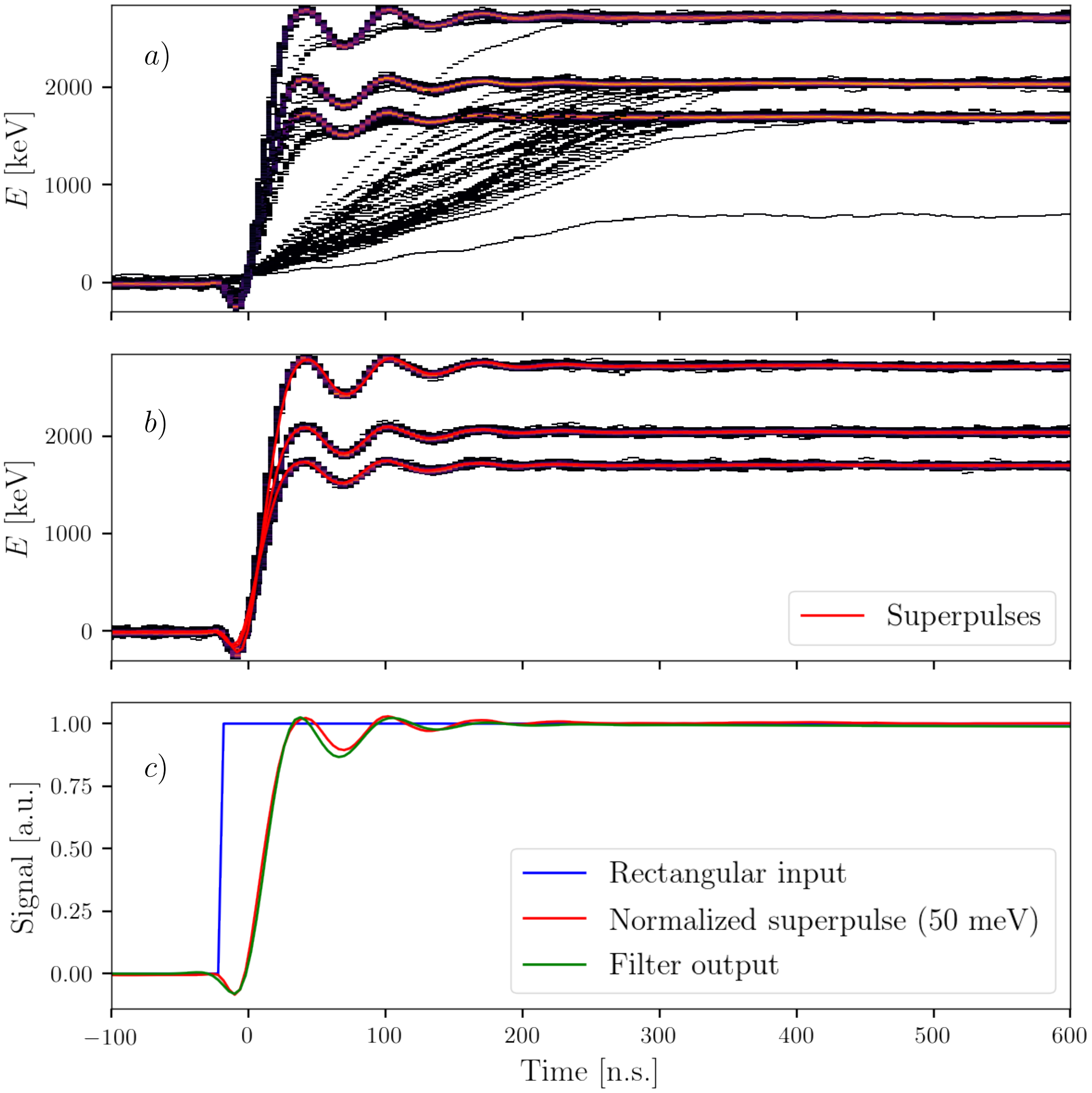

Figure 6.21.: (a): 2D-Histogram filled with the pulses in the $\pm1\sigma$ energy intervals around the three peaks in the energy histograms shown in Fig. 6.20 (b,c,d). (b): Pulses, which are used to form superpulses, also shown in red. (c): Normalized superpulse (red), rectangular input pulse (blue) and input pulse folded with the filter function (green).

6.7 Segment Response Function

The response functions of all segment channels were deduced from data, because it was not possible to feed test pulses into the segment channels[3]. This could only be done after fixing the impurity model and the drift parameters as described in the following sections. Here, it is assumed that the response functions for all segments are identical. This is justified as they have the same electronics as described in Sec. 4.1.2.

The superpulses of alphas entering from the side from two measurements of the scan SSAmRotMid, one measurement where the beam-spot of the alphas illuminated a fast crystal axis ($\varphi_\mathrm{m} = 137.9° \approx \langle 100 \rangle$) and one measurement where it illuminated a slow axis ($\varphi_\mathrm{m} = 92.9° \approx \langle 110 \rangle$), were used to model the electronic response of the segments by comparing the superpulses of the collecting segments to the simulated pulses. This is shown in Fig. 6.22.

It should be noted, that for both, data and simulations, the pulses are time aligned such that the 1 %-level of the core channel is at $t = 0\,\mathrm{ns}$, because the core channel triggers the DAQ. This explains the different start times of the simulated pulses and the data in Fig. 6.22 a), where no electronic response is applied to the segment pulses in the simulation.

A test was performed, where the electronic response function of the core was also used for the segments. The resulting simulated pulses are shown in Fig. 6.22 b). They, are closer to the data but still do not match well. Especially, no ringing is observed. This might be related to the different electronics between core and the segments, or the ringing might be caused through higher frequencies (fast rising pulses), or both.

Different combinations of BiQuad filter and parameter were tested to find an acceptable response function for the segments. The final response function for the segments applied to the simulated pulses is shown in Fig. 6.22 c). The exact filter and corresponding coefficients are provided in Appx. B. The response of the segments could not perfectly reproduced by an electronic response function. Most likely there are two reasons: First, in the simulation, the charge cloud is just a single point and no effects of diffusion and self-repulsion are taken into account.[4] Secondly, the electric response of the segments are slightly different in contrast to the assumption made at the beginning of this section.

Thus, in the future, the response functions for all segments should be determined individually by feeding test pulses directly into the channels as it was done for the core channel. However, this requires modifications of the electronic board of GALATEA.

---

[3] In order to do so changes of the connections inside GALATEA are needed for each channel and the measurement for each channel would take the time of a whole pumping-cooling and warming-up cycle, what is more than a week.

[4] These effects are currently under study and development in the SolidStateDetectors.jl package.

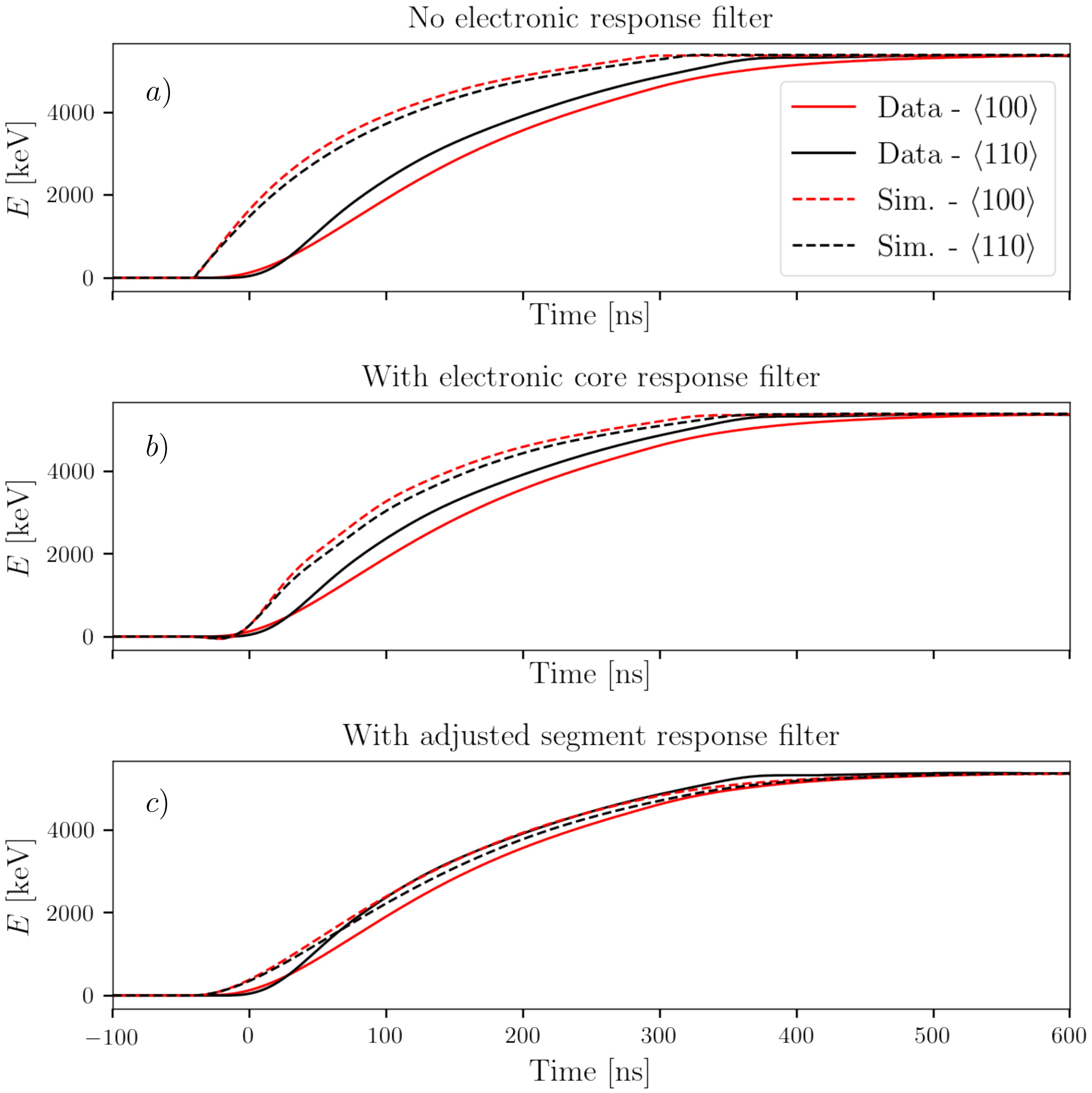

Figure 6.22.: Superpulses (solid lines) of the collecting segments of alpha events from two measurements along the ⟨100⟩ and ⟨110⟩ axes of the scan SSAmRotMid together with the respective simulated pulses (dashed lines). No electronic response (a), the electronic response function as determined for the core (b), final response function determined for the segments (c) folded into the simulated pulses.

6.8 Impurity Model

Besides the geometry of the detector and its environment, the impurity density profile of the germanium detector has to be defined in order to simulate its electric potential. As already mentioned in Sec. 3.0.1 and 3.0.2, there is a huge uncertainty on those profiles. In the case of Super Siegfried, only two values were provided by the manufacturer of the crystal. One value for the impurity density at the top plate and one value for the bottom of the detector:

$$N_{\text{top}} = 0.44 \times 10^{10}\,\text{cm}^{-3} \quad , \tag{6.15}$$
$$N_{\text{bot}} = 1.3 \times 10^{10}\,\text{cm}^{-3} \quad . \tag{6.16}$$

Between these two values, a linear profile in z is generally assumed, with no dependence on φ or r. However, it turned out that this simple profile cannot reflect reality. A detector simulation with this profile shows that the detector would not be fully depleted at its standard operation voltage. This is shown in Fig. 6.23, where the simulated depleted and undepleted regions are shown for the impurity profile as provided by the crystal manufacturer. In contrast, measurements of the capacity for different applied

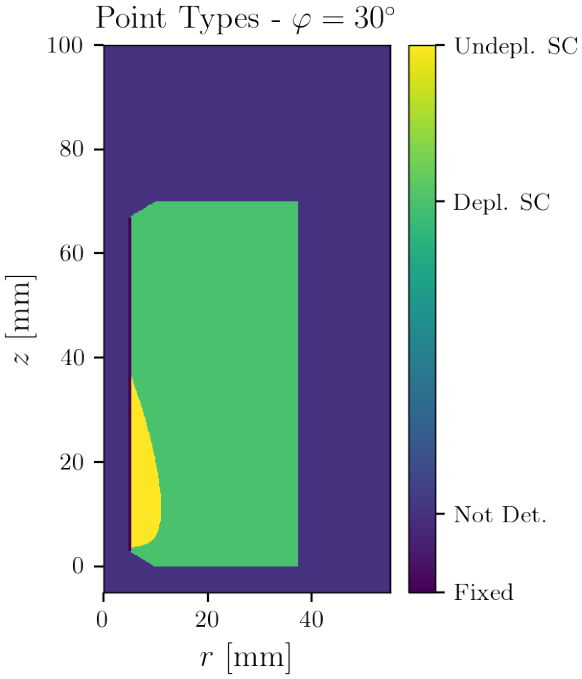

Figure 6.23.: Simulated point types as provided by SSD for Super Siegfried for the impurity profile provided by the crystal manufacturer at the operation voltage of 3000 V. The green area marks the depleted region of the semiconductor, whereas the yellow region marks the undepleted region.

bias voltages, performed by the detector manufacturer, confirm that the detector is already fully depleted at much lower voltages, e.g. around 2000 V. This capacity-vs-bias-voltage scan is depicted in Fig. 6.24. The operation voltage is usually defined a few hundreds volts above the voltage where the capacitance stabilizes. Thus, the operation voltage of Super Siegfried was set to be 3000 V. Also shown in Fig. 6.24 are simulated capacitances for three different assumptions on the impurity profile:

- Zero impurity profile: It assumes that there are no impurities. This yields the theoretical (lower) limit of the capacitance for a given detector geometry and environment. The results for all other impurity profiles have to converge towards this value with increasing bias voltage.
- Manufacturer impurity profile: Linear impurity profile in z according to N_{top} and N_{bot}.
- Scaled manufacturer impurity profile: The manufacturer profile scaled down by one factor, f_{imp}, determined by a fit with SSD.

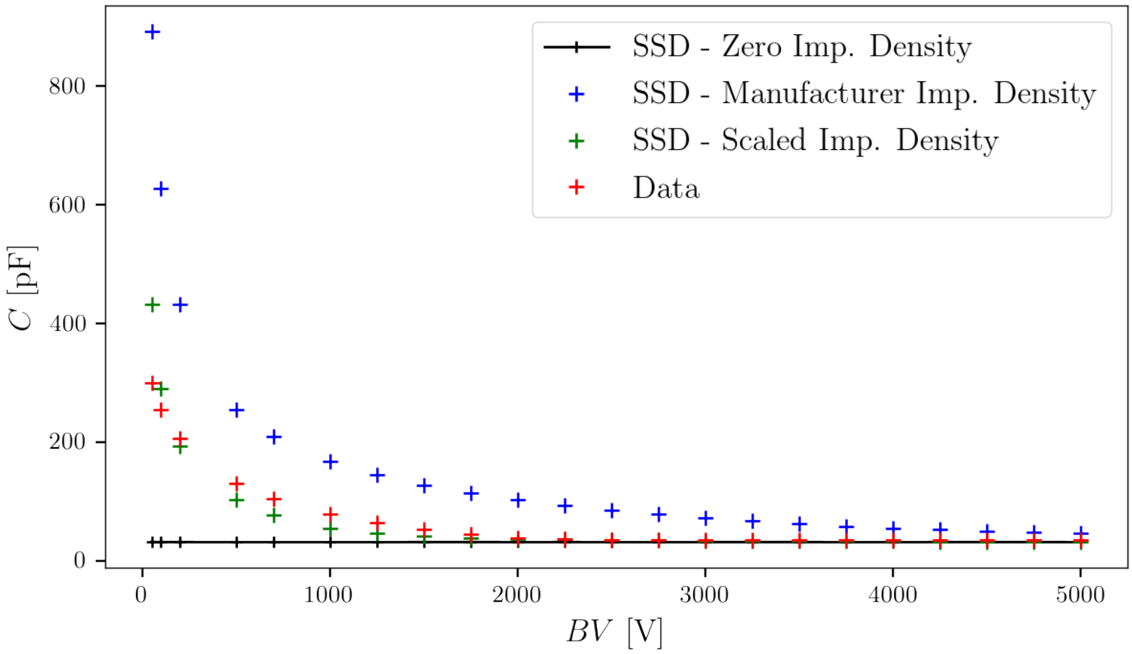

Figure 6.24.: Red: measured (by the detector manufacturer) detector capacitances for different bias voltages. Simulated capacitances for the zero impurity density (black), the impurity profile provided by the crystal manufacturer (blue) and the scaled impurity profile as optimized with SSD (green).

Scaling down the overall level of the profile by a factor f_{imp}, the simulated capacitances match the measured values much better. The scaled impurity density with $f_{\text{imp}} = 0.25$ (determined by an optimization fit) is the impurity profile used for all further simulations of Super Siegfried presented in this thesis.

6.8.1 Discussion on the Impurity Density Problem

The capacitance versus bias-voltage values were provided by the manufacturer without uncertainties. In addition, the procedure how exactly the capacitances were measured as well as the environment in which the capacitances were measured are unknown. Certainly, the environment was different than what was implemented in the simulation (the GALATEA setup).

In addition, the impurity models (except the zero density profile), violate the charge neutrality, Eq. 2.17, within the depleted region of a diode, as no p-type region was assumed. Thus, the distribution used as the source term in Gauss Law', right side of Eq. 2.14, is fundamentally wrong. Even though the p-type region (layer) is very thin, in case of n-type germanium detectors, its absolute values are compensatingly high and, thus, have an impact on the electric potential.

At the time of writing, a new dedicated test setup was under construction at the Max-Planck-Institute for Physics to measure the capacitance of detectors for different bias voltages in a known environment. Together with new improvements implemented in SSD, which is now capable to also simulate thin p-type layers, improved studies of the impurity profile of germanium detectors are going to be performed. In addition, a new Compton scanner at the Max-Planck-Institute for Physics [86], which is basically some kind of CT / PET scanner for germanium detectors, allows the determination (imaging) of the depleted volume of a detector for different bias voltages as it can determine the position of events inside the germanium detector. Comparisons between measured and simulated volumes will provide more input to the determination of more realistic impurity profiles.

6.9 Parameters of the Drift Model

The drift model used in the simulation was already introduced in Sec. 3.2.1. There, it was also stated that the parameters of the model have to be determined for each detector as the total mobility is influenced by the (not only electrically active) impurities.

The pulses of alpha events on the surface of the mantle are only generated by the drift of the electrons towards the inner borehole as the holes are basically immediately collected and do not contribute to the pulses. Thus, these events are ideal to determine the electron drift parameters. In order to determine the hole drift parameters one would need events at the inner borehole where the electrons are directly collected and the holes drift towards the mantle. However, such measurements were not yet done and, thus, the parameters given in [58, 59] were used as the parameters of the hole drift.

The two measurements of the rotational scan SSAmRotMid at $\varphi_\mathrm{m} = 137.9° \approx \langle 100 \rangle$ and $\varphi_\mathrm{m} = 92.9° \approx \langle 110 \rangle$ were also used to determine the electron drift parameters. The z-coordinate of the beam-spot was $z = 40.0\,\mathrm{mm}$, ensuring a drift far enough from the end plates of the detector and, thus, avoiding surface effects.

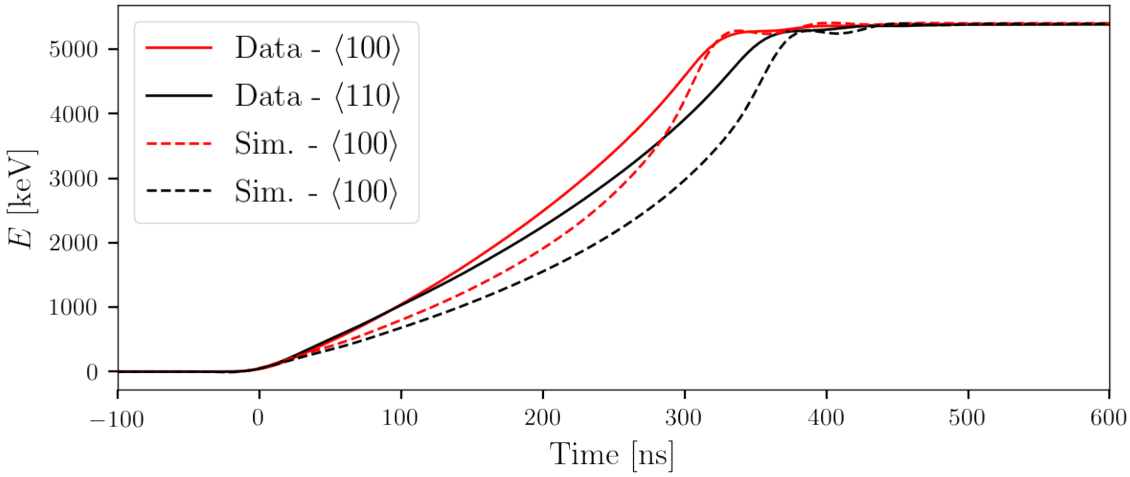

Figure 6.25.: Superpulses (solid lines) of the core channel for alpha events from two measurements on the ⟨100⟩ and ⟨110⟩ axes of the scan SSAmRotMid. The respective simulated pulses, using the electron drift parameter of [58, 59], are shown with dashed lines.

For both measurements, alpha events were selected by energy and superpulses were formed for all channels. The two superpulses of the core channel are shown in Fig. 6.25 together with simulated pulses using the drift parameters of [58, 59]. It is clearly visible that the simulation does not match the data well. By adjusting the electron drift parameters by eye, the simulated pulses become closer to the superpulses as shown in Fig. 6.26. However, they seem to be to fast at the end (close to the inner borehole). Figure 6.27 shows the simulated electric field strength and the absolute value of the electron drift velocities vs r for the drift parameters of [58, 59]. Figure 6.28 shows the simulated electric field strength and the absolute value of the electron drift velocities vs r for the drift parameters adjusted by eye. The predicted electric field strength increases towards the inner borehole. This is expected for the coaxial geometry of the detector. However, the superpulses indicate a decreasing drift velocity near the core. The adjusted parameters indicate, see Fig. 6.28, that the maximal possible velocity is reached over most of the bulk, see Fig. 6.28. Within the drift model, it is not possible to decrease the velocity further for increasing electric field strengths. Thus, the terminal velocity across the detector, described through the adjusted parameters, is the closest solution. The adjusted parameters are given in App. C.

In order to slow down the drift near the core, a virtual volume, a tube with a radius of 1.5 cm (thus, starting 1 cm beyond the borehole), was added to the simulation in which the drift is modulated (decreased) linearly down to 40 % of its original value at the inner borehole. This is equivalent to assuming additional impurities in this volume [53]. The resulting simulated pulses are shown in Fig. 6.29. The resulting simulation describes the data very well. This drift modulation is present in all further simulation presented in this thesis.

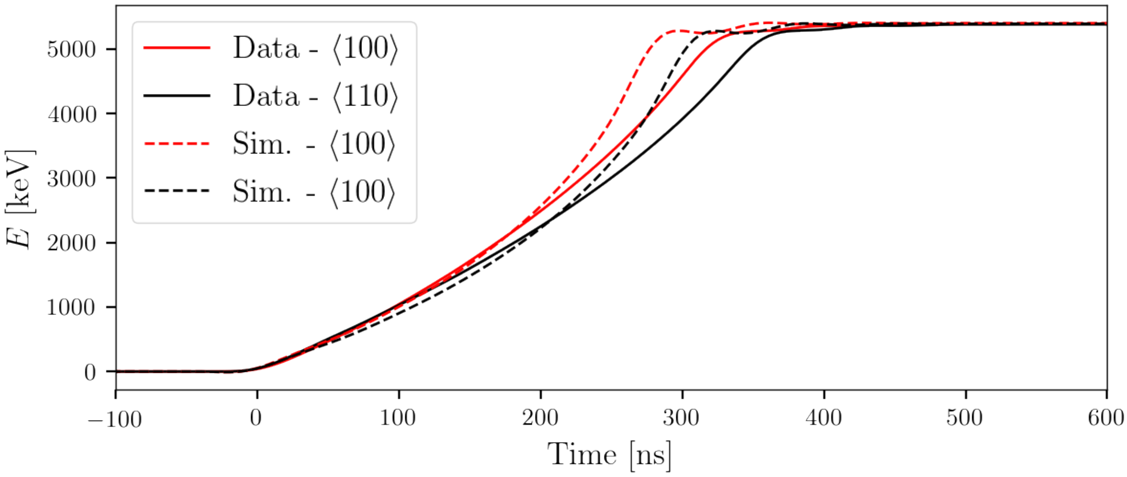

Figure 6.26.: Superpulse (solid lines) of the core channel of alpha events from two measurements of the scan SSAmRotMid. The respective simulated pulses, using adjusted (see text) electron drift parameter, are shown as dashed lines.

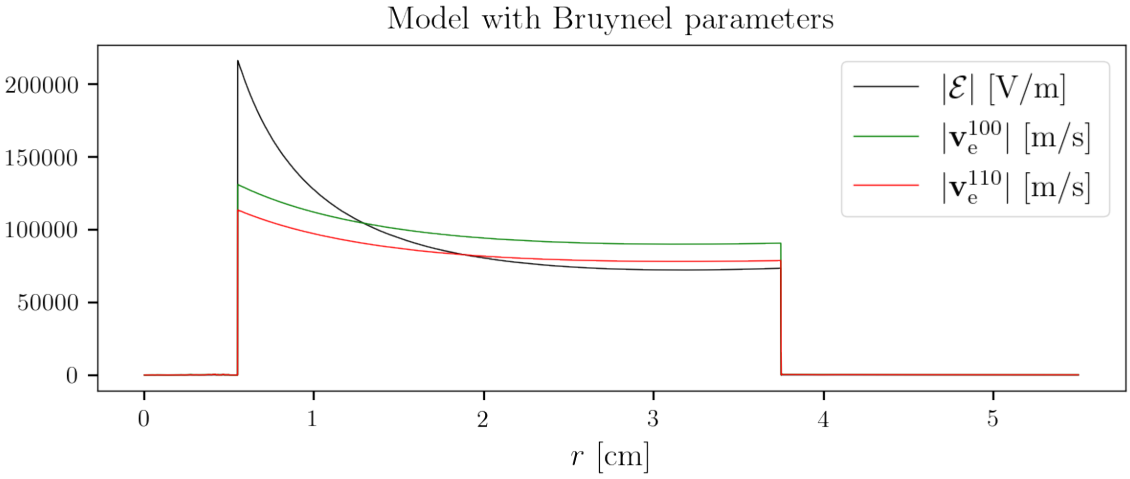

Figure 6.27.: Electric field strength and the absolute electron velocity along the fast and slow axes versus r. The drift parameters of [58, 59] were used for the calculations of the velocities.

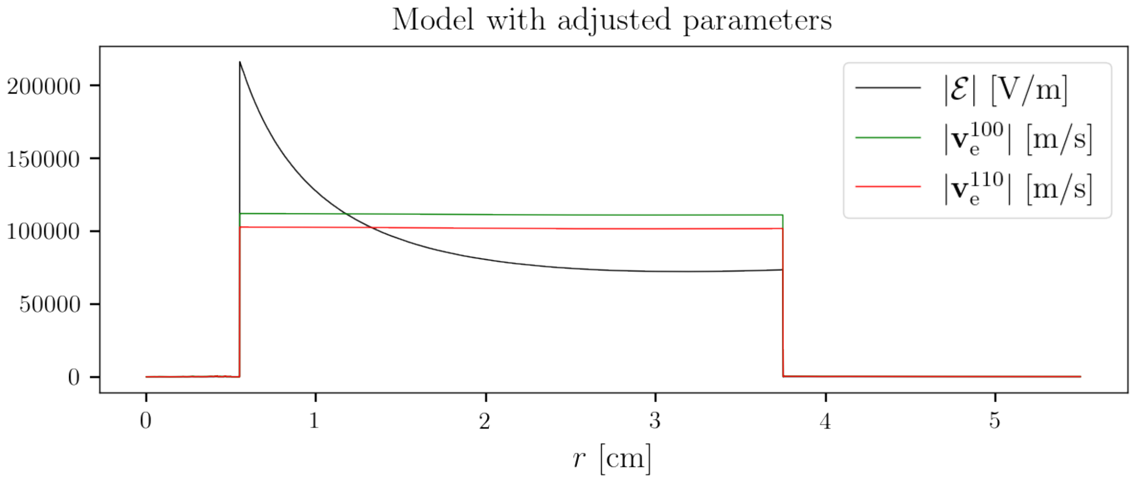

Figure 6.28.: Electric field strength and the absolute electron velocity along the fast and slow axes versus r. The adjusted (see text) electron drift parameters were used for the calculations of the velocities.

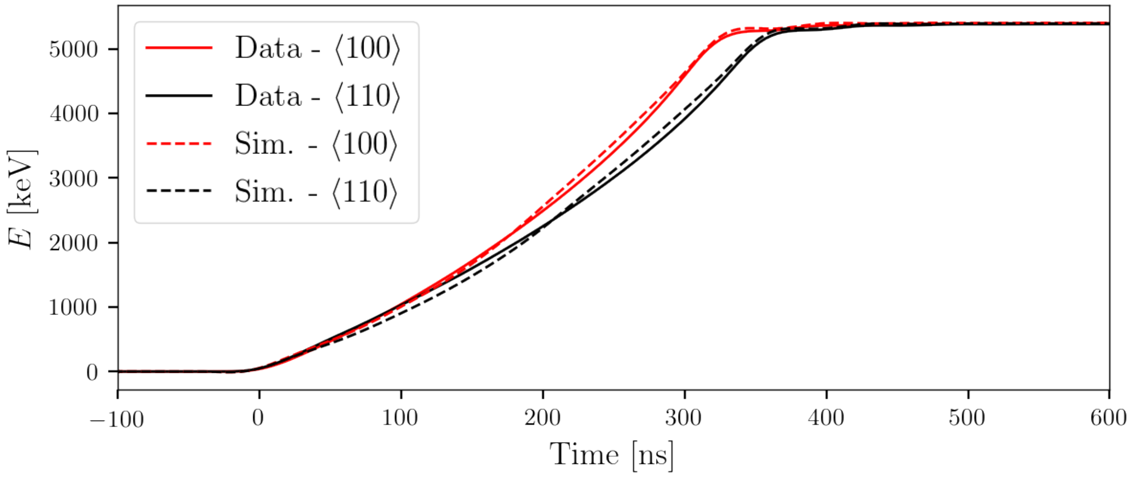

Figure 6.29.: Superpulse (solid lines) of the core channel of alpha events from two measurements of the scan SSAmRotMid. The respective simulated pulses, using adjusted electron drift parameter as well as the drift modulation at lower r, are shown as dashed lines.

In addition, at all other beam-spot positions of the scan SSAmRotMid events were simulated and their rise times $\mathcal{T}_{10-90}$ were determined. These simulated rise times, together with the already determined rise times from the superpulses, see Sec. 6.5, are shown in Fig. 6.30. The amplitude of the oscillation of the rise time is smaller in the simulation than in data. However, this difference is only about 10 ns, which corresponds to two to three pulse samples. Figure 6.29 shows, that, especially along the slow axis, the simulated pulses are a bit to slow at the beginning and a bit to fast at the end, which leads to a slightly decreased (faster) rise time in agreement with the smaller oscillation amplitude.

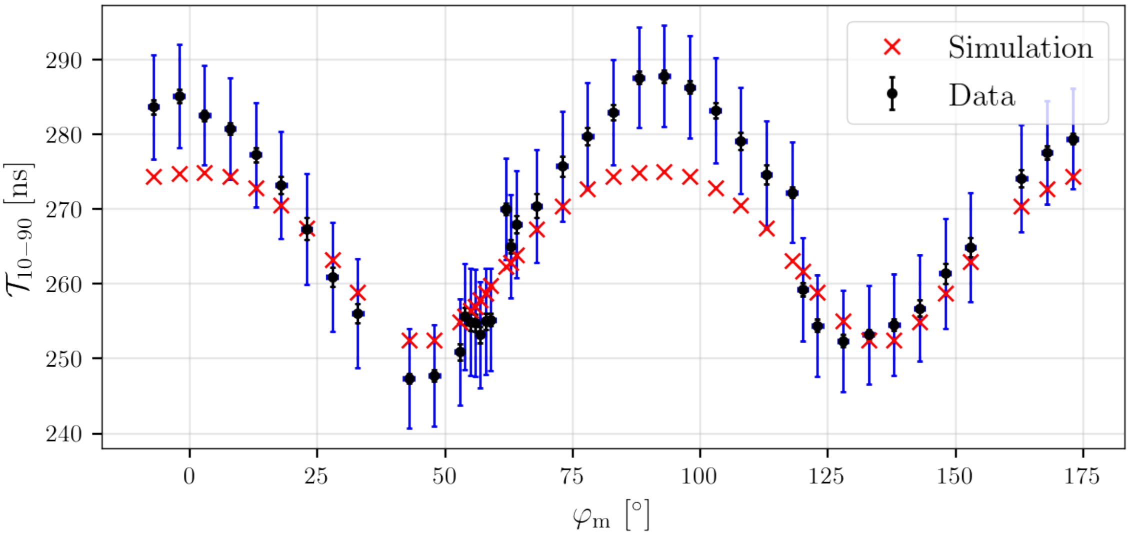

Figure 6.30.: Simulated and measured rise-times in the core channel of events induced by alphas entering from the side from the scan SSAmRotMid.

Possible Reasons for the Drift Modulation

The reason for the observed slow down of charge carriers close to the central borehole is unclear. It could be related to the electrical active impurity profile as this is important for the electric field. However, as the already saturated drift velocity is not enough, the slow down is probably caused by something else, which influences the mobility tensor, see Sec. 2.4, like neutral impurities [53].

It might also have something to do with the Li-drifted n^+-contact. In order to investigate this further, it would be beneficial to irradiate the volume close to the borehole and study events created close to core contact. However, this requires difficult modifications of the GALATEA setup or the detector holder for placing a radioactive source in the borehole of the detector. As an alternative, the already mentioned Compton scanner setup [86] might be used for such studies.

Another possible reason might be the effects of finite charge clouds, see Sec. 2.7.3. In the presented simulation, the electrons and holes were treated as singularities. However, this does not describe reality. The charge carriers are distributed over a volume. This alone, leads to slightly different pulses as the weighting potentials change also over that volume. In addition, the charge cloud distribution changes during the drift. There are three effects which lead to a deformation of the charge carrier distribution and (may) have to be considered:

- Spreaded charge cloud: Individual charge carriers of the charge cloud experience a different electric field due to their different positions.
- Diffusion: The ensemble of charge carriers diffuses over time.
- Self-repulsion: The charge carriers experience an additional electric field created by all other charge carriers of the cloud.

At the time of writing these effects are being implemented and studied in SSD. However, as they are preliminary, they are not part of the simulations presented in this thesis.

Chapter 7: Response to Alphas and Gammas on the Passivated Top Plates

Energy depositions from alpha decays at the surface of detectors made up a large part of the backgrounds in the GERDA and MAJORANA experiments, see Sec. 1.5.1. Even though a parameter was found to identify most of those alpha events for some of the detectors, it is necessary to further study those events. In addition, a better understanding of the physics of germanium detectors at their surfaces, especially passivated surfaces, will help to find new techniques to identify alphas and design new detectors with better background identification capabilities. The important issues are the determination of the precise fiducial volume and mass of the individual detectors and the efficiency of background reduction techniques.

In this chapter, the response of Super Siegfried and Siegfried III to alphas and, for comparison, to low-energy gammas, both originating from ^{241}Am, are presented.

7.1 Geant-4 Simulation of Americium

A Geant-4 simulation, see 5.1, of the irradiation of the Super Siegfried detector with the ^{241}Am source inside the top collimator of GALATEA was performed. The beam-spot on the top surface was simulated for $r = 20\,\mathrm{mm}$. The $2\,\mu$m thick silicon dioxide passivation layer of Super Siegfried was included in the detector simulation as an inactive volume.

The spectra, normalized to an integral of one, are shown in Fig. 7.1 for the two important energy windows. They are a measure for the probability, p, of a particle emitted by the source to be observed with a certain energy. Figure 7.1 *a*) shows that the passivation layer has no impact on the low energy gammas as they have the full energy of Q_{γ}^{Np}. The alphas, however, are impacted by the passivation layer as shown in Fig. 7.1 *b*). They are expected to deposit $\approx 320\,\mathrm{keV}$ of their energy inside the inactive passivation layer. Also shown in Fig. 7.1 *b*), for comparison, is the observed core energy spectrum as measured on the side surface of Super Siegfried with the second, identical, ^{241}Am source. There, the alphas deposited about $\approx 95\,\mathrm{keV}$ inside the inactive layer of the p^{+} implantation. The stopping power for alphas in germanium at 5.44 MeV is [87]

$$S_{\mathrm{Ge}}^{\alpha}(5.44\,\mathrm{MeV}) = 383.3\,\mathrm{cm}^2\mathrm{MeV/g} \qquad . \tag{7.1}$$

With the density of germanium of $\approx 5.3\,\mathrm{g/cm}^3$, the energy loss of $\approx 95\,\mathrm{keV}$ translates

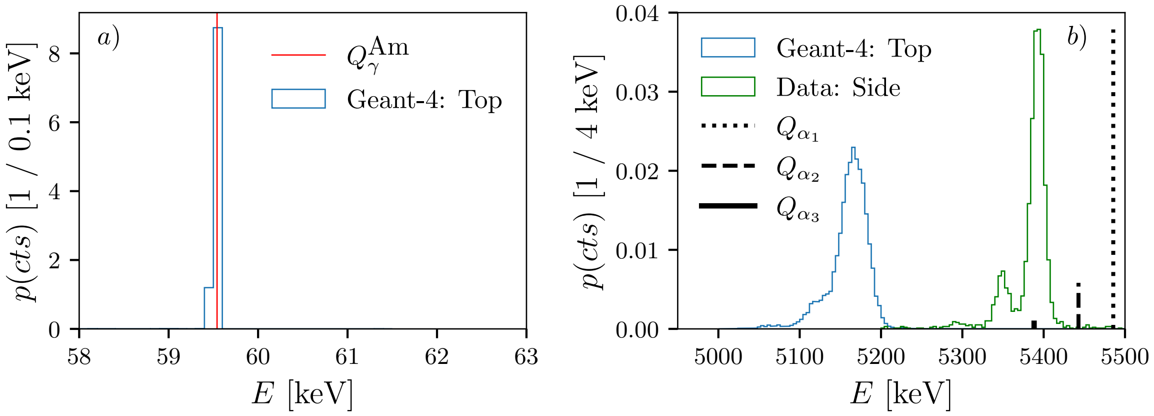

Figure 7.1.: Expected energy spectrum of Super Siegfried as simulated for the ^{241}Am source inside the top collimator of GALATEA. a): low-energy gamma line, b): high-energy alpha lines. The emitted lines are shown as black vertical lines with heights representing the branching ratios. The spectra of simulated energy depositions are shown in blue, whereas the core energy spectrum obtained from a measurement, where the side of the detector was irradiated, is shown in green.

into a thickness of the inactive (conductive) boron implementation layer of

$$d_{p^+} \approx 0.5\,\mu\mathrm{m} \qquad , \tag{7.2}$$

which is in agreement with information provided by the detector manufacturer.

The simulated energy-weighted hit distributions are shown in Fig. 7.2. They are a measure for the probability, p, for a particle emitted by the source to deposit energy in a certain volume. To first approximation, the distributions look normally distributed. Also visible, especially for the alphas, is the additional collimating effect of the slit of the IR shield surrounding the detector in GALATEA.

The energy-weighted hit distribution in x and z for the gammas is shown in Fig. 7.3 a), whereas the energy loss of the alphas in germanium is shown in Fig. 7.3 b). The distribution of the energy loss of alphas was not simulated with Geant-4, but was calculated using the stopping powers for alphas in germanium as listed in the ASTAR database [87]. The initial energy of the alphas at $z = 0\,\mu$m was set to the mean of the most dominant alpha peak in the simulated energy spectrum shown in Fig. 7.1 *b*), i.e., $\approx 5165\,$keV. The energy loss distribution shows a typical Bragg peak and the maximal penetration depth of alphas of this energy in germanium is $\approx 17\,\mu$m.

The simulations predict that alphas from the top source (top-alphas) deposit around 5 MeV of energy. However, the observed energy of alphas, E_α^{obs}, is further reduced as shown in Fig. 7.4, depicting a typical spectrum. At this position of the top beam-spot, $(\varphi_{\mathrm{m}}^{\mathrm{t}} = 92.9°, r_{\mathrm{m}} = 23.8\,\mathrm{mm})$, E_α^{obs} is reduced to $\approx 2.6\,$MeV and even below. This demonstrates the danger of alpha decays on the surfaces of germanium detectors to

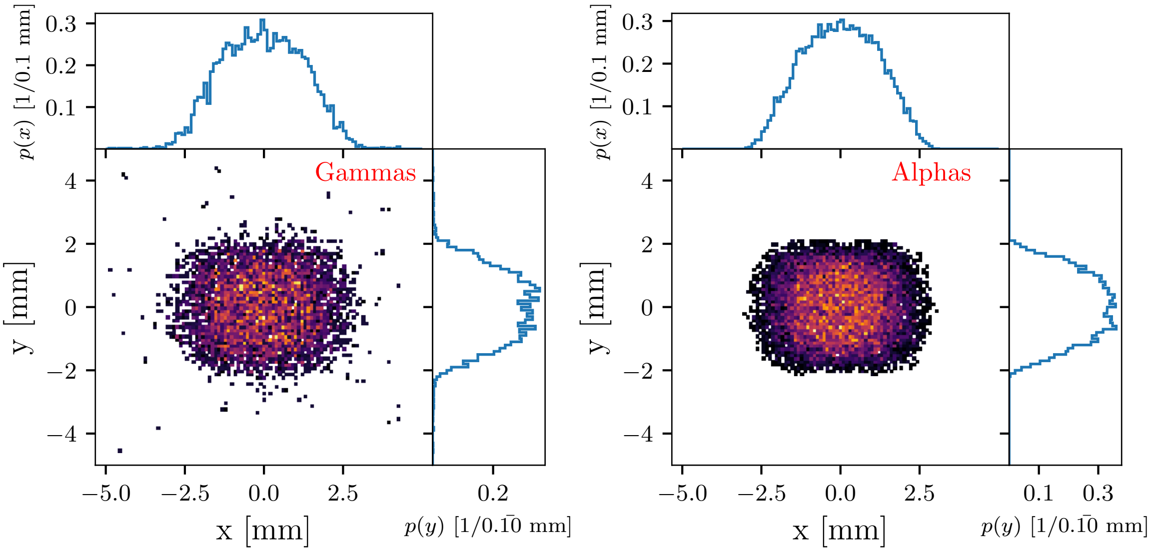

Figure 7.2.: Simulated energy-weighted hit distributions in x and y induced by gammas (left) and alphas (right) from the collimated ^{241}Am source on top of the detector. The coordinate system is chosen such that the hits are centered around (0 mm,0 mm) and the x-axis (y-axis) corresponds to the radial (polar) direction.

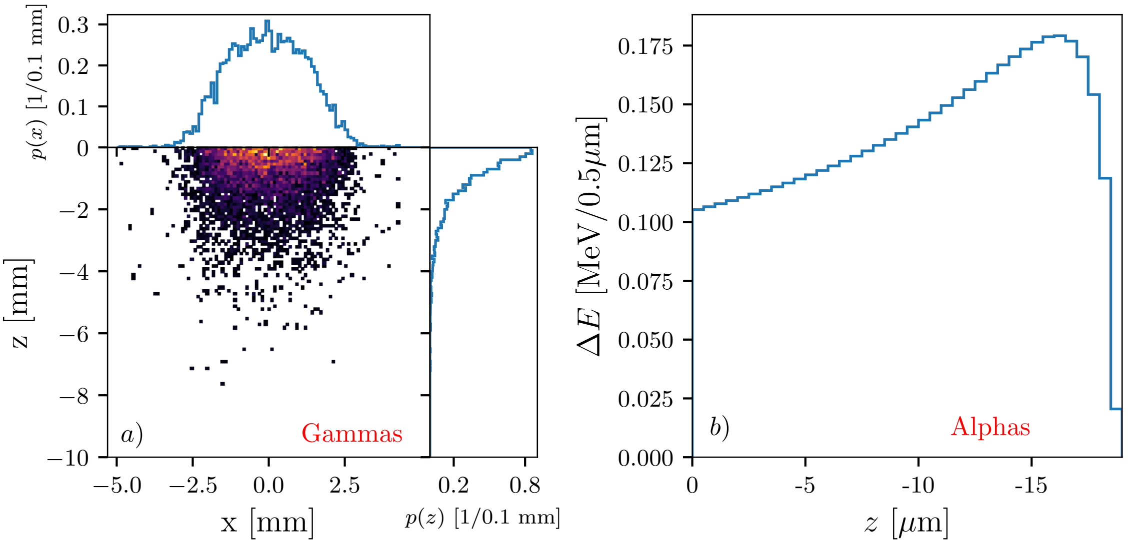

Figure 7.3.: a): Simulated energy-weighted hit distributions in x and z induced by gammas. b): Calculated energy loss, ΔE, of alphas in germanium. The coordinate system is chosen such that the hits are centered around (0 mm,0 mm) and the x-axis corresponds to the radial direction. The detector top surface is chosen as the origin of the z-axis. The passivation layer is in positive z and hits there are not shown. Note the two different units for z: mm for gammas and μm for alphas.

$0\nu\beta\beta$ experiments. E_α^{obs} is reduced from the Q-value and can fall into the signal region around $Q_{\beta\beta}$ and, as the event is a single-site event, can be misidentified as a $0\nu\beta\beta$ event.

The reduction of E_α^{obs} also prohibits the selection of alpha-induced events by energy only, since the Compton background becomes too large in this energy region. Thus, other selection criteria had to be developed, which will later also help to reduce the background in $0\nu\beta\beta$ experiments.

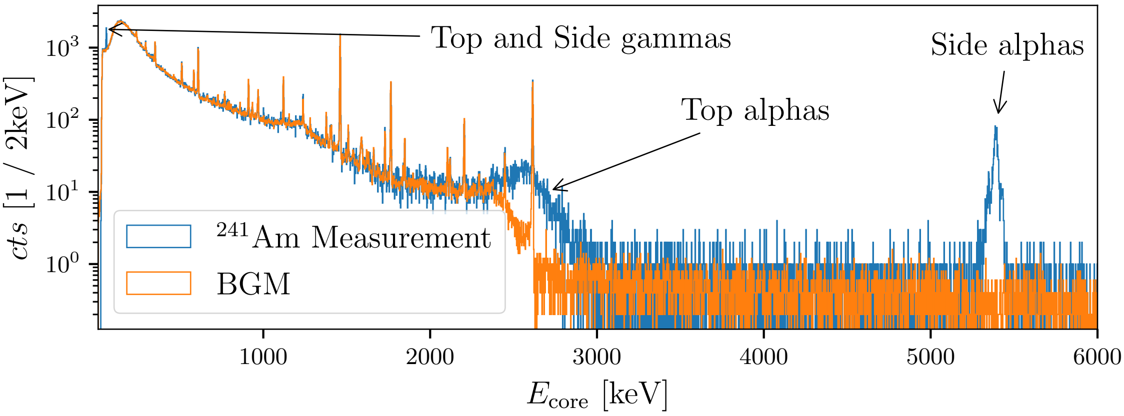

Figure 7.4.: Core energy spectra of the background measurement BGM (orange) and a typical ^{241}Am measurement from the scan SSAmRotMid with the top beam-spot at ($\varphi_{\mathrm{m}}^{\mathrm{t}} = 92.9°, r_{\mathrm{m}} = 23.8\,\mathrm{mm}$) and the side beam-spot at ($\varphi_{\mathrm{m}}^{\mathrm{s}} = 2.9°, z_{\mathrm{m}} = 40.0\,\mathrm{mm}$). The spectrum of the background measurement is normalized in time to the ^{241}Am measurement.

7.2 Selection of Top-Alpha Events

In order to select events induced by alphas from the top source and discriminate them against background events, two cuts were defined. For both cuts, the collecting segment, $i = cs$, was chosen according to the position of the top beam-spot. In the case of the selection of events in Super Siegfried, which were induced by alphas from the top source, the collecting segment was always the top segment, $cs = 19$.

7.2.1 Soft Single Segment Cut

The first cut is based on the information provided by the segmentation of Super Siegfried and Siegfried III.

Alpha events are single-site events. Thus, only one segment should be a collecting segment and the energy recorded in it, E_{cs}, should be equal to the energy recorded in the core, whereas no energy should be recorded in all other segments. However, as alpha events can be affected by charge trapping the usual (strong) single-segment condition, $E_{cs} = E_{\text{core}}$, can not be used, because trapped charges still induce signals in all channels based on the strength of the respective weighting potential, leading to a difference between the observed energies E_{cs} and E_{core}. Fortunately, charge trapping also leads to characteristic pulse shapes in the neighbouring segments. After reaching the maximum pulse amplitude, MPA_{seg}, during the drift, the pulses of these non-collecting

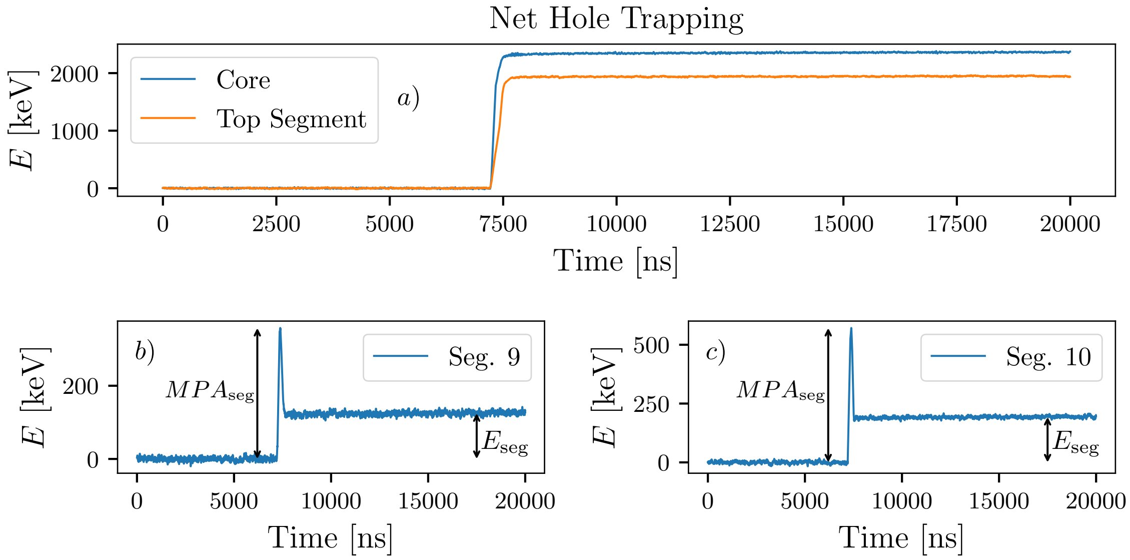

Figure 7.5.: Pulses of the (a) core and top segment and the two segments (b) 9 and (c) 10 of an event with net hole trapping from scan SSAmRad181 at $r_{\text{m}} = 18.8\,\text{mm}$. The segments 9 and 10 are the two segments underneath the top segment closest to the position of the event.

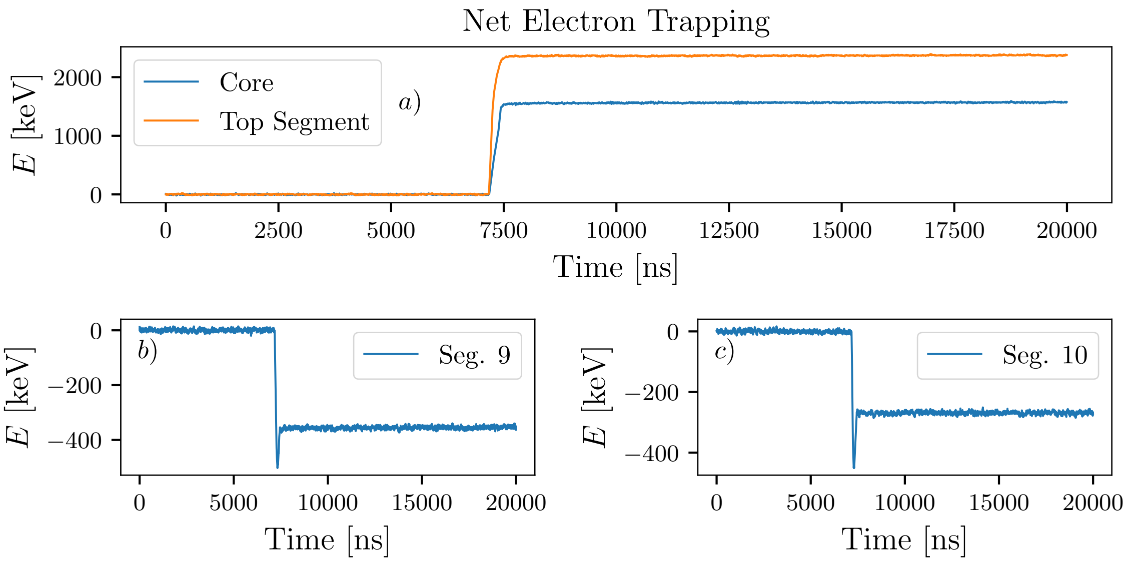

Figure 7.6.: Pulses of the (a) core and top segment and the two segments (b) 9 and (c) 10 of an event with net electron trapping from scan SSAmRad181 at $r_\mathrm{m} = 32.8\,\mathrm{mm}$. The segments 9 and 10 are the two segments underneath the top segment closest to the position of the event.

segments do not return completely to the baseline, but a collection of charge is mimicked as an observed energy E_seg. Such pulses are called truncated mirror pulses. This scenario is shown in Fig. 7.5 for an event with net hole trapping and in Fig. 7.6 for an event with net electron trapping.

Thus, a modified single segment cut had to be applied in order to select all events induced by alphas: Since the weighting potential of the collecting segment is usually the strongest weighting potential along the drift trajectory, the collecting segment should still record the highest energy of all segments for single-site events, even if the event is affected by charge trapping. Therefore, the first cut was defined such that the recorded energy of the collecting segment of an event has to be larger than the sum of the energies recorded in the other segments,

$$E_{cs} > \sum_{i>0, i\neq cs} E_i \quad . \tag{7.3}$$

This cut is referred to as the soft single segment cut, S-cut, throughout this thesis.

7.2.2 Delayed Charge Recovery Cut

The second cut is based on the shape of the tail of the pulses recorded in the core and the collecting segment. This powerful technique to identify alpha events on certain passivated surfaces [88, 89, 90] is based on the feature that the tail slope is non-zero as shown in Fig. 7.7[1]. Small amounts of charge carriers are still drifting long after most of the charge carriers are collected on the electrodes.

There are two possible explanations for the non-zero tail slope:

- Charge carriers are trapped during the drift and are in part slowly released, causing a delayed increase of the signal tail.
- A very low mobility very close to the surface causes the charge carriers at different positions inside the charge cloud to drift with different velocities. The carriers very close to the surface would be very slow and, thus, would drift much longer. This would also explain the non-zero tail slope.

The first explanation would a priori result in a step-like signal. However, this depends on the amount and time scale of the trapping and releasing. Thus, also the observed continuous increase could be modeled and explained. A combination of both phenomena is likely.

The positive tail-slope leads to an increased decay constant of the raw pulses, see Sec. 6.2. Thus, the second cut, the τ-cut, is defined such that only events, for which the decay constants of the core, τ_{core}, and the collecting segment, τ_{cs}, are within a certain range, are selected. The decay constant ranges, $\Delta\tau_{\text{core}}$ and $\Delta\tau_{cs}$, are determined for each measurement. This is demonstrated in Fig. 7.8. After the application of the S-cut, second peaks become visible in the distributions of the decay constants of the core and the collecting segment. These peaks are fitted with a Gaussian on top of a linear background. The $\pm 1\sigma$ intervals around the peaks are taken as the selection ranges for the core and collecting segment. The τ-cut is always used in combination with the S-cut

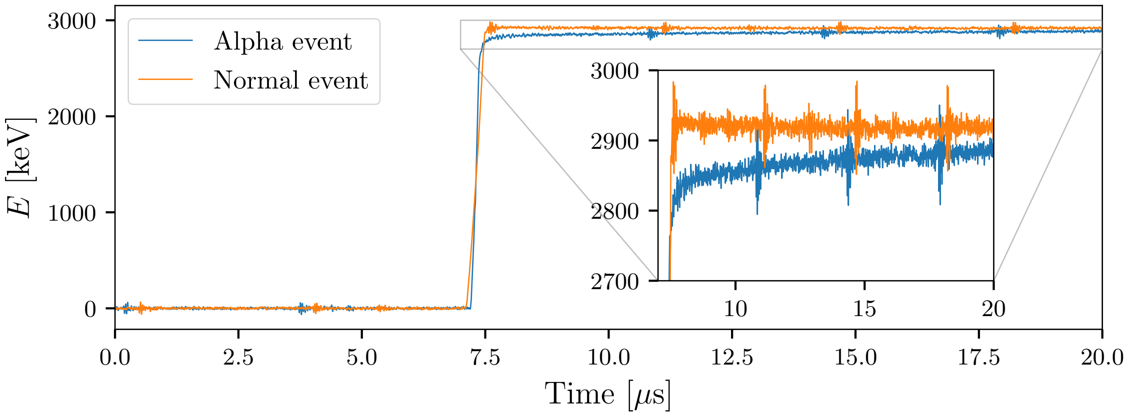

Figure 7.7.: Pulses of the core channel of an alpha event (blue) on the surface and a gamma event (orange). The inset shows a zoom into the tail of the pulses, showing the non-zero tail slope for the alpha event.

---

[1] A clear periodic ($\approx 4\,\mu$s) noise on the core pulses was present during most of the measurements taken for this thesis. It is most likely due to some ground loop present in GALATEA, which could not be eliminated. However, the regularity of the noise makes it negligible for the analysis of the pulses.

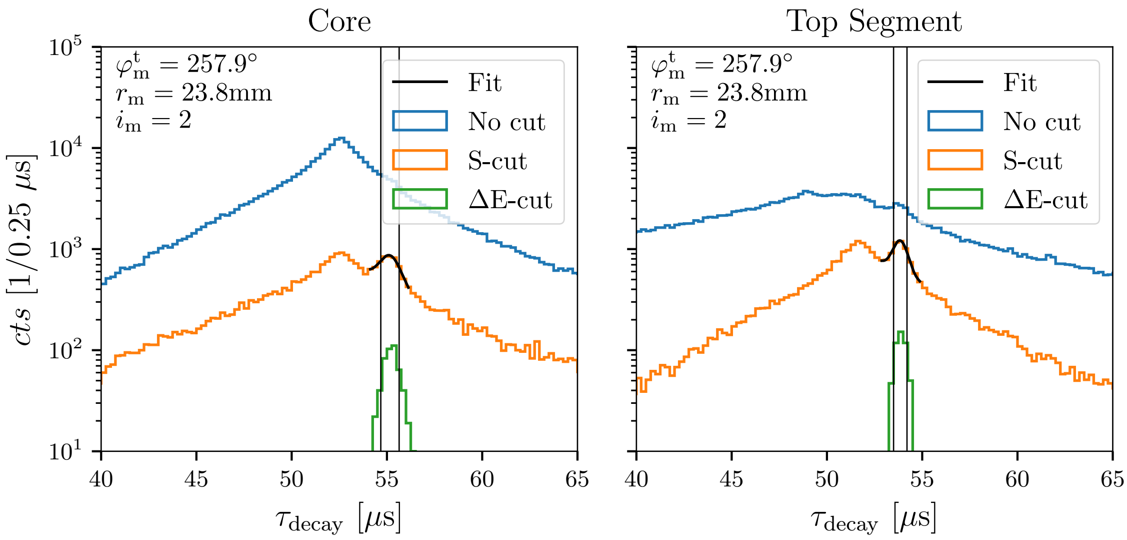

Figure 7.8.: Distributions of the pulse decay-constants of the core (left) and of the top segment (right) from the scan SSAmRotMid at ($r_{\rm m} = 23.8\,$mm$, \varphi^{\rm t}_{\rm m} = 257.9°$) before and after application of the S-cut. The peaks emerging after the S-cut are fitted with Gaussians on top of linear backgrounds. The $\pm 1\sigma$ ranges around the second peaks are indicated with vertical lines and provide the ranges for the τ-cut. A selection based on $E^{\rm obs}_{\alpha}$, see Fig. 7.9, is also shown.

throughout this thesis. This is labeled as Sτ-cut.

The energy spectra before and after the application of the cuts for a typical measurement from the scan SSAmRotMid and the background measurement BGM are shown in Fig. 7.9. The core and the segment spectra feature broad peaks with reduced energies around 3000 keV, with slightly more energy observed in the segment. The core spectrum before segment-19 specific cuts also features a narrow peak above 5 MeV corresponding to the alpha events on the side (side-alphas) of the detector. The background above 3 MeV in the two spectra without cuts on the top segment originates from saturation events, induced by high-energetic particles, e.g. cosmic muons. They deposit more than 11 MeV in the detector. This is the maximum detectable energy of the DAQ in GALATEA[2]. The deposited energy is divided between multiple segments, forming a continuous background in the segments. In the core, these saturation events are not visible in Fig. 7.9 as they form a peak at 11 MeV and the spectrum is only shown up to 6 MeV. The broad alpha "peaks" survive both cuts, whereas the background is reduced by about two orders of magnitude. The remaining events with observed energies $< 1000\,$keV are low-energy single-segment gamma events. The relative size of the electronic noise increases for these low-energy events and, thus, the noise causes fluctuations in the individual decay constants. It should be noted that the τ-cut cannot be defined from the background measurement as there are no secondary peaks to be fitted in the

---

[2] With the settings of the DAQ used for all measurements.

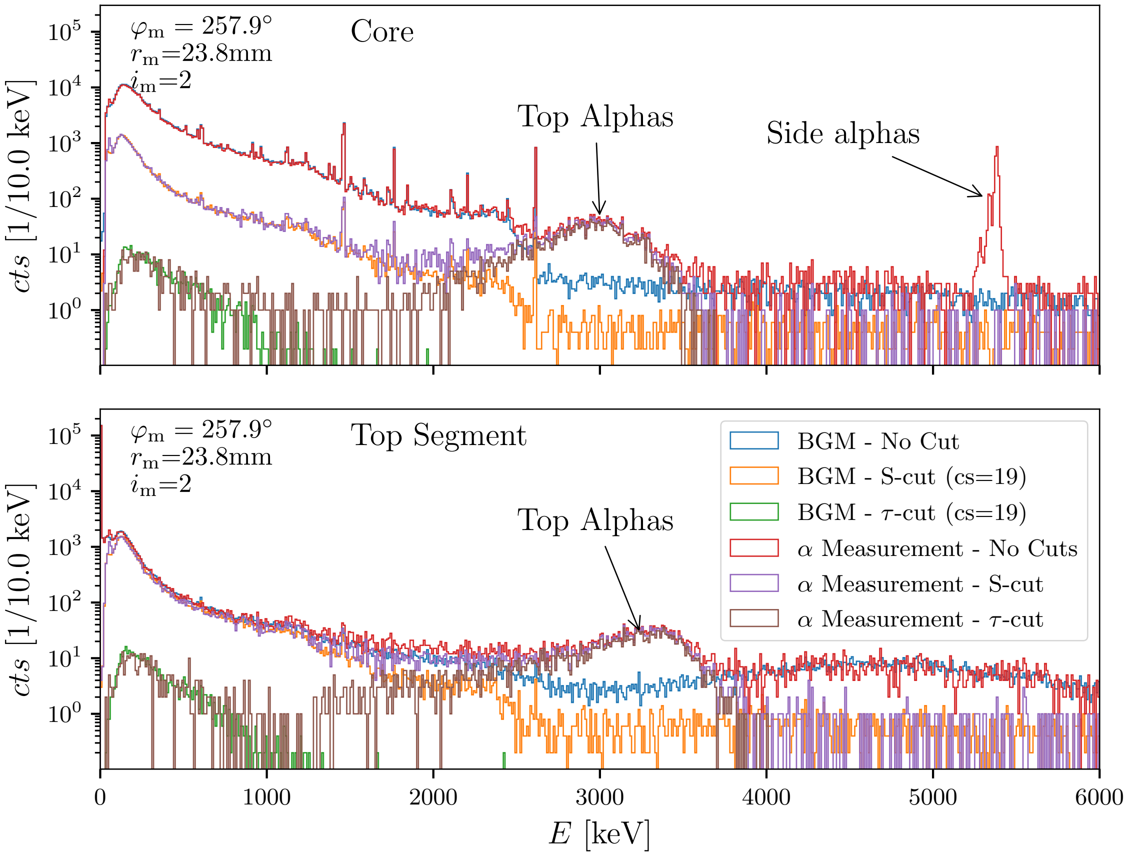

Figure 7.9.: Energy spectra of the core and the top segment of a measurement from the scan SSAmRotMid at ($r_\mathrm{m} = 23.8\,\mathrm{mm}, \varphi^\mathrm{t}_\mathrm{m} = 257.9°$) and of the background measurement BGM after the different cuts. The background spectra are normalized by time to match the measurement with ^{241}Am.

decay constant distributions. The selection ranges for the decay constants as determined for the alpha measurement were used.

7.2.3 Crosschecking the Selection of Top-Alpha Events

Crosscheck based on $\mathrm{E}_\alpha^\mathrm{obs}$

The alphas still form broad "peaks" in the energy spectra after the application of the Sτ-cut, see Fig. 7.9. To verify that the second peaks in the τ distributions really come from alphas, another cut, the ΔE-cut, was introduced, which selects only events which have E_core and E_{cs} within the $\pm 1\sigma$ intervals of the corresponding broad alpha "peaks"[3]. The events selected with the ΔE-cut show τ_decay values which correspond to the second peaks in the τ_decay distributions, see Fig. 7.8. This confirms the Sτ selection, which is

---

[3] The exact definition and determination of the $\pm 1\sigma$ energy intervals will be discussed in the next section, Sec. 7.3

more general as it also allows to select alpha events below the broad peaks.

Crosscheck based on Truncated Mirror Pulses

In previous studies of the detector Super Siegfried [71], it was shown that truncated mirror pulses are a characteristic feature in the neighbouring segments next to the collecting segment of events affected by charge trapping. Examples were already shown in Fig. 7.5 (Fig. 7.6) for an event affected by net hole (electron) trapping. In order to quantify the pulse characteristics of the closest neighbouring segments the quantity

$$TR_{\mathrm{seg}} = \frac{MPA_{\mathrm{seg}} - E_{\mathrm{seg}}}{E_{\mathrm{core}}} \tag{7.4}$$

was introduced, which is the difference between the maximum pulse amplitude and E_{seg} normalized to E_{core} of the event.

The TR_{seg} against E_{seg} histograms of the three segments closest to the beam-spot underneath the top segment are shown in Fig. 7.10. The top beam-spot illuminated the top segment above segment 8. Thus, TR_8 is in general higher than TR_7 and TR_9. In all three segments, 7, 8 and 9, a vertical line of events is visible at $E_{\mathrm{seg}} = 0$. These are normal mirror pulses, where the pulse of the channel differs from zero during the drift but returns to zero at the end as no charges are collected in this channel. The truncated mirror pulses form bands with TR_{seg} decreasing with increasing E_{seg}.

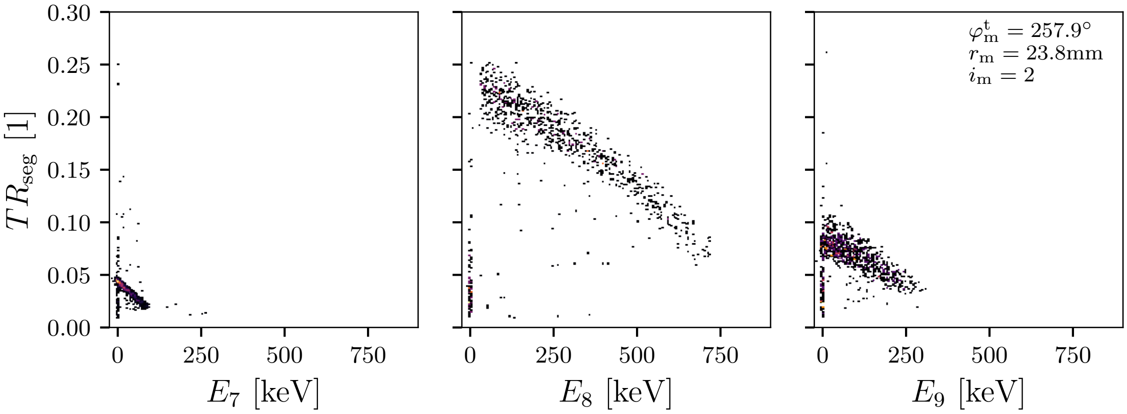

Figure 7.10.: TR_{seg} against E_{seg} histograms of the three segments, 7, 8 and 9, underneath the top segment for all events remaining after the Sτ-cut from the scan SSAmRotMid at ($r_{\mathrm{m}} = 23.8\,\mathrm{mm}, \varphi^{\mathrm{t}}_{\mathrm{m}} = 257.9°$).

These truncated mirror pulses can be used to distinguish events affected by charge trapping from multi-segment events, which also have at least two collecting segments, because the collecting pulses of multi-segment events are (in most cases[4]) not truncated mirror pulses. Thus, for these events, $MPA_{\mathrm{seg}} - E_{\mathrm{seg}} \approx 0\,\mathrm{keV}$, and, hence, $TR_{\mathrm{seg}} \approx 0$.

---

[4] Multi-segment events can also feature pulses looking like truncated mirror pulses but only the in

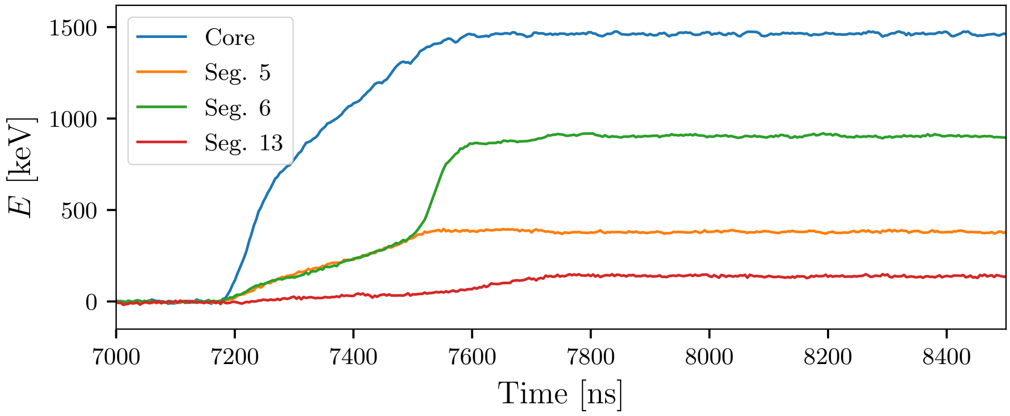

Figure 7.11.: All collecting pulses of a multi-segment event with a core energy in the 1460.83 keV gamma peak of ^{40}K from the measurement of the scan SSAmRotMid at ($r_\mathrm{m} = 23.8\,\mathrm{mm}, \varphi^\mathrm{t}_\mathrm{m} = 257.9°$).

Such pulses are normal collecting pulses. These normal collecting pulses of a multi-segment event are shown in Fig. 7.11. This event is most probably induced by a Compton scattered photon, originating from a gamma decay of ^{40}K in the surroundings of the detector, because it is a multi-site event and $E_\mathrm{core} \approx 1460.83\,\mathrm{keV}$ [83].

For the three segments, 7, 8 and 9, the distributions of TR_seg for events with $E_\mathrm{core} = 1460.83\,\mathrm{keV} \pm 1.5\,\mathrm{keV}$ and $E_\mathrm{cs} \geq 20\,\mathrm{keV}$ are shown in Fig. 7.12. The vertical lines of normal mirror pulses are visible at $E_\mathrm{seg} = 0$. In contrast to the values of TR_seg observed for the pulses in these segments for alpha-induced events, see Fig. 7.10, most of the

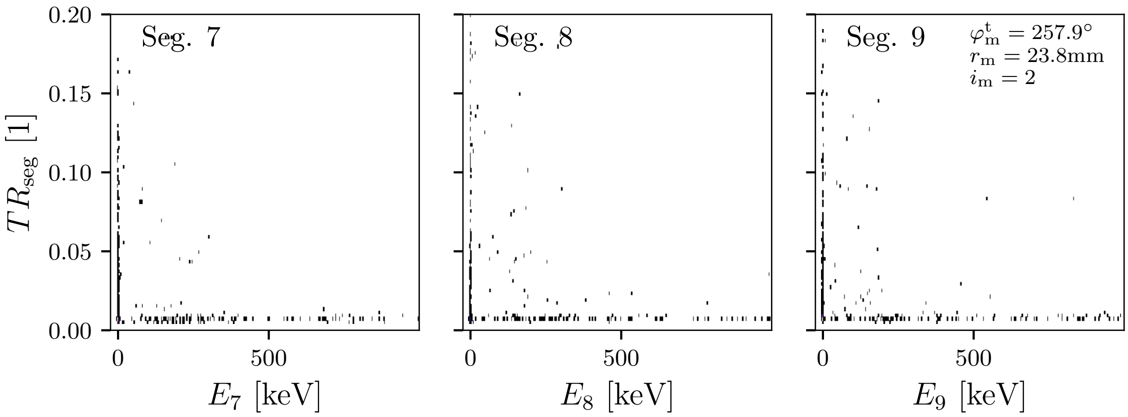

Figure 7.12.: TR_seg distributions of the segments 7, 8 and 9 of all events with E_core within $\pm 1\sigma$ around the ^{40}K gamma peak from the scan SSAmRotMid at ($r_\mathrm{m} = 23.8\,\mathrm{mm}, \varphi^\mathrm{t}_\mathrm{m} = 257.9°$).

---

rare cases when the charge depositions are close to a boundary between the volumes of two collecting segments. Then, during the drift, the charge carriers also induce a strong signal in the respective neighbouring segment, creating a superposition of a mirror and a collecting pulse.

values of TR_{seg} form a horizontal line close to zero[5]. There are a few values of TR_{seg} which are in none of the two lines. This could be alpha-induced events with low E_{seg}, see Fig. 7.9, or rare multi-site events on segment boundaries[3]. In summary, the observation of truncated mirror pulses provides a confirmation of the effectiveness of the Sτ-cut.

7.3 Observed Alpha Energies

Charge trapping and other event topologies are represented in E_{seg} against E_{core} plots. Such a plot is shown in Fig. 7.13 for the top segment (19) with data from a background measurement, BGM. There are different groups of events. All events in the horizontal line, $E_{19} = 0\,\text{keV}$, are events where no energy is deposited in the top segment, whereas the diagonal line, $E_{19} = E_{\text{core}}$, are single segment events where the top segment collects all the holes. Above the diagonal line, all events have net electron trapping as the segment collects more holes (measures more energy) than the core collects electrons. For events below the diagonal, the situation is not as clear. It cannot be decided from

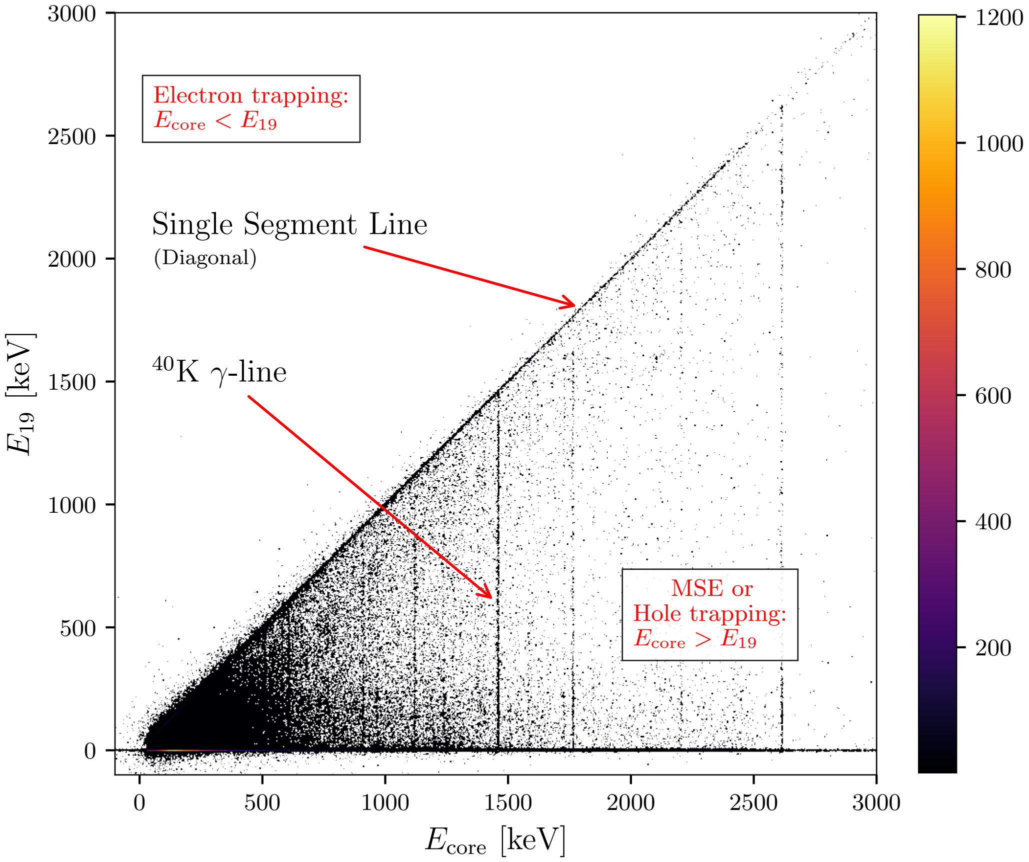

Figure 7.13.: E_{19} against E_{core} of all events from BGM.

---

[5] They are never exactly at zero as the maximum value of a pulse, MPA_{seg}, is always larger than the derived energy, E_{seg}, due to electronic noise.

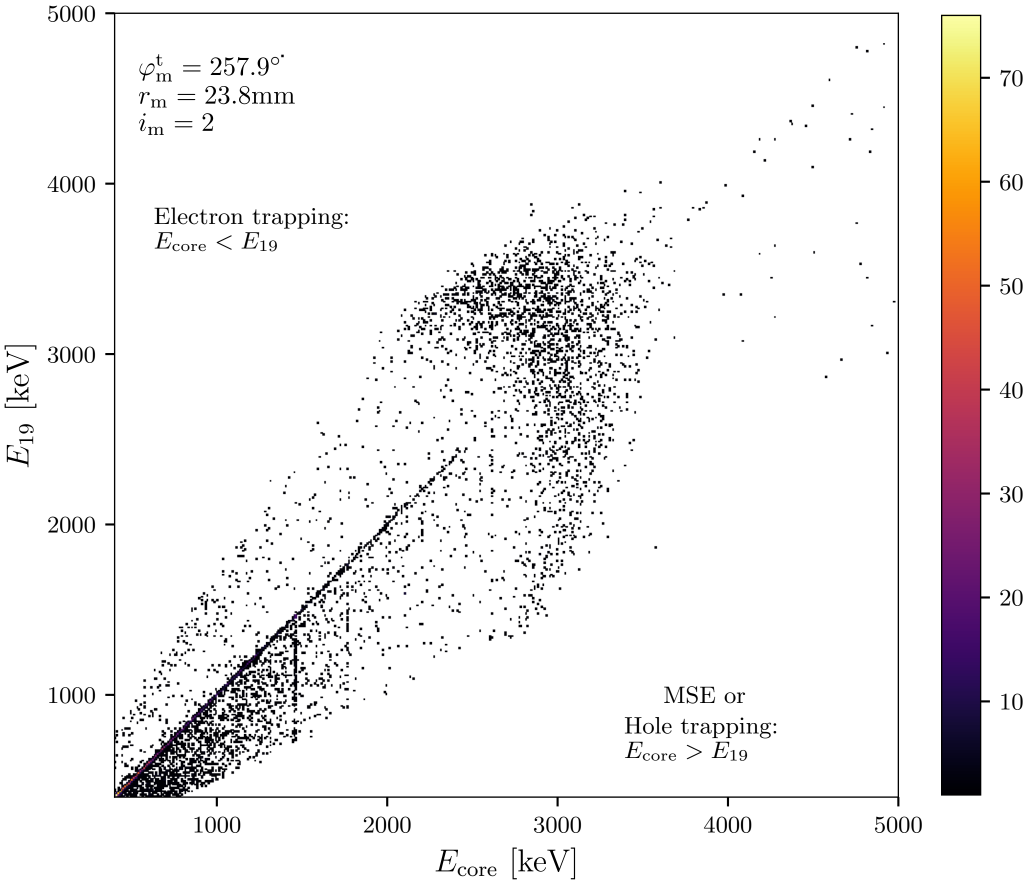

Figure 7.14.: E_{19} against E_{core} of all events remaining after only the S-cut from the scan SSAmRotMid at ($r_{\mathrm{m}} = 23.8\,\mathrm{mm}, \varphi_{\mathrm{m}}^{\mathrm{t}} = 257.9°$). A cluster around $E_{\mathrm{core}} \approx 3000\,\mathrm{keV}$ is visible, which represents the alpha events. The γ line of potassium at 1460 keV is still visible.

this plot alone, whether there is net hole trapping or whether it is a multi-segment event. Also visible are vertical lines at distinct energies. These events indicate certain gamma-decays where the full energy of the initial photon was detected in the core, but, due to Compton scattering, divided between multiple segments. Most of the events between these vertical lines also originate from gamma interactions, but only part of the full energy was detected as Compton scattered photons left the detector.

The E_{19} against E_{core} plot of an ^{241}Am measurement is shown in Fig. 7.14 for all remaining events after only the S-cut. A large number of background events remain from the Compton background where photons deposit only some part of their energy in the volume belonging to the segment. Those remaining background events are removed by the τ-cut as was confirmed earlier on the basis of TR_{seg} and is now also demonstrated by Fig. 7.15. Also shown are the two marginalizations, which are the E_{core} and E_{19} spectra of the remaining events. The shapes of these energy spectra were fitted with the

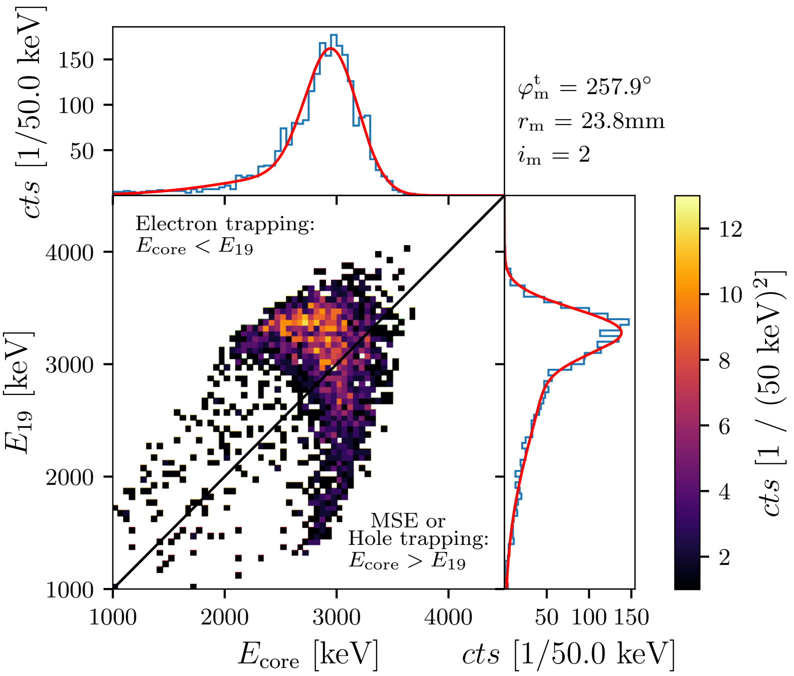

Figure 7.15.: Top segment energy over core energy for all events remaining after the Sτ-cut from the measurement of the scan SSAmRotMid at ($r_{\mathrm{m}} = 23.8\,\mathrm{mm}, \varphi_{\mathrm{m}}^{\mathrm{t}} = 257.9°$). Also shown are the two marginalizations together with fitted model functions $\mathcal{M}$, see text, in red.

following model function

$$\begin{aligned} \mathcal{M}(E|A, R, E_\mu, \sigma_1, \Delta E_\mu, \sigma_2, s) = A \cdot [&(1 - R) \cdot \mathcal{N}(E|E_\mu, \sigma_1) \\ &+ R \cdot \mathcal{N}(E|E_\mu - \Delta E_\mu, \sigma_2) \\ &\cdot (\mathrm{erf}(-s \cdot (E - (E_\mu - \Delta E_\mu))) + 1)] \quad , \end{aligned} \tag{7.5}$$

where A is a scaling parameter, R is the ratio between the two normal distributions $\mathcal{N}(E|E_\mu, \sigma_1)$ and $\mathcal{N}(E|E_\mu - \Delta E_\mu, \sigma_2)$ and s is a stretching factor for the error function. The error function suppresses the second normal distribution on its right side, such that the shape becomes like a normal distribution with a tail to the left side (towards lower energies). E_μ is a measure for the most-likely observed energy for the alphas in the core and the top segment. The ΔE-cut as used for Fig. 7.8 was defined to select events in the interval $E_\mu \pm 1\sigma_1$ for the core and the top segment, respectively.

The local modes of the parameter E_μ, together with the values of σ_1 as error bars, determined for the scan SSAmRotMid are shown in Fig. 7.16. The uncertainties on the E_μ values are much smaller than the σ_1 values and are not shown. Three conclusions can be drawn from the figure:

1. At this radial position, $r_{\mathrm{m}} = 23.8\,\mathrm{mm}$, there is overall more electron trapping than hole trapping as $E_{19} > E_{\mathrm{core}}$ holds for all positions of the beam-spot.
2. There are a few measurements which deviate from the overall pattern. They are

marked with crosses. Those measurements were taken several months after the original scan in order to improve the alignment procedure. Thus, it can be concluded that the amount of trapping is not stable over time. There was a warming-cooling cycle between the measurements, which could have caused a change in surface conditions. Some part of the effect might also be related to the crystal temperature, which is not completely stable in GALATEA, see Sec. 4.1.4.

3. There is a clear effect of the crystal axes on E_μ for both the core and the top segment. Near a fast axis, more energy is recorded. Thus, there the dead layer is thinner or there is less net trapping of charge carriers. This is reasonable as the mobility for drifts along crystal axes is higher than for drifts between the axes. This effect on the alphas was not observed in previous studies in GALATEA, where fewer data were available.

Figure 7.17 shows the parameter E_μ together with the values of σ_1 presented as error bars determined for the measurements of the radial scans SSAmRad181 and SSAmRad136. For both scans, a similar transition from more hole trapping at lower radii to more electron trapping at larger radii is observed. This is somewhat expected, as the drift paths for the electrons (holes) become longer (shorter) at larger radii.

Comparing the two scans, the effect of the crystal axes can be seen again. The scan SSAmRad181 is along a slow axis, whereas the scan SSAmRad136 is along a fast axis. The E_μ values for the scan along the fast axis are ≈ 500 keV higher than those for the scan along the slow axis.

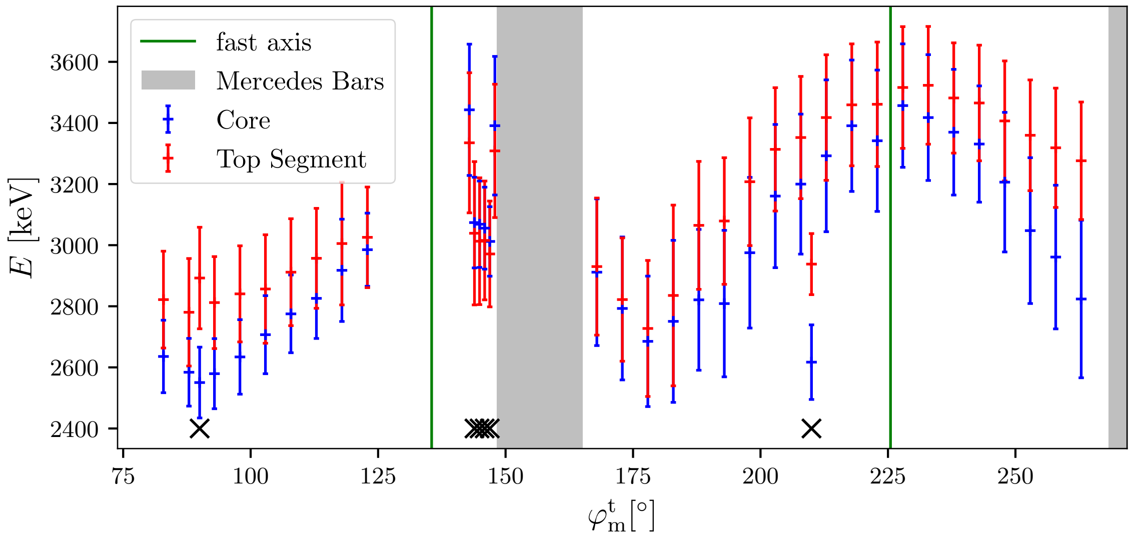

Figure 7.16.: Local modes of the parameter E_μ together with the σ_1 represented by error bars as determined from the rotational scan SSAmRotMid at $r_\mathrm{m} = 23.8$ mm for the core and the top segment. Also shown are the positions of the fast axes as well as the positions and widths of the mercedes bars. The grey crosses at the bottom mark measurements which were taken some time (months, see Table A.2) after the other measurements.

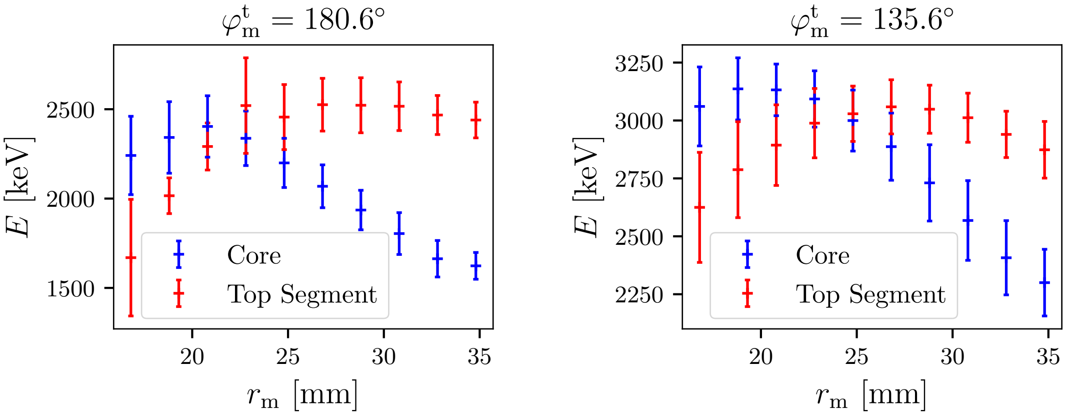

Figure 7.17.: Local modes of the parameter E_μ together with the values of σ_1 presented as error bars for the radial scans SSAmRad181 (left), which is along a slow axes, and SSAmRad136 (right), which is along a fast axis.

The question arises whether there is a completely dead layer of germanium underneath the passivation layer, which causes some net reduction of E equally for the core and the top segment. This reduction happens because electron-hole pairs directly recombine in such a dead layer. However, this cannot be easily answered, as the signal in the top segment (core) is not only caused by the holes (electrons), but also by the trapped electrons (holes), which reduce the signal in the segment (core), see Eq. 3.22. This question will be investigated using simulations in Sec. 9.2.2.

7.4 Metallization Studies with Alphas

Prior to the measurements performed for this thesis, the top segment (19) of the detector Super Siegfried was only partially metallized, i.e. in the area where the cable was connected[6] at $\varphi_{\mathrm{m}}^{\mathrm{C}} \approx 130°$. It was observed that the pulses of the top segment at $r_{\mathrm{m}} = 26\,\mathrm{mm}$ were much longer, about 730 ns, far away from $\varphi_{\mathrm{m}}^{\mathrm{C}}$ than for events close to $\varphi_{\mathrm{m}}^{\mathrm{C}}$. This is shown in Fig. 7.18. The core rise-times seemingly were also affected by the partial metallization, but not as much as the rise-times of the top segment. The pulses were only about 50 ns slower far away from the metallization than next to it.

In order to investigate whether the full metallization changed the situation, the rise times $\mathcal{T}_{10-90}$ were determined for the events at $r_{\mathrm{m}} = 23.8\,\mathrm{mm}$ remaining after the Sτ- and the ΔE-cut. The normalized pulses of the core and the top segment of the selected events are shown in Fig. 7.19 in form of a heatmap. They all have very similar shapes, which confirms that they are all induced by alphas originating from the beam-spot.

The distributions of the rise times $\mathcal{T}_{10-90}$ are shown in Fig. 7.20. The mean value and standard deviation of these distributions were calculated[7] and the respective normal distributions are also shown in Fig. 7.20. The mean values and standard deviations of

---

[6] Estimated by eye from a picture, see Fig. 6.1.

[7] Rise times far away (3σ) from the corresponding mean value were excluded.

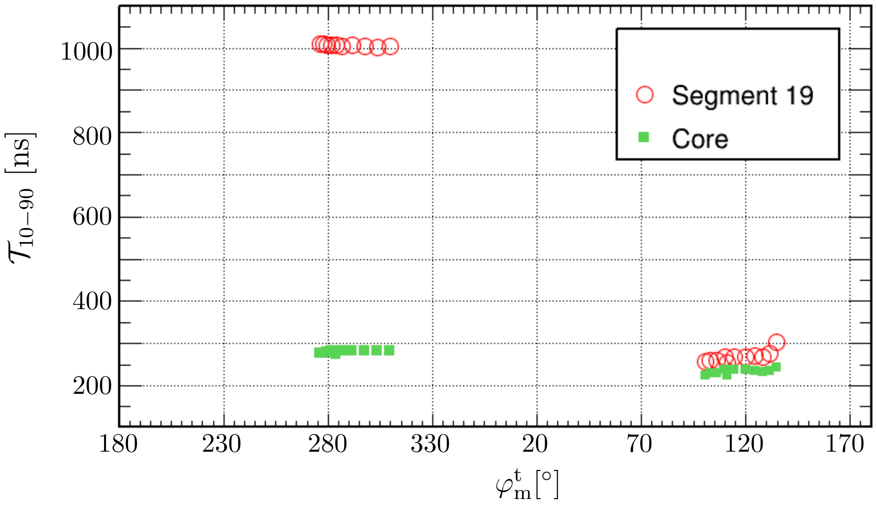

Figure 7.18.: Figure taken from [82]. The x-axis has been modified to match the coordinate system chosen for this thesis. The data points are the rise times $\mathcal{T}_{10-90}$ for alpha events for the core (green) and the top segment (red). The metallization was centered around $\varphi_\mathrm{m}^\mathrm{C} \approx 130°$. The radial position of the beam-spot in this rotational scan was $r_\mathrm{m} = 26\,\mathrm{mm}$.

the alpha rise-time distributions determined for all measurements of the rotational scan SSAmRotMid are shown in Fig. 7.21. The situation clearly changed with respect to the

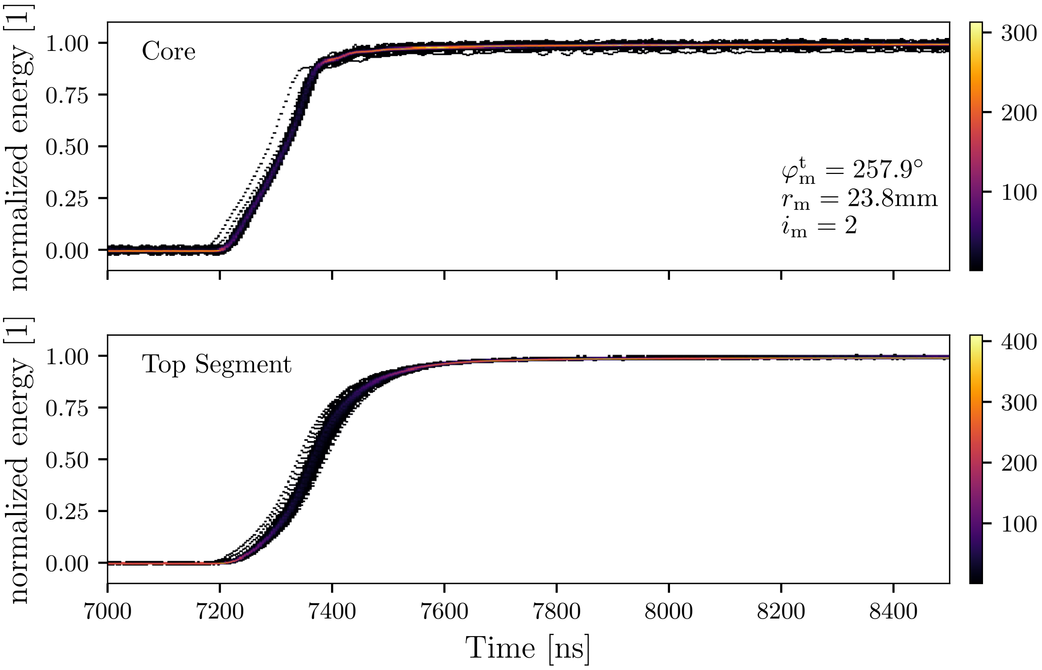

Figure 7.19.: Normalized pulses of the core and the top segment of the events after the S$\mathcal{T}$- and ΔE-cut in form of heatmaps from the scan SSAmRotMid at ($r_\mathrm{m} = 23.8\,\mathrm{mm}, \varphi_\mathrm{m} = 257.9°$).

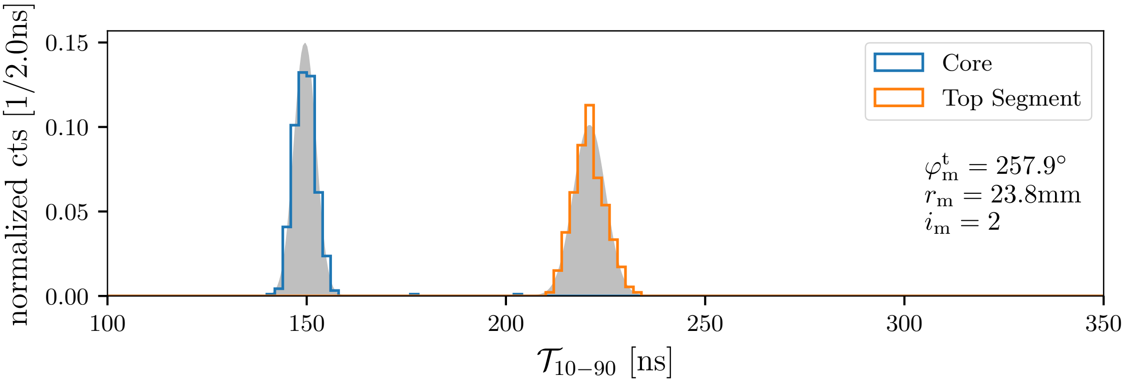

Figure 7.20.: To area normalized distributions of individual rise times $\mathcal{T}_{10-90}$ of alpha events from the scan SSAmRotMid at ($r_{\mathrm{m}} = 23.8\,\mathrm{mm}, \varphi_{\mathrm{m}} = 257.9°$). In grey: Normal distributions with means and standard deviations calculated from the respective individual rise times.

previous studies, see Fig. 7.18: A slowdown of the pulses is not noticeable anymore for the core. Thus, the full metallization seems to increase the electric field and makes it more homogenous over φ. However, for the top segment, a difference between the rise times of events close to $\varphi^{\mathrm{C}}_{\mathrm{m}}$ and measurements far away from $\varphi^{\mathrm{C}}_{\mathrm{m}}$ is still present. But, the difference is only about 100 ns whereas for the previous measurements it was ≈ 730 ns.

Close to $\varphi^{\mathrm{C}}_{\mathrm{m}}$, the top segment pulses are also longer than the pulses in the core. However, this is mainly due to the different electronic response functions. The influence of the crystal axes appears as a small additional modulation in Fig. 7.21. This is better seen for the core, but also visible for the segment. The oscillation does not look as pronounced as in Fig. 6.19, because the y-axis spans a larger range.

The mean values and standard deviations of the rise-time distributions of alpha events determined for all measurements of the two radial scans SSAmRad136 and SSAmRad181 are shown in Fig. 7.22. For both scans, the core and the top segment rise-times have their minimum around $r_{\mathrm{m}} = 26\,\mathrm{mm}$ and increase towards larger and lower radii. This is expected as the signal is induced by both type of charge carries, electrons and holes. And at $r_{\mathrm{m}} \approx 26\,\mathrm{mm}$ both type of charge carrier reach their collecting electrode at about the same time. Thus, there, the rise times are the shortest. At lower (larger) radii, the holes (electrons) have to drift longer which increases the rise times in both channels. The radial position of the minima, $r_{\mathrm{m}} \approx 26\,\mathrm{mm}$[8], is not the radial center of the detector, $r_{\mathrm{mid}} = (37.5\,\mathrm{mm} - 5\,\mathrm{mm})/2 = 16.25\,\mathrm{mm}$. This is also expected as the mobility of holes is lower than the mobility of electrons and, hence, holes need more time for the same drift distance. Therefore, the radial position for the minimal rise times is shifted towards the mantle.

---

[8] The position of the minimum differs slightly for both scans. This is expected as the drift is along different directions with respect to the crystal axes and the influence of the crystal axes on the drift velocity is different for holes and electrons.

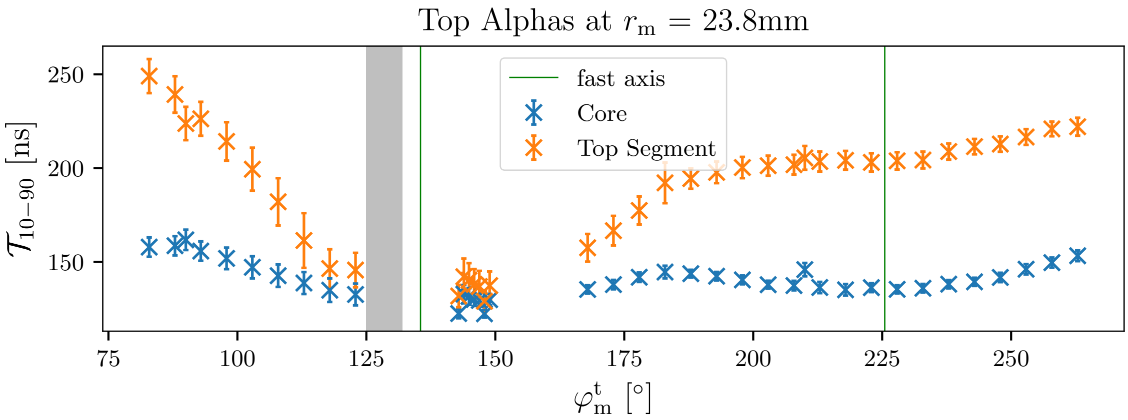

Figure 7.21.: Mean of the rise-time distributions determined from the scan SSAmRotMid. The error bars are not the uncertainties but the standard deviation of the distributions. The grey area marks the position of the old metallization where also the read-out cable was and is connected to the segment.

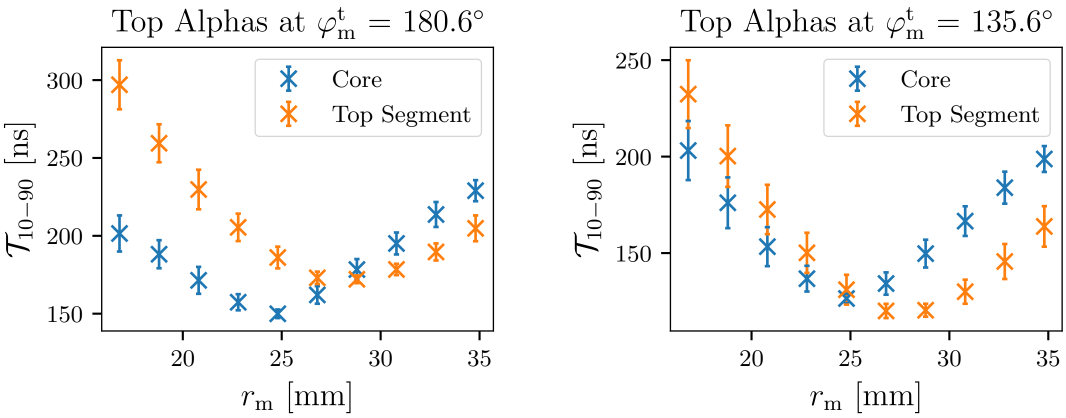

Figure 7.22.: Mean of the rise-time distributions determined from the two radial scans SSAmRad181 (left, along slow axis) and SSAmRad136 (right, along fast axis). The error bars are not the uncertainties but the standard deviation of the distributions.

7.5 Metallization Studies with Gammas

Similar to the effect of the partial metallization of the top segment on the alpha pulses, also the rise times of events induced by gammas from ^{237}Np were observed to be affected in previous studies as shown in Fig. 7.23. The effect on gamma pulses were of the same order of magnitude as on alpha pulses for the core. For the segment, however, the effect was a bit smaller for the gamma pulses compared to the effect on the alpha pulses as the rise times far away from $\varphi_{\mathrm{m}}^{\mathrm{C}}$ only increased by about 430 ns.

The question is whether also events induced by 59.5 keV gammas from Neptunium still show a dependence of the rise times on their distance to $\varphi_{\mathrm{m}}^{\mathrm{C}}$.

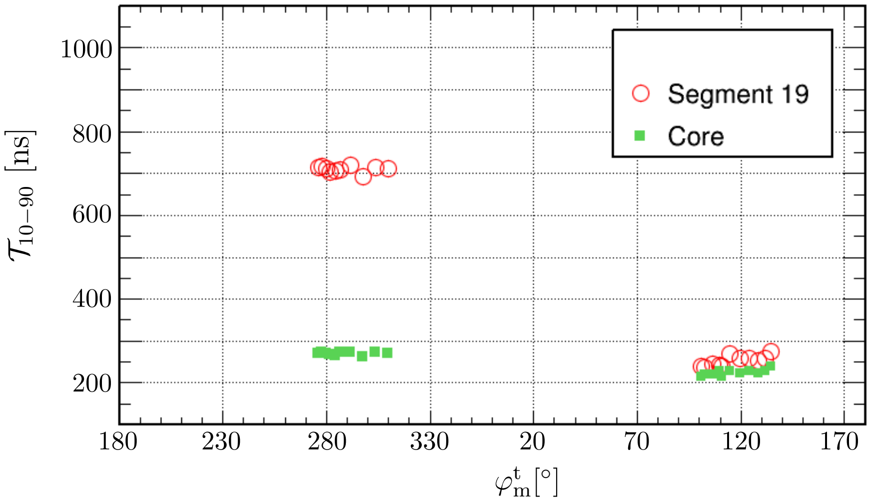

Figure 7.23.: Figure taken from [82]. The x-axis has been modified to match the coordinate system chosen for this thesis. The data points are the rise times $\mathcal{T}_{10-90}$ of ^{237}Np gamma events for the core (green) and the top segment (red). The radial position of the beam-spot in this rotational scan was $r_{\mathrm{m}} = 26$ mm.

7.5.1 Superpulses of Gamma Events

The gammas form a peak in the energy spectrum of the core and of the top segment at Q_{γ}^{Np} as shown in Fig. 7.24 and Fig. 7.25 for two measurements of the radial scan SSAm-Rad181 (along a slow axis) at the radial positions $r_{\mathrm{m}} = 10.8$ mm and $r_{\mathrm{m}} = 16.8$ mm. The observation of the full energy at 59.5 keV in both the core and the top-segment channel indicates that gamma events are not affected by charge trapping. As the gamma-induced events deposit energy predominantly within one millimeter below the surface, see Fig. 7.3, the layer can not be significantly thicker than tens of micrometers. The strong single segment cut, $|E_{\mathrm{core}} - E_{\mathrm{seg}}| \leq 3$ keV, was used as the gammas were not affected by charge trapping and they are single site events, since the cross-section of photon absorption is much larger than the cross-section of Compton scattering at such

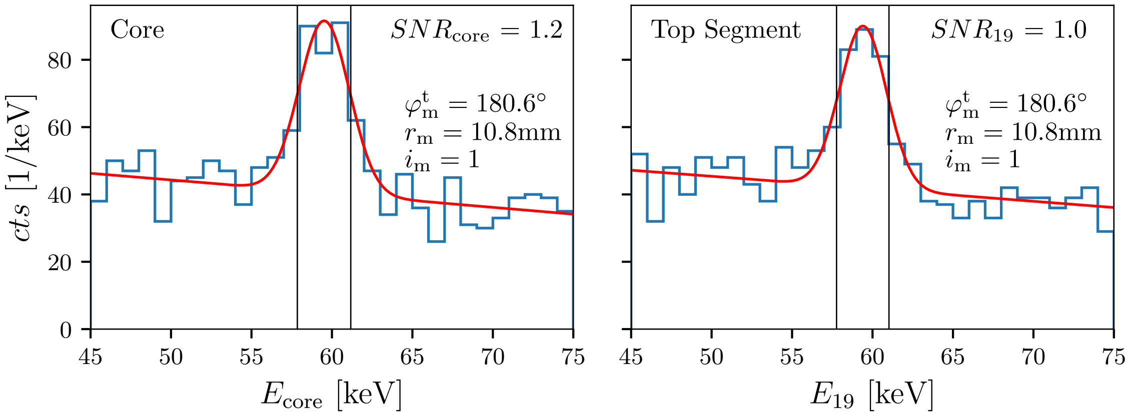

Figure 7.24.: Energy spectra of the core (left) and the top segment (right) of single segment events from the scan SSAmRad181 at ($r_m = 10.8\,\text{mm}, \varphi_m = 180.6°$). In red: Gaussian plus linear background fitted to the two spectra. The black lines mark the $\pm1\sigma$ interval of the Gaussian.

low energies.

Rise times could not be determined for single pulses of gamma events as the electronic noise was too large at the energy of 59.5 keV. Therefore, superpulses from all individual gamma pulses in one location had to be formed. The gamma events were selected by two additional cuts. First, by a ΔE-cut. In order to determine the energy windows for the core and the top segment, a Gaussian plus a linear function was fitted to the energy spectra filled with only single segment events. The results of the fit are also shown in Fig. 7.24 and Fig. 7.25. The $\pm1\sigma$ window of the Gaussian in both channels were used as

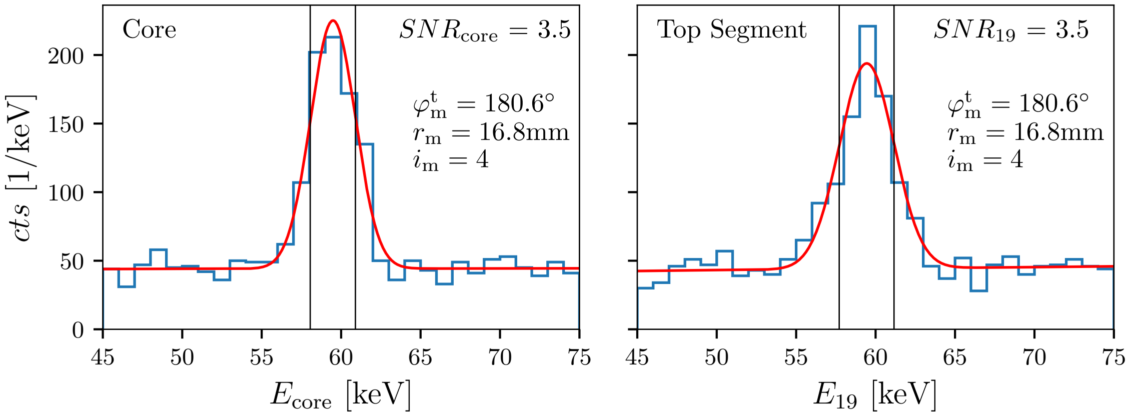

Figure 7.25.: Energy spectra of the core (left) and the top segment (right) of single segment events from the scan SSAmRad181 at ($r_m = 16.8\,\text{mm}, \varphi_m = 180.6°$). In red: Gaussian plus linear background fitted to the two spectra. The black lines mark the $\pm1\sigma$ interval of the Gaussian.

the energy windows for the ΔE-cut and to determine the signal to noise ratios (SNR). At the radial position of $r_\mathrm{m} = 10.8\,\mathrm{mm}$, only a part of the beam-spot covers the top segment as one half is blocked by the teflon piece of the holding structure, which has a radius of 10 mm. Thus, the SNR is only about 1 at this position, see Fig. 7.24. For all other radial positions within the detector radius, the SNR was constant at about 3.5 as shown in Fig. 7.25.

The distribution of pulses of the events remaining after the application of the ΔE-cut are shown in Fig. 7.26 for the measurement at $r_\mathrm{m} = 10.8\,\mathrm{mm}$ and in Fig. 7.27 for the measurement at $r_\mathrm{m} = 16.8\,\mathrm{mm}$. The core pulses all look very similar, because the signal of the core channel is dominated by the drift of the charge carriers through the volume where the weighting potential of the core is large and changes rapidly, i.e. close to the borehole. Thus, also background events which might be located at a larger radii, will have the same shape as the signal events located at about 10.8 mm or 16.8 mm. In the segment, however, a difference between the signal events and background events is visible. Thus, using all of those events to form a superpulse would produce a distorted superpulse, which is also demonstrated in Fig. 7.24 and Fig. 7.25.

A cut on the likelihood was introduced to select signal events: The heatmaps of the pulses in the time interval from 7 μs to 8 μs were turned into probability distributions and the likelihood of the individual pulses belonging to these distributions were evaluated. The

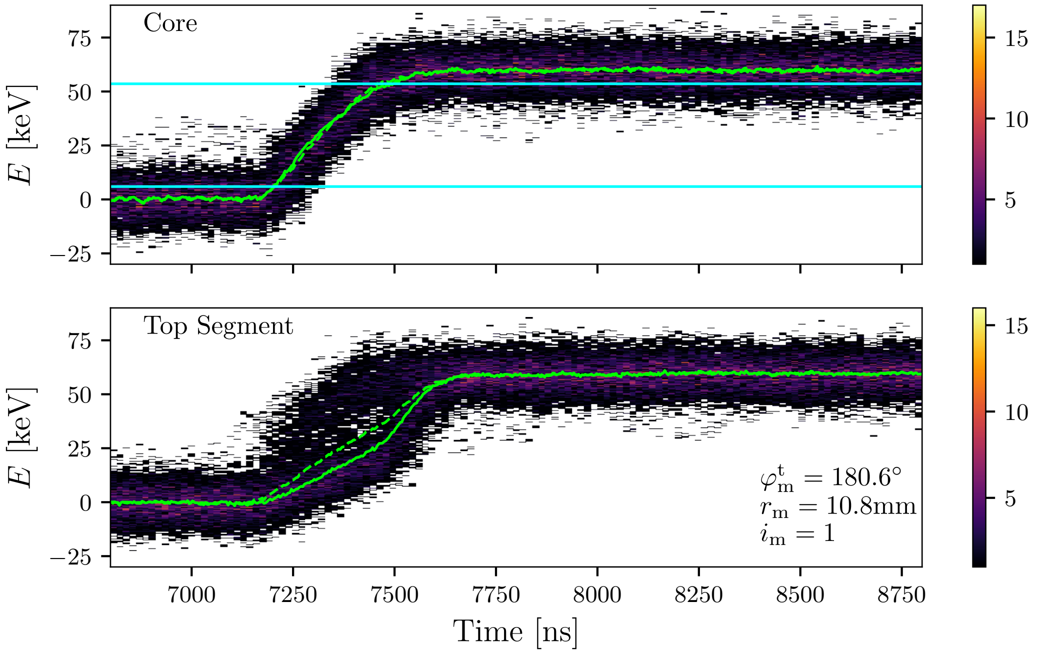

Figure 7.26.: Heatmaps of the pulses of selected gamma events of the core (top) and the top segment (bottom) from the scan SSAmRad181 at ($r_\mathrm{m} = 10.8\,\mathrm{mm}, \varphi_\mathrm{m} = 180.6°$). The dashed (solid) green lines are the superpulses formed by all events remaining after the application of the ΔE (and LLH-cut). The horizontal cyan lines indicate the 10 % and 90 % levels of the core superpulse.

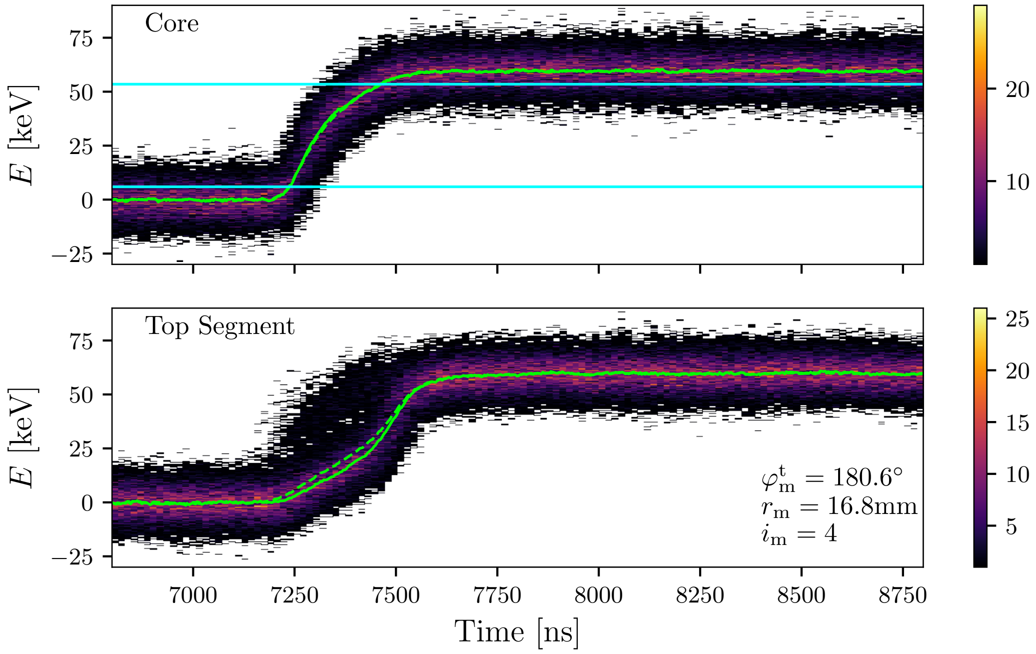

Figure 7.27.: Heatmaps of the pulses of selected gamma events of the core channel (top) and the top segment (bottom) from the scan SSAmRad181 at ($r_{\mathrm{m}} = 16.8\,\mathrm{mm}, \varphi_{\mathrm{m}} = 180.6°$). The dashed (solid) green lines are the superpulses formed by all events remaining after the application of the ΔE (and LLH-cut). The horizontal cyan lines indicate the 10 % and 90 % levels of the core superpulse.

distribution of likelihoods of all previously selected pulses is shown in Fig. 7.28 for the measurement at $r_{\mathrm{m}} = 10.8\,\mathrm{mm}$. As the SNR was at least about 1, the likelihood of signal events should be larger than the likelihood of background events, because, even in the worst case of $SNR = 1$, some of the background events are located, by accident, in the same region as the signal events and, thus, have the same shape. Therefore, the probability distribution should peak around the shape of the signal events even for the worst case of SNR of about 1.

Only events with a likelihood larger than the mean of the likelihood distribution were selected to form the superpulse. This selection is called the LLH-cut. The superpulses formed by the events remaining after the application of the LLH-cut are also shown in Fig. 7.26 and Fig. 7.27.

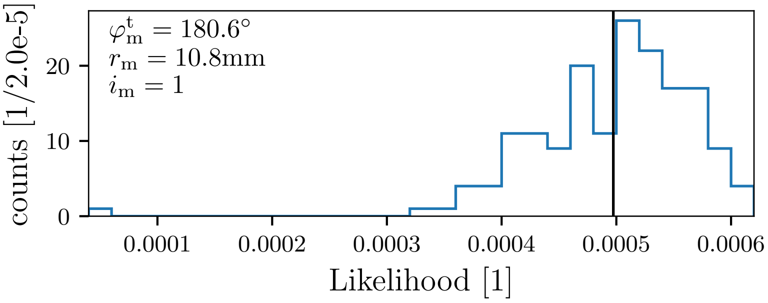

Figure 7.28.: Distribution of likelihoods determined for the selected gamma events remaining after the application of the ΔE-cut from the scan SSAmRad181 at ($r_\mathrm{m} = 10.8\,\mathrm{mm}, \varphi_\mathrm{m} = 180.6°$). The vertical black line is the mean value of the individual likelihood values.

7.5.2 Rise Times of Gamma Superpulses

The rise times $\mathcal{T}_{10-90}$ were determined for the superpulses of the gamma events from the rotational top scan SSAmRotMid, see Fig. 7.29, and the two radial top scans SSAmRad181 and SSAmRad136, see Fig. 7.30.

The rotational scan, see Fig. 7.29, shows a very similar φ dependence of the rise times for gamma events as for alpha events, see Fig. 7.20. For the core, the dependence is quite small. However, the pulses of the top segment are faster close to $\varphi_\mathrm{m}^\mathrm{C}$ and slower further away from $\varphi_\mathrm{m}^\mathrm{C}$. Like for the alphas, the effect is much smaller than prior to the full metallization. The effect of the crystal axes on the rise time is not visible. This is most likely due to the events being located at $r_\mathrm{m} = 23.8\,\mathrm{mm}$, where the drift time of holes and electrons is equal. Events close to the mantle, which were used to determine

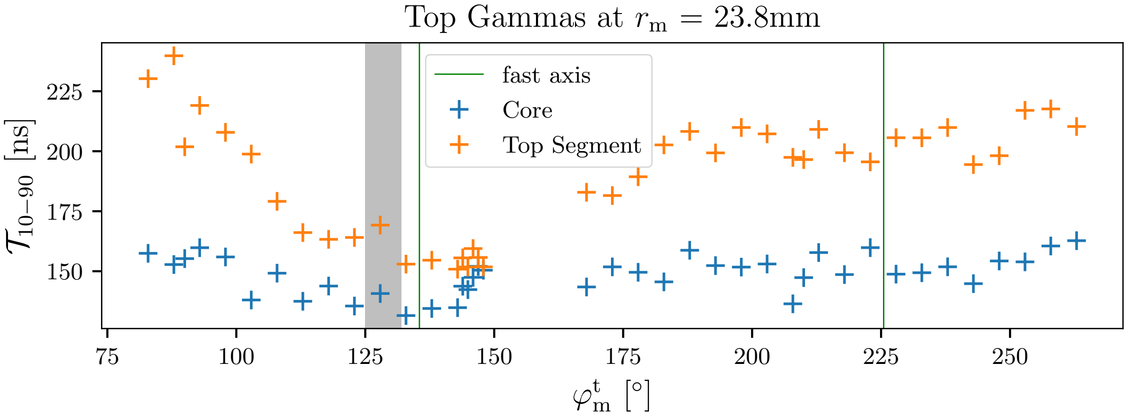

Figure 7.29.: Rise times $\mathcal{T}_{10-90}$ of the superpulses formed by gamma events of ^{237}Np from the rotational scan SSAmRotMid. The grey area marks the position of the old metallization where also the read-out cable was and is connected to the segment.

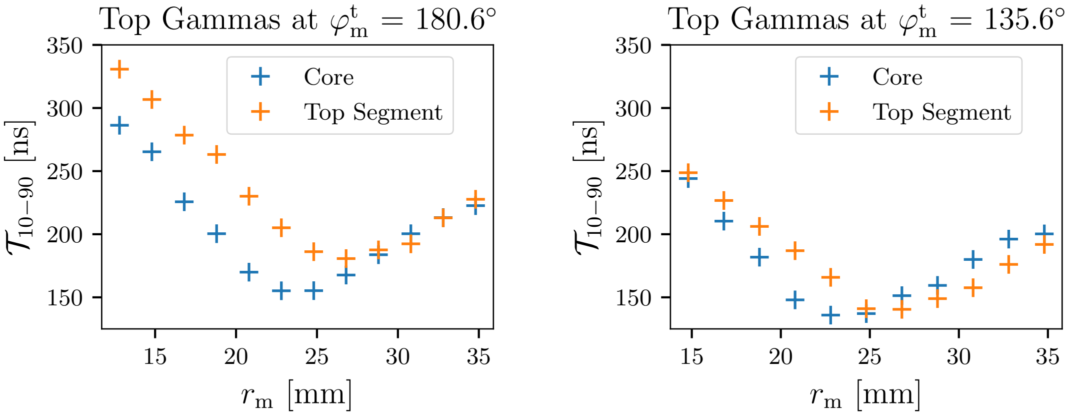

Figure 7.30.: Rise times $\mathcal{T}_{10-90}$ of the superpulses formed by gamma events of ^{237}Np from the two radial scans (left) SSAmRad181 along a slow axis and (right) SSAmRad136 along a fast axis.

the crystal axes, see Sec. 6.5, have rise times entirely determined by the electrons, which have to drift through the entire bulk and, thus, the drift time is longer and the effect of the crystal axes is more pronounced.

The comparison between the two radial scans, one along a fast axis and one along a slow axis reveal the axes effect, see Fig. 7.30. When comparing the rise times of the core and the top segment of the two scans at the most inner and outer radial positions, the influence of the crystal axes is significant. In both channels, the rise times of the scan along the slow axis are larger than the rise times of the scan along the fast axis at these positions. Overall, the two scans show a very similar r dependence of the rise times of gamma pulses as observed for alpha pulses, see Fig. 7.22.

Side Scan of the Top Segment

An influence of the metallization of the top segment was also observed on the rise times of 121.8 keV gamma events from ^{152}Eu for collimated gammas entering the top segment from the side at $z_{\mathrm{m}} = 68.5$ mm [55], see Fig. 7.31 *a*) and *b*). In the core, the partial metallization had no impact on the rise times. The effect of the crystal axes is pronounced as these events are located close to the mantle of detector and, thus, the electron drift path is long. In the segment, like for the alphas, the effect of the partial metallization on the rise times of the pulses was huge. The rise times are ≈ 200 ns close to $\varphi_{\mathrm{m}}^{\mathrm{C}}$, whereas they are about 5 times longer, ≈ 1000 ns, far away from $\varphi_{\mathrm{m}}^{\mathrm{C}}$.

The rise times $\mathcal{T}_{10-90}$ of superpulses formed by gamma events of ^{237}Np for the fully metallized top segment are shown in Fig. 7.31 *c*). The data come from the rotational side scan SSAmRotSeg19. The situation had changed dramatically. The pulses in the top segment were only ≈ 20 ns faster close to $\varphi_{\mathrm{m}}^{\mathrm{C}}$ than far away from $\varphi_{\mathrm{m}}^{\mathrm{C}}$. This difference is much smaller than prior to the full metallization. In addition, the effect of the crystal

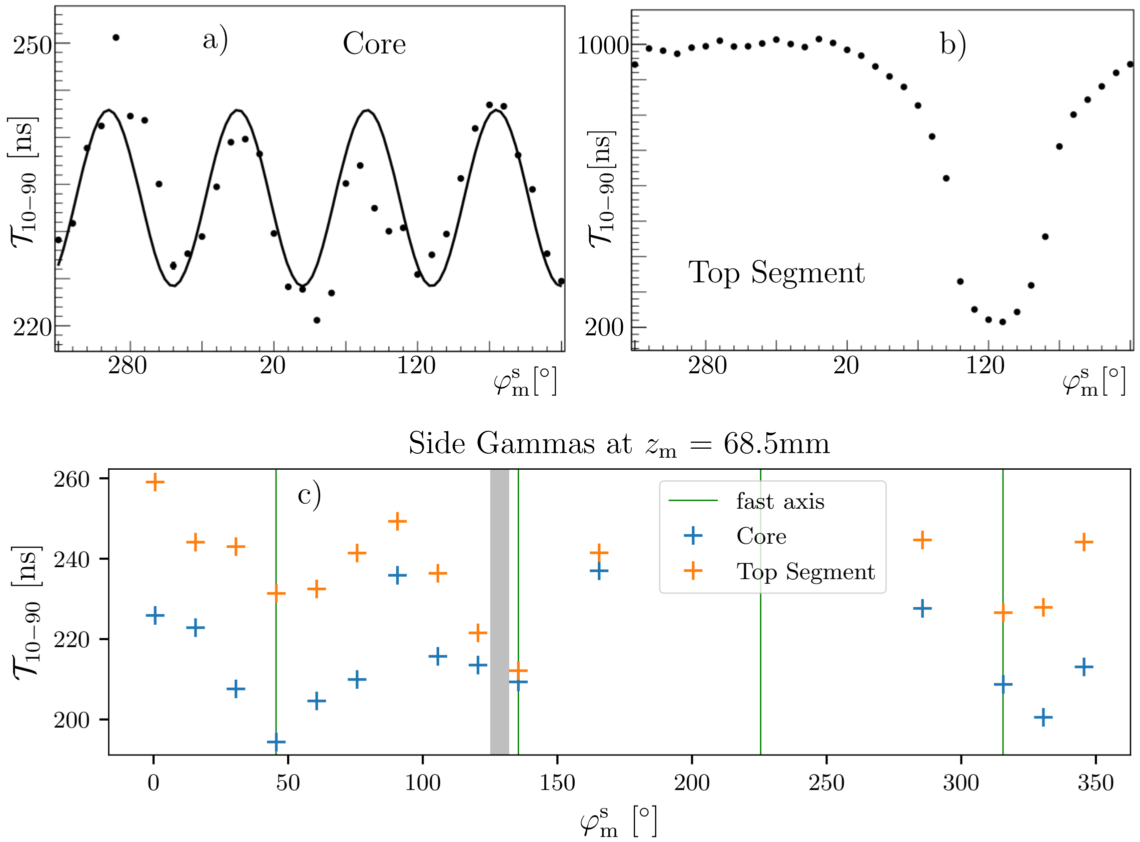

Figure 7.31.: *a*) and *b*) taken from [82]. The x-axes were modified to match the coordinate system chosen for this thesis. The data points are the averaged rise times $\mathcal{T}_{10-90}$ of events of collimated 121.8 keV gammas from ^{152}Eu entering the top segment from the side for (*a*) the core and (*b*) the top segment. *c*): Rise times $\mathcal{T}_{10-90}$ determined from the superpulses formed from the gamma events of ^{237}Np from the rotational side scan SSAmRotSeg19. The grey area marks the position of the old metallization where the read-out cable was and is connected to the segment.

axes is now also visible in the segment.

It can be concluded that the full metallization of the segment strengthens the electric field right underneath the top surface of Super Siegfried and makes it more homogenous. Especially, the collection of holes was impacted very significantly by the partial metallization. The effect of the crystal axes on the hole drift was not present for the only partially metallized top segment. A possible explanation might be that the applied bias voltage was not distributed homogenously over the full segment and, thus, that the electric field lines did not run radially towards the segment implantation. First simulations of a top segment contact, which is not perfectly conductive, are presented in Sec. 9.1.

7.6 Response of Siegfried III to Americium Events

7.6.1 Alignment and Datasets

The germanium detector Siegfried III is very similar to Super Siegfried. Siegfried III is depicted in Fig. 7.32. It is an n-type true coaxial detector where the borehole is the only n^+-contact. The mantle surface is segmented into 18 p^+-contacts of equal size in a 6×3 (φ, z) geometry. It does not have an additional 19th segment on top. The segments of the middle and bottom row are fully metallized whereas the segments of the top row are only partially metallized in form of central dots (1 cm diameter) on which the Kapton printed circuit board makes contact with the segments.

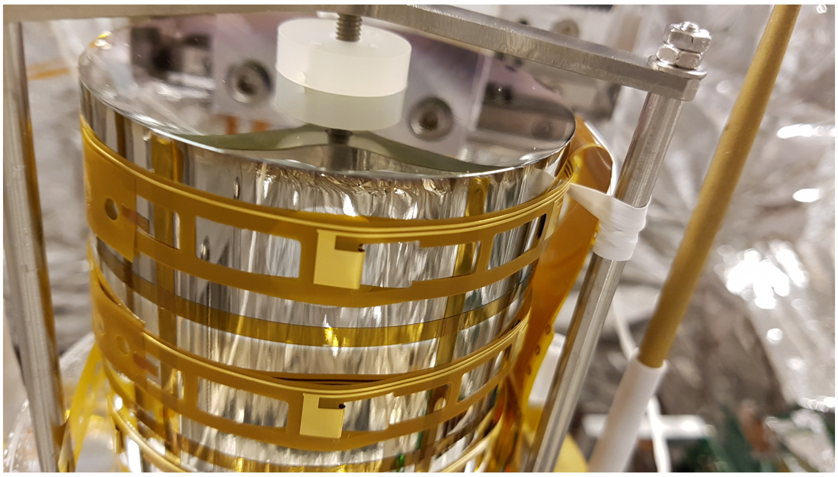

Figure 7.32.: Picture of Siegfried III. A Kapton printed circuit board is wrapped around the detector to read out the segments. Also visible are parts of the holding structure, including the teflon piece, which has a radius of 1 cm, on top of the borehole.

Just like for Super Siegfried, rotational, vertical and radial scans were performed in order to determine the detector alignment and crystal orientation. A map of the beam-spot positions of those scans are are shown in Fig. 7.33 and Fig. 7.34, and the result of the crystal axes fit is shown in Fig. 7.35. The datasets are summarized in App. A.3. Note, that in the rotational scan S3AmRotMid, the detector was irradiated by the top and the side source simultaneously.

The determined positions (local mode) of the fast axes are indicated in dashed green lines in Fig. 7.35. The green, yellow and red areas show the 68.3%, 95.5% and 99.7% credibility intervals of the rise time.

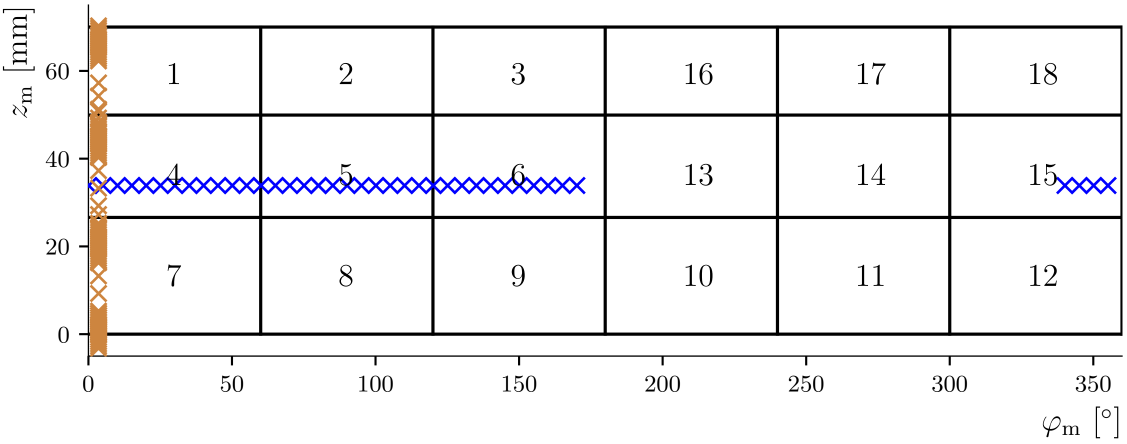

Figure 7.33.: Map of the side beam-spot positions of the rotational scan S3AmRotMid (blue crosses) and the vertical scan S3AmVert4 (brown crosses) on the mantle surface of Siegfried III.

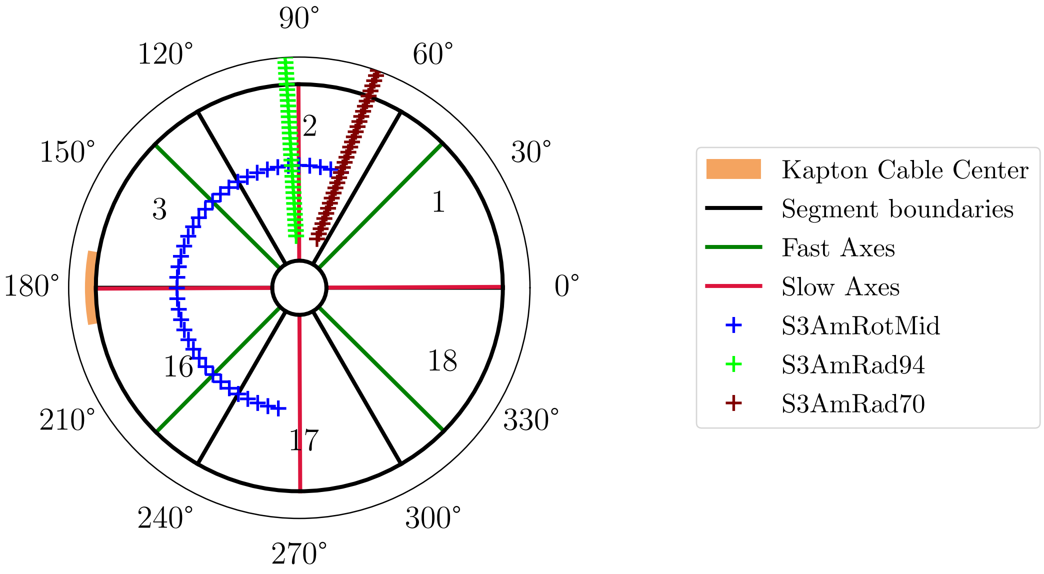

Figure 7.34.: Map of the top beam-spot positions of the rotational scan S3AmRotMid and the two radial scans S3AmRad70 and S3AmRad94 on the top surface of Siegfried III.

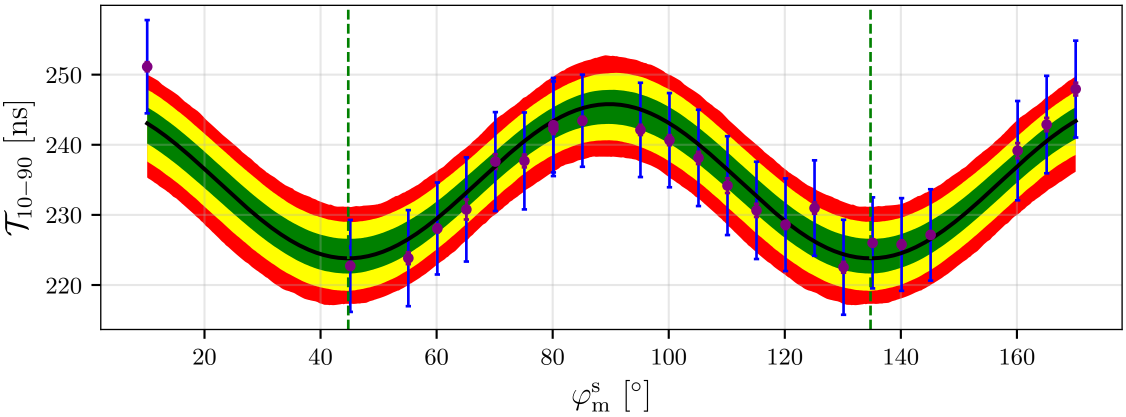

Figure 7.35.: Rise time $\mathcal{T}_{10-90}$ of alpha-induced events from the side source from the rotational scan S3AmRotMid (purple dots). The statistical uncertainty ranges are barely visible as they are very small. The assumed systematic uncertainty is shown in blue. The model function, Eq. 6.13, describing the oscillation of the rise time with the local mode as parameters is shown as a solid black line.

7.6.2 Observed Alpha Energies

The ^{241}Am source of the top collimator irradiated two of the six segments of the top row of Siegfried III simultaneously when the beam-spot covered a segment boundary. For each measurement, the collecting segment, $i = \mathrm{cs}$, was determined as the segment with the highest number of detected alpha and gamma events from ^{241}Am. These alpha and gamma events were identified and selected in the same way as for Super Siegfried and the same analysis on the events induced by alphas and gammas was performed.

The mean observed energy of the alphas, described by the parameter E_μ of the model distribution (Eq. 7.5) are shown versus $\varphi^{\mathrm{t}}_{\mathrm{m}}$ in Fig. 7.36. The effect of the crystal axes on E_μ is only visible in the segments 3, 16 and 17. In segment 2, no effect due to the crystal axes is visible. This indicates a high ohmic contact between the Kapton printed circuit board and this particular segment[9]. In the two radial scans S3AmRad70 and S3AmRad94, this segment was irradiated. The values of E_μ determined for these two scans are shown in Fig. 7.37. In contrast to the radial scans of Super Siegfried, see Fig. 7.17, there is one major difference: the segment detects more energy than the core for all radial positions. Thus, there always seems to be more net electron trapping. The reason for this is not clear. However, there might be inhomogeneities in the passivation layer of this detector. It might also be related to different crystal properties, e.g. different levels of impurities throughout the bulk.

---

[9] In GALATEA, it occasionally happens that the contact between the Kapton printed circuit board and a segment becomes bad (high ohmic). This can sometimes be fixed by simply performing a warming-cooling cycle. However, the problem seems to have persisted for the complete time of data taking with Siegfried III.

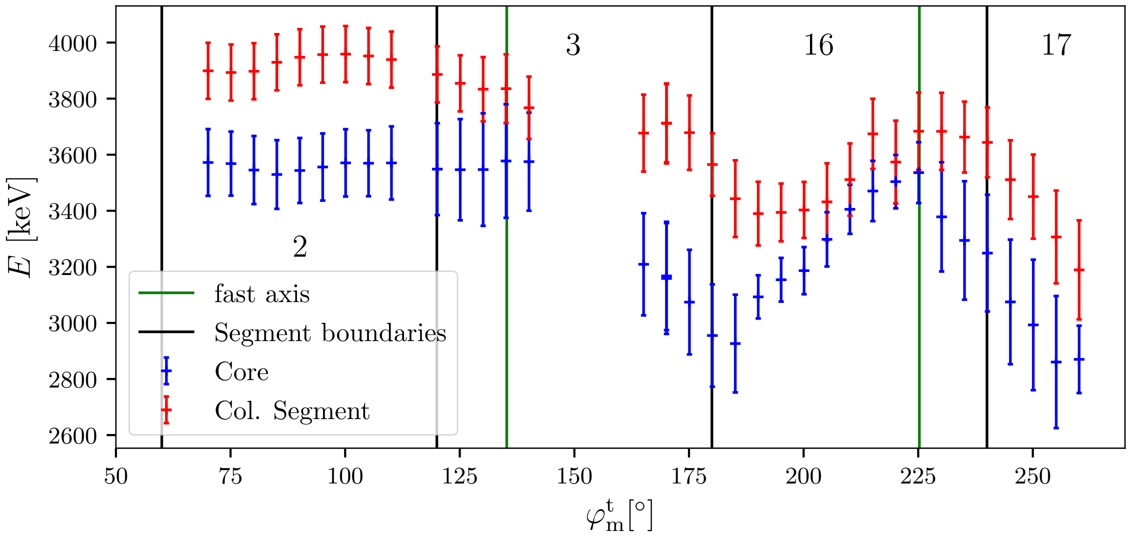

Figure 7.36.: Local modes of the parameter E_μ, together with the values of σ_1 presented as error bars, from alpha-induced events from the top source from the scan S3AmRotMid at $r_\mathrm{m} = 22.6\,\mathrm{mm}$. Also shown are the fast axes and segment boundaries and the numbers of the segments.

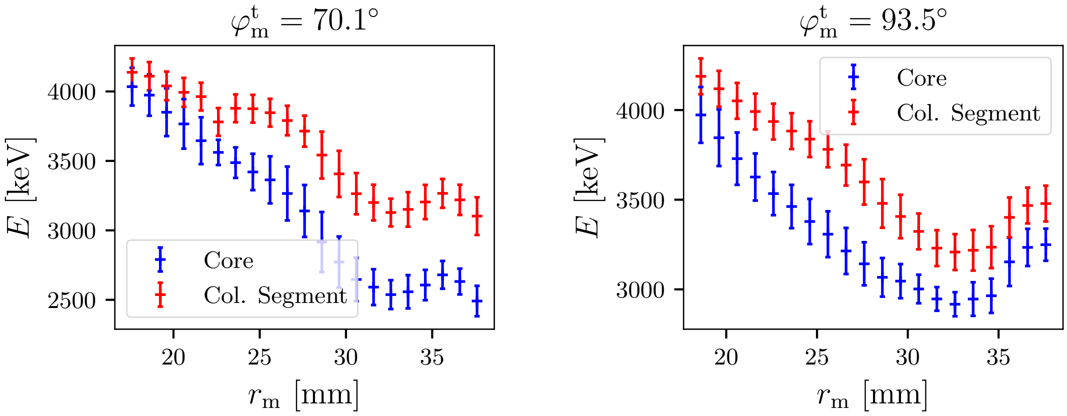

Figure 7.37.: Local modes of the parameter E_μ, together with the values of σ_1 presented as error bars, from alpha-induced events from the radial scans S3AmRad70 (left) and S3AmRad94 (right). The collecting segment is segment 2 in both cases.

7.6.3 Rise Times of Alpha Events

The means and standard deviations of the rise-time distributions of alpha events from the rotational scan S3AmRotMid are shown in Fig. 7.38 and from the two radial scans in Fig. 7.39.

The effect of the crystal axes is visible in the rotational scan for both the core and the segments 3, 16, and 17. The jumps in the rise times between the segments, e.g. between segment 16 and segment 17, is due to the different electronic response functions of these channels. There is also a jump between segments 2 and 3. However, the φ dependence of the rise time in segment 2 does not mirror the core rise time and is contrary to the predicted dependence of the crystal axes. This also indicates, that segment 2 had a high ohmic contact during this scan.

The data from the two radial scans do not show the same behavior than the data from the radial scans of Super Siegfried, where the core rise times became longer than the segment rise times at larger radii, see Fig. 7.22. This might be due to the contact problem of segment 2.

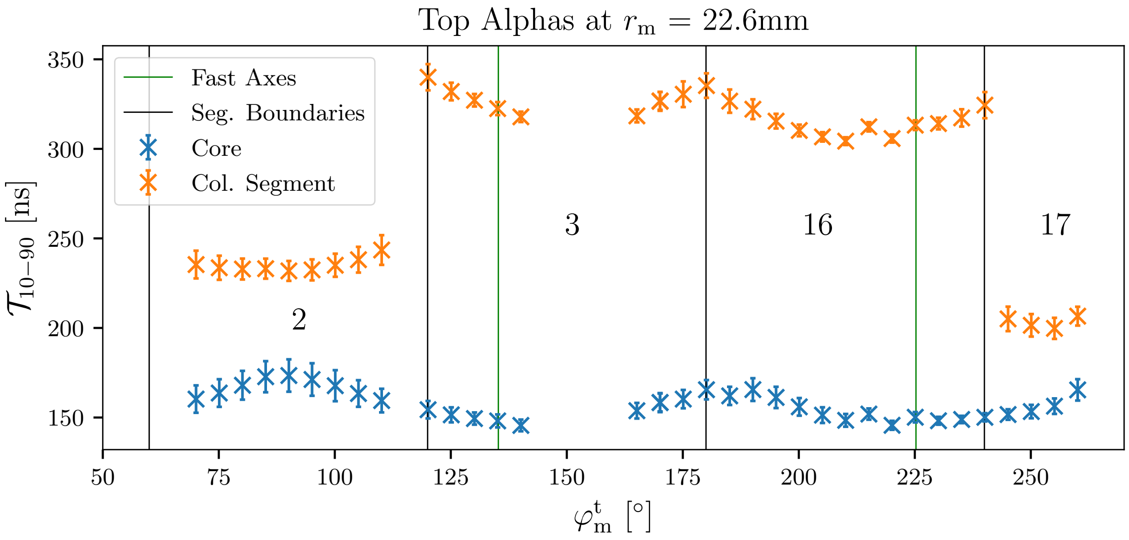

Figure 7.38.: Mean of the rise-time distributions of alpha-induced events from the top source from the scan S3AmRotMid. The error bars are not the uncertainties but the standard deviation of the rise-time distributions. Also shown are the positions of the fast axes as well the positions of the segment boundaries and the numbers of the segments.

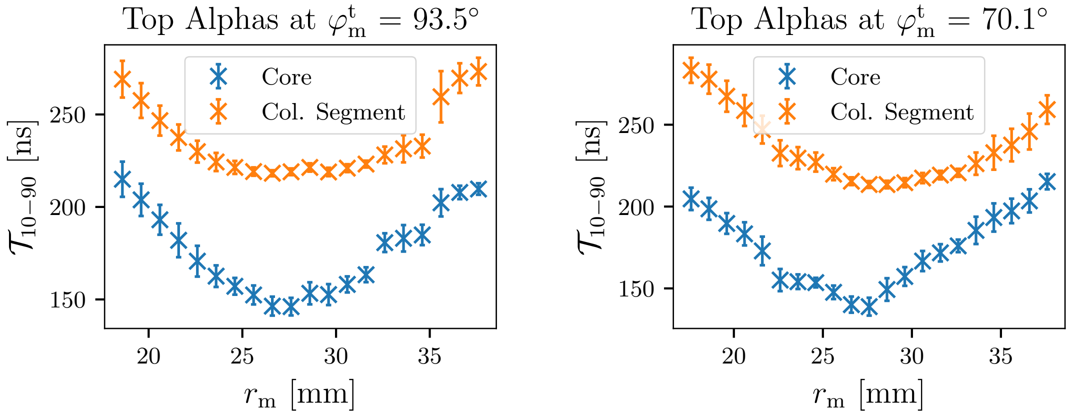

Figure 7.39.: Mean of the rise-time distributions of alpha events from the two radial scans S3AmRad70 (left) and S3AmRad94 (right). The error bars are not the uncertainties but the standard deviation of the distributions. The collecting segment is segment 2 in both cases.

7.6.4 Rise Times of Gamma Events

The means and standard deviations of the rise-time distributions of gamma events from the rotational scan S3AmRotMid are shown in Fig. 7.38 and from the two radial scans in Fig. 7.39.

They show the same φ dependence as for the alphas. The fact that segment 2 behaves for the low-energy gamma events as for alpha events strengthens the assumption of a high ohmic contact of segment 2, because the events induced by gammas are not located directly underneath the surface and, thus, should be less affected by surface effects.

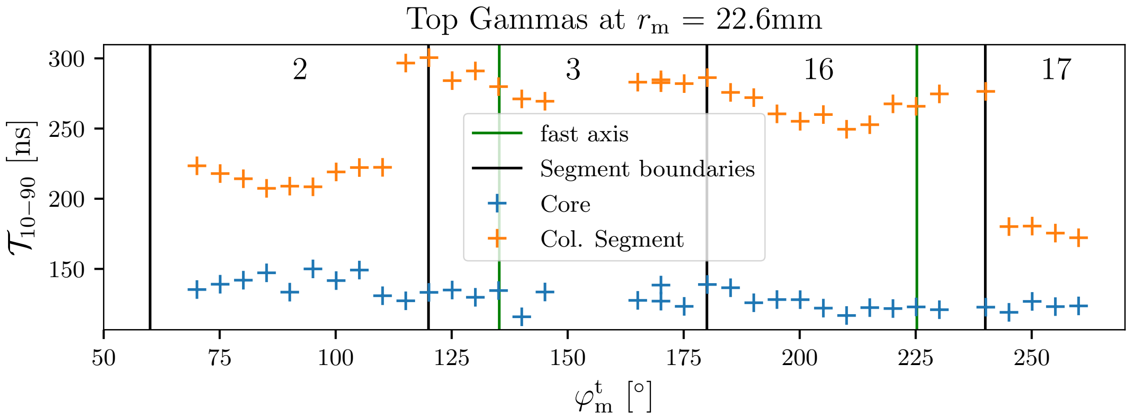

Figure 7.40.: Rise times $\mathcal{T}_{10-90}$ of the superpulses of the gamma events of ^{237}Np from the rotational scan S3AmRotMid. Also shown are the position of the fast axes as well the position of the segment boundaries and the numbers of the segments.

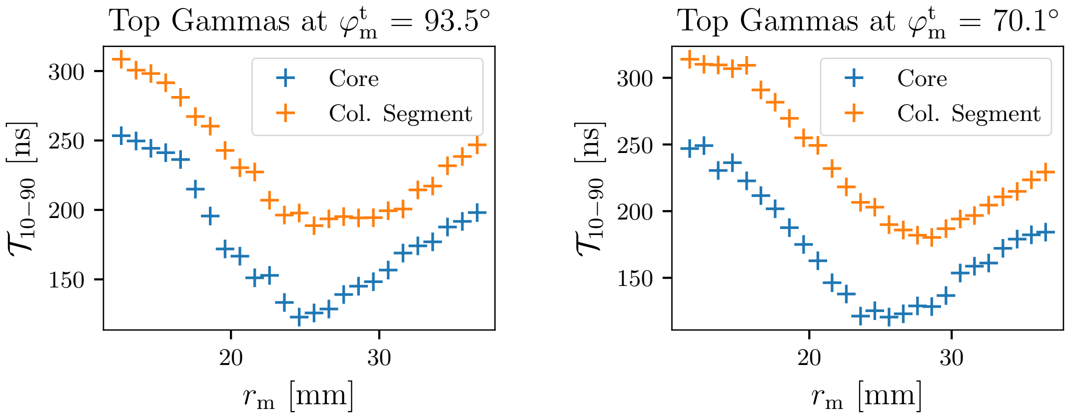

Figure 7.41.: Rise times $\mathcal{T}_{10-90}$ of the superpulses of the gamma events of ^{237}Np from the two radial scans S3AmRad70 (left) and S3AmRad94 (right). The collecting segment is segment 2 in both cases.

7.6.5 Conclusion

The behavior of segment 2 is not really understood. The segment did not behave like the other top segments, see Fig. 7.36. E_{μ} is constant at $r_{\mathrm{m}} = 22.6\,\mathrm{mm}$ over the whole φ range of the segment. The analysis of the two radial scans on top of segment 2, see Fig. 7.37, indicate that there was always more net electron trapping than hole trapping even for low radii. Also the dependence of the rise time of segment 2 on φ is against the expectation, see Fig. 7.38 and Fig. 7.40, As mentioned before, all this is probably due to a high ohmic contact of segment 2 during the data taking. However, this is not certain. It is planned to remeasure this segment after the Kapton tape is secured more tightly.

For the other segments 3, 16 and 17, the response of Siegfried III was similar to the response of Super Siegfried. Thus, it can be concluded that similar surfaces behave similarly. If detectors are made by the same manufacturer using the same production process, results from one detector can be used to predict the behavior of the others.

7.7 Summary of the Analysis of Alpha and Gamma Events

In this chapter, it was shown that events induced by alphas at the passivated surfaces of both detectors, Super Siegfried and Siegfried 3, are affected by charge trapping. This confirms previous studies [55, 70, 71, 82] with additional information obtained.

The dependence of charge trapping on the event position (r, φ) was further investigated. A strong φ-dependence was observed for the first time: Less charge trapping was observed for alphas located close to a fast axis than close to a slow axis, such that the observed energies differed by $\approx 1\,\mathrm{MeV}$, see Fig. 7.16. This effect of the crystal axes on the observed alpha energies was observed for both detectors.

In the previous studies, the top segment of Super Siegfried was only partially metallized and very long rise times up to 1000 ns were observed for the top segment for alpha interactions, see Fig. 7.18, and also for gamma interactions, see Fig. 7.23, located deeper in the bulk of the top segment. The core was also affected, but not as strong. The data presented in this chapter show that the reprocessing of Super Siegfried resulting in a fully metallized top segment changed the situation: The rise times for alpha interactions, see Fig. 7.21, and for gamma interactions, see Fig. 7.29, are no longer that long. However, a small dependence of the rise times in the top segment, ≈ 100 ns, on the distance in φ between the event location and the contact position of the top segment was still observable. In the core channel, no dependence could be observed anymore.

Chapter 8: Response to Betas

In the first phase of the LEGEND experiment currently under construction, the germanium detectors will be deployed in liquid Argon as it was done in the GERDA experiment. As described in Sec. 1.5.1, the decay chain of ^{42}Ar includes a beta decay above the $Q_{\beta\beta}$ of ^{76}Ge, which is a source of background. Such beta events have the same event topology as $0\nu\beta\beta$ events as the germanium detectors cannot resolve the two electrons of a $0\nu\beta\beta$ decay. The only difference is that background beta events will always be at the surface of a detector. Therefore, identifying and rejecting events very close to the surface would decrease the overall background level.

The germanium detector Super Siegfried was irradiated in GALATEA from the top and the side with betas from ^{90}Sr sources. The analysis of the data is presented in this chapter.

8.1 Radioactive Source Strontium: ^{90}Sr

The isotope ^{90}Sr beta decays into ^{90}Y, which beta decays into the stable isotope ^{90}Zr [83]. The two Q-values are

$$Q_\beta^{\mathrm{Sr}} = 546.0 \pm 1.4\,\mathrm{keV} \qquad (\mathrm{BR} = 100\,\%)\ , \tag{8.1}$$

$$Q_\beta^{\mathrm{Y}} = 2280.1 \pm 1.6\,\mathrm{keV} \qquad (\mathrm{BR} = 100\,\%)\ . \tag{8.2}$$

The stopping power for electrons of 2.2 MeV in silicon dioxide is about 1.6 MeVcm^2/g [91]. With an assumed density of sputtered silicon dioxide of 2.65 g/cm^3, the electrons on average deposit only about 0.85 keV in the 2 μm passivation layer on the top surface of Super Siegfried. This is negligible for the studies presented here.

8.2 Geant-4 Simulation for Strontium

The energy spectrum predicted by Geant-4 for Super Siegfried for a ^{90}Sr source in the top collimator of GALATEA, see Sec. 5.1, is shown in Fig. 8.1. Normalized, it is a predicted probability, p, for a particle emitted by the source to be observed with a certain energy. It shows the typical continuous spectrum of the two beta decays of Strontium and Yttrium. In addition to the simulated spectrum, the calculated beta emission spectrum of ^{90}Y above Q_β^{Sr} is shown [92]. Overall, the simulation matches the calculation very well. However, at lower (higher) energies, $<$ ($>$) 800 keV, the simulation

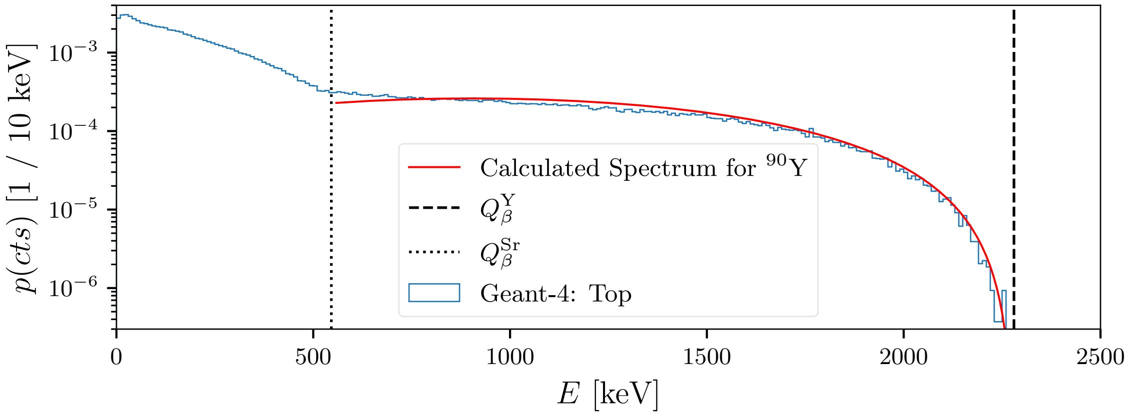

Figure 8.1.: Predicted to area normalized energy spectrum of Super Siegfried for a ^{90}Sr source inside the top collimator of GALATEA irradiating the top surface of the detector. The analytically calculated beta spectrum of ^{90}Y above Q_β^{Sr} is also shown.

predicts a bit more (less) betas than the analytic calculation. This can be explained by electrons being back scattered and not depositing all of their energy in the detector. This increases (decreases) the number of events with lower (higher) energies in the spectrum.

The normalized energy-weighted hit distributions of all simulated events are shown in Fig. 8.2. They are a measure for the probability, p, for a particle emitted by the source to deposit energy in a certain volume. Especially of interest is the penetration depth of electrons, see Fig. 8.2 a): In contrast to alphas, which deposit their energy within

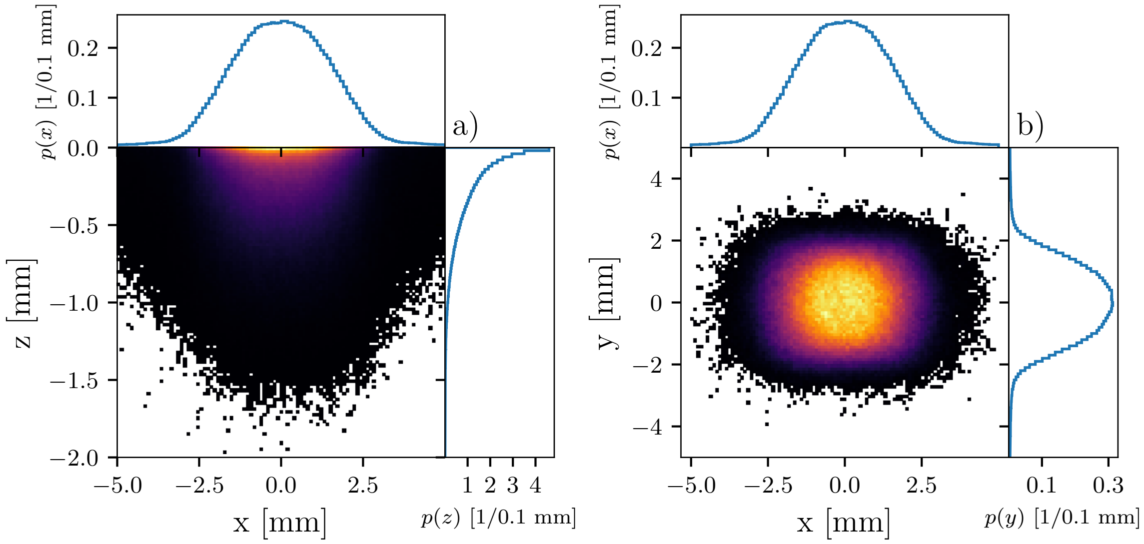

Figure 8.2.: Simulated energy-weighted hit distributions in a) x and z and in b) x and y induced by betas from the collimated ^{90}Sr source on top of the detector. The coordinate system is chosen such that the hits are centered around ($x = 0\,\mathrm{mm}, y = 0\,\mathrm{mm}$) and the origin of z corresponds to the detector top surface. The passivation layer is in positive z and hits there are not shown. Marginalizations along the corresponding dimension are also shown.

a few μm, electrons deposit their energy within $\approx 1\,$mm, because they are lighter and carry less charge than the alphas, see Sec. 2.7. This is compatible to the penetration depth of the 59.5 keV gammas of ^{237}Np. However, as can also be seen in Fig. 8.2 a) most of the energy is deposited close to the surface, even though the initial charge cloud for beta-induced events is larger than the initial charge cloud for alpha-induced events.

8.3 Scans with Strontium

One rotational scan, SSSrRot, and one radial scan, SSSrRad, were performed, see App. A.2. The position of the beam-spots of the measurements of both scans are shown in Fig. 8.3 and Fig. 8.4. During the rotational scan, the top and mantle were both irradiated at the same time. The activity of the source in the top collimator, $\approx 28\,$MBq, was more than one order of magnitude larger than the activity of the source in the side collimator, $\approx 1.3\,$MBq. Thus, for all measurements, the energy threshold of the DAQ was set to $\approx 500\,$keV, because, otherwise, the event rate from the top would have been to high for the DAQ to handle. Hence, only the continuous spectrum of ^{90}Y was recorded. As the low energy events from ^{90}Sr are not relevant for $0\nu\beta\beta$ background studies, the high energy threshold does not restrict the results significantly.

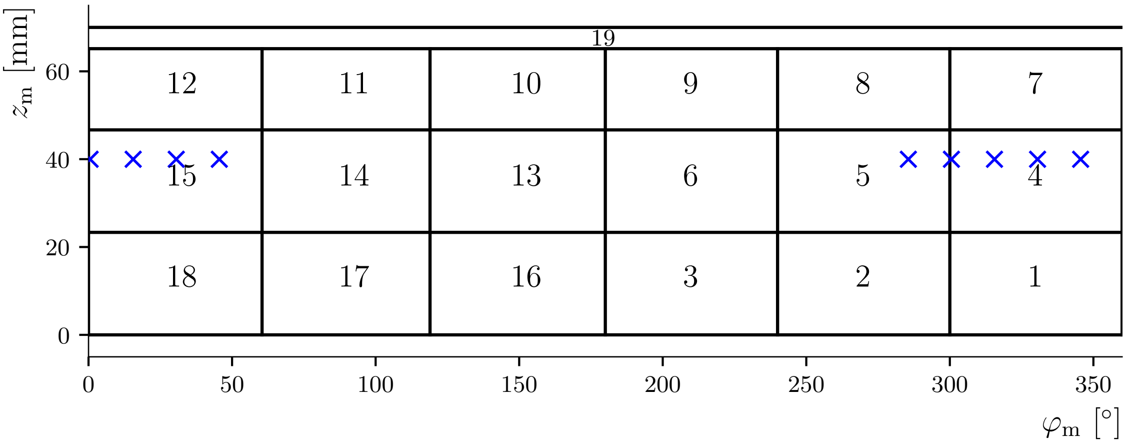

Figure 8.3.: Map of the side beam-spot positions of the rotational scan SSSrRot (blue) on the mantle surface of Super Siegfried.

8.4 Beta Event Selection

Beta events are single-site events. Thus, the S-cut, see Sec. 7.2.1, is used again to select all possible beta events of the respective collecting segment, $i = cs$. In all ^{90}Sr measurements both sources were irradiating the detector. Thus, cs was chosen either to be 19 in order to select and analyze betas from the top source or cs was chosen depending on the position of the side beam-spot in order to select and analyze the betas from the side source. The energy spectra of the core and the collecting segment before and after

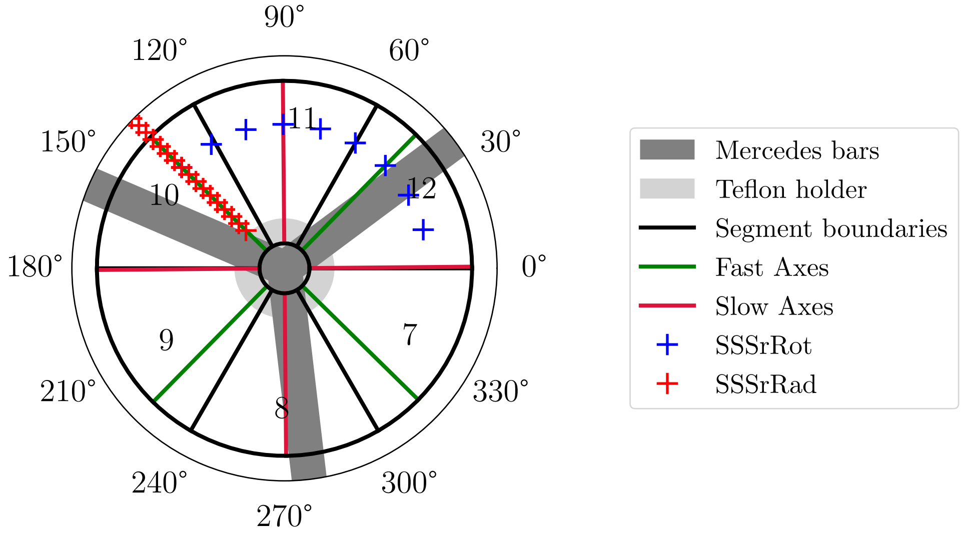

Figure 8.4.: Map of the top beam-spot positions of the rotational scan SSSrRot (blue) and the radial scan SSSrRad (red) on the top surface of Super Siegfried.

the application of the S-cut from two typical measurements are shown in Fig. 8.5 for the selection of betas on the side (side-betas) and in Fig. 8.6 for the selection of betas on the top (top-betas). The respective energy spectra from a background measurement are also shown.

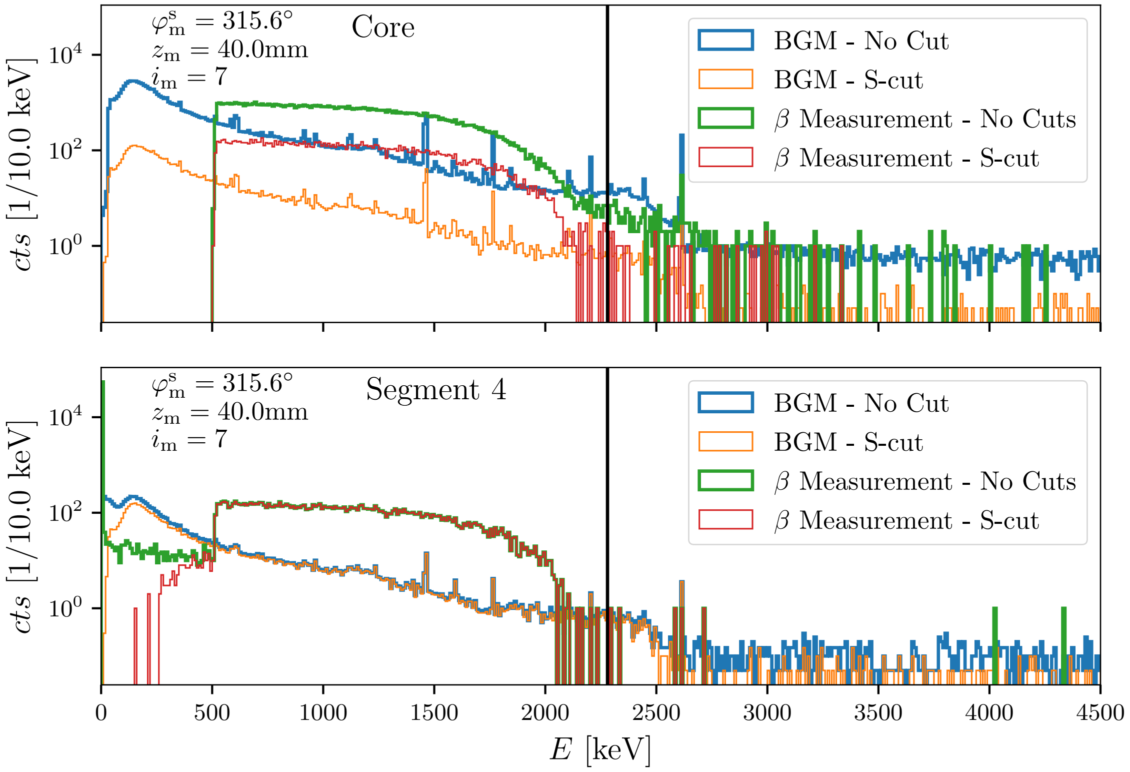

Figure 8.5.: Energy spectra before and after the S-cut ($cs = 4$) from the measurement at ($z_{\mathrm{m}} = 40.0\,\mathrm{mm}, \varphi^{\mathrm{s}}_{\mathrm{m}} = 315.6°$) from the side scan SSSrRot and from the background measurement, BGM. The BGM spectra are normalized to the run time of the measurement with ^{90}Sr. Q^{Y}_{β} is marked by a black line.

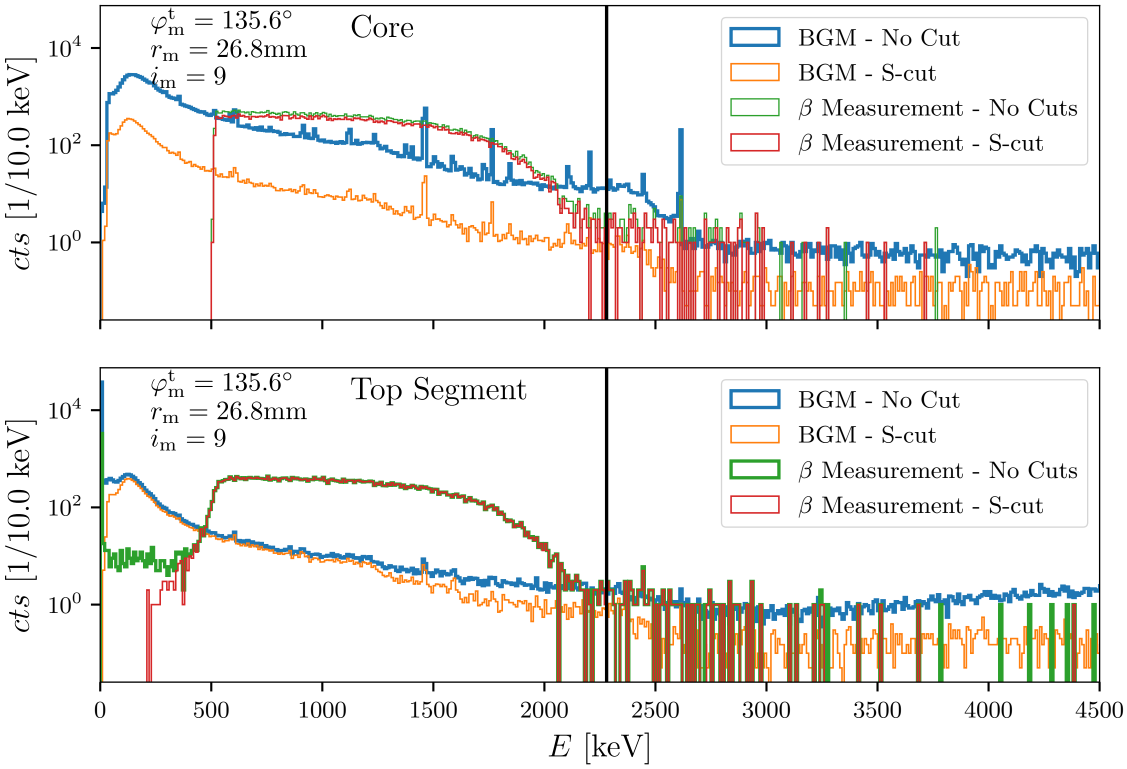

Figure 8.6.: Energy spectra before and after the S-cut ($cs = 19$) from the measurement at ($r_{\mathrm{m}} = 26.8\,\mathrm{mm}, \varphi_{\mathrm{m}}^{\mathrm{t}} = 135.6°$) from the top scan SSSrRad and from the background measurement, BGM. The BGM spectra are normalized to the run time of the measurement with ^{90}Sr. Q_{β}^{Y} is marked by a black line.

For the side-betas, see Fig. 8.5, the signal to noise ratio after the S-cut, count rate for the ^{90}Sr measurement over the count rate for the background measurement, is about one order of magnitude, $SNR \approx 10$, over the hole range between 500-2000 keV. In the core spectrum from the ^{90}Sr measurement before the S-cut, most events are beta-induced events from the top source, because it had a much higher activity than the side source. These events were removed efficiently with the S-cut, here $cs = 4$.

For the top-betas, see Fig. 8.6, the signal to noise ratio after the cut is even larger: almost two order of magnitude, $SNR \approx 100$, over the hole range between 500-2000 keV.

8.5 Beta Events on the Side

The analysis of events induced by betas on the side is presented first, because it is known from the measurements with ^{241}Am, that the inactive p$^+$-layer is very thin, $\approx 0.5\,\mu$m. Thus, for electrons, neither a reduction of the observed energy nor charge trapping is expected.

8.5.1 Spectral Analysis

The spectra of the core and of the collecting segment, here segment 4, after the application of the S-cut as previously shown in Fig. 8.5 are shown again in Fig. 8.7 together with the simulated beta spectrum from Fig. 8.1.

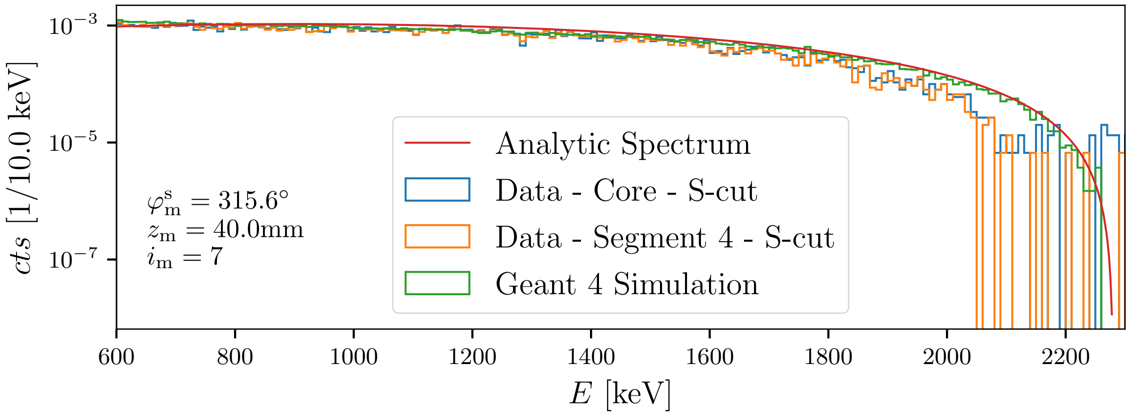

Figure 8.7.: Energy spectra after the S-cut from the scan SSSrRot at ($z_{m} = 40.0\,\text{mm}, \varphi^{s}_{m} = 315.6°$). The simulated beta spectrum and the calculated beta spectrum of ^{90}Y are also shown.

The simulation, which was performed for events on the top plate, can be used here for a comparison to data from the side because the energy reduction due to the passivation layer is negligible. Starting at around 1300 keV, both measured spectra show fewer entries than expected. The endpoints of the spectra seem to be reduced by $\approx 100 - 200\,\text{keV}$. This is most probably due to the thin encapsulation of the Strontium source, which reduces the energy of all electrons and shifts the whole spectrum towards lower energies. In addition, the source itself is a ball of powder with strontium mixed in. It has a diameter of 1 mm. Thus, only electrons at or near the surface of the source retain the full energy. Most of the betas pass through the powder for a short distance and lose some energy. This also leads to a reduced number of beta events with higher energies.

8.5.2 Search for Charge Trapping

The correlation between the segment 4 and core energy for events from a typical measurement of the scan SSSrRot after the application of the S-cut is shown in Fig. 8.8. The vast majority of selected events are single-segment events with equal segment and core energy.

Search for Electron Trapping

There are basically no events in the region of net electron tapping on the top left side of the diagonal, $E_4 > E_{\text{core}}$. Thus, no net electron trapping could be observed for events

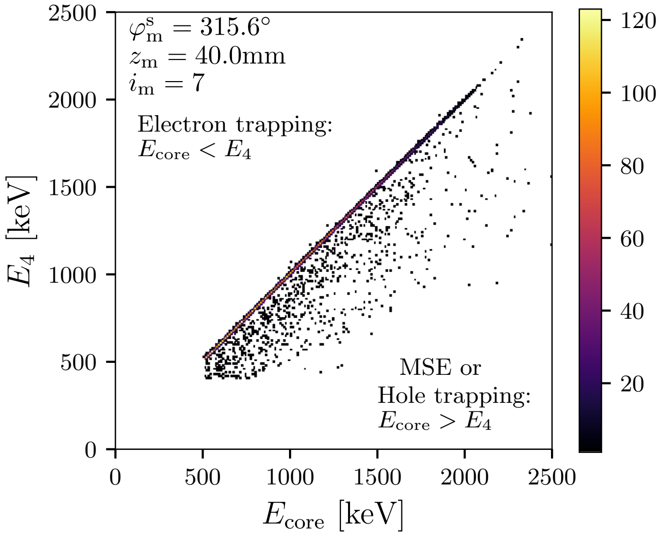

Figure 8.8: Correlation between segment 4 and core energy for all events remaining after the S-cut from the side scan SSSrRot at ($z_m = 40.0\,\text{mm}, \varphi_m = 315.6°$).

induced by betas on the side. This applies not only to surface effects at the mantle, but also to possible small amounts of bulk trapping during the drift of the electrons from the mantle through the bulk to the core.

Search for Hole Trapping

There are some events where the segment 4 energy is lower than the core energy, which can be background events from Compton scattered photons or beta events affected by hole trapping. These events were selected by the condition $E_{core} \geq E_{cs} + 5\,\text{keV}$, which is labeled as the *PHT*-cut (for *P*ossible *H*ole *T*rapping).

The information on the event position based on the pulses of the neighbouring segments was used for a further selection: All events induced by betas from the side source should produce negative mirror pulses as the event position is directly at the mantle surface and the holes are collected immediately and only the electrons induce signals on the neighbouring segments nS during their drift towards the core. The pulses of the core, collecting segment and neighbouring segments, here $nS \in \{1, 5, 7, 15\}$, of a typical beta event with $E_{core} \approx E_4$ from the side scan SSSrRot at ($z_m = 40\,\text{mm}, \varphi^{s}_{m} = 315.6°$) are shown in Fig. 8.9. Because for this measurement, the beam-spot lies in the upper left site of segment 4, see Fig. 8.3, the amplitudes of the negative mirror pulses in the segments to the left and on top are larger than the amplitudes of the negative mirror pulses in the segments to the right and underneath. All the mirror pulses return to the baseline and, thus, an energy of $\approx 0\,\text{keV}$ is measured. An energy of $\approx 0\,\text{keV}$ was observed in all other non-collecting segments rS for this event.

In case of hole trapping, the neighbouring segments would show a positive signal induced by the trapped holes after the collection of the electrons. As these holes would be close to segment 4, basically at the position of the event, the highest signals would be induced in one of the neighbouring segments.

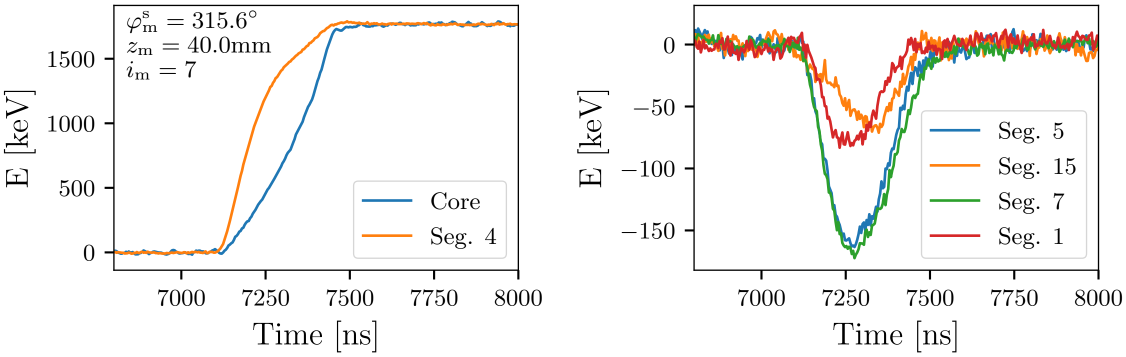

Figure 8.9.: Pulses of a typical beta event from the side scan SSSrRot at ($z_{\mathrm{m}} = 40\,\mathrm{mm}, \varphi^{\mathrm{s}}_{\mathrm{m}} = 315.6°$) in the core and the collecting segment (Seg. 4) on the left and in the neighbouring segments (left: Seg. 5, top: Seg. 7, right: Seg. 15, below: Seg. 1) on the right.

Therefore, the NHT-cut (for Neighbor and Hole Trapping) was defined. It removes all events where the maximum of recorded energies of the neighbouring segments nS, $\max\{E_{nS}\}$, is smaller than the maximum of the recorded energies in the remaining non-collecting segments rS, $\max\{E_{rS}\}$.

Only 3.6 % of the events selected with the S-cut remained after the application of the combined PHT+NHT-cut. However, the remaining events are not necessarily events affected by hole trapping. They can still be background events from Compton scattered photons.

Sum of the Segment Energies

The sum of the segment energies, $E_{\Sigma\mathrm{Segs}}$, always equals E_{core} for events not affected by charge trapping. Thus, the quantity

$$\Delta E^{\mathrm{core}}_{\Sigma\mathrm{Segs}} = E_{\Sigma\mathrm{Segs}} - E_{\mathrm{core}} \tag{8.3}$$

should be centered around zero in the absence of charge trapping. The distributions of $\Delta E^{\mathrm{core}}_{\Sigma\mathrm{Segs}}$ for events after and prior to the application of the PHT+NHT-cut from a typical side-beta measurement and the background measurement are shown in Fig. 8.10. Both distributions from BGM are centered around zero as expected. Both distributions from the beta measurement are centered at about 1.1 keV. Thus, there is no difference between events with $E_{\mathrm{core}} \approx E_{cs}$ and events remaining after the cuts. The small shift of 1.1 keV would actually be an indication for electron trapping, even though these events lie in the region of possible hole trapping in Fig. 8.8. However, this is most probably just due to an imperfect cross-talk correction [51] as the beta measurements were shorter[1] than the background measurement and had much less background gamma-line events used for the calibration procedure. This lead to a worse energy resolution and larger

---

[1] In order to keep the amount of data reasonable due to the high activity of the beta source in the top collimator.

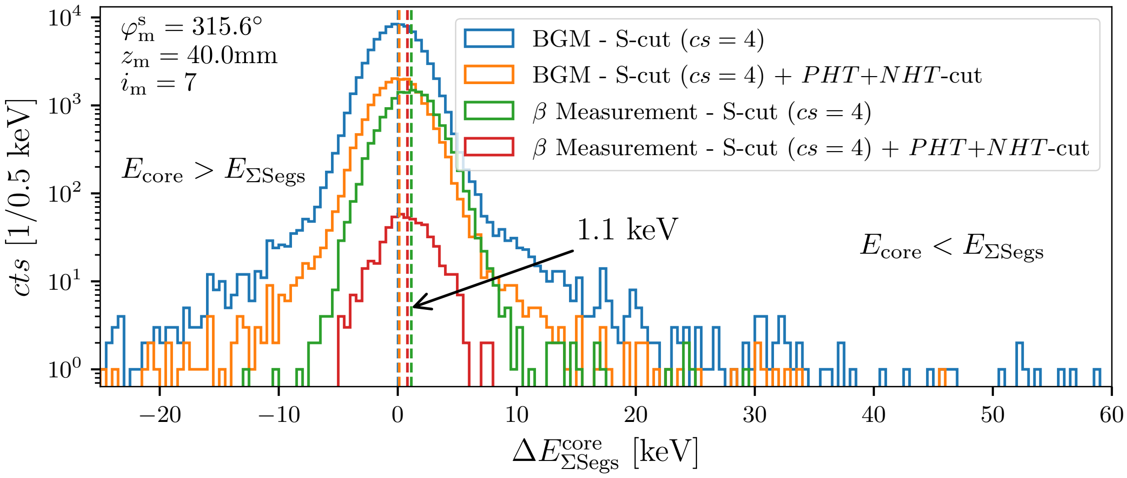

Figure 8.10.: Distributions of $\Delta E_{\Sigma\mathrm{Segs}}^\mathrm{core}$ from the scan SSSrRot at ($z_\mathrm{m} = 40.0\,\mathrm{mm}, \varphi_\mathrm{m} = 315.6°$) and from the BGM. Segment 4 was chosen in the background measurement as the collecting segment for the S-Cut. The dashed vertical lines mark the means of the distributions.

systematic uncertainties on the calculated energies and, thus, on $E_{\Sigma\mathrm{Segs}}$.

However, the condition $E_{\Sigma\mathrm{Segs}} \approx E_\mathrm{core}$ for the events after the PHT+NHT-cut does not exclude charge trapping, because the weighting potentials do add up to 1 (within the energy resolution) along the drift paths of the events induced by side-betas ($z_\mathrm{m} = 40\,\mathrm{mm}$). This is shown in Fig. 8.11. The weighting potentials only do not add up to one close to the floating surface. Thus, $E_{\Sigma\mathrm{Segs}} \approx E_\mathrm{core}$ only shows that holes (or electrons) did not vanish.

In conclusion, there is no sign of charge trapping for beta events on the side, but an effect on the below one-permille level cannot be excluded.

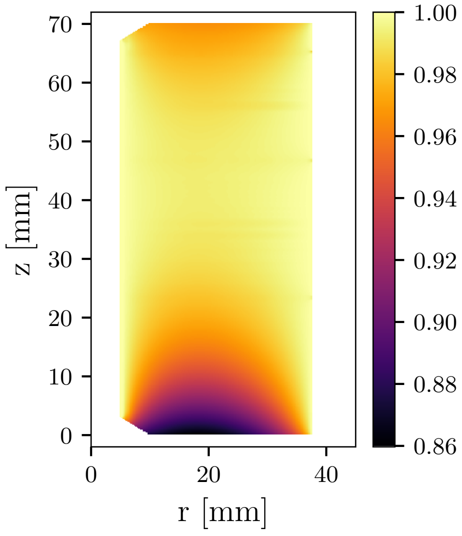

Figure 8.11: Sum of all weighting potentials of Super Siegfried inside the detector at $\varphi = 30°$ as simulated with SSD.

Identification of Side-Betas

It can be concluded that events induced by betas on the side cannot be identified by studying the energies observed in the core or the collecting segment. In addition, no pulse-shape characteristic, like DCR for top-alphas, could be identified by looking at the pulses of beta events, e.g. see Fig. 8.9. This was also not expected, because the detector response to side-alphas was also such that they could not be identified.

8.6 Beta Events on the Top

The question is whether beta-induced events on the top of the detector can be identified.

8.6.1 Spectral Analysis

The spectra of the core and of the top segment after the application of the S-cut as previously shown in Fig. 8.6 are shown again in Fig. 8.12 together with the simulated beta spectrum from Fig. 8.1. The source on the top had a similar encapsulation as the source on the side, resulting in a similar shift of the spectrum towards lower energies.

The spectra of the top- and the side-betas look very similar. In order to quantify this, the mean values of the core histograms after the S-cut in the energy interval 1600-2200 keV, $\overline{E}_{\mathrm{core}}^{1.6-2.2}$, were determined for each measurement of the two scans. For the rotational scan, the values of $\overline{E}_{\mathrm{core}}^{1.6-2.2}$ were also determined for the beta-induced events from the side (selected with the respective S-cut). The expectation value and standard deviation of the values of $\overline{E}_{\mathrm{core}}^{1.6-2.2}$ are given in Tab. 8.1. The values for the top- and side-betas agree within statistical uncertainties.

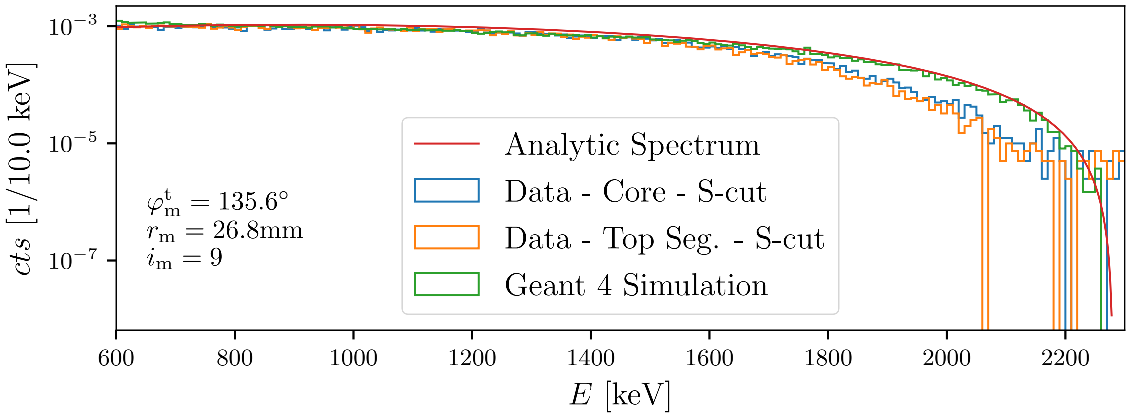

Figure 8.12.: Energy spectra after the S-cut from the scan SSSrRad at ($r_{\mathrm{m}} = 26.8$ mm, $\varphi_{\mathrm{m}}^{\mathrm{t}} = 135.6°$). The simulated beta spectrum and the calculated beta spectrum of ^{90}Y are also shown.

Scan	Top/Side	$E[\overline{E}_{\text{core}}^{1.6-2.2}]$	$\sigma[\overline{E}_{\text{core}}^{1.6-2.2}]$
SSSrRot	Side	1756 keV	5 keV
SSSrRot	Top	1748 keV	3 keV
SSSrRad	Top	1750 keV	2 keV

Table 8.1.: Expectation values and standard deviations of the mean values $\overline{E}_{\text{core}}^{1.6-2.2}$ of the spectra from each dataset. For the scan SSSrRot the values were determined for both sources.

8.6.2 Search for Charge Trapping

The correlation between the observed energies in the top segment and the core for events from a typical measurement from the top scan SSSrRad after the application of the S-cut, $cs = 19$, is shown in Fig. 8.13. Overall, it looks similar to the correlation as observed for events induced by side-betas, see Fig. 8.8. Most of the beta events lie on the diagonal line associated with single-segment events and unusual clusters are not present. However, there are more entries on both side of the diagonal, showing that some part of the beta-induced events are affected by charge trapping at the top surface.

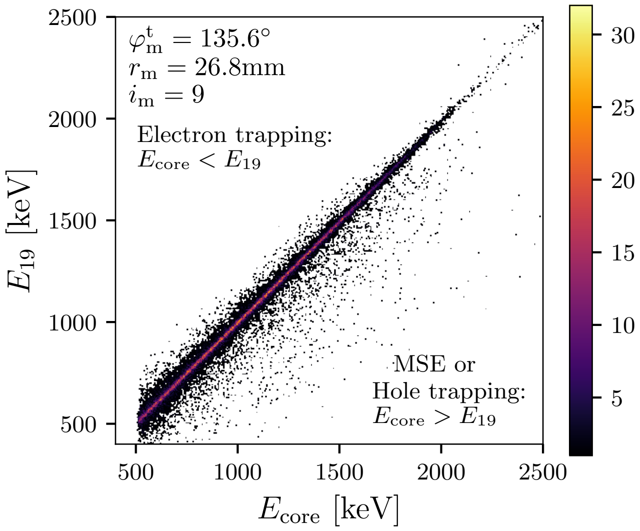

Figure 8.13: Correlation between the energy observed in the top segment and the core energy for all events remaining after the S-cut with $cs = 19$ from the scan SSSrRad at ($r_{\text{m}} = 26.8$ mm, $\varphi^{\text{t}}_{\text{m}} = 135.6°$).

Search for Electron Trapping

The events in the region of possible electron trapping are selected by the condition $E_{cs} - E_{\text{core}} > 5$ keV. This cut is labeled as the PET-cut (for Possible Electron Trapping), which 17 % of the S-cut selected events pass.

The top beam-spot covered the top segment above segment 10 for all measurements of

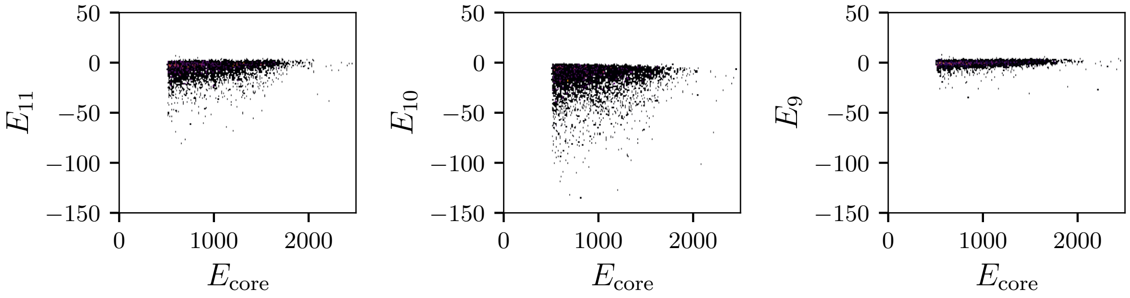

Figure 8.14.: Correlations between the observed energies in the segments 9, 10 and 11 and the core energy for all events remaining after the S-cut and the *PET*+*NET*-cuts from the scan SSSrRad at ($r_\text{m} = 26.8\,\text{mm}, \varphi^\text{t}_\text{m} = 135.6°$).

the top scan SSSrRad, see Fig. 8.4. Thus, in case of net electron trapping, segment 10 should always detect more "negative energy" than all other remaining non-collecting segments, rs. Therefore, the *NET*-cut (for *N*eighbor and *E*lectron *T*rapping) was defined which removes all events where the recorded energy of segment 10, E_{10}, is larger than the minimum of the recorded energies in the remaining non-collecting segments, $E_{10} > \min\{E_{rS}\}$. 86 % of the PET-cut selected events passed the *NET*-cut.

The correlations between the energies observed in the segments underneath the top segment closest to the top beam-spot, segments 9, 10 and 11, and the core energy of the events remaining after the S-cut and the *PET*+*NET*-cuts are shown in Fig. 8.14. Segment 11 shows more "negative energy" than segment 9 for these events because the top beam-spot was covering segment 10 closer to segment 11 than to segment 9, see Fig. 8.4. The appearance of large "negative energies" in segment 10 is a clear indication of some net electron trapping in part of the events.

Search for Hole Trapping

The events in the region of possible hole trapping, $E_{cs} < E_\text{core}$, were selected by the *PHT*-cut, see Sec. 8.5.2. 63 % of the S-cut selected events from the scan SSSrRad at 26.8 mm passed the *PHT*-cut.

In addition, the *NHT*-cut was applied in order to remove events induced by Compton scattered photons with $\max\{E_{nS}\} = E_{10}$ for the radial top scan SSSrRad. In this case, 53 % of the S- and PHT-cut selected events passed the *NHT*-cut.

The correlations between the energies observed in the segments underneath the top segment closest to the top beam-spot, segments 9, 10 and 11, and the core energy of the events remaining after the S-cut and the *PHT*+*NHT*-cuts from a typical top-beta measurement of the top scan SSSrRad are shown in Fig. 8.15. Segment 11 detects more energy than segment 9 for these events because the top beam-spot was covering segment 10 closer to segment 11 than to segment 9, see Fig. 8.4. The appearance of large positive energy in segment 10 is an indication of some net hole trapping in part of the events.

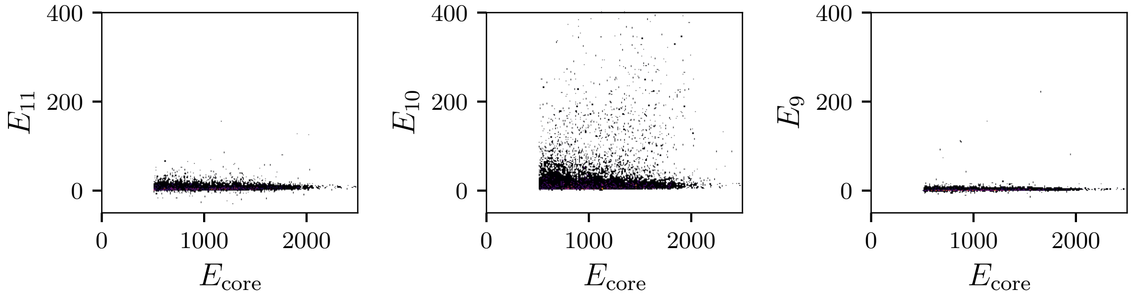

Figure 8.15.: Correlations between the observed energies in the segments 9, 10 and 11 and the core energy for all events remaining after the S-cut and the *PHT*+*NHT*-cuts from the top scan SSSrRad at ($r_{\rm m}$ = 26.8 mm, $\varphi^{\rm t}_{\rm m}$ = 135.6°).

Sum of the Segment Energies

For events at the floating surface affected by hole trapping $E_{\Sigma\rm Segs}$ should be smaller than $E_{\rm core}$, because the weighting potentials to not add up to 1 in this area, see Fig. 8.11. The distributions of $\Delta E^{\rm core}_{\Sigma\rm Segs}$ determined for events prior and after the application of the *PHT*+*NHT*-cut from a typical top-beta measurement of the scan SSSrRad are shown in Fig. 8.16.

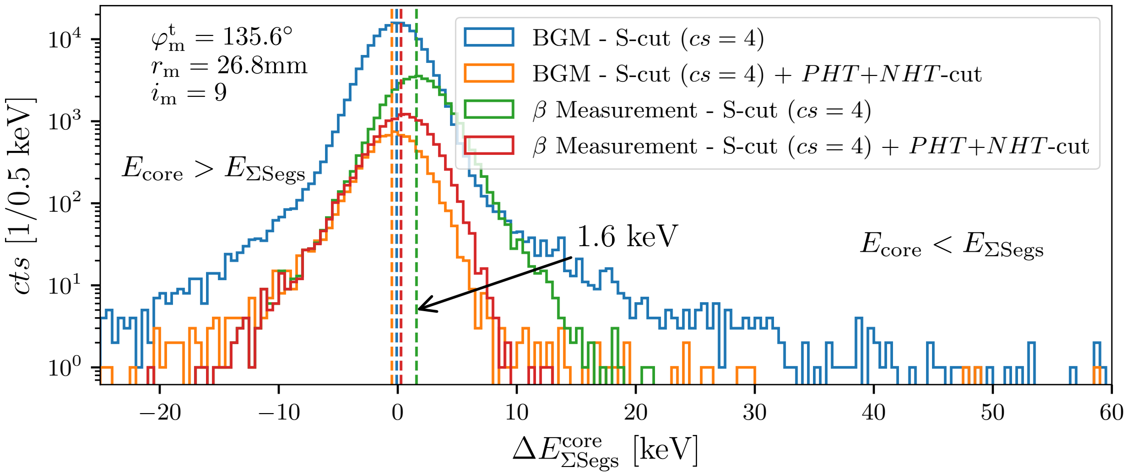

Figure 8.16.: $\Delta E^{\rm core}_{\Sigma\rm Segs}$ distributions from the top scan SSSrRad at ($r_{\rm m}$ = 26.8 mm, $\varphi^{\rm t}_{\rm m}$ = 135.6°) and from the BGM. Segment 19 was chosen in the background measurement as the collecting segment for the S-Cut. The dashed vertical lines mark the mean of the distributions.

The shift of 1.6 keV of the mean of the distribution of the beta measurement after the S-cut is, again, most probably due to an imperfect cross-talk correction. However, there is a small difference of the distribution in comparison to the distributions of events induced by betas from the side, see Fig. 8.10. The distribution of the beta measurement after the *PHT*+*NHT*-cut is slightly shifted, ≈ 1.3 keV, towards lower values which is an indication for net hole trapping. The shift is that small because most of the events are close to the diagonal line of single-segment events in Fig. 8.12 and the difference between the sum of the weighting potentials and 1 is only on the percent level. Thus, it took a very good energy resolution in all channels to detect this small difference $\Delta E^{\text{core}}_{\Sigma\text{Segs}}$ indicating small amounts of trapped charges in a minority of events.

Fractions of Events affected by Charge Trapping

The survival probabilities of S-cut selected events for the $PHT+NHT$-cut or the $PET+NET$-cut to select events with possible hole or electron trapping as determined for the radial scan SSSrRad are shown in Fig. 8.17.

On average, the combined survival probabilities do not exceed 0.5. Thus, at least half of the events induced by betas at the top are not affected by any net charge trapping. And at least $\sim 90\,\%$ are not affected by electron trapping.

Some small radial dependence is observed. It looks like more events could be affected by net electron charge trapping at higher radii whereas hole trapping seems more probable at lower radii. In both cases, the probability of trapping increases for longer drifts. A dip in the probability for hole trapping at $r_\text{m} = 24.8\,\text{mm}$ is visible. At this radius, the drift time of electrons and holes is about the same. Thus, the net trapping is more likely to be zero which leads to a decreased identification probability.

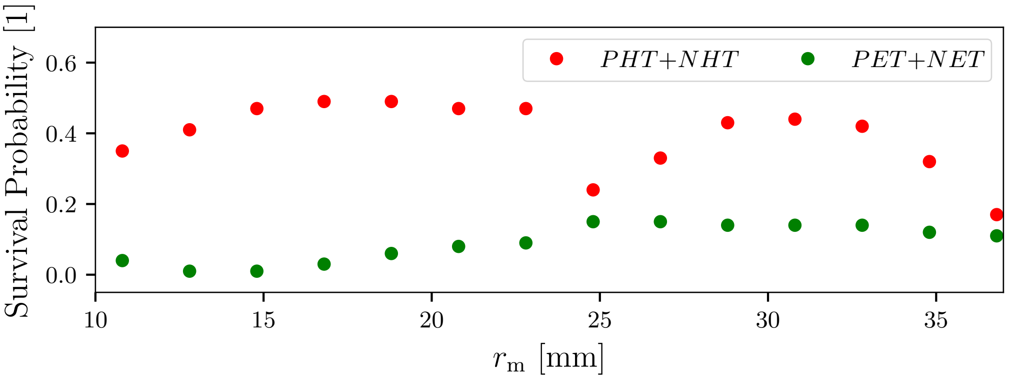

Figure 8.17.: Survival probabilities of S-cut selected events for the PHT-cut and NHT-cut or the PET-cut and NET-cut determined from the radial scan SSSr-Rad.

8.6.3 Pulses of the Neighbouring Segment

For the radial scan SSSrRad the segment underneath was always segment 10. The correlations between TR_{10}, see Sec. 7.2.3, and E_{10} for S-cut selected events for three different radial positions of the scan SSSrRad are shown in Fig. 8.18.

For all three position, a vertical line at $E_{10} = 0\,\text{keV}$ is visible. These are events where

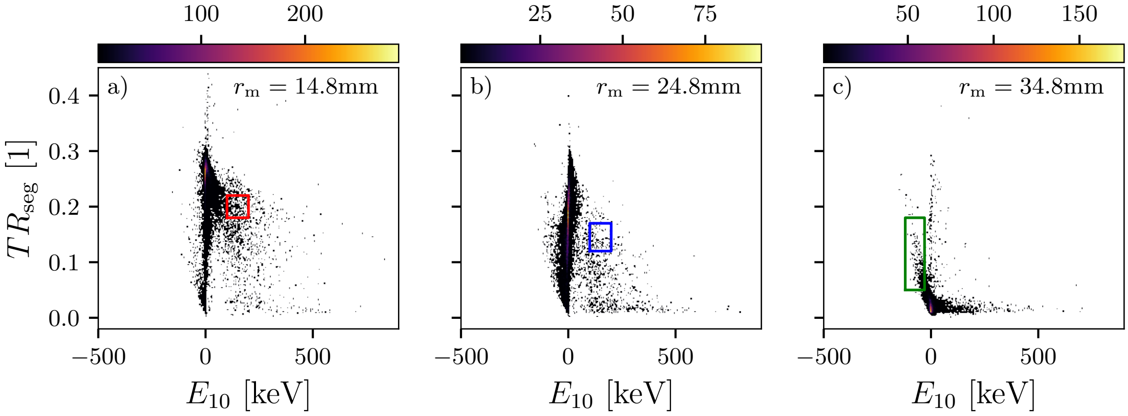

Figure 8.18.: Correlations between TR_{10} and E_{10} for S-cut selected events for three different radial positions of the scan SSSrRad. The bin width of the x-axis (y-axis) is 1 keV (0.001). The boxes mark areas used to select events for the demonstration of pulse shapes, see Fig 8.19.

the pulse in segment 10 is a normal mirror pulse. Thus, there is no net charge trapping. In addition, there is a horizontal line at $TR_{10} = 0$ visible for all positions. Multi-site events induced by Compton scattered photons fall into this region as explained earlier, see Sec. 7.2.3.

A cluster of events appears on the right side of the vertical line and above the horizontal line of $TR_{10} = 0$ for lower radii, see Fig. 8.18 a). These are events which are affected by hole trapping. This is expected because at lower radii, the drift path of the holes is longer. In Fig. 8.18 b), events affected by net hole trapping and net electron trapping both occur, while as seen in Fig. 8.18 c), at larger radii, more events are affected by net electron trapping as now the drift path of the electrons is longer. Thus, the clustering of events at $r_\mathrm{m} = 24.8\,\mathrm{mm}$ around the vertical line of $E_{10} = 0\,\mathrm{keV}$ is in agreement with the explanation for the dip in the survival probability of the $PHT{+}NHT$-cut, see Fig. 8.17.

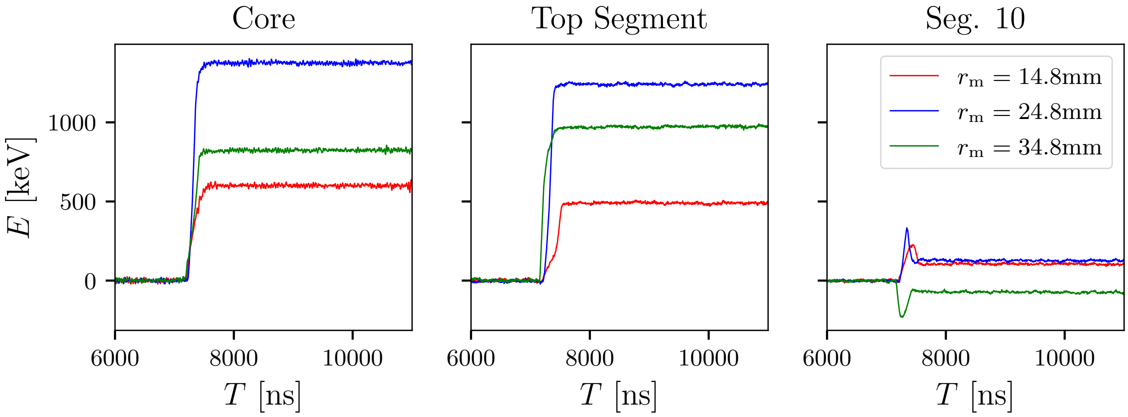

Figure 8.19.: Pulses of typical events from the scan SSSrRad at three different radial positions selected from the corresponding (matching colors) areas shown in Fig. 8.18.

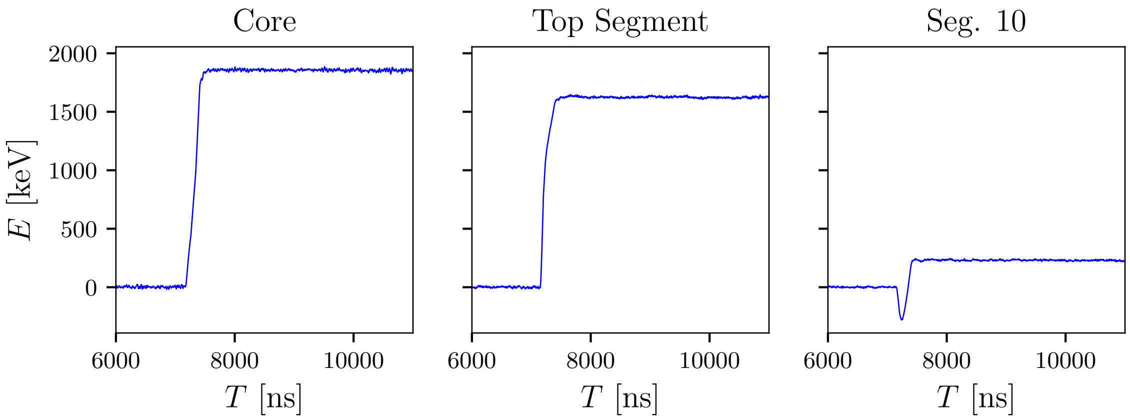

Figure 8.20.: Pulses of an event from the scan SSSrRad at $r_\mathrm{m} = 34.8\,\mathrm{mm}$ selected from the horizontal line in Fig. 8.18 c).

The pulses of the core, the top segment and the segment underneath (Seg. 10) of selected events for three different radial positions r_m, see Fig. 8.18, are shown in Fig. 8.19. For the core and top segment, normal collecting pulses are observed. The segment underneath, however, shows truncated mirror pulses.

Figure 8.18 c) shows that at the position of $r_\mathrm{m} = 34.8\,\mathrm{mm}$, the horizontal line at $TR_{10} = 0$ is also filled with more events. These are events where the signal during the drift is dominated by the electrons resulting in negative mirror pulses. Thus, $MPA_{10} \approx E_{10}$ and $TR_{10} \approx 0$. After the drift, the signal is dominated by the trapped holes which are close to segment 10. Thus, $E_{10} > 0\,\mathrm{keV}$. Such an event with a mixed truncated mirror pulse in the segment 10 is shown in Fig. 8.20.

8.6.4 Analysis of the Tail of the Pulses

The decay constant distributions for all events before and after the application of the S-cut from a typical measurement of the scan SSSrRad are shown in Fig. 8.21. Due to the large activity of the source, most of the events are beta-induced events. Thus, the background events would form a second smaller peak in these decay constant distributions if DCR, see Sec. 7.2.2, would be present for top-beta events.

All distributions for the core are aligned. For the segment, the distribution from BGM after S-cut does not perfectly align with the distributions from the beta measurement. However, this does not mean that there is DCR in the segment pulses, as this is probably due to different environmental conditions in GALATEA between the two measurements, i.e. the pre-amplifiers are very sensitive to temperature changes.

To verify that DCR does not occur for beta events, the linear slopes of the tails were determined for events from a beta and an alpha measurement within the same region of the top plate and the distributions of those are shown in Fig. 8.22. The alpha events form peaks clearly separated from the peaks at 0, which are composed of "normal" events

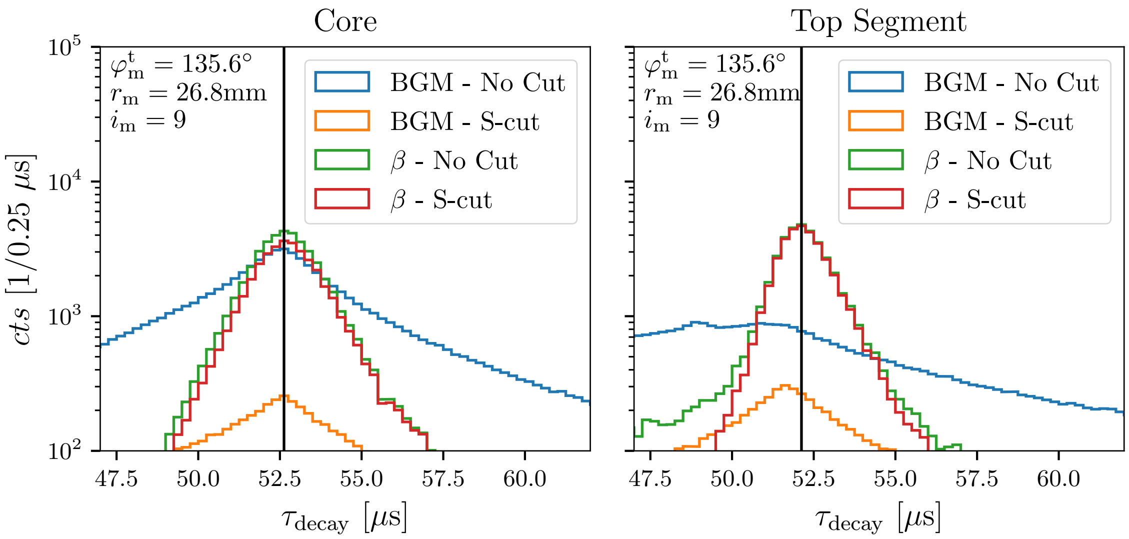

Figure 8.21.: Distributions of individual decay constants as determined for events before and after the application of the S-cut of the core (left) and the top segment (right) from the top scan SSSrRad at ($r_m = 26.8$ mm, $\varphi_m = 135.6°$) and from the background measurement BGM. The black line is the mode of the distribution from the beta measurement after the S-cut.

while the distribution for the beta events is merely broadened. Thus, the search for DCR is only effective for alpha-induced events.

The tails to the right side in all distributions consists of multi-site, saturation and pile-up events. This was checked by looking at the individual pulses of those events.
In summary, DCR due to charge trapping in beta-induced events could not be identified.

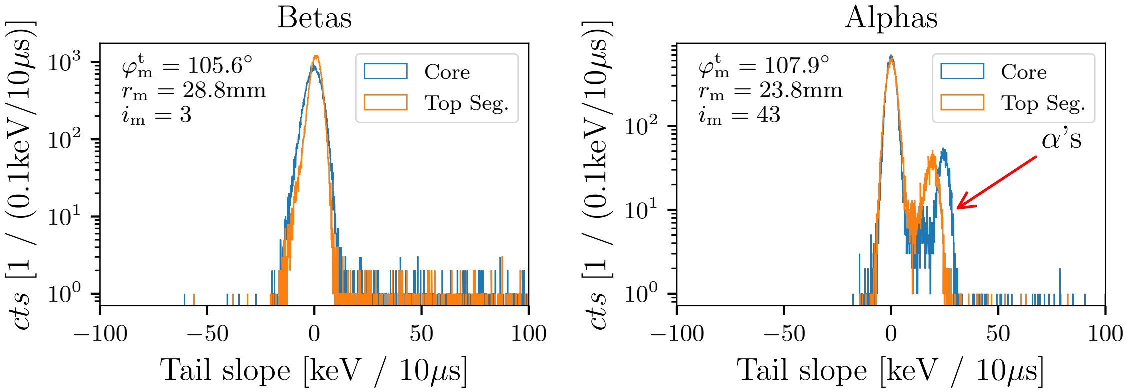

Figure 8.22.: Distributions of the tail slopes as determined for events after the application of the S-cut (left) from the top scan SSSrRot at ($r_m = 28.8$ mm, $\varphi_m = 105.6°$) and (right) from the top scan SSAmRotMid at ($r_m = 23.8$ mm, $\varphi_m = 107.9°$).

8.6.5 Distributions of Pulses

The distributions of normalized pulses of the core and the top segment were used to look for special pulse-shape characteristics to identify beta-induced events based on single pulses without using the information of multiple channels. Figure 8.23 shows two such distributions in form of histograms filled with the pulses of events remaining after the S-Cut and which have a core energy in the interval[2] 1500-1510 keV.

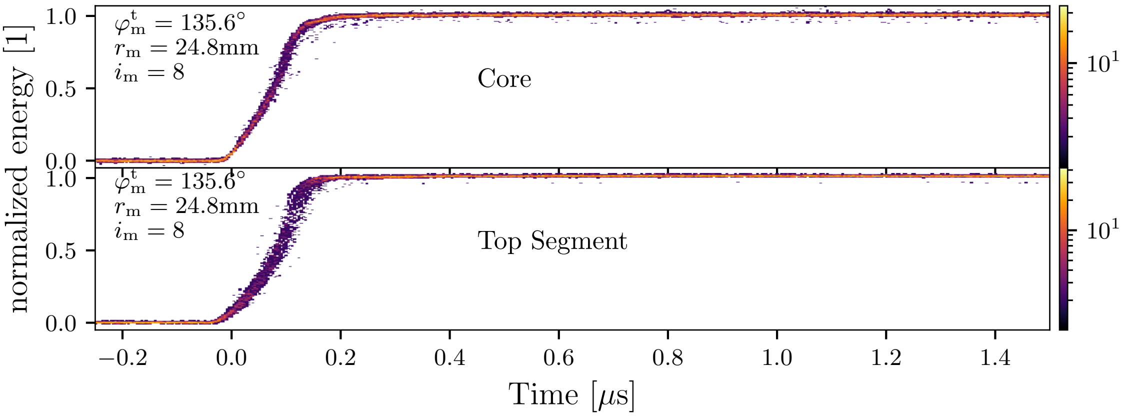

Figure 8.23.: Heatmap filled with normalized pulses from the core and the top segment of the measurement of the scan SSSrRad at ($r_\mathrm{m} = 28.8\,\mathrm{mm}, \varphi_\mathrm{m} = 105.6°$) of S-cut selected events with $E_\mathrm{core} \in [1500\,\mathrm{keV}, 1510\,\mathrm{keV}]$. Only bins with at least two entries are shown for reasons of visibility. The pulses were aligned by time such that the normalized core amplitude equals to 0.05 at 0 μs.

The pulses are very fast as they reach their full amplitude already within $\approx 200\,\mathrm{ns}$ and no DCR is observable. For the core, some pulses with slow end are observed. However, these are just a minority of the events and they could be background events. The majority of pulses show no unusual pulse characteristics. Thus, beta events cannot be effectively identified in detectors where only the core is read out.

---

[2] These distributions of pulses were checked for all measurements and also for different intervals of core energy.

8.7 Comparison to Alphas and Conclusion for LEGEND

Events induced by betas on the side of the detector, at the p$^+$-contact, looked like normal events without any special characteristics. This was expected as, events induced by alphas in this region did not show any special characteristics. This makes n-type detectors undesirable for LEGEND, if beta-induced events in the region of interest are present.

At the top surface of Super Siegfried, however, the beta events were affected by charge trapping. About half of the events showed either net electron or hole trapping. Even though the trapping is not as strong as for the alphas, it is still on a measureable scale. However, this requires at least a two-channel read-out, because neither the DCR effect was observed nor any other special pulse characteristics could be identified for beta events. The passivated surfaces of n-type detectors behave very similar to the passivated surface of p-type detectors as shown by a study on a p-type point contact detector in GALATEA [93].

Currently, in the LEGEND experiment, it is planned to read out only one channel in order to reduce the material close to the detectors and, thus, to minimize the amount of radioactivity close to the detector. Therefore, beta events can not be identified. As a consequence, it will be critical to increase the purity of the LAr in case the detectors will be directly submerged into LAr. An alternative solution would be to not deploy the detectors directly into LAr, but to encapsulate them with a scintillating material like polyethylene naphthalate (PEN) [45]. Those capsules would be filled with, e.g. a nitrogen atmosphere and would be submerged in LAr. By this approach, the very good background identification of the LAr veto could be used without the additional intrinsic background coming from ^{42}Ar. In addition, no expensive underground LAr would have to be procured.

As technical solutions for encapsulations are still in the R&D phase, the response of beta-induced surface events should be further studied with germanium detectors of different types like point contact detectors [93] and inverted coax detectors, which will probably be the most used detector types in LEGEND. They feature preferred pulse characteristic with respect to background identification as mentioned in Sec. 1.5.3. In addition, detectors with different types of passivation layers and metallization close to the passivation layer should be studied as this will most likely influence the response to events close to it. This becomes clear when comparing the response of Super Siegfried to alphas before and after metallization of the top segment.

Chapter 9: Simulation of Surface Effects

SSD, in its first version, did not include surface effects like charge trapping. In this chapter, possibilities to include the effects described in the previous chapters are discussed.

9.1 Partially Metallized Top Segment

In measurements prior to the full metallization of the top segment of Super Siegfried, very long rise times of up to $\approx 1000\,\mathrm{ns}$ were observed in the top segment for energy depositions underneath the top surface far away from the metallization, see Figures 7.18, 7.23 and 7.31.

In this section, a first attempt to simulate the partial metallization with SSD is presented. To do so, the electrode of the top segment contact was only defined for the volume, $r \in [37.49\,\mathrm{mm}, 37.5\,\mathrm{mm}], \varphi \in [125°, 135°], z \in [65.5\,\mathrm{mm}, 70\,\mathrm{mm}]$, as is shown in Fig. 9.1.

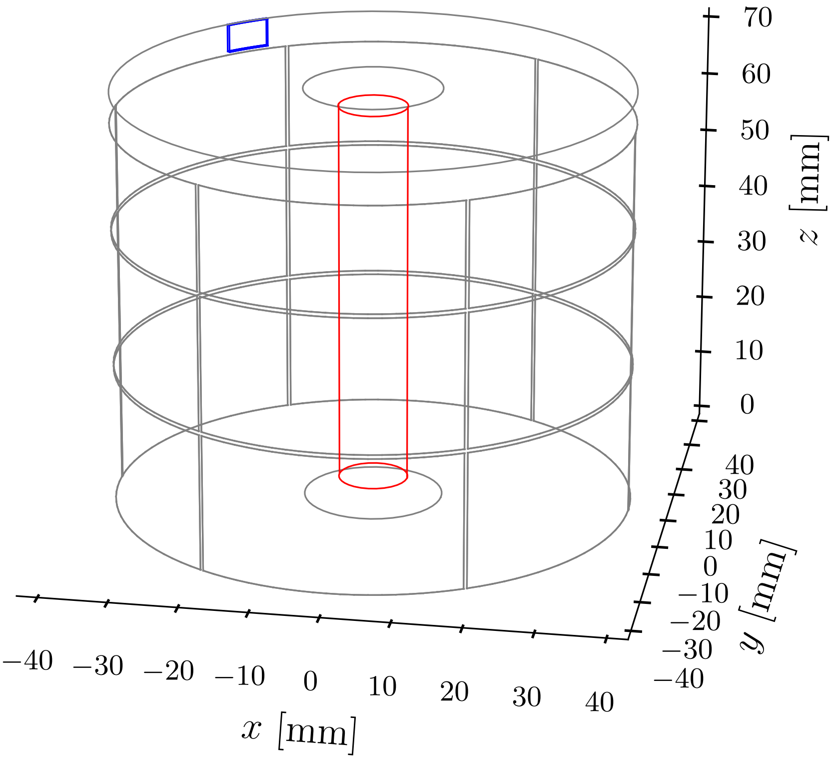

Figure 9.1: Visualization of Super Siegfried in SSD. The core contact is shown in red, the top segment contact is shown in blue. All other p$^+$-segments and crystal boundaries are shown in grey.

As described in Sec. 3.0.2, the over-doped n^+- and p^+-layer are undepleted and conductive. Thus, their dielectric permittivity should approach infinity and the applied potential should distribute equally over the whole layer. However, the observed long rise times indicate that this was not the case for the thin p^+-layer of the top segment of Super Siegfried. Therefore, the dielectric permittivity of the p^+-layer, $\epsilon_\mathrm{r}^{\mathrm{p}^+}$, was scaled by a factor, $\epsilon_\mathrm{r}^\mathrm{s}$, in the ring of the top segment ($r \in [37.49\,\mathrm{mm}, 37.5\,\mathrm{mm}], \varphi \in [0°, 360°], z \in [65.5\,\mathrm{mm}, 70\,\mathrm{mm}]$):

$$\epsilon_\mathrm{r}^{\mathrm{p}^+} = \epsilon_\mathrm{r}^\mathrm{s} \cdot \epsilon_\mathrm{r}^\mathrm{Ge} \qquad . \tag{9.1}$$

Three cases were simulated for different values of $\epsilon_\mathrm{r}^\mathrm{s}$:

1. $\epsilon_\mathrm{r}^\mathrm{s} = 1$: Lower limit of reasonable values for $\epsilon_\mathrm{r}^{\mathrm{p}^+}$, which is the dielectric permittivity of high purity germanium.
2. $\epsilon_\mathrm{r}^\mathrm{s} = 10^3$: Dielectric permittivity of germanium increased by three orders of magnitude.
3. $\epsilon_\mathrm{r}^\mathrm{s} = 10^6$: Approximation of the higher limit for $\epsilon_\mathrm{r}^{\mathrm{p}^+} \to \infty$.

The weighting potentials of the reduced electrode calculated for these three cases are shown in Fig. 9.2. For the case $\epsilon_\mathrm{r}^\mathrm{s} = 1$, the weighting potential does not spread around the ring and drops very fast to zero. For $\epsilon_\mathrm{r}^\mathrm{s} = 10^3$, it spreads partially around the ring, however, not as completely as for the case of $\epsilon_\mathrm{r}^\mathrm{s} = 10^6$. The latter case results in basically the same weighting potential as if the whole ring were defined as the contact and the weighting potential becomes 1 for the whole the ring.

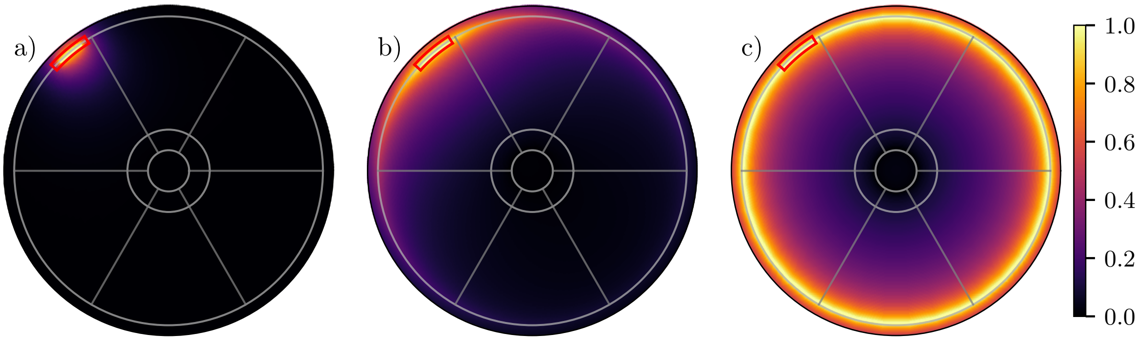

Figure 9.2.: Weighting potential of the reduced top segment, $\mathcal{W}_{19}$, at $z = 68\,\mathrm{mm}$ calculated for different scale factors $\epsilon_\mathrm{r}^\mathrm{s}$ of the relative permittivity in the undepleted p^+-layer of the top segment: a) $\epsilon_\mathrm{r}^\mathrm{s} = 1$, b) $\epsilon_\mathrm{r}^\mathrm{s} = 10^3$ and c) $\epsilon_\mathrm{r}^\mathrm{s} = 10^6$. The area of the metallization is framed in red. The segment boundaries and the borehole are indicated with grey lines.

The electric potential inside the ring along φ is shown in Fig. 9.3. The segments are all set to 0 V whereas the core is set to 3000 V. For the case of $\epsilon_\mathrm{r}^\mathrm{s} = 1$, the electric potential increases to almost 300 V within about 20° and than stays constant along φ. Away from the contact, the potential is mostly influenced by the voltages applied to the segments underneath and to the core. The constant level of about 300 V decreases for lower z,

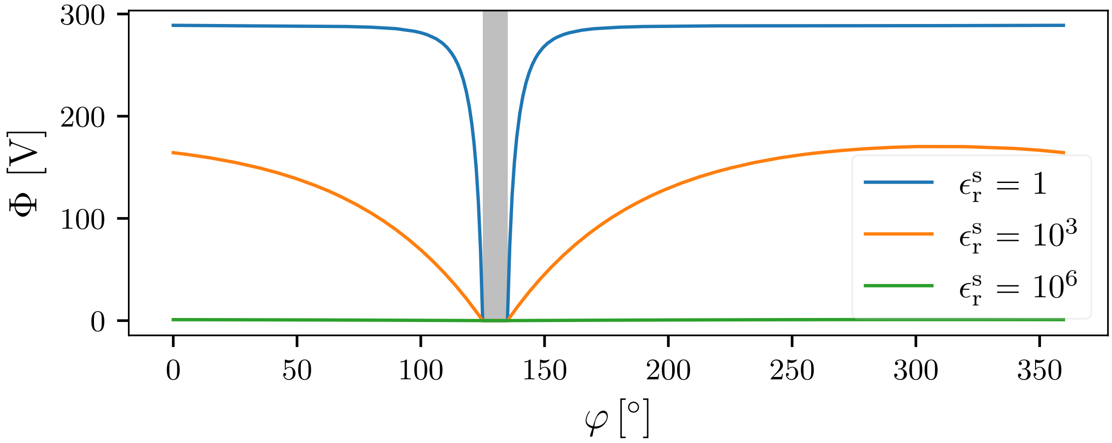

Figure 9.3.: Electric potentials depending on φ at $r = 37.5\,\mathrm{mm}$ and $z = 68\,\mathrm{mm}$, calculated for different scale factors ϵ_r^s. The area of the contact of the top segment, which is at the fixed potential of 0 V, is marked in grey.

i.e. closer to the segments underneath, and increases for higher z, i.e. closer to the top surface of the detector. This z-dependence is not shown in Fig. 9.3.

For the case of $\epsilon_r^s = 10^6$, the applied potential of 0 V spreads around the whole ring. For the case of $\epsilon_r^s = 10^3$, the potential increases over the ring but never saturates like for the case of $\epsilon_r^s = 1$. This leads to a non-zero electric field component in φ, which can also be seen in the drift trajectories of events underneath the top surface, which were simulated for the three cases and are shown in Fig. 9.4[1]. Axes effects were included in the simulation.

In Fig. 9.4 a), which shows the trajectories for the case $\epsilon_r^s = 1$, most of the holes are collected by the respective segment underneath the top segment and not by the top segment itself. Only the holes of events located very close to the top contact reach this contact. This is not at all what was observed.

In Fig. 9.4 b), which shows the trajectories for the case $\epsilon_r^s = 10^3$, most of the holes first drift to the mantle. At the mantle, they drift along the surface in the azimutal direction with the shortest path to the top contact. Only the holes from events located opposite from the top contact drift downwards to the respective segment underneath. The drift in the azimutal direction inside the ring of the top segment is very slow. As the simulation of the drift was stopped after 2000 ns, some holes did not reach the top contact. The simulated drifts through the top segment ring are much slower than the observed pulses which had $\mathcal{T}_{10-90}$ of about 1000 ns. However, this prediction approaches what was observed.

In Fig. 9.4 c), which shows the trajectories for the case $\epsilon_r^s = 10^6$, all holes of the events drift to the mantle and stay there as the electric potential is constant along the ring

---

[1] For future simulations, a very high grid point density, $\sim 1/10\,\mu\mathrm{m}$, has to be reached close to the surfaces to obtain precise predictions

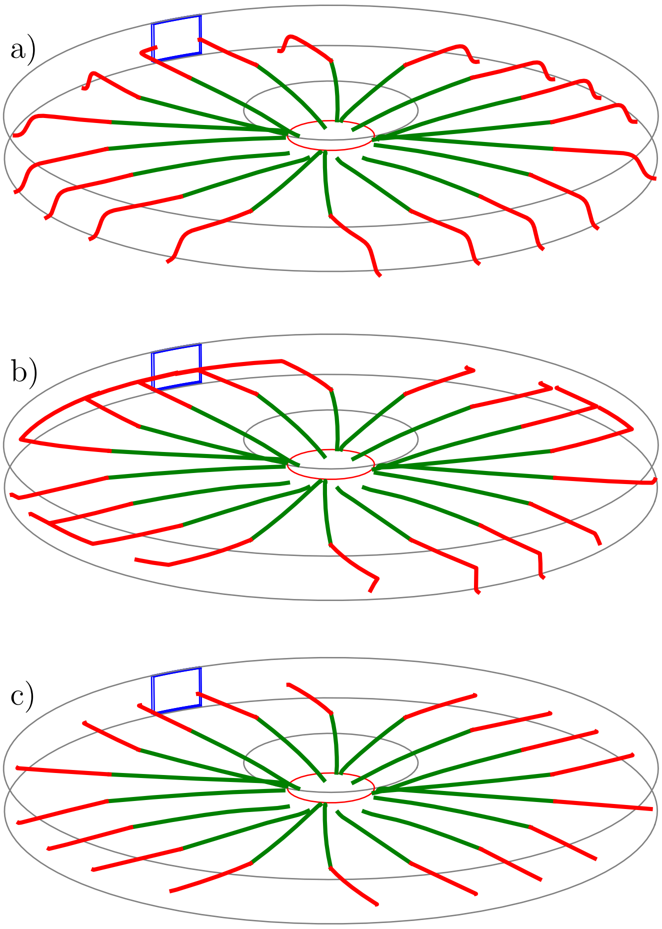

Figure 9.4.: Drift trajectories of events spawned at different φ just underneath the top surface of Super Siegfried at an radius of 26 mm and $z = 68$ mm as predicted for the fields calculated for different scale factors: a) $\epsilon_{\mathrm{r}}^{\mathrm{s}} = 1$, b) $\epsilon_{\mathrm{r}}^{\mathrm{s}} = 10^3$ and c) $\epsilon_{\mathrm{r}}^{\mathrm{s}} = 10^6$.

and, thus, the electric field is zero. As, in that case, the weighting potential is 1 over the whole ring, all events show their full energy at that point. Figure 9.5, which shows the simulated raw pulses[2] for the core and the top segment for the three cases, confirms this. This prediction is the closest one to the observation for the fully metallized top segment, see Sec. 7.4, where the top segment was the collecting segment for all event locations. Even for events located on the opposite side of the top contact.

In Fig. 9.5 a) and d) the simulated raw pulses of the set of events for the case $\epsilon_{\mathrm{r}}^{\mathrm{s}} = 1$ are shown. The core always collects the full charge. The slow rise at the end of the long core pulses is due to the slow drift of the holes towards the respective segment underneath the top segment. In the core pulses, the influence of the crystal axes is also visible. This interferes with the effect of the non-metallization, causing the order of pulses to appear "mixed".

---

[2] Pulses prior to the application of electronic response.

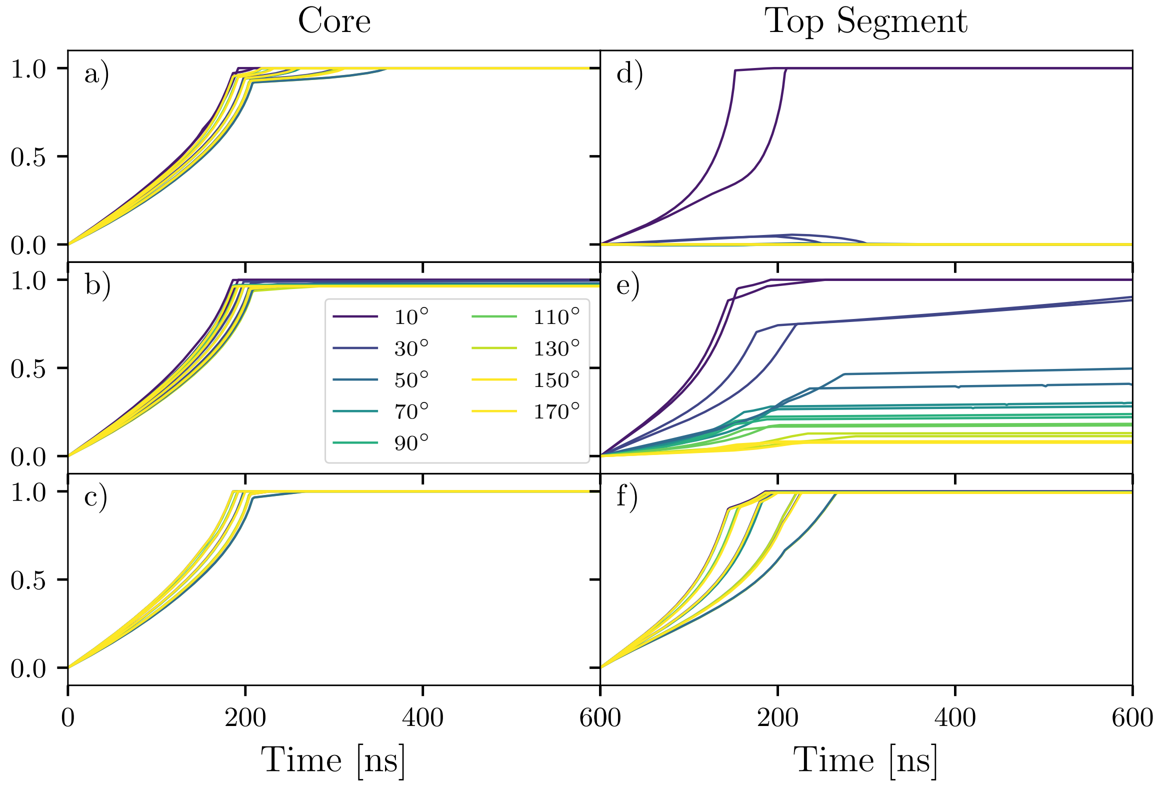

Figure 9.5.: Raw pulses for the core, a) - c), for the top segment, d) - f), of the events, shown in Fig. 9.4, spawned at different φ just underneath the top surface of Super Siegfried, calculated using the fields simulated for different scale factors: a) & d) $\epsilon_r^s = 1$, b) & e) $\epsilon_r^s = 10^3$ and c) & f) $\epsilon_r^s = 10^6$. The color of each pulse represents the azimutal distance between the event location and the center of the metallization, $\Delta\varphi^C_{\text{evt}}$.

The effect of the crystal axes can also be seen in Fig. 9.5 c) and f), where the raw pulses are shown for case 3, which mimics a full metallization. Here, the pulse lengths do not depend on the azimutal distance between the event location and the location of the top contact, $\Delta\varphi^C_{\text{evt}}$, but only on the crystal axes. The kinks in the pulses of the segment (core) mark the times, at which the electrons (holes) are collected at the core (segment).

In Fig. 9.5 b) and e), the pulses are shown for case 2, $\epsilon_r^s = 10^3$. In the segment pulses, the effect of the crystal axes cannot be seen. Instead, there is a strong and clear dependence of the segment signal on $\Delta\varphi^C_{\text{evt}}$. With increasing $\Delta\varphi^C_{\text{evt}}$, the length of the segment pulse increases significantly. At some point the holes do not reach the electrode anymore, but drift to the respective segment underneath. Thus, their top segment pulses are only mirror pulses returning to the baseline, which is not visible in Fig. 9.5 e) as only the first 600 ns are shown. Since the drift inside the ring of the top segment is very slow, the signals of the segment pulses stay almost constant after the holes reach the mantle.

The reason for the slow drift is the low electric field inside the ring of the top contact, which is the gradient of the electric potential shown in Fig. 9.3. It becomes clear, that in order to mimic a conductive material it is not enough to only increase the dielectric permittivity. The drift model also has to be changed in that volume. The drift model used here, which is the one for high purity germanium, does not describe the charge drift inside highly over-doped and undepleted germanium, because the band structure is different in that volume. Thus, in order to increase the simulated drift times such that they match the observed rise times of about 1000 ns, the mobility would need to be increased. However, it is strange that the observed rise times were basically constant for $\Delta\varphi^{\mathrm{C}}_{\mathrm{evt}} > 100°$, see Fig. 7.31. At this point, it is unclear how this could be explained by just a modification of the mobility inside the layer. But, the simulations presented here are just a first step towards understanding the complex situation. In addition, not only the rise times of the observed pulses, but also their shapes should be used to guide future simulations. More effects like surface charges and the influence of the environment might have to be considered in order to fully understand how the metallization impacts signal formation.

9.2 Charge Carrier Trapping

In this section, a first simulation of the trapping of electrons and holes underneath the top surface of Super Siegfried as observed for events from the radial Americium scan SSAmRad136, see Fig. 7.17, is presented.

The r-dependent average reduced E_μ values, see Fig. 7.17, show that the observed core and segment energies are different. This can only be explained by the trapping of charge carriers during the drift. A dead layer alone, which would reduce the energy in both channels equally, cannot explain the observation.

9.2.1 Modulation of the Surface Drift of Charge Carriers

Single electron-hole pairs were spawned at the positions of the beam-spots of the scan SSAmRad136, $17\,\mu$m underneath the top surface, which is the position of the Bragg peak for ≈ 5.4 MeV alphas in germanium, see Fig. 7.3.

The drift trajectories, simulated without any modulation of the drift model, are shown in Fig. 9.6 for two different simulations of the electric field. In Fig. 9.6 a), the field simulation was limited to the volume of the detector and reflecting boundaries were used at the floating top (and bottom) surfaces of the detector for the calculations. Due to the reflecting boundary condition at the top surface, the z-component of the electric field becomes 0 at the top surface. Thus, charge carriers will, once close to the surface, always drift parallel to the surface. In Fig. 9.6 b), the field simulation also included the grounded IR shield and the grounded detector holding plate of GALATEA, resulting in a different electric field and, thus, also in different drift trajectories: The electrons (holes) are predicted to drift away from the surface of the detector for $r < (>)\ 33$ mm.

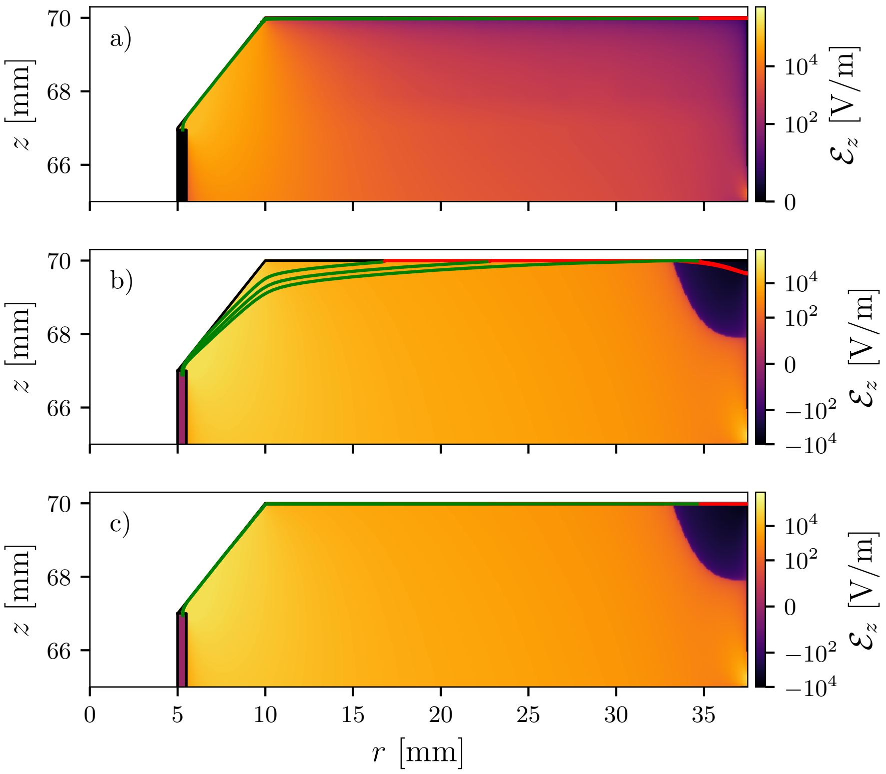

Figure 9.6.: The heatmaps show the value of the z-component of the electric fields. The green (red) lines are the drift trajectories of the electrons (holes) of three events simulated at 3 positions of the scan SSAmRad136. In a), the field simulation was limited to the volume of the detector. In b) and c), the heatmap is the same. Here, the field simulation included the IR shield and detector base plate of GALATEA. In c), the drift model was modified, forcing the charge carries to drift along the surface.

However, as trapping was not observed for low-energy gamma-induced events, which deposited energy at the mm level underneath the surface, it is most likely that the charge carriers drift along the surface in a surface channel, see Sec. 2.5. Therefore, a virtual volume was added to the simulation. The volume is a thin tubus, $r \in [10.1\,\mathrm{mm}, 37.4\,\mathrm{mm}]$, $z \in [69.95\,\mathrm{mm}, 70\,\mathrm{mm}]$, underneath the top surface. Inside this volume, the z-component of the drift vector is set to zero leading to a modulated drift vector $\mathbf{v}_\mathrm{d}^\mathrm{mod}$. The resulting drift trajectories are shown in Fig. 9.6 c). This modification is on one hand motivated by the observed difference between alpha and gamma events and on the other hand also by the different band structure at the surface of a crystal. The assumptions made for the derivation of the band structure, see Sec. 2.2, are not valid at the surface. A modified band structure leads to a modified mobility tensor. The well motivated theory is that the mobility perpendicular to the surface approaches zero.

With the modulation of the drift, the drift trajectories are basically the same as for the case with reflecting boundary conditions, see Fig. 9.6 a). However, there is a difference

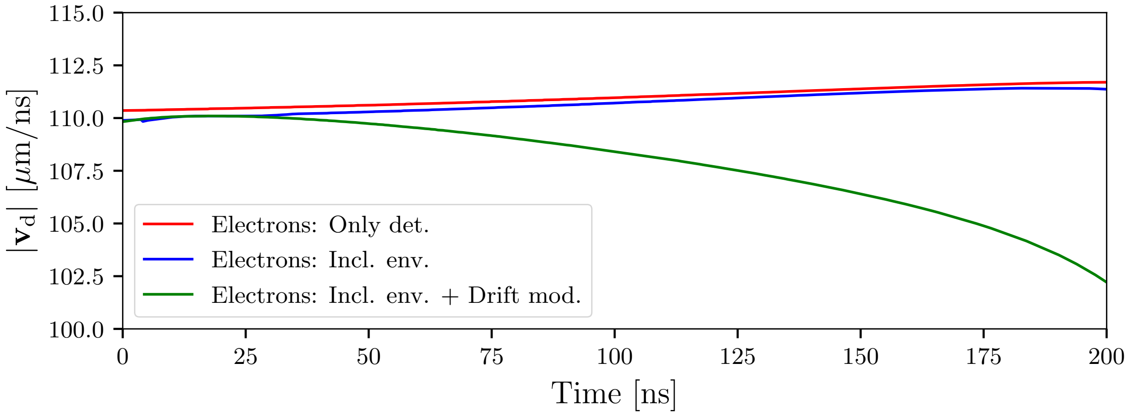

Figure 9.7.: Absolute drift velocity of the electron with the start position at $r = 34.8\,\mathrm{mm}$.

in the speed of the drift. Figure 9.7 shows the absolute drift velocity of the electrons for the three cases during the first 200 ns of the drift. This difference is quite important as it leads to different values for the mobility if they are determined from comparisons of simulation to data.

It should be noted, that the modulation of the drift close to the borehole as described in Sec. 6.9 only affected drifts at $z \leq 67\,\mathrm{mm}$ and, therefore, had no impact on the surface simulations presented here.

9.2.2 Probabilistic Charge Trapping Model

A modification of the drift as described in the previous section results in a fixed modification of the observed signal. If the mobilities were massively reduced, the charge carriers would not be collected in time such that the observed energy would indeed be reduced. However, the data show a wide distribution of the reduction of E_core and E_{19} and the pulses suggest that the majority of the charge carriers are collected within typical drift times of up to 300 ns, see Fig. 7.22. Therefore, in addition to the modification of the drift as described in the previous section, a probability was added that a charge carrier gets trapped during the drift through the virtual volume. Furthermore, a dead layer varying with r was added to reduce the number of created electron-holes pairs.

The results of the combination of the drift modulation, an r-dependent dead layer and a probabilistic charge trapping model for electrons and holes are shown in Fig. 9.8. This model describes the data quite well.

The dead layer was modeled as a quadratic function,

$$DL(r) = a_{DL}(r - d_{DL})^2 + e_{DL} \tag{9.2}$$

with the three coefficients a_{DL}, d_{DL} and e_{DL}. The dead layer leads to a reduced deposition of energy, $Q^*_\alpha(r)$, in the active volume of the detector. This reduction is calculated by integrating the energy loss of the alphas in germanium, see Fig. 7.3, over the given dead layer thickness.

The trapping of electron and holes was modeled in a probabilistic way. Two parameters were defined: One for electrons, $p^{\mathrm{e}}_{\mathrm{t},0}$, and one for holes, $p^{\mathrm{h}}_{\mathrm{t},0}$. They define a trapping probability, $p^{\mathrm{e/h}}_{\mathrm{t}}$. In each step of the drift, depending on $\mathbf{v}^{\mathrm{mod}}_{\mathrm{d}}$ and the time interval, Δt,

$$p^{\mathrm{e/h}}_{\mathrm{t}}(\mathbf{v}^{\mathrm{mod}}_{\mathrm{d}}) = p^{\mathrm{e/h}}_{\mathrm{t},0} \cdot \Delta t / |\mathbf{v}^{\mathrm{mod}}_{\mathrm{d}}| \qquad . \tag{9.3}$$

A flat random number between 0 and 1 was generated for each step and if it was below $p^{\mathrm{e/h}}_{\mathrm{t}}(\mathbf{v}_{\mathrm{d}})$ the charge carrier was stopped at the current position. A release probability was not implemented. This would be needed to model the DCR effect observed for alpha-induced events. A search in the parameter space guided by educated guesses led to the parameters listed in Tab. 9.1. The dead layer and resulting $Q^*_\alpha(r)$ at the positions of the scan are also shown in Fig. 9.8.

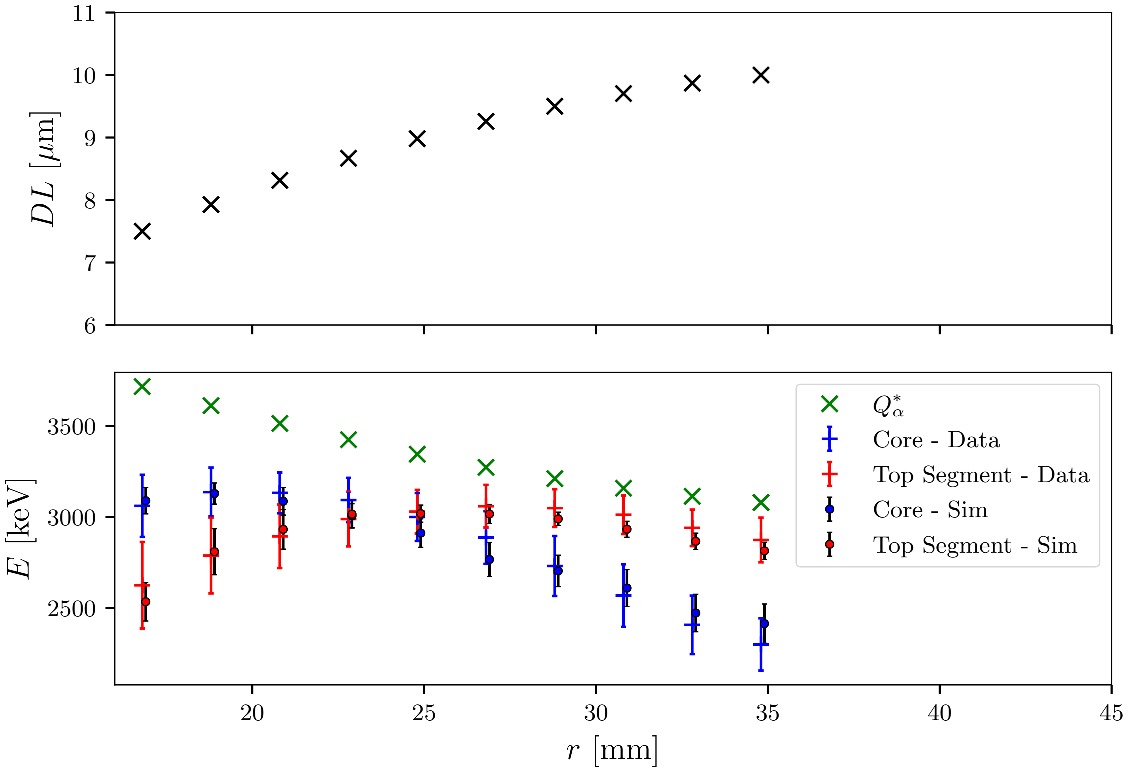

Figure 9.8.: Top: Assumed dead layer thickness in dependence of r. Bottom: The observed alpha energies in the core and the top segment which were already shown in Fig. 7.17 are shown together with the results achieved from the simulation as described in the text. The radial positions for the simulation are shifted by 0.1 mm for reasons of visibility. In addition, the energies deposited below the dead layer, $Q^*_\alpha(r)$, are shown. For the simulation, the red marker covers the blue marker at $r = 22.8$ mm.

a_{DL}	$-0.005\,\mu\text{m}/\text{mm}^2$
d_{DL}	$40.8\,\text{mm}$
e_{DL}	$10.2\,\mu\text{m}$
$p^{\text{e}}_{\text{t},0}$	$0.15\,\mu\text{m}/\text{ns}^2$
$p^{\text{h}}_{\text{t},0}$	$0.04\,\mu\text{m}/\text{ns}^2$

Table 9.1.: Parameters of the dead layer and charge trapping model evaluated by testing.

All simulation were performed for 20 events at each radial position of the scan SSAm-Rad136, each event with 100 electron-hole pairs, which could get trapped individually at different locations. The signal induced by each charge carrier was weighted with $Q^*_\alpha(r)/100\,\text{keV}$. The mean values and standard deviations of the obtained 20 core and top segment energies for each position are shown in Fig. 9.8 and compared to the observed energies. The spread of the observed energies is still underpredicted. However, self repulsion and diffusion are expected to play a role here and need to be implemented before further adjustments can be made.

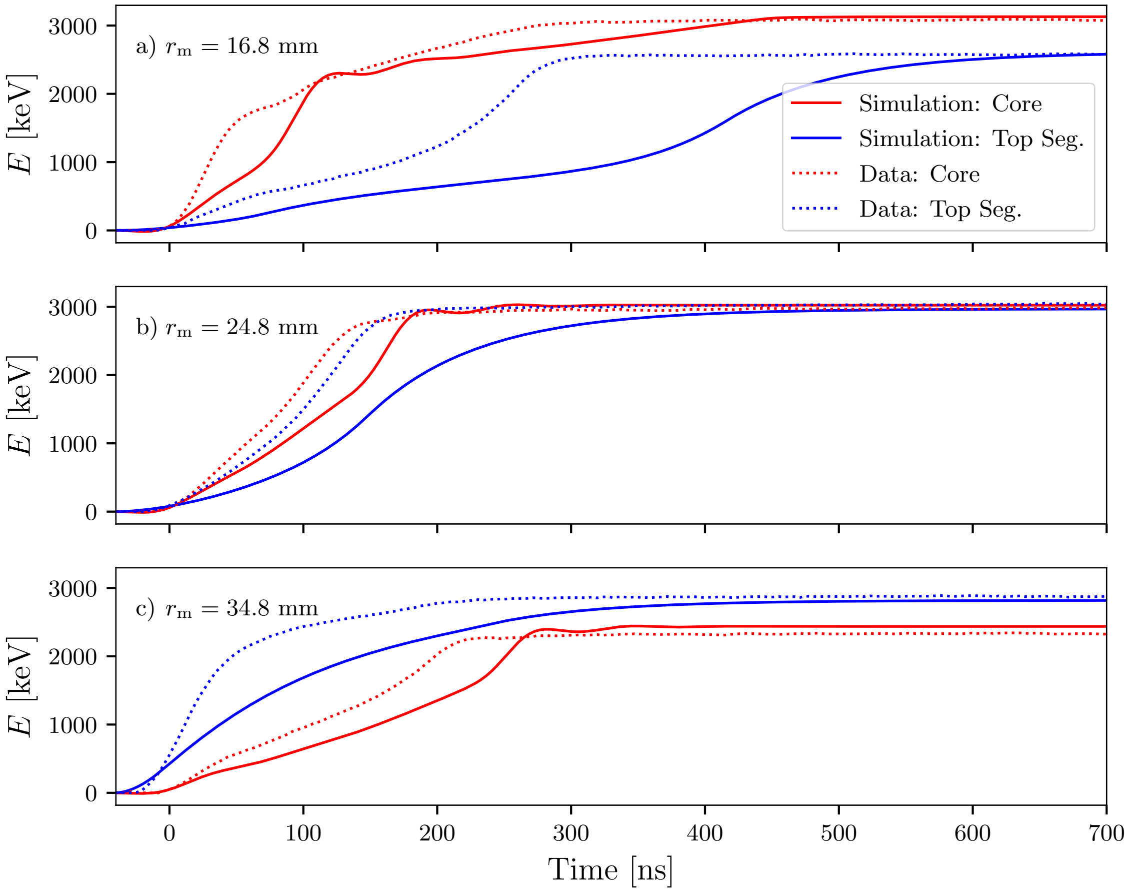

Figure 9.9.: Predicted and observed pulses of alpha-induced events from the scan SSAm-Rad136 at three different radial positions.

Observed pulses of alpha-induced events from the scan SSAmRad136 at three different radial positions are shown together with predicted pulses for such events in Fig. 9.9. Overall, the shapes of the predicted pulses are similar to the observed shapes. However, the simulated pulses are too slow. Thus, the assumed mobility is too low along the drift path at the surface. Scaling the time would result in a very reasonable description of the data. Only for the smallest $r_\mathrm{m} = 16.8\,\mathrm{mm}$, see Fig. 9.9 a), the shape of predicted core pulse does not match the observed alpha pulse well. This might be explained with the slower predicted drift of the holes, which, when created at $r_\mathrm{m} = 16.8\,\mathrm{mm}$, need more time until they leave the region, in which they influence the core signal. Thus, they still reduce the induced signal on the core. The shape of the predicted core pulses match the data better for larger radii.

The discrepancy between simulated and observed core pulses for $r_\mathrm{m} = 16.8\,\mathrm{mm}$ might also be related to the predicted drift of the electrons through the region close to the widening of the borehole in which the modulation of the mobility forced the electrons to drift along the surface as shown in Fig. 9.6 c). The teflon from the holding structure also presses against the surface of the widening of the borehole, for $0.5\,\mathrm{cm} \leq r \leq 1\,\mathrm{cm}$. This piece of teflon was not included in the simulation. Its influence on the drift should be studied in the future. In addition, charge cloud effects, diffusion and self repulsion, will also influence the drift. In addition, the discrepancy can also be caused by the limited knowledge on the impurity density of the crystal and its influence on the mobility which are important inputs to the simulation. Most likely, it is combination of all these effects, which have to be disentangled by dedicated measurements, especially sensitive to one of these influences.

While small effects remain, the model of a varying dead layer and probabilistic trapping of charge carriers can predict the radial dependence of the observed energy of alpha-induced events quite well. This model is sufficient for studies related to identifying background events in experiments like LEGEND.

9.3 Importance of the Environment for the Pulses

In the last section of this chapter, the importance of taking the environment of a detector into account is discussed. The inverted coax detector (IVC) already introduced in Sec. 5.2.8 was simulated[3] for two cases:

- LAr case: The detector is submerged in liquid argon.
- Isolated case: The simulation of the detector is limited to the volume of the detector. The reflecting boundary condition is chosen at $z = 0\,\mathrm{mm}$ where the floating surface of the detector is located.

The electric potential as calculated for the LAr case and its difference to the potential

---

[3] The inverted (n-type → p-type crystal) impurity model of Super Siegfried was chosen in order to use a realistic impurity model.

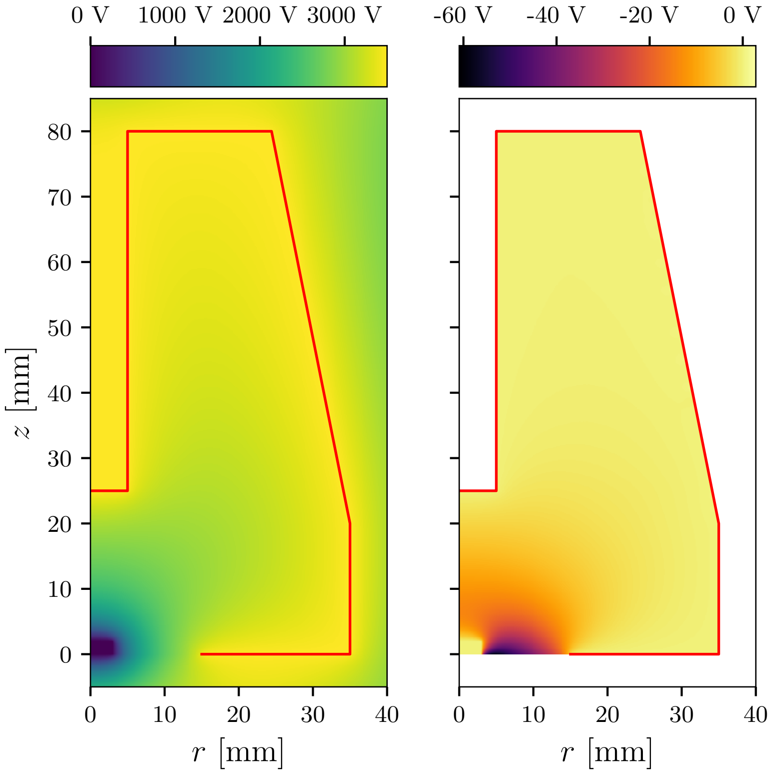

Figure 9.10.: Left: Electric potential of the IVC detector as calculated for the LAr case. Right: Difference between the electric potential calculated for the two cases (isolated - LAr). The mantle contact is drawn in red.

of the isolated case are shown in Fig. 9.10. The maximum of the difference between the two potentials is about 60 V, which is ≈ 1.7 % of the applied bias voltage. In addition, the weighting potentials of the contacts are different in the two cases. The difference of the weighting potentials of the point contact close to the floating surface of the detector is shown in Fig. 9.11. The maximum difference between these weighting potentials is ≈ 1.5 %. This is a slightly smaller relative difference than for the electric potential, since the charge distribution is set to zero in the calculation of the weighting potential, see Sec. 3.3.1.

The difference in the electric potential translates into a difference in the electric field and, thus, also in the drift fields. Therefore, the drift trajectories of the charge carriers are also affected as was already shown in Fig. 9.6. The effect is demonstrated in Fig. 9.11 (left) for an event spawned at ($r = 10\,\text{mm}$, $z = 0.1\,\text{mm}$).

As the drift trajectories are influenced, the resulting pulses also change. They are shown in Fig. 9.11 (right), together with their differentials. The charge signals are almost identical. However, the deviations are on the percent level and should be detectable in the signals of the high precision detectors used in searches for $0\nu\beta\beta$. However, the limited bandwidth of the electronics might obscure the small change in the charge signal. The difference in the differentials, i.e. the current, is much larger. A difference up to ≈ 25 % is predicted. The maximum amplitude of the current was used in one of the

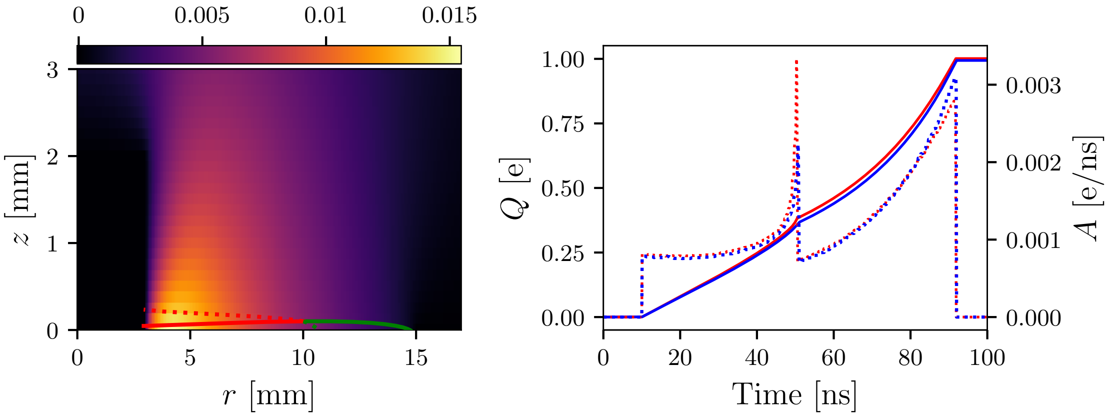

Figure 9.11.: Left: Difference between the weighting potentials of the IVC detector calculated for the two cases (isolated - LAr). Only the area close to the floating surface of the detector is shown. The red and green lines (dots) are the drift trajectories of holes and electrons for the isolated (LAr) case. Right: Simulated pulses (solid lines) and their differential form (dotted lines) for both cases (red: isolated, blue: LAr).

key pulse-shape analysis techniques, the so-called A/E cut [15, 37], to identify multi-site events in GERDA. It will also be used in LEGEND. The large influence of the environment makes its inclusion in the simulation absolutely necessary when cuts based on pulse shapes are studied.

The case of the event shown in Fig. 9.11 is an extreme case. The differences are significantly smaller for events which do not drift close to the floating surfaces. However, as was already mentioned, the biggest source of background in GERDA came from surface contaminations and this is currently also expected for the LEGEND experiment. This makes it particularly important to understand such pulses as well as possible.

Chapter 10: Summary and Outlook

The search for $0\nu\beta\beta$ is one of the most promising searches for physics beyond the standard model. If discovered, $0\nu\beta\beta$ changes the picture of the universe fundamentally. Germanium detectors are one of the most promising technologies for this search. The recently completed germanium based experiments, MAJORANA and GERDA, presented strong limits on the halflife of ^{76}Ge and the upcoming LEGEND experiment is based on the developments leading to their success. The biggest challenge for LEGEND is the further reduction of the experimental background by a factor of about 50. A large fraction of the background events in GERDA and MAJORANA originated from alpha and beta decays on the passivated surfaces of the germanium detectors. This motivated the studies presented in this thesis.

Two n-type true-coaxial germanium detectors, Super Siegfried and Siegfried III, provided a large amount of data to study events on their passivated surfaces. The response to alpha-induced events was studied for both detectors while beta-induced events became for the first time available in Super Siegfried. Events induced by low-energy gammas were always used for comparisons. The data were obtained by scans of the detector surfaces in the test facility GALATEA, especially designed for studies with alpha and beta particles.

The alpha data showed that the dead layer under the passivated surfaces of both detectors is extremely thin, only of the order of $10\,\mu$m. However, the observed energy is not only reduced by the thin dead layer but also by charge trapping during the drift of charge carriers directly underneath the passivated surface. The charge trapping was found to be a stochastic process with the probability of trapping not only dependent on the radial position of the event but also strongly on the position relative to the crystallographic axes. The amount of charge trapping is reflected in the energy observed in the event. Alpha-induced events located close to a fast axis were recorded with up to 1 MeV higher energies than alpha-induced events located close to a slow axis.

The results on alpha-induced events were compared to results of previous studies, for which the data were taken when the segment close to the passivated surface of Super Siegfried was not yet fully metallized. Prior to the full metallization, extremely long rise times of up to ~ 1000 ns were observed for the segment signals for events not located close to the contact of the segment. After the full metallization of this segment, these extremely long rise times were not observed anymore. The pulses had significantly shorter rise times. However, a small position dependence of the rise times persisted with observed differences in rise times of up to ~ 100 ns depending on the event position relative to the location of the contact of the segment. Prior to metallization, the rise times in the core channel were also affected, even though much less than the segment rise times. After the metallization, no such effect was present in the core channel.

The scans with beta radiation revealed that also up to 50 % of the beta-induced events are affected by charge trapping. However, the effect is much more subtle than for alpha-induced events, i.e. the share of charge carriers trapped is much smaller due to the deeper penetration of beta-induced events. Like for alpha-induced events, the amount of charge trapping in beta-induced events depends on the radial position. The events with charge trapping were identified by analyzing the signals from multiple channels as available for the test detector Super Siegfried. However, no special pulse-shape characteristics in the core, like the evidence for delayed charge recovery observed in alpha-induced events, could be identified in the pulses of beta-induced events. Thus, beta-induced events cannot be identified with only the core channel available and as beta spectra are continuous they can become background events in the $0\nu\beta\beta$ signal region. This is relevant for LEGEND and has to be taken into account for the choice of detector technology and the evaluation of beta-induced backgrounds.

The new open-source pulse-shape simulation software package *SolidStateDetectors.jl* [18] was developed for the analyses presented in this thesis. It was introduced and its features presented in detail. Simulations of pulses with *SolidStateDetectors.jl* were compared successfully to data. The possibility do define virtual volumes, in which the drift of the charge carriers can be modulated, provided a simple way to test models for special drift characteristics and charge trapping at surfaces. A model combining a position-dependent dead layer and probabilistic trapping of charge carriers during the drift was shown to describe some of the main features observed for alpha-induced events.

SolidStateDetectors.jl takes the environment of a detector into account when calculating the electric field. It was demonstrated, that the changes in the field due to an environment like liquid Argon have a measurable impact on the signals. This is especially important for events near the surface, which also for LEGEND are expected to provide a major share of the background events. The LEGEND detectors in their holding structures submerged in LAr can now be simulated. Furthermore, since the simulation is not limited to rotationally symmetric geometries, the effect of detector asymmetries can be studied.

In general, *SolidStateDetectors.jl* offers new possibilities for future studies on germanium detectors or other semiconductor detectors. The fast three-dimensional field calculation allows for fitting of impurity density models to measured capacity versus bias-voltage curves of individual detectors. This can be used to tackle the known problem of the huge uncertainties on the impurity density profiles as provided by the manufacturers. Another uncertainty in the simulation of germanium detectors is the mobility tensor. The software provides a simple interface to modulate the mobility tensor. This allows to study the impact of modifications like a position dependent mobility tensor due to any impurity density profile of the crystal. The modular structure of the package also allows the testing of new and improved models of charge carrier drift. In the near future, an option to take charge cloud effects into account will become public. This will result in even more realistic predictions of pulse shapes.

In this thesis, the data taking of alpha-, beta- and gamma-induced events and their analysis was presented. The analysis revealed charge trapping close to passivated surfaces and the potential of such events to become background events in the future LEGEND experiment. A new open-source pulse-shape simulation package was introduced and used to describe and understand the data.

Appendix A: Datasets

A.1 Collimator Configuration

In general, each collimator segment has a thickness of 10 mm.

All measurements with Americium were performed with one collimator configuration: The source in the top (side) collimator was held by two (one in front and one behind) teflon (copper) collimator segments with a borehole radius of 1 mm (1.25 mm). For both sources, three copper collimator segments with a borehole radius of 1 mm were placed in front (towards the detector).

All measurements with Strontium were performed with one collimator configuration: Both sources were held by two teflon collimator segments with a borehole radius of 0.5 mm. Only these teflon segments were 15 mm thick each. Four tungsten collimator segments were placed in front (towards the detector). The first (closest to the source), had a borehole radius of 0.75 mm. The other 3, had a borehole radius of 1 mm.

A.2 Super Siegfried

A.2.1 Datasets with Americium

Table A.1 – Background Measurement (BGM)

i_m	$\varphi^\mathrm{s}_\mathrm{m}$ [°]	$\varphi^\mathrm{t}_\mathrm{m}$ [°]	r_m [mm]	z_m [mm]	Duration [s]	Date [y-m-d H:M]
1	172.900	262.900	51.800	74.500	18000	2018-10-10 11:50

Table A.1.: Background measurement (BGM) of Super Siegfried.

Table A.2 – Dataset SSAmRotMid

i_m	$\varphi^\mathrm{s}_\mathrm{m}$ [°]	$\varphi^\mathrm{t}_\mathrm{m}$ [°]	r_m [mm]	z_m [mm]	Duration [s]	Date [y-m-d H:M]
1	172.900	262.900	23.800	40.000	3600	2018-10-11 14:56
2	167.900	257.900	23.800	40.000	3600	2018-10-11 16:32
3	162.900	252.900	23.800	40.000	3600	2018-10-11 18:8
4	157.900	247.900	23.800	40.000	3600	2018-10-11 19:44
5	152.900	242.900	23.800	40.000	3600	2018-10-11 21:20

Continued on next page

Table A.2 – continued from previous page

i_m	$\varphi^\mathrm{s}_\mathrm{m}$ [°]	$\varphi^\mathrm{t}_\mathrm{m}$ [°]	r_m [mm]	z_m [mm]	Duration [s]	Date [y-m-d H:M]
6	147.900	237.900	23.800	40.000	3600	2018-10-11 22:56
7	142.900	232.900	23.800	40.000	3600	2018-10-12 0:33
8	137.900	227.900	23.800	40.000	3600	2018-10-12 2:9
9	132.900	222.900	23.800	40.000	3600	2018-10-12 9:15
10	127.900	217.900	23.800	40.000	3600	2018-10-12 10:55
11	122.900	212.900	23.800	40.000	3600	2018-10-12 12:32
12	120.000	210.000	23.800	40.000	3600	2019-02-25 23:47
13	117.900	207.900	23.800	40.000	3600	2018-10-12 14:8
14	112.900	202.900	23.800	40.000	3600	2018-10-12 15:44
15	107.900	197.900	23.800	40.000	3600	2018-10-12 21:44
16	102.900	192.900	23.800	40.000	3600	2018-10-12 23:24
17	97.900	187.900	23.800	40.000	3600	2018-10-13 1:1
18	92.900	182.900	23.800	40.000	3600	2018-10-13 2:37
19	87.900	177.900	23.800	40.000	3600	2018-10-13 4:13
20	82.900	172.900	23.800	40.000	3600	2018-10-13 13:55
21	77.900	167.900	23.800	40.000	3600	2018-10-13 15:31
22	72.900	162.900	23.800	40.000	3600	2018-10-13 17:11
23	67.900	157.900	23.800	40.000	3600	2018-10-13 18:48
24	63.900	153.900	23.800	40.000	3600	2019-02-22 16:46
25	62.900	152.900	23.800	40.000	3600	2018-10-13 20:25
26	61.900	151.900	23.800	40.000	3600	2019-02-25 19:10
27	60.900	150.900	23.800	40.000	3600	2019-02-22 13:9
28	60.900	150.900	23.800	40.000	3600	2019-02-22 14:45
29	59.900	149.900	23.800	40.000	3600	2019-02-22 11:35
30	58.900	148.900	23.800	40.000	3600	2019-02-22 9:59
31	57.900	147.900	23.800	40.000	3600	2018-10-13 22:4
32	56.900	146.900	23.800	40.000	3600	2019-02-20 19:7
33	55.900	145.900	23.800	40.000	3600	2019-02-20 23:13
34	54.900	144.900	23.800	40.000	3600	2019-02-21 0:48
35	53.900	143.900	23.800	40.000	3600	2019-02-21 2:25
36	52.900	142.900	23.800	40.000	3600	2018-10-13 23:43
37	47.900	137.900	23.800	40.000	3600	2018-10-14 1:20
38	42.900	132.900	23.800	40.000	3600	2018-10-14 2:58
39	37.900	127.900	23.800	40.000	3600	2018-10-14 4:39
40	32.900	122.900	23.800	40.000	3600	2018-10-15 11:14
41	27.900	117.900	23.800	40.000	3600	2018-10-15 12:50
42	22.900	112.900	23.800	40.000	3600	2018-10-15 14:25
43	17.900	107.900	23.800	40.000	3600	2018-10-15 16:1
44	12.900	102.900	23.800	40.000	3600	2018-10-15 17:36
45	7.900	97.900	23.800	40.000	3600	2018-10-15 19:12
46	2.900	92.900	23.800	40.000	3600	2018-10-15 20:48
47	0.000	90.000	23.800	40.000	3600	2019-02-25 21:17
48	357.900	87.900	23.800	40.000	3600	2018-10-15 22:24

Continued on next page

Table A.2 – continued from previous page

i_m	$\varphi^\mathrm{s}_\mathrm{m}$ [°]	$\varphi^\mathrm{t}_\mathrm{m}$ [°]	r_m [mm]	z_m [mm]	Duration [s]	Date [y-m-d H:M]
49	352.900	82.900	23.800	40.000	3600	2018-10-16 0:1

Table A.2.: Dataset SSAmRotMid: A rotational scan of the top and side surface of Super Siegfried with two open ^{241}Am sources.

Table A.3 – Dataset SSAmRotSeg19

i_m	$\varphi^\mathrm{s}_\mathrm{m}$ [°]	$\varphi^\mathrm{t}_\mathrm{m}$ [°]	r_m [mm]	z_m [mm]	Duration [s]	Date [y-m-d H:M]
1	165.500	255.500	52.800	68.500	3600	2019-01-16 9:33
2	135.500	225.500	52.800	68.500	3600	2019-01-11 14:54
3	120.500	210.500	52.800	68.500	3600	2019-01-15 15:52
4	105.600	195.600	52.800	68.500	3600	2019-01-14 8:43
5	90.600	180.600	52.800	68.500	3600	2019-01-16 11:29
6	75.600	165.600	52.800	68.500	3600	2019-01-14 10:26
7	60.600	150.600	52.800	68.500	3600	2019-01-15 19:14
8	45.600	135.600	52.800	68.500	3600	2019-01-14 12:6
9	30.600	120.600	52.800	68.500	3600	2019-01-15 20:57
10	15.600	105.600	52.800	68.500	3600	2019-01-14 13:46
11	0.600	90.600	52.800	68.500	3600	2019-01-15 22:40
12	345.600	75.600	52.800	68.500	3600	2019-01-18 12:45
13	330.500	60.500	52.800	68.500	3600	2019-01-25 9:59
14	315.600	45.600	52.800	68.500	3600	2019-01-14 17:7
15	285.600	15.600	52.800	68.500	3600	2019-01-18 15:0

Table A.3.: Dataset SSAmRotSeg19: A rotational scan of side surface of Segment 19 of Super Siegfried with an open ^{241}Am source.

Table A.4 – Dataset SSAmVert

i_m	$\varphi^\mathrm{s}_\mathrm{m}$ [°]	$\varphi^\mathrm{t}_\mathrm{m}$ [°]	r_m [mm]	z_m [mm]	Duration [s]	Date [y-m-d H:M]
1	45.600	135.600	51.800	72.000	3600	2018-11-26 9:13
2	45.600	135.600	51.800	71.000	3600	2018-11-26 10:33
3	45.600	135.600	51.800	70.000	3600	2018-11-26 11:54
4	45.600	135.600	51.800	69.000	3600	2018-11-26 13:15
5	45.600	135.600	51.800	68.000	3600	2018-11-26 14:36
6	45.600	135.600	51.800	67.000	3600	2018-11-26 15:56
7	45.600	135.600	51.800	66.000	3600	2018-11-26 17:17
8	45.600	135.600	51.800	65.500	3600	2019-02-26 9:38
9	45.600	135.600	51.800	65.000	3600	2018-11-26 18:38

Continued on next page

Table A.4 – continued from previous page

i_m	$\varphi^\mathrm{s}_\mathrm{m}$ [°]	$\varphi^\mathrm{t}_\mathrm{m}$ [°]	r_m [mm]	z_m [mm]	Duration [s]	Date [y-m-d H:M]
10	45.600	135.600	51.800	64.500	3600	2019-02-26 10:58
11	45.600	135.600	51.800	64.000	3600	2018-11-26 19:59
12	45.600	135.600	51.800	63.000	3600	2018-11-26 21:19
13	45.600	135.600	51.800	50.800	3600	2019-02-26 12:19
14	45.600	135.600	51.800	48.800	3600	2019-02-26 13:39
15	45.600	135.600	51.800	48.300	3600	2019-02-26 15:42
16	45.600	135.600	51.800	47.800	3600	2019-02-26 17:2
17	45.600	135.600	51.800	47.300	3600	2019-02-26 18:22
18	45.600	135.600	51.800	46.800	3600	2019-02-26 19:41
19	45.600	135.600	51.800	46.300	3600	2019-02-26 21:1
20	45.600	135.600	51.800	45.800	3600	2019-02-26 22:21
21	45.600	135.600	51.800	45.300	3600	2019-02-26 23:41
22	45.600	135.600	51.800	44.800	3600	2019-02-27 1:1
23	45.600	135.600	51.800	42.800	3600	2019-02-27 2:21

Table A.4.: Dataset SSAmVert: A vertical scan of the side surface of Super Siegfried with an open ^{241}Am source.

Table A.5 – Dataset SSAmRad181

i_m	$\varphi^\mathrm{s}_\mathrm{m}$ [°]	$\varphi^\mathrm{t}_\mathrm{m}$ [°]	r_m [mm]	z_m [mm]	Duration [s]	Date [y-m-d H:M]
1	90.600	180.600	10.800	40.000	3600	2018-11-07 15:52
2	90.600	180.600	12.800	40.000	3600	2018-11-07 17:13
3	90.600	180.600	14.800	40.000	3600	2018-11-07 18:34
4	90.600	180.600	16.800	40.000	3600	2018-11-07 19:54
5	90.600	180.600	18.800	40.000	3600	2018-11-07 21:15
6	90.600	180.600	20.800	40.000	3600	2018-11-07 22:36
7	90.600	180.600	22.800	40.000	3600	2018-11-07 23:57
8	90.600	180.600	24.800	40.000	3600	2018-11-08 1:18
9	90.600	180.600	26.800	40.000	3600	2018-11-08 2:39
10	90.600	180.600	28.800	40.000	3600	2018-11-08 4:0
11	90.600	180.600	30.800	40.000	3600	2018-11-08 5:21
12	90.600	180.600	32.800	40.000	3600	2018-11-08 6:42
13	90.600	180.600	34.800	40.000	3600	2018-11-08 8:3
14	90.600	180.600	36.800	40.000	3600	2018-11-08 9:23
15	90.600	180.600	38.800	40.000	3600	2018-11-08 10:44
16	90.600	180.600	40.800	40.000	3600	2018-11-08 12:7
17	90.600	180.600	42.800	40.000	3600	2018-11-08 13:28
18	90.600	180.600	44.800	40.000	3600	2018-11-08 14:48

Continued on next page

Table A.5 – continued from previous page

i_m	$\varphi^\mathrm{s}_\mathrm{m}$ [°]	$\varphi^\mathrm{t}_\mathrm{m}$ [°]	r_m [mm]	z_m [mm]	Duration [s]	Date [y-m-d H:M]

Table A.5.: Dataset SSAmRad181: A radial scan of the top surface of Super Siegfried with an open ^{241}Am source. A second open ^{241}Am source was irradiating the mantle of the detector.

Table A.6 – Dataset SSAmRad136

i_m	$\varphi^\mathrm{s}_\mathrm{m}$ [°]	$\varphi^\mathrm{t}_\mathrm{m}$ [°]	r_m [mm]	z_m [mm]	Duration [s]	Date [y-m-d H:M]
1	45.600	135.600	10.800	40.000	3600	2018-11-16 11:57
2	45.600	135.600	12.800	40.000	3600	2018-11-16 13:18
3	45.600	135.600	14.800	40.000	3600	2018-11-16 14:38
4	45.600	135.600	16.800	40.000	3600	2018-11-16 15:59
5	45.600	135.600	18.800	40.000	3600	2018-11-16 17:19
6	45.600	135.600	20.800	40.000	3600	2018-11-16 18:40
7	45.600	135.600	22.800	40.000	3600	2018-11-16 20:0
8	45.600	135.600	24.800	40.000	3600	2018-11-16 21:21
9	45.600	135.600	26.800	40.000	3600	2018-11-16 22:42
10	45.600	135.600	28.800	40.000	3600	2018-11-17 0:2
11	45.600	135.600	30.800	40.000	3600	2018-11-17 1:23
12	45.600	135.600	32.800	40.000	3600	2018-11-17 2:44
13	45.600	135.600	34.800	40.000	3600	2018-11-17 4:4
14	45.600	135.600	36.800	40.000	3600	2018-11-17 5:25
15	45.600	135.600	38.800	40.000	3600	2018-11-17 6:46
16	45.600	135.600	40.800	40.000	3600	2018-11-17 8:6
17	45.600	135.600	42.800	40.000	3600	2018-11-17 9:27
18	45.600	135.600	44.800	40.000	3600	2018-11-17 10:47

Table A.6.: Dataset SSAmRad136: A radial scan of the top surface of Super Siegfried with an open ^{241}Am source. A second open ^{241}Am source was irradiating the mantle of the detector.

Table A.7 – Dataset SSAmRad23

i_m	$\varphi^\mathrm{s}_\mathrm{m}$ [°]	$\varphi^\mathrm{t}_\mathrm{m}$ [°]	r_m [mm]	z_m [mm]	Duration [s]	Date [y-m-d H:M]
1	293.100	23.100	10.800	40.000	3600	2019-02-19 18:13
2	293.100	23.100	12.800	40.000	3600	2019-02-19 19:34
3	293.100	23.100	14.800	40.000	3600	2019-02-19 20:55
4	293.100	23.100	16.800	40.000	3600	2019-02-19 22:16
5	293.100	23.100	18.800	40.000	3600	2019-02-19 23:37

Continued on next page

Table A.7 – continued from previous page

i_m	$\varphi^\mathrm{s}_\mathrm{m}$ [°]	$\varphi^\mathrm{t}_\mathrm{m}$ [°]	r_m [mm]	z_m [mm]	Duration [s]	Date [y-m-d H:M]
6	293.100	23.100	20.800	40.000	3600	2019-02-20 0:59
7	293.100	23.100	22.800	40.000	3600	2019-02-20 2:20
8	293.100	23.100	24.800	40.000	3600	2019-02-20 3:41
9	293.100	23.100	26.800	40.000	3600	2019-02-20 5:3
10	293.100	23.100	28.800	40.000	3600	2019-02-20 6:24
11	293.100	23.100	30.800	40.000	3600	2019-02-20 7:45
12	293.100	23.100	32.800	40.000	3600	2019-02-20 9:7
13	293.100	23.100	34.800	40.000	3600	2019-02-20 10:28
14	293.100	23.100	36.800	40.000	3600	2019-02-20 11:49
15	293.100	23.100	38.800	40.000	3600	2019-02-20 15:54
16	293.100	23.100	40.800	40.000	3600	2019-02-20 17:15

Table A.7.: Dataset SSAmRad23: A radial scan of the top surface of Super Siegfried with an open ^{241}Am source. A second open ^{241}Am source was irradiating the mantle of the detector.

Table A.8 – Dataset SSAmRad1

i_m	$\varphi^\mathrm{s}_\mathrm{m}$ [°]	$\varphi^\mathrm{t}_\mathrm{m}$ [°]	r_m [mm]	z_m [mm]	Duration [s]	Date [y-m-d H:M]
1	270.600	0.600	10.800	40.000	3600	2019-02-15 12:36
2	270.600	0.600	12.800	40.000	3600	2019-02-15 13:57
3	270.600	0.600	14.800	40.000	3600	2019-02-15 15:18
4	270.600	0.600	16.800	40.000	3600	2019-02-15 16:39
5	270.600	0.600	18.800	40.000	3600	2019-02-15 18:0
6	270.600	0.600	20.800	40.000	3600	2019-02-15 19:21
7	270.600	0.600	22.800	40.000	3600	2019-02-15 20:43
8	270.600	0.600	24.800	40.000	3600	2019-02-15 22:4
9	270.600	0.600	26.800	40.000	3600	2019-02-15 23:25
10	270.600	0.600	28.800	40.000	3600	2019-02-16 0:46
11	270.600	0.600	30.800	40.000	3600	2019-02-16 2:8
12	270.600	0.600	32.800	40.000	3600	2019-02-16 3:29
13	270.600	0.600	34.800	40.000	3600	2019-02-16 4:50
14	270.600	0.600	36.800	40.000	3600	2019-02-16 6:12
15	270.600	0.600	38.800	40.000	3600	2019-02-16 7:33
16	270.600	0.600	40.800	40.000	3600	2019-02-16 8:54

Table A.8.: Dataset SSAmRad1: A radial scan of the top surface of Super Siegfried with an open ^{241}Am source. A second open ^{241}Am source was irradiating the mantle of the detector.

A.2.2 Datasets with Strontium

Table A.9 – Dataset SSSrRot

i_{m}	$\varphi^{\mathrm{s}}_{\mathrm{m}}$ [°]	$\varphi^{\mathrm{t}}_{\mathrm{m}}$ [°]	r_{m} [mm]	z_{m} [mm]	Duration [s]	Date [y-m-d H:M]
1	45.600	135.600	28.800	40.000	900	2019-03-26 10:37
2	30.600	120.600	28.800	40.000	900	2019-03-26 11:23
3	15.600	105.600	28.800	40.000	900	2019-03-26 12:12
4	0.600	90.600	28.800	40.000	900	2019-03-26 15:2
5	345.600	75.600	28.800	40.000	900	2019-03-26 16:11
6	330.500	60.500	28.800	40.000	900	2019-03-29 9:24
7	315.600	45.600	28.800	40.000	900	2019-03-29 10:28
8	300.600	30.600	28.800	40.000	900	2019-03-29 11:33
9	285.600	15.600	28.800	40.000	900	2019-03-29 12:37

Table A.9.: Dataset SSSrRot: A rotational scan of the top and side surface of Super Siegfried with two ^{90}Sr sources.

Table A.10 – Dataset SSSrRad

i_{m}	$\varphi^{\mathrm{s}}_{\mathrm{m}}$ [°]	$\varphi^{\mathrm{t}}_{\mathrm{m}}$ [°]	r_{m} [mm]	z_{m} [mm]	Duration [s]	Date [y-m-d H:M]
1	45.600	135.600	10.800	40.000	900	2019-03-20 17:1
2	45.600	135.600	12.800	40.000	900	2019-03-20 17:29
3	45.600	135.600	14.800	40.000	900	2019-03-20 18:2
4	45.600	135.600	16.800	40.000	900	2019-03-20 18:35
5	45.600	135.600	18.800	40.000	900	2019-03-20 19:8
6	45.600	135.600	20.800	40.000	900	2019-03-20 19:41
7	45.600	135.600	22.800	40.000	900	2019-03-20 20:14
8	45.600	135.600	24.800	40.000	900	2019-03-25 9:36
9	45.600	135.600	26.800	40.000	900	2019-03-25 10:8
10	45.600	135.600	28.800	40.000	900	2019-03-25 10:41
11	45.600	135.600	30.800	40.000	900	2019-03-25 11:14
12	45.600	135.600	32.800	40.000	900	2019-03-25 11:47
13	45.600	135.600	34.800	40.000	900	2019-03-25 12:20
14	45.600	135.600	36.800	40.000	900	2019-03-25 12:53
15	45.600	135.600	38.800	40.000	900	2019-03-25 13:26
16	45.600	135.600	40.800	40.000	900	2019-03-25 13:58
17	45.600	135.600	42.800	40.000	900	2019-03-25 14:26

Table A.10.: Dataset SSSrRad: A radial scan of the top surface of Super Siegfried with a ^{90}Sr source. A second ^{90}Sr source was irradiating the mantle of the detector.

A.3 Siegfried III

A.3.1 Datasets with Americium

Table A.11 – Dataset S3AmRotMid

i_m	$\varphi^\mathrm{s}_\mathrm{m}$ [°]	$\varphi^\mathrm{t}_\mathrm{m}$ [°]	r_m [mm]	z_m [mm]	Duration [s]	Date [y-m-d H:M]
1	170.100	260.100	22.600	33.900	3600	2018-05-02 15:48
2	165.100	255.100	22.600	33.900	3600	2018-05-02 17:25
3	160.100	250.100	22.600	33.900	3600	2018-05-02 19:2
4	155.100	245.100	22.600	33.900	3600	2018-05-02 20:40
5	150.100	240.100	22.600	33.900	3600	2018-05-02 22:18
6	145.100	235.100	22.600	33.900	3600	2018-05-02 23:56
7	140.100	230.100	22.600	33.900	3600	2018-05-03 1:35
8	135.100	225.100	22.600	33.900	3600	2018-05-03 3:15
9	130.100	220.100	22.600	33.900	3600	2018-05-03 14:36
10	125.100	215.100	22.600	33.900	3600	2018-05-03 6:31
11	120.100	210.100	22.600	33.900	3600	2018-05-03 16:13
12	115.100	205.100	22.600	33.900	3600	2018-05-03 17:50
13	110.100	200.100	22.600	33.900	3600	2018-05-03 19:26
14	105.100	195.100	22.600	33.900	3600	2018-05-03 21:2
15	100.100	190.100	22.600	33.900	3600	2018-05-03 22:37
16	95.100	185.100	22.600	33.900	3600	2018-05-04 0:13
17	90.100	180.100	22.600	33.900	3600	2018-05-04 1:48
18	85.100	175.100	22.600	33.900	3600	2018-05-04 3:24
19	80.100	170.100	22.600	33.900	3600	2018-05-04 4:59
20	80.100	170.100	22.600	33.900	3600	2018-05-04 6:34
21	75.100	165.100	22.600	33.900	3600	2018-05-04 18:8
22	70.100	160.100	22.600	33.900	3600	2018-05-04 8:10
23	65.100	155.100	22.600	33.900	3600	2018-05-04 19:44
24	60.100	150.100	22.600	33.900	3600	2018-05-04 21:19
25	55.100	145.100	22.600	33.900	3600	2018-05-04 22:53
26	50.100	140.100	22.600	33.900	3600	2018-05-05 0:27
27	45.100	135.100	22.600	33.900	3600	2018-05-05 2:2
28	40.100	130.100	22.600	33.900	3600	2018-05-05 3:36
29	35.100	125.100	22.600	33.900	3600	2018-05-05 5:11
30	30.100	120.100	22.600	33.900	3600	2018-05-05 6:45
31	25.100	115.100	22.600	33.900	3600	2018-05-05 8:20
32	20.100	110.100	22.600	33.900	3600	2018-05-05 9:55
33	15.100	105.100	22.600	33.900	3600	2018-05-05 11:30
34	10.100	100.100	22.600	33.900	3600	2018-05-05 13:4
35	5.100	95.100	22.600	33.900	3600	2018-05-05 14:39
36	0.100	90.100	22.600	33.900	3600	2018-05-05 16:14
37	355.100	85.100	22.600	33.900	3600	2018-05-05 18:13
38	350.100	80.100	22.600	33.900	3600	2018-05-05 19:49

Continued on next page

Table A.11 – continued from previous page

i_m	$\varphi^\mathrm{s}_\mathrm{m}$ [°]	$\varphi^\mathrm{t}_\mathrm{m}$ [°]	r_m [mm]	z_m [mm]	Duration [s]	Date [y-m-d H:M]
39	345.100	75.100	22.600	33.900	3600	2018-05-05 21:24
40	340.100	70.100	22.600	33.900	3600	2018-05-05 23:0

Table A.11.: Dataset S3AmRotMid: A rotational scan of the top and side surface of Siegfried III with two open ^{241}Am sources.

Table A.12 – Dataset S3AmVert4

i_m	$\varphi^\mathrm{s}_\mathrm{m}$ [°]	$\varphi^\mathrm{t}_\mathrm{m}$ [°]	r_m [mm]	z_m [mm]	Duration [s]	Date [y-m-d H:M]
1	3.500	93.500	49.600	70.300	3600	2018-05-22 11:36
2	3.500	93.500	49.600	69.800	3600	2018-05-22 12:46
3	3.500	93.500	49.600	69.300	3600	2018-05-22 13:57
4	3.500	93.500	49.600	68.800	3600	2018-05-22 15:8
5	3.500	93.500	49.600	68.300	3600	2018-05-22 16:19
6	3.500	93.500	49.600	67.800	3600	2018-05-22 17:30
7	3.500	93.500	49.600	67.300	3600	2018-05-22 18:40
8	3.500	93.500	49.600	66.800	3600	2018-05-22 19:51
9	3.500	93.500	49.600	66.300	3600	2018-05-23 10:36
10	3.500	93.500	49.600	65.800	3600	2018-05-23 11:47
11	3.500	93.500	49.600	65.300	3600	2018-05-23 12:58
12	3.500	93.500	49.600	64.800	3600	2018-05-23 16:9
13	3.500	93.500	49.600	64.300	3600	2018-05-23 17:20
14	3.500	93.500	49.600	63.800	3600	2018-05-23 18:30
15	3.500	93.500	49.600	63.300	3600	2018-05-23 19:41
16	3.500	93.500	49.600	62.800	3600	2018-05-23 20:52
17	3.500	93.500	49.600	62.300	3600	2018-05-23 22:3
18	3.500	93.500	49.600	57.300	3600	2018-05-24 12:16
19	3.500	93.500	49.600	54.300	3600	2018-05-24 13:27
20	3.500	93.500	49.600	51.300	3600	2018-05-24 14:38
21	3.500	93.500	49.600	50.800	3600	2018-05-24 15:49
22	3.500	93.500	49.600	49.300	3600	2018-05-24 16:59
23	3.500	93.500	49.600	48.300	3600	2018-05-24 18:10
24	3.500	93.500	49.600	48.300	3600	2018-05-24 19:21
25	3.500	93.500	49.600	47.800	3600	2018-05-24 20:32
26	3.500	93.500	49.600	47.300	3600	2018-05-24 21:43
27	3.500	93.500	49.600	46.800	3600	2018-05-25 9:58
28	3.500	93.500	49.600	46.300	3600	2018-05-25 11:8
29	3.500	93.500	49.600	45.800	3600	2018-05-25 12:19
30	3.500	93.500	49.600	45.300	3600	2018-05-25 14:50
31	3.500	93.500	49.600	44.800	3600	2018-05-25 16:0
32	3.500	93.500	49.600	44.300	3600	2018-05-25 17:11

Continued on next page

Table A.12 – continued from previous page

i_m	$\varphi^\mathrm{s}_\mathrm{m}$ [°]	$\varphi^\mathrm{t}_\mathrm{m}$ [°]	r_m [mm]	z_m [mm]	Duration [s]	Date [y-m-d H:M]
33	3.500	93.500	49.600	43.800	3600	2018-05-25 18:22
34	3.500	93.500	49.600	43.300	3600	2018-05-25 19:33
35	3.500	93.500	49.600	42.800	3600	2018-05-25 20:43
36	3.500	93.500	49.600	42.300	3600	2018-05-25 21:54
37	3.500	93.500	49.600	41.800	3600	2018-05-28 10:11
38	3.500	93.500	49.600	41.300	3600	2018-05-28 11:22
39	3.500	93.500	49.600	40.800	3600	2018-05-28 12:33
40	3.500	93.500	49.600	40.300	3600	2018-05-28 13:43
41	3.500	93.500	49.600	37.300	3600	2018-05-28 14:55
42	3.500	93.500	49.600	33.300	3600	2018-05-28 16:6
43	3.500	93.500	49.600	29.300	3600	2018-05-28 17:17
44	3.500	93.500	49.600	27.300	3600	2018-05-28 18:28
45	3.500	93.500	49.600	25.300	3600	2018-05-28 19:39
46	3.500	93.500	49.600	24.800	3600	2018-05-28 20:50
47	3.500	93.500	49.600	24.300	3600	2018-05-29 7:42
48	3.500	93.500	49.600	23.800	3600	2018-05-29 8:53
49	3.500	93.500	49.600	23.300	3600	2018-05-29 10:4
50	3.500	93.500	49.600	22.800	3600	2018-05-29 11:15
51	3.500	93.500	49.600	22.300	3600	2018-05-29 12:26
52	3.500	93.500	49.600	21.800	3600	2018-05-29 13:37
53	3.500	93.500	49.600	21.300	3600	2018-05-29 14:47
54	3.500	93.500	49.600	20.800	3600	2018-05-29 15:58
55	3.500	93.500	49.600	20.300	3600	2018-05-30 9:23
56	3.500	93.500	49.600	19.800	3600	2018-05-30 10:34
57	3.500	93.500	49.600	19.300	3600	2018-05-30 11:45
58	3.500	93.500	49.600	18.800	3600	2018-05-30 12:56
59	3.500	93.500	49.600	18.300	3600	2018-05-30 14:7
60	3.500	93.500	49.600	17.800	3600	2018-05-30 15:17
61	3.500	93.500	49.600	17.300	3600	2018-05-30 16:28
62	3.500	93.500	49.600	16.800	3600	2018-05-30 17:39
63	3.500	93.500	49.600	16.300	3600	2018-06-18 11:26
64	3.500	93.500	49.600	13.300	3600	2018-05-30 20:1
65	3.500	93.500	49.600	9.300	3600	2018-05-30 21:13
66	3.500	93.500	49.600	5.300	3600	2018-05-30 22:24
67	3.500	93.500	49.600	4.800	3600	2018-06-01 10:54
68	3.500	93.500	49.600	4.800	3600	2018-06-01 12:5
69	3.500	93.500	49.600	4.300	3600	2018-06-01 13:16
70	3.500	93.500	49.600	4.300	3600	2018-06-01 14:26
71	3.500	93.500	49.600	3.800	3600	2018-06-01 15:37
72	3.500	93.500	49.600	3.800	3600	2018-06-01 16:48
73	3.500	93.500	49.600	3.300	3600	2018-06-01 17:59
74	3.500	93.500	49.600	3.300	3600	2018-06-01 19:9
75	3.500	93.500	49.600	2.800	3600	2018-06-01 20:20

Continued on next page

Table A.12 – continued from previous page

i_m	$\varphi^\mathrm{s}_\mathrm{m}$ [°]	$\varphi^\mathrm{t}_\mathrm{m}$ [°]	r_m [mm]	z_m [mm]	Duration [s]	Date [y-m-d H:M]
76	3.500	93.500	49.600	2.800	3600	2018-06-01 21:31
77	3.500	93.500	49.600	2.300	3600	2018-06-01 22:42
78	3.500	93.500	49.600	2.300	3600	2018-06-01 23:53
79	3.500	93.500	49.600	1.800	3600	2018-06-04 6:46
80	3.500	93.500	49.600	1.300	3600	2018-06-04 7:57
81	3.500	93.500	49.600	0.800	3600	2018-06-04 9:8
82	3.500	93.500	49.600	0.300	3600	2018-06-04 10:19
83	3.500	93.500	49.600	-0.200	3600	2018-06-04 11:30
84	3.500	93.500	49.600	-0.700	3600	2018-06-04 12:41
85	3.500	93.500	49.600	-1.200	3600	2018-06-04 13:52
86	3.500	93.500	49.600	-1.700	3600	2018-06-04 15:2
87	3.500	93.500	49.600	-2.200	3600	2018-06-04 16:13
88	3.500	93.500	49.600	-2.700	3600	2018-06-04 17:24
89	3.500	93.500	49.600	-3.200	3600	2018-06-04 18:35

Table A.12.: Dataset S3AmVert4: A vertical scan of the side surface of Siegfried III with an open ^{241}Am source.

Table A.13 – Dataset S3AmRad70

i_m	$\varphi^\mathrm{s}_\mathrm{m}$ [°]	$\varphi^\mathrm{t}_\mathrm{m}$ [°]	r_m [mm]	z_m [mm]	Duration [s]	Date [y-m-d H:M]
1	340.100	70.100	19.600	72.800	3600	2018-04-19 18:12
2	340.100	70.100	22.600	72.800	3600	2018-03-07 18:44
3	340.100	70.100	23.600	72.800	3600	2018-04-24 14:38
4	340.100	70.100	9.600	72.800	3600	2018-04-27 11:24
5	340.100	70.100	10.600	72.800	3600	2018-04-27 12:34
6	340.100	70.100	11.600	72.800	3600	2018-04-27 13:45
7	340.100	70.100	12.600	72.800	3600	2018-04-27 14:55
8	340.100	70.100	13.600	72.800	3600	2018-04-27 16:6
9	340.100	70.100	14.600	72.800	3600	2018-04-25 15:25
10	340.100	70.100	15.600	72.800	3600	2018-04-25 16:35
11	340.100	70.100	16.600	72.800	3600	2018-04-25 17:46
12	340.100	70.100	17.600	72.800	3600	2018-04-25 18:57
13	340.100	70.100	18.600	72.800	3600	2018-04-25 20:8
14	340.100	70.100	20.600	72.800	3600	2018-04-19 19:23
15	340.100	70.100	21.600	72.800	3600	2018-04-19 20:33
16	340.100	70.100	24.600	72.800	3600	2018-04-24 15:49
17	340.100	70.100	25.600	72.800	3600	2018-04-20 0:6
18	340.100	70.100	26.600	72.800	3600	2018-04-20 1:17
19	340.100	70.100	27.600	72.800	3600	2018-04-20 2:27
20	340.100	70.100	28.600	72.800	3600	2018-04-20 3:38

Continued on next page

Table A.13 – continued from previous page

i_m	$\varphi^\mathrm{s}_\mathrm{m}$ [°]	$\varphi^\mathrm{t}_\mathrm{m}$ [°]	r_m [mm]	z_m [mm]	Duration [s]	Date [y-m-d H:M]
21	340.100	70.100	29.600	72.800	3600	2018-04-20 4:49
22	340.100	70.100	30.600	72.800	3600	2018-04-20 7:34
23	340.100	70.100	31.600	72.800	3600	2018-04-20 8:45
24	340.100	70.100	32.600	72.800	3600	2018-04-20 9:56
25	340.100	70.100	33.600	72.800	3600	2018-04-20 11:7
26	340.100	70.100	34.600	72.800	3600	2018-04-20 12:17
27	340.100	70.100	35.600	72.800	3600	2018-04-20 13:28
28	340.100	70.100	36.600	72.800	3600	2018-04-20 14:39
29	340.100	70.100	37.600	72.800	3600	2018-04-24 17:1
30	340.100	70.100	38.600	72.800	3600	2018-04-24 18:12
31	340.100	70.100	39.600	72.800	3600	2018-04-24 19:22
32	340.100	70.100	40.600	72.800	3600	2018-04-24 20:33
33	340.100	70.100	41.600	72.800	3600	2018-04-24 21:44
34	340.100	70.100	42.600	72.800	3600	2018-04-24 22:54
35	340.100	70.100	43.600	72.800	3600	2018-04-25 0:5
36	340.100	70.100	44.600	72.800	3600	2018-04-25 11:49
37	340.100	70.100	45.600	72.800	3600	2018-04-25 12:59
38	340.100	70.100	46.600	72.800	3600	2018-04-25 14:10

Table A.13.: Dataset S3AmRad70: A radial scan of the top surface of Siegfried III with an open ^{241}Am source.

Table A.14 – Dataset S3AmRad94

i_m	$\varphi^\mathrm{s}_\mathrm{m}$ [°]	$\varphi^\mathrm{t}_\mathrm{m}$ [°]	r_m [mm]	z_m [mm]	Duration [s]	Date [y-m-d H:M]
1	3.500	93.500	9.600	72.800	3600	2018-06-13 8:46
2	3.500	93.500	10.600	72.800	3600	2018-06-12 13:5
3	3.500	93.500	11.600	72.800	3600	2018-06-12 14:16
4	3.500	93.500	12.600	72.800	3600	2018-06-12 15:27
5	3.500	93.500	13.600	72.800	3600	2018-06-12 16:38
6	3.500	93.500	14.600	72.800	3600	2018-06-12 17:49
7	3.500	93.500	15.600	72.800	3600	2018-06-12 19:0
8	3.500	93.500	16.600	72.800	3600	2018-06-12 20:11
9	3.500	93.500	17.600	72.800	3600	2018-06-12 21:23
10	3.500	93.500	18.600	72.800	3600	2018-06-12 22:34
11	3.500	93.500	19.600	72.800	3600	2018-06-12 23:45
12	3.500	93.500	20.600	72.800	3600	2018-06-13 0:56
13	3.500	93.500	21.600	72.800	3600	2018-06-13 2:7
14	3.500	93.500	22.600	72.800	3600	2018-06-13 3:18
15	3.500	93.500	23.600	72.800	3600	2018-06-13 4:29
16	3.500	93.500	24.600	72.800	3600	2018-06-13 12:55

Continued on next page

Table A.14 – continued from previous page

i_m	$\varphi^\mathrm{s}_\mathrm{m}$ [°]	$\varphi^\mathrm{t}_\mathrm{m}$ [°]	r_m [mm]	z_m [mm]	Duration [s]	Date [y-m-d H:M]
17	3.500	93.500	25.600	72.800	3600	2018-06-13 14:6
18	3.500	93.500	26.600	72.800	3600	2018-06-13 15:17
19	3.500	93.500	27.600	72.800	3600	2018-06-14 22:0
20	3.500	93.500	28.600	72.800	3600	2018-06-14 23:11
21	3.500	93.500	29.600	72.800	3600	2018-06-15 10:49
22	3.500	93.500	30.600	72.800	3600	2018-06-15 12:0
23	3.500	93.500	31.600	72.800	3600	2018-06-15 13:11
24	3.500	93.500	32.600	72.800	3600	2018-06-15 14:22
25	3.500	93.500	33.600	72.800	3600	2018-06-15 15:33
26	3.500	93.500	34.600	72.800	3600	2018-06-15 16:44
27	3.500	93.500	35.600	72.800	3600	2018-06-15 17:54
28	3.500	93.500	36.600	72.800	3600	2018-06-15 19:5
29	3.500	93.500	37.600	72.800	3600	2018-06-15 20:16
30	3.500	93.500	38.600	72.800	3600	2018-06-15 21:27
31	3.500	93.500	39.600	72.800	3600	2018-06-15 22:38
32	3.500	93.500	40.600	72.800	3600	2018-06-15 23:49
33	3.500	93.500	41.600	72.800	3600	2018-06-16 1:0
34	3.500	93.500	42.600	72.800	3600	2018-06-16 2:11
35	3.500	93.500	43.600	72.800	3600	2018-06-17 18:45
36	3.500	93.500	44.600	72.800	3600	2018-06-17 19:56
37	3.500	93.500	45.600	72.800	3600	2018-06-17 21:7
38	3.500	93.500	46.600	72.800	3600	2018-06-17 22:18

Table A.14.: Dataset S3AmRad94: A radial scan of the top surface of Siegfried III with an open ^{241}Am source.

Appendix B: Super Siegfried - Electronic Filters

A BiQuad filter has 5 parameters: $\mathcal{BQ}(b_0, b_1, b_2, a_1, b_2)$.

The electronic response of the core channel of Super Siegfried in GALATEA is simulated through applying 6 BiQuad filter in forward direction, $\mathcal{BQ}_{\mathrm{f}}^{i}$, in ascending order and 1 BiQuad filter in reversed direction, $\mathcal{BQ}_{0,\mathrm{r}}$, at the end:

$$\begin{aligned}
\mathcal{BQ}_{0,\mathrm{f}}^{1} &= \mathcal{BQ}(1, -7.999\,360\,051\,195\,904 \times 10^{-5}, 0, -0.9999200063994881, 0)\\
\mathcal{BQ}_{0,\mathrm{f}}^{2} &= \mathcal{BQ}(0.13381262850046263, 0, 0, -0.8661873714995374, 0)\\
\mathcal{BQ}_{0,\mathrm{f}}^{3} &= \mathcal{BQ}(0.8830106439366491, -1.062508067199202, 0.39500243358276366,\\
&\qquad\qquad -1.062508067199202, 0.27801307751941284)\\
\mathcal{BQ}_{0,\mathrm{f}}^{4} &= \mathcal{BQ}(0.14517753480356801, 0.29035506960713603, 0.14517753480356801,\\
&\qquad\qquad -0.5268338305497745, 0.10754396976404651)\\
\mathcal{BQ}_{0,\mathrm{f}}^{5} &= \mathcal{BQ}(0.03114385947154449, 0.06228771894308898, 0.03114385947154449,\\
&\qquad\qquad -1.7107595476166255, 0.8353349855028034)\\
\mathcal{BQ}_{0,\mathrm{f}}^{6} &= \mathcal{BQ}(1.1693983953403495, -0.7217690444178493, -0.013658795400333207,\\
&\qquad\qquad -0.7217690444178493, 0.15573959994001624)\\
\mathcal{BQ}_{0,\mathrm{r}} &= \mathcal{BQ}(1.132489179905904, -1.2032788896658313, 0.3148468021630763,\\
&\qquad\qquad -1.2032788896658313, 0.44733598206898034)
\end{aligned}$$

The electronic response of the segments of Super Siegfried in GALATEA is simulated through a applying 2 BiQuad filter in forward direction, $\mathcal{BQ}_{\mathrm{S,f}}^{i}$, in ascending order:

$$\begin{aligned}
\mathcal{BQ}_{\mathrm{S,f}}^{1} &= \mathcal{BQ}(1.0, -7.999\,360\,051\,195\,904 \times 10^{-5}, 0, -0.9999200063994881, 0))\\
\mathcal{BQ}_{\mathrm{S,f}}^{2} &= \mathcal{BQ}(0.038461538461538464, 0, 0, -0.9615384615384616, 0)
\end{aligned}$$

Note, that these filters have to be applied on pulses in their differential form, thus, charge current and not induced charge per sample.

Appendix C: Super Siegfried - Charge Drift Parameters

The parameter for the electron drift, see Sec. 3.2.1, used for the simulation presented in this thesis are

$$\mu_{0,\mathrm{e}}^{100} = 3.8609 \ , \tag{C.1}$$

$$\beta_{\mathrm{e}}^{100} = 4.0 \ , \tag{C.2}$$

$$\mathcal{E}_{0,\mathrm{e}}^{100} = 32000 \ , \tag{C.3}$$

$$\mu_{n,\mathrm{e}}^{100} = 0 \ , \tag{C.4}$$

$$\mu_{0,\mathrm{e}}^{111} = 3.8536 \ , \tag{C.5}$$

$$\beta_{\mathrm{e}}^{111} = 4.0 \ , \tag{C.6}$$

$$\mathcal{E}_{0,\mathrm{e}}^{111} = 40000 \ , \tag{C.7}$$

$$\mu_{n,\mathrm{e}}^{111} = 0 \ . \tag{C.8}$$

They were determined through data, see Sec. 6.9.

For the hole drift parameters, values from [58, 59] were used, because in order to determine those for Super Siegfried, events located at the core electrode (at the inner borehole) are needed. In such events, the electrons are directly collected and the holes have to drift through the bulk towards the mantle.

Temperature Dependence

The temperature dependence of the charge drift is modeled, as described in Sec. 3.2.1, with 8 parameters:

$$p_{1,\mathrm{e}}^{100} = 10.427414 \ , \quad p_{2,\mathrm{e}}^{100} = 59.226418 \ , \tag{C.9}$$

$$p_{1,\mathrm{e}}^{111} = 1147.3456 \ , \quad p_{2,\mathrm{e}}^{111} = 488.61563 \ , \tag{C.10}$$

$$p_{1,\mathrm{h}}^{100} = 51.427414 \ , \quad p_{2,\mathrm{h}}^{100} = 59.226418 \ , \tag{C.11}$$

$$p_{1,\mathrm{h}}^{111} = 1147.3456 \ , \quad p_{2,\mathrm{h}}^{111} = 488.61563 \ . \tag{C.12}$$

A crystal temperature of 92 K was assumed in the simulation, see Sec. 4.1.4.

Bibliography

[1] R.L. Helmer. “First results from the Sudbury Neutrino Observatory”. In: *Nuclear Physics B - Proceedings Supplements* 111 (Nov. 2002), pp. 122–127. DOI: `10.1016/S0920-5632(02)01693-6`.

[2] X. Qian and P. Vogel. “Neutrino mass hierarchy”. In: *Progress in Particle and Nuclear Physics* 83 (2015), pp. 1–30. ISSN: 0146-6410. DOI: `https://doi.org/10.1016/j.ppnp.2015.05.002`.

[3] Maury Goodman. “The Deep Underground Neutrino Experiment”. In: *Advances in High Energy Physics* 2015 (Dec. 2015), pp. 1–9. DOI: `10.1155/2015/256351`.

[4] “Status and perspectives of the JUNO experiment”. In: *Journal of Physics: Conference Series* 1056 (July 2018). DOI: `10.1088/1742-6596/1056/1/012048`.

[5] E. Akhmedov and Salvatore Esposito. “Majorana neutrinos and other Majorana particles: theory and experiment”. In: *The Physics of Ettore Majorana: Theoretical, Mathematical, and Phenomenological.* Cambridge University Press, 2014, pp. 303–353. DOI: `10.1017/CBO9781107358362.015`.

[6] Michelle Dolinski, Alan Poon, and Werner Rodejohann. “Neutrinoless Double-Beta Decay: Status and Prospects”. In: *Annual Review of Nuclear and Particle Science* 69 (Oct. 2019). DOI: `10.1146/annurev-nucl-101918-023407`. arXiv: `1902.04097`.

[7] Pasquale Di Bari. “An introduction to leptogenesis and neutrino properties”. In: *Contemporary Physics* 53.4 (2012), pp. 315–338. DOI: `10.1080/00107514.2012.701096`. eprint: `https://doi.org/10.1080/00107514.2012.701096`.

[8] K Ackermann et al. “The GERDA experiment for the search of $0\nu\beta\beta$ decay in ^{76}Ge”. In: *The European Physical Journal C* 73 (Mar. 2013), p. 2330.

[9] Yoann Kermaidic. “GERDA, Majorana and LEGEND - Towards a background-free ton-scale Ge76 experiment”. In: Neutrino 2020 (Online, July 1, 2020). 2020.

[10] M. Agostini et al. “Probing Majorana neutrinos with double-β decay”. In: *Science* 365.6460 (2019), pp. 1445–1448. ISSN: 0036-8075. DOI: `10.1126/science.aav8613`. URL: `https://science.sciencemag.org/content/365/6460/1445`.

[11] M. Agostini et al. “Final Results of GERDA on the Search for Neutrinoless Double-β Decay”. In: *Phys. Rev. Lett.* 125 (25 Dec. 2020), p. 252502. DOI: `10.1103/PhysRevLett.125.252502`.

[12] M. Agostini, M. Allardt, A. M. Bakalyarov, et al. “Background free search for neutrinoless double beta decay with GERDA Phase II”. In: *Nature* Volume 544 (Mar. 2, 2017). DOI: `10.1038/nature21717`. arXiv: `1703.00570v2 [nucl-ex]`.

[13] LEGEND Collaboration. *The Large Enriched Germanium Experiment for Neutrinoless Double Beta Decay LEGEND*. Sept. 2017. arXiv: `1709.01980v1`.

[14] Glenn F. Knoll. *Radiation Detection and Measurement*. JOHN WILEY & SONS INC, Aug. 11, 2010. ISBN: 0470131489.

[15] M. Agostini et al. "Pulse shape discrimination for GERDA Phase I data". In: *Eur. Phys. J. C* 73.10 (2013), p. 2583. DOI: `10.1140/epjc/s10052-013-2583-7`. arXiv: `1307.2610 [physics.ins-det]`.

[16] M. Agostini and the GERDA Collaboration. "The background in the $0\nu\beta\beta$ experiment GERDA". In: *The European Physical Journal C* 74.4 (Apr. 2014), p. 2764. ISSN: 1434-6052. DOI: `10.1140/epjc/s10052-014-2764-z`.

[17] GERDA Collaboration. "Modeling of GERDA Phase II data". In: *Journal of High Energy Physics* 2020 (Mar. 2020). DOI: `10.1007/JHEP03(2020)139`.

[18] I. Abt et al. "Simulation of semiconductor detectors in 3D with SolidStateDetectors.jl". In: *Journal of Instrumentation* 16.08 (Aug. 2021), P08007. DOI: `10.1088/1748-0221/16/08/p08007`. URL: `https://doi.org/10.1088/1748-0221/16/08/p08007`.

[19] Weizsäcker. "Zur Theorie der Kernmassen". In: *Zeitschrift für Physik* (June 1935).

[20] A. S. Barabash. "Average and recommended half-life values for two neutrino double beta decay". In: *Nucl. Phys. A 935 (2015) 52* (2015). DOI: `10.1016/j.nuclphysa.2015.01.001`. eprint: `arXiv:1501.05133`.

[21] Dusan Stefanik et al. "Reexamining the light neutrino exchange mechanism of the $0\nu\beta\beta$ decay with left- and right-handed leptonic and hadronic currents". In: *Physical Review C* 92 (Nov. 2015).

[22] Ivan Esteban et al. "Global analysis of three-flavour neutrino oscillations: synergies and tensions in the determination of θ_23, δ_{CP}, and the mass ordering". In: *JHEP* 01 (2019), p. 106. DOI: `10.1007/JHEP01(2019)106`. arXiv: `1811.05487 [hep-ph]`.

[23] Matteo Agostini, Giovanni Benato, and Jason A. Detwiler. "Discovery probability of next-generation neutrinoless double-beta-decay experiments". In: *Phys. Rev. D* (2017). DOI: `10.1103/PhysRevD.96.053001`. eprint: `arXiv:1705.02996`.

[24] Allen Caldwell et al. "A Global Bayesian Analysis of Neutrino Mass Data". In: *Phys. Rev. D* (2017). DOI: `10.1103/PhysRevD.96.073001`. eprint: `arXiv:1705.01945`.

[25] Massimiliano Lattanzi and Martina Gerbino. "Status of Neutrino Properties and Future Prospects — Cosmological and Astrophysical Constraints". In: *Frontiers in Physics* 5 (Dec. 2017). DOI: `10.3389/fphy.2017.00070`.

[26] The PLANCK Collaboration. "Planck 2015 results". In: *Astronomy & Astrophysics* 594 (Sept. 2016), A13. DOI: `10.1051/0004-6361/201525830`.

[27] M. Tanabashi et al. "Review of Particle Physics". In: *Phys. Rev. D* 98 (3 Aug. 2018). DOI: `10.1103/PhysRevD.98.030001`.

[28] The KATRIN Collaboration. “An improved upper limit on the neutrino mass from a direct kinematic method by KATRIN”. In: *Phys. Rev. Lett.* (2019). DOI: `10.1103/PhysRevLett.123.221802`. eprint: `arXiv:1909.06048`.

[29] A. Gando et al. “Search for Majorana Neutrinos Near the Inverted Mass Hierarchy Region with KamLAND-Zen”. In: *Phys. Rev. Lett.* 117 (8 Aug. 2016). DOI: `10.1103/PhysRevLett.117.082503`.

[30] L. Cardani. “Neutrinoless Double Beta Decay Overview”. In: *SciPost Phys. Proc.* 1 (2019), p. 024. DOI: `10.21468/SciPostPhysProc.1.024`. arXiv: `1810.12828 [nucl-ex]`.

[31] *INFN Gran Sasso National Laboratory (LNGS)*. `https://www.lngs.infn.it/`. Accessed: 2020-06-25.

[32] M. Agostini et al. “Upgrade for Phase II of the Gerda experiment”. In: *Eur. Phys. J. C* 78.5 (2018), p. 388. DOI: `10.1140/epjc/s10052-018-5812-2`. arXiv: `1711.01452`.

[33] M. Agostini et al. “LArGe: active background suppression using argon scintillation for the Gerda $0\nu\beta\beta$ -experiment”. In: *Eur. Phys. J. C* 75.10 (2015), p. 506. DOI: `10.1140/epjc/s10052-015-3681-5`. arXiv: `1501.05762`.

[34] A. C. Wegmann. “Characterization of the liquid argon veto of the GERDA experiment and its application for the measurement of the ^{76}Ge half-life”. PhD Thesis. Ruperto-Carola-University of Heidelberg, Jan. 2017.

[35] K. H. Ackermann et al. “The GERDA experiment for the search of $0\nu\beta\beta$ decay in ^{76}Ge”. In: *Eur. Phys. J. C* 73.3 (Mar. 2013), p. 2330. ISSN: 1434-6052. DOI: `10.1140/epjc/s10052-013-2330-0`. arXiv: `1212.4067`.

[36] A. Lubashevskiy et al. “Mitigation of ^{42}Ar/^{42}K background for the GERDA Phase II experiment”. In: *Eur. Phys. J. C* (2018). DOI: `10.1140/epjc/s10052-017-5499-9`. eprint: `arXiv:1708.00226`.

[37] P. Holl et al. “Deep learning based pulse shape discrimination for germanium detectors”. In: *Eur. Phys. J. C* 79.6 (2019), p. 450. DOI: `10.1140/epjc/s10052-019-6869-2`. arXiv: `1903.01462 [physics.ins-det]`.

[38] The MAJORANA Collaboration. “The Majorana Neutrinoless Double-Beta Decay Experiment”. In: *IEEE Nucl. Sci. Symp.* (2008). DOI: `10.1109/NSSMIC.2008.4774740`. eprint: `arXiv:0811.2446`.

[39] D. G. Phillips II et al. “The Majorana experiment: an ultra-low background search for neutrinoless double-beta decay”. In: *J. Phys. Conf. Ser.* 381 (2012). DOI: `10.1088/1742-6596/381/1/012044`. arXiv: `1111.5578`.

[40] S. I. Alvis et al. “A Search for Neutrinoless Double-Beta Decay in ^{76}Ge with 26 kg-yr of Exposure from the MAJORANA DEMONSTRATOR”. In: *Phys. Rev. C* (2019). DOI: `10.1103/PhysRevC.100.025501`. eprint: `arXiv:1902.02299`.

[41] N. Abgrall et al. “The Majorana Low-noise Low-background Front-end Electronics”. In: *Physics Procedia* 61 (2015), pp. 654–657. ISSN: 1875-3892. DOI: `https://doi.org/10.1016/j.phpro.2014.12.066`.

[42] J. M. López-Castaño et al. “Recent Results of the Majorana Demonstrator Experiment”. In: *AIP Conf. Proc.* 2165.1 (2019). DOI: `10.1063/1.5130979`. arXiv: `1909.07509`.

[43] M. Agostini et al. “Production, characterization and operation of ^{76}Ge enriched BEGe detectors in GERDA”. In: *Eur. Phys. J. C* (2014). DOI: `10.1140/epjc/s10052-014-3253-0`. eprint: `arXiv:1410.0853`.

[44] A. Domula et al. “Pulse shape discrimination performance of Inverted Coaxial Ge detectors”. In: *Nucl. Instrum. Meth. A* 891 (2018), p. 106. DOI: `10.1016/j.nima.2018.02.056`. arXiv: `1711.01433`.

[45] Y. Efremenko et al. “Use of polyethylene naphthalate as a self-vetoing structural material”. In: *Journal of Instrumentation* 14 (July 2019). DOI: `10.1088/1748-0221/14/07/P07006`.

[46] LEGEND Collaboration. *LEGEND-1000 Preconceptual Design Report.* 2021. arXiv: `2107.11462`.

[47] J. Bardeen, W. H. Brattain, and W. Shockley. “The Transistor, A Semi-Conductor Triode”. In: *Phys. Rev. 74, 230* (July 15, 1948). DOI: `https://doi.org/10.1103/PhysRev.74.230`.

[48] Bernard Bailey James Patterson. *Solid-State Physics: Introduction to the Theory.* Springer, 2018. ISBN: 978-3-319-75321-8.

[49] *Electronic Band Structure.* `https://en.wikipedia.org/wiki/Electronic_band_structure`. Accessed: 2020-07-22.

[50] James R. Chelikowsky Marvin L. Cohen. *Electronic Structure and Optical Properties of Semiconductors.* Springer, 1988. ISBN: 978-3-642-97082-5.

[51] Lukas Hauertmann. “Influence of the Metallization on the Charge Collection Efficiency of Segmented Germanium Detectors”. MA thesis. Technische Universität München, 2017. URL: `https://wwwgedet.mpp.mpg.de/publication/thesis_final_20170330_compressed.pdf`.

[52] Guojian Wang et al. “High purity germanium crystal growth at the University of South Dakota”. In: *Journal of Physics: Conference Series* 606 (May 2015). DOI: `10.1088/1742-6596/606/1/012012`.

[53] Hao Mei et al. “The impact of neutral impurity concentration on charge drift mobility in n-type germanium”. In: *Journal of Instrumentation* 12 (May 2017). DOI: `10.1088/1748-0221/12/07/P07003`.

[54] B. Majorovits et al. “Aluminum as a source of background in low background experiments”. In: *Nuclear Instruments and Methods in Physics Research Section A* 647.1 (May 18, 2011), pp. 39–45. DOI: `10.1016/j.nima.2011.05.042`.

[55] D. Lenz. “Pulse Shapes and Surface Effects in Segmented Germanium Detectors”. PhD Thesis. Technische Universität München, Mar. 2010.

[56] Claudio Canali et al. “Electron and hole drift velocity measurements in silicon and their empirical relation to electric field and temperature”. In: *IEEE Transactions on Electron Devices* 22 (1975), pp. 1045–1047.

[57] L. Mihailescu et al. “The influence of anisotropic electron drift velocity on the signal shapes of closed-end HPGe detectors”. In: *Nucl. Instrum. Meth. A* 447 (2000), p. 350. DOI: `10.1016/S0168-9002(99)01286-3`.

[58] Bart Bruyneel, Peter Reiter, and Gheorghe Pascovici. “Characterization of large volume HPGe detectors. Part I: Electron and hole mobility parameterization”. In: *Nucl. Instrum. Meth. A* 569 (2006), p. 764. DOI: `10.1016/j.nima.2006.08.130`.

[59] B. Bruyneel, B. Birkenbach, and P. Reiter. “Pulse shape analysis and position determination in segmented HPGe detectors: The AGATA detector library”. In: *Eur. Phys. J. A* 52.3 (2016), p. 70. DOI: `10.1140/epja/i2016-16070-9`.

[60] R.N. Dexter, H.J. Zeiger, and Benjamin Lax. “Cyclotron Resonance Experiments in Silicon and Germanium”. In: *Phys. Rev.* 104 (1956), p. 637. DOI: `10.1103/PhysRev.104.637`.

[61] H. G. Reik and H. Risken. “Drift Velocity and Anisotropy of Hot Electrons in n Germanium”. In: *Phys. Let.* 126 (1962), p. 1737. DOI: `doi.org/10.1103/PhysRev.126.1737`.

[62] M.S. Tyagi. *Introduction to Semiconductor Materials and Devices.* John Wiley & Sons Australia, Limited, 2003. ISBN: 9780471671336.

[63] M. B. Prince. “Drift Mobilities in Semiconductors. I. Germanium”. In: *Phys. Rev.* 92 (1953), p. 681. DOI: `10.1103/PhysRev.92.681`.

[64] I. Abt et al. “Measurement of the temperature dependence of pulse lengths in an n-type germanium detector”. In: *Eur. Phys. J. Appl. Phys.* 56 (Dec. 21, 2011). DOI: `10.1051/epjap/2011110110`. arXiv: `1112.5033v1 [nucl-ex]`.

[65] W. Shockley. “Currents to Conductors Induced by a Moving Point Charge”. In: *Journal of Applied Physics 9* (1938).

[66] S. Ramo. “Currents Induced by Electron Motion”. In: *Proceedings of the IRE* 27.9 (1939), pp. 584–585. DOI: `10.1109/JRPROC.1939.228757`.

[67] F. Faulstich. “Inbetriebnahme des GALATEA Teststandes zur Untersuchung segmentierter Germanium-Detektoren”. Diploma Thesis. Ludwig-Maximilians-Universität, May 2011.

[68] I. Abt et al. “The GALATEA test-facility for high purity germanium detectors”. In: *Nuclear Instruments and Methods in Physics Research Section A* 782 (May 2015), pp. 56–62. DOI: `10.1016/j.nima.2015.02.007`. arXiv: `1409.0493`.

[69] I. Abt and et al. “The GALATEA Test-Facility”. In: *Physics Procedia* 61 (2015), pp. 750–758. ISSN: 1875-3892. DOI: `http://dx.doi.org/10.1016/j.phpro.2014.12.095`.

[70] S. Irlbeck. “The GALATEA Test Facility and a First Study of α-induced Surface Events in a Germanium Detector”. PhD Thesis. Ludwig-Maximilians-Universität, Mar. 2014.

[71] L. Garbini. “Alpha-event characterization for germanium detectors”. PhD Thesis. Ludwig-Maximilians-Universität, May 2016.

[72] *SIS3316 Family 16 Channel VME Digitizer*. Struck Innovative Systeme GMBH. 2014. URL: `http://www.struck.de/sis3316-2014-03-20.pdf`.

[73] S. Agostinelli et al. “Geant4 — A Simulation Toolkit”. In: *Nuclear Instruments and Methods in Physics Research Section A* 506.3 (2003), pp. 250–303. ISSN: 0168-9002. DOI: `https://doi.org/10.1016/S0168-9002(03)01368-8`.

[74] J. Allison et al. “Geant4 developments and applications”. In: *IEEE Transactions on Nuclear Science* 53.1 (2006), pp. 270–278.

[75] J. Allison et al. “Recent developments in Geant4”. In: *Nuclear Instruments and Methods in Physics Research Section A* 835 (2016), pp. 186–225. ISSN: 0168-9002. DOI: `https://doi.org/10.1016/j.nima.2016.06.125`.

[76] D. Radford. *Majorana Siggen*. `https://radware.phy.ornl.gov/MJ/mjd_siggen/`. Accessed: 2020-08-26.

[77] L. Hauertmann et al. *SolidStateDetectors.jl Website*. `https://github.com/JuliaPhysics/SolidStateDetectors.jl`. Accessed: 2020-08-26.

[78] Jeff Bezanson et al. “Julia: A fresh approach to numerical computing”. In: *SIAM Review* 59.1 (2017), p. 65. DOI: `10.1137/141000671`.

[79] Jeff Bezanson et al. *Julia Website*. `https://julialang.org/`. Accessed: 2020-08-26.

[80] Jeffrey Regier et al. In: *Journal of Parallel and Distributed Computing* 127 (2019), pp. 89–104. ISSN: 0743-7315. DOI: `https://doi.org/10.1016/j.jpdc.2018.12.008`.

[81] James R. Nagel. *Solving the Generalized Poisson Equation Using the Finite-Difference Method (FDM)*. Feb. 2012.

[82] Iris Abt et al. “Alpha-event and surface characterisation in segmented true-coaxial HPGe detectors”. In: *Nuclear Instruments and Methods in Physics Research Section A* 858 (June 2017), pp. 80–89. DOI: `10.1016/j.nima.2017.03.057`. arXiv: `1611.00165v1`.

[83] *The Lund/LBNL Nuclear Data Search*. `http://nucleardata.nuclear.lu.se/toi/`. 2020.

[84] Oliver Schulz et al. “BAT.jl: A Julia-Based Tool for Bayesian Inference”. In: *SN Computer Science* 2.3 (Apr. 2021), p. 210. ISSN: 2661-8907. DOI: `10.1007/s42979-021-00626-4`. URL: `https://doi.org/10.1007/s42979-021-00626-4`.

[85] Allen Caldwell et al. “Integration with an adaptive harmonic mean algorithm”. In: *International Journal of Modern Physics A* 35.24 (2020), p. 2050142. DOI: `10.1142/S0217751X20501420`.

[86] Felix Hagemann. “Dependence of signal development in germanium detectors on temperature and operating voltage”. MA thesis. Technische Universität Berlin, 2020. URL: `https://publications.mppmu.mpg.de/2020/MPP-2020-177/FullText.pdf`.

[87] *ASTAR Database - National Institute of Standards and Technology - Physical Meas. Laboratory.* `https://physics.nist.gov/PhysRefData/Star/Text/ASTAR.html`. 2021.

[88] J. Gruszko et al. "Delayed charge recovery discrimination of passivated surface alpha events in P-type point-contact detectors". In: *Journal of Physics: Conference Series* 888 (Oct. 2016). DOI: `10.1088/1742-6596/888/1/012079`.

[89] S. I. Alvis et al. "A Search for Neutrinoless Double-Beta Decay in ^{76}Ge with 26 kg-yr of Exposure from the MAJORANA DEMONSTRATOR". In: *Phys. Rev. C* 100 (2019), p. 025501. DOI: `10.1103/PhysRevC.100.025501`. arXiv: `1902.02299 [nucl-ex]`.

[90] I. J. Arnquist et al. "α-event Characterization and Rejection in Point-Contact HPGe Detectors". In: *Submitted to Phys. Rev. C* (June 2020). arXiv: `2006.13179`.

[91] *ESTAR Database - National Institute of Standards and Technology - Physical Meas. Laboratory.* `https://physics.nist.gov/PhysRefData/Star/Text/ESTAR.html`. 2021.

[92] *Energy and Momentum Spectra for Beta Decay.* `http://hyperphysics.phy-astr.gsu.edu/hbase/Nuclear/beta2.html`. Accessed: 2021-03-24.

[93] I. Abt, F. Edzards, C. Gooch, L. Hauertmann, B. Lehnert, X. Liu,S. Mertens, D. C. Radford, O. Schulz, M. Willers. "Surface characterization of p-type point contact germanium detectors". In: *To be published* (2021).